APPLIED COMPUTATIONAL ELECTROMAGNETICS SOCIETY JOURNAL

September 2020
Vol. 35 No. 9
ISSN 1054-4887

The ACES Journal is abstracted in INSPEC, in Engineering Index, DTIC, Science Citation Index Expanded, the Research Alert, and to Current Contents/Engineering, Computing & Technology.

The illustrations on the front cover have been obtained from the research groups at the Department of Electrical Engineering, The University of Mississippi.

SEPTEMBER 2020 REVIEWERS: REGULAR PAPERS

Amit Bage
Toni Björninen
Veysel Demir
Manohar Deshpande
Aliou Diallo
Tijana Dimitrijevic
Nunzia Fontana
Omid Hoseini Izadi
Binke Huang
Kathir I.
Michael Johnson
Long Li
Riyadh Mansoor
Nasimuddin Nasimuddin
Andrew Peterson
Mohammd Pourbagher
Prasanna R.
Kamalesh Sainath
R. Seetharaman
Hussein Shaman
Surinder Singh
Yu Tian
Farzad Tofigh
Bojan Trkulja
Masood Ur-Rehman
Steven Weiss
Salah Yahya
Kai-Wen Yang
Peng Yang
Xiaokang Yin
Hao Zeng
Hao Zhang
Xingqi Zhang
Bo Zhu
Wei-Hua Zong

THE APPLIED COMPUTATIONAL ELECTROMAGNETICS SOCIETY JOURNAL

Vol. 35 No. 9 September 2020

TABLE OF CONTENTS – REGULAR PAPERS

Debye Parameters of Humidity-Varying Soils for Induction Logging Techniques

Andres Velasco, Atef Z. Elsherbeni, Joseph E. Diener, and Mohammed F. Hadi

Department of Electrical Engineering
Colorado School of Mines, Golden, CO, 80401, United States
avelasco@mines.edu, aelsherb@mines.edu, jdiener@mines.edu, mhadi@mines.edu

Abstract ─ This paper focuses on the tabulation of calculated Debye coefficients for a wide range of soils for source waves ranging from 300 MHz to 2 GHz. Debye coefficients of different soils will produce accurate FDTD dispersive simulations for wireline logging purposes. The FDTD dispersion analysis is based on an Auxiliary Differential Equation (ADE) method which depends on the Debye coefficients. A complex set of soil data is acquired and used in a two-step numerical solver to calculate the Debye coefficients. For a wide range of soils, Debye coefficients were developed for one, two, and three pole expansions. Most fits for one pole fits were highly inaccurate, so the coefficients generated were disregarded. Coefficients for two and three term expansions were accurate and were generated and tabulated here.

Index Terms ─ Complex media, Debye, dispersion analysis, FDTD method, induction logging, moisture content, soils.

I. INTRODUCTION

The finite-difference time-domain (FDTD) method has been proven to efficiently simulate the propagation of waves in dispersive media [1]-[4]. With the aid of the FDTD method as well as post-processing techniques, an accurate model for oil and gas exploration can be performed [1]-[2]. It is essential to consider the electrical properties of soils in FDTD simulations to ensure an accurate model of propagating waves in them is developed. Methods to determine electrical properties of soils surrounding a borehole are known as induction logging techniques. Induction logging techniques have been developed and improved in the past years and have helped to extract natural resources [5].

Soils are characterized as dispersive media, and if the electrical properties of a particular soil are known, proper analysis and simulations can be performed [6],[7]. When adapting a cylindrical model, the comparison between the results produced by the simulation and the results obtained via wireline logging can indicate pockets of natural resources. Multi-pole models have been used in FDTD formulations to adapt dispersive wave propagation. Such multi-pole models include the Cole-Cole and Debye models [8]-[9]. Due to the nature of soils, propagating waves experience a dampening force that can be best described by a linear, first order differential equation on the polarization state of the particles within the soil [10]. This differential equation gives rise to the Debye electrical permittivity model, which can be easily implemented in an FDTD algorithm. Although the Debye model is a special case of the Cole-Cole model, using a Cole-Cole model will complicate greatly a dispersive FDTD algorithm. This is in addition to it being a model that does not accurately describe the linear dampening nature that the propagating waves experience in soils. The Debye model describes the dispersion relation for waves within the soil experiencing this relaxation. Papers like [11],[12] perform permittivity fits to determine the Debye coefficients for a variety of human tissues for frequencies up to 20 GHz, since human tissues behave in a similar manner to soils [4]. Thus, a similar analysis to the one presented in [11] can be used in this paper. In induction logging applications, low frequencies are desired to extend the distance that the wave will propagate through the soil. Therefore, the focus in this paper will be on frequencies up to 2 GHz.

Given that soils are dispersive and their permittivities change as a function of frequency of the source wave, the electric field response will be different depending on the frequency content of said source wave. In the FDTD analysis, the Debye model is used to simplify the inclusion of dispersive soils by means of an auxiliary differential equation (ADE) [4]. The ADE will have an order equal to the number of desired terms in the Debye model. Since discretizing the ADE is required, keeping a low number of terms for the Debye fit will be computationally efficient. A model is adapted where the soils are dispersive and isotropic, so their electrical properties will change with frequency, but will not change as a function of the coordinate's direction at each point in the soil. The calculation of Debye coefficients can be used in any coordinate system since the assumed medium is isotropic.

Submitted On: March 25, 2020
Accepted On: August 8, 2020

https://doi.org/10.47037/2020.ACES.J.350901

Via a 2-step numerical solver, Debye coefficients for a range of soils containing different amounts of water content are calculated and tabulated in this paper. The accuracy of the fits presented by the Debye coefficients is shown for all soil types for two and three term expansions. On a practical application, soils have a noticeable water content, so soils with a 0% moisture content were disregarded.

This paper is an extension of [7], as the method outlined in it has been improved to produce more accurate fits. Modifications on this developed method provide fits where having a higher number of poles becomes more relevant due to the higher accuracy produced.

II. BACKGROUND ON THE DEBYE MODEL

Soils change the dispersion relation of the waves propagating through them, which in turn alters their phase and group velocities. When entering soils, the dispersion model to be adapted is the Debye Model [11],[12]. This is due to how particles inside them experience a first order relaxation dampening force [10]. Much like it was performed in [11],[12], all analysis methods in this paper follow the same structure shown in them. The method adapted in this paper will also deal with the usage of attenuation values from a source wave.

We initially begin with a relaxation differential equation describing the polarization of the arranged particles within the material [13]:

$$\tau\dot{\mathbf{P}} + \mathbf{P} = \epsilon_0(\epsilon_s - \epsilon_\infty)\mathbf{E}, \tag{1}$$

where τ is the relaxation time coefficient, ε_∞ is the relative permittivity at high frequencies, and ε_s is the static permittivity. In (1), the time derivative term corresponds to the polarization rate of change of the particles.

When dealing with waves entering the material, the response of the material is described by a non-linear polarization of the molecules containing different k^{th}-order susceptibility terms $\chi^{(k)}$ the form of a Taylor expansion [10]:

$$\begin{aligned} \mathbf{P}_s &= \epsilon_o\left(\chi^{(1)}\mathbf{E} + \chi^{(2)}\mathbf{E}^2 + \chi^{(3)}\mathbf{E}^3 + ...\right) \\ \mathbf{P}_s &= \gamma^{(1)}\mathbf{P} + \gamma^{(2)}\mathbf{P}^2 + \gamma^{(3)}\mathbf{P}^3 + ... \end{aligned} \tag{2}$$

Similarly, the electric field will adapt an expansion form similar to that in (2). Each higher order magnitude will have an associated different magnitude and is denoted by $\gamma^{(k)}$. To solve for the polarization state **P**, each polarization term will be associated with the corresponding electric field term having the same order. Therefore, inserting (2) into (1) and transforming to frequency domain, it is seen that the solution for each higher order term adapts the same form. A weighting coefficient A_k will rise from the nature of the Taylor coefficients as well as different relaxation terms τ_k for each term. Thus, the polarization state in frequency domain is given by:

$$\mathbf{P}(\omega) = \sum_{k=1}^{\infty} \frac{A_k\epsilon_o(\epsilon_s - \epsilon_\infty)}{1 + j\omega\tau_k}\eta^{(k)}\mathbf{E}^k . \tag{3}$$

With the use of the auxiliary $D(\omega)$ field, one can extract the relative permittivity of the medium in frequency domain. Thus, introducing now a pole weight given by $\Delta\epsilon_k = A_k\eta^{(k)}(\epsilon_s - \epsilon_\infty)$, the Debye permittivity model is introduced as:

$$\epsilon_r(\omega) = \epsilon_\infty + \sum_{k=1}^{N}\frac{\Delta\epsilon_k}{1 + j\omega\tau_k} . \tag{4}$$

When being compared to a non-dispersive medium, the Debye model differs by the following terms:

- N : Number of terms in Debye model,
- ε_∞ : Permittivity at high frequencies,
- $\Delta\varepsilon_k$: Pole weight,
- τ_k : Relaxation time.

III. FORMULATION AND TABULATION OF DEBYE COEFFICIENTS

To properly tabulate the Debye coefficients for a given medium, dielectric measurements are needed. That is, one needs the real and imaginary components of the electrical permittivity of the soils as functions of frequency. These values will be used on a two-step algorithm that will generate an algebraic expression as a function of frequency for the relative permittivity. The coefficients within said algebraic expression will correspond to the Debye coefficients.

A. Formulation

For each associated frequency of an incoming source wave, a complex function of the permittivity is given by:

$$\epsilon_r(\omega) = \epsilon' - j\epsilon'' . \tag{5}$$

By having the set of permittivity values at each associated frequency, the MATLAB function *invfreqs* can make a rational expression for the set of permittivity values, given by:

$$\begin{aligned} \epsilon_r(j\omega) &= \frac{\sum_{k=1}^{N} b_{k-1}(j\omega)^{k-1}}{\sum_{k=1}^{N+1} a_{k-1}(j\omega)^{k-1}} , \\ &= \frac{b_0 + b_1(j\omega) + b_2(j\omega)^2 + ... + b_{N-1}(j\omega)^{N-1}}{a_0 + a_1(j\omega) + a_2(j\omega)^2 + ... + a_N(j\omega)^N} . \end{aligned} \tag{6}$$

The MATLAB *residues* function will decompose (6) as a multi-pole form similar to the form of (4), resulting in:

$$\begin{aligned} \epsilon_r(j\omega) = R + \frac{(-r_N / p_N)}{1 + j\omega(-1/p_N)} + \frac{(-r_{N-1} / p_{N-1})}{1 + j\omega(-1/p_{N-1})} + ... \\ + \frac{(-r_1 / p_1)}{1 + j\omega(-1/p_1)} . \end{aligned} \tag{7}$$

The permittivity form shown in (7) will make R be ε_∞, the $-r_k/p_k$ terms be $\Delta\varepsilon_k$, and the $-1/p_k$ be the τ_k terms, when compared with (4).

B. Data processing for fitting algorithm

Electromagnetic measurements of soils are obtained from [14], where the attenuation α and relative permittivity ε' are measured for select values of frequencies. Two samples of soils are shown in Table 1.

Table 1: Electromagnetic measurements of soils at various humidity moisture contents [14]

Clay Loam 6% Moisture		
Frequency (MHz)	**Relative Dielectric Constant ε'**	**Attenuation (dB/cm) α**
300	5.667	0.283
500	5.108	0.387
1000	4.649	0.568
2000	4.151	0.761
4000	4.024	1.14
9300	3.826	2.31
Sand 8% Moisture		
Frequency (MHz)	**Relative Dielectric Constant ε'**	**Attenuation (dB/cm) α**
300	6.957	0.249
500	6.792	0.278
1000	6.708	0.335
2000	6.533	0.535
4000	6.425	1.27
9300	5.854	2.86

Within a lossy medium, there is an associated loss factor α that can be derived from Maxwell's equations [10]. This attenuation factor depends on the imaginary term of the permittivity ε":

$$\alpha = \omega \sqrt{\frac{\mu_0 \epsilon_0 \epsilon'}{2} \left(\sqrt{1 + \left(\frac{\epsilon''}{\epsilon'} \right)^2} - 1 \right)}, \tag{8}$$

where after some algebraic manipulations, the imaginary term of the permittivity can be evaluated as:

$$\epsilon'' = \epsilon' \sqrt{\left(\frac{2\alpha^2}{\mu_0 \epsilon_0 \epsilon' \omega^2} + 1 \right)^2 - 1}, \tag{9}$$

where ε' is the relative permittivity, and ω is the angular frequency. Table 1 shows how there are six data points for each associated soil. Fits were first performed using a polynomial interpolation on the data points but resulted in larger errors on 2 pole fits than 3 pole fits. This problem was no longer present when there was no interpolation performed on the original data points. The processing of the attenuation values in Table 1 made possible the creation of the frequency-dependent values described in (5). Similar fits for the remaining soil samples were produced to obtain a larger set of complex permittivity values.

C. Results and determination of Debye coefficients

A MATLAB algorithm was developed based off of the formulation described from (4)-(7). Fits were produced for one, two, and three terms for the soils used. Papers like [11] and [12] demonstrated the validity of using this range of terms for dispersive media following the Debye model. The fits shown in Figs. 1 and 2 were produced by the current algorithm for the soils shown in Table 1.

Although all data ranged from 300 MHz - 9.3 GHz, all data was trimmed and fitted for 300 MHz - 2 GHz, since it is our range of interest for the application to be developed in the FDTD algorithm.

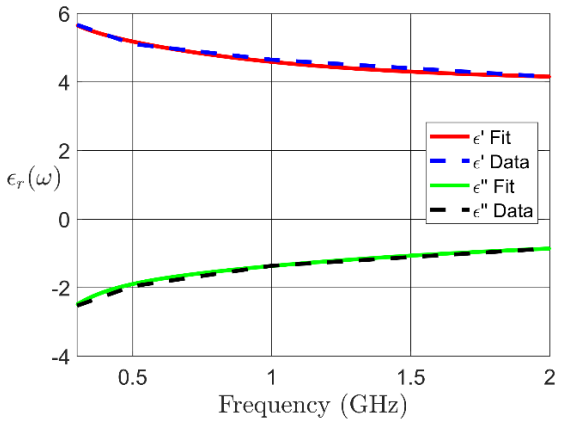

Fig. 1. 2 pole Debye fit vs. interpolated data for clay loam 6%.

Table 2: Two term Debye coefficients for clay loam 6% humidity

ε_∞	$\Delta\varepsilon_1$	$\Delta\varepsilon_2$	τ_1 (ns)	τ_2 (ns)
3.911	1.485	10.336	0.183	2.590

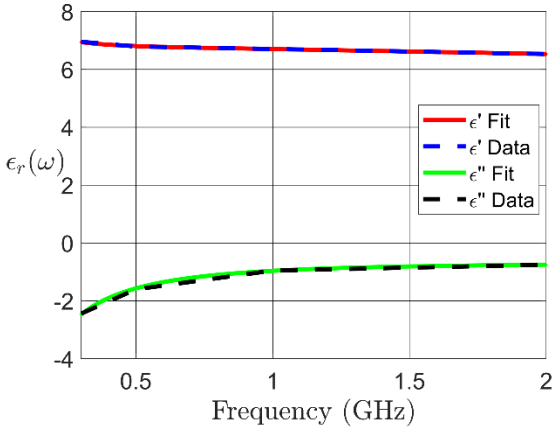

Fig. 2. 2 pole Debye fit vs. interpolated data for sand 8%.

Table 3: Two term Debye coefficients for sand 8% humidity

ε_∞	$\Delta\varepsilon_1$	$\Delta\varepsilon_2$	τ_1 (ns)	τ_2 (ns)
5.863	0.895	29.667	0.047	6.531

D. Tabulation of Debye coefficients for humidity-varying soils

The data for different types of soils was computed for one term, two terms, and three terms in the Debye expansion. Although it is desired to have fits for two poles to reduce the complexity of the ADE, it is necessary to compute fits with a higher number of poles to reduce the difference error as much as possible. Tables 4 and 5 display the computed coefficients for various soils along with their respective maximum error differences in the complex permittivity. The difference errors were computed as:

$$\% \text{ Error} = \left| \frac{\epsilon_f^{(\chi_i)} - \epsilon_d^{(\chi_i)}}{\epsilon_d^{(\chi_i)}} \right| * 100\% . \quad (10)$$

Where $\varepsilon_f^{(\chi i)}$ is the permittivity value from the fit points for either the real or imaginary part, and $\varepsilon_d^{(\chi i)}$ is the permittivity value from the data points for either the real or imaginary part. Here, (χ_i) denotes which part of the permittivity is used, either the real or imaginary part. One pole fits produced maximum errors of 31%, so they were disregarded.

Two pole fits produced errors ranging from 0.23% to 19%. While the latter percentage may seem troublesome, this error generated was a singularity in the entire frequency range. That is, the fit produced accurate results except at one point. To testify the accuracy of the fit, the root-mean-square error (RMSE) was calculated for all fits. For instance, the fit producing a 19% error in ε" also has an RMSE of 0.054, which is marginally low. The RMSE values obtained for all soil fits ranged from 0.008 to 0.087 in both ε' and ε", respectively, thus showing that the 2 pole fits were accurate. As expected, three pole fits produced more accurate fits, as is seen in Table 5.

Few values of Debye coefficients in both Tables 4 and 5 are large or negative. While this may seem concerning, they are acceptable parameters to use on the FDTD algorithm. Large valued Debye coefficients were also seen in [11],[12],[15].

Some fits for three pole expansions produced complex coefficients. For every complex coefficient produced, there was a complex conjugate coefficient associated. That is, from Table 5, whenever $\Delta\varepsilon_2$ and τ_2 are complex, $\Delta\varepsilon_3 = \Delta\varepsilon_3^*$ and $\tau_3 = \tau_3^*$. There is the case when this also holds true for $\Delta\varepsilon 1$ and $\Delta\varepsilon_2$ as well as τ_1 and τ_2. Although it may seem troublesome to have complex coefficients for the FDTD implementation, it is safe to use them because the ADE will be purely real once these coefficients are substituted in the corresponding updating equation. This is due to the linearity of the ADE produced by the Debye model and the complex conjugate pairs cancelling all imaginary components within the ADE.

IV. CONCLUSION AND FUTURE REMARKS

The Debye model is adapted to produce permittivity fits of humidity-varying soils. Adapting dielectric measurements as data to construct a set of complex permittivity values, fits were produced for the frequency range of 300 MHz - 2 GHz. Numerical fits were produced for one, two, and three poles, finding that two and three poles produced accurate fits. It was concluded that while producing a fit with a higher number of poles, there is a trade off by having a more complicated ADE to develop. A proper tabulation of the Debye coefficients for all soils encountered was produced for those seeking to use such coefficients.

Table 4: Debye fit for humidity-varying soils (2-poles fit) [300 MHz - 2 GHz]

Soil Type	ε_∞	$\Delta\varepsilon_1$	$\Delta\varepsilon_2$	τ_1 (ns)	τ_2 (ns)	**Max % Error in ε'**	**Max % Error in ε"**
Sand 1%	2.958	0.155	1.080	0.112	1.544	0.376	9.562
Sand 2%	2.915	-0.159	0.672	-0.295	0.600	0.534	11.677
Sand 4%	3.854	0.240	15.966	0.110	6.400	0.755	3.358
Sand 8%	5.863	0.895	29.667	0.047	6.531	0.227	2.831
Sandy Loam 1.5%	3.168	0.989	-0.719	0.259	-0.559	4.339	15.930
Sandy Loam 3%	3.154	0.802	-45.642	0.188	-30.193	2.572	6.393
Sandy Loam 6%	4.172	1.638	31.021	0.196	5.013	1.275	2.189
Silt Loam 2.5%	2.660	0.436	23.667	0.190	21.708	2.445	7.663
Silt Loam 5%	3.243	1.286	52.499	0.221	22.123	1.909	1.925
Clay Loam 1%	2.990	0.595	-0.262	0.352	-0.369	1.165	19.196
Clay Loam 3%	2.700	0.389	2.166	0.124	1.221	0.522	4.859
Clay Loam 6%	3.911	1.485	10.336	0.183	2.590	1.334	3.635
Clay 1%	2.683	0.301	14.247	0.162	16.212	2.108	9.735
Clay 3.5%	3.201	0.949	-3.378	0.264	-2.213	2.536	3.250
Clay 7%	4.017	3.403	230.460	0.329	113.882	7.473	16.126

Table 5: Debye fit for humidity-varying soils (3-poles fit) [300 MHz - 2 GHz]

Soil Type	ε_∞	$\Delta\varepsilon_1$	$\Delta\varepsilon_2$	$\Delta\varepsilon_3$	τ_1 (ns)	τ_2 (ns)	τ_3 (ns)	Max % Error in ε'	Max % Error in ε"
Sand 1%	2.963	0.119	-0.035	0.673	0.094	-0.237	0.879	0.118	0.572
Sand 2%	2.897	0.058	-0.079	1.105	0.098	-0.210	1.155	0.181	1.591
Sand 4%	3.852	0.211	-0.422	5.267	0.097	-0.947	2.401	0.574	1.596
Sand 8%	5.863	0.902	5.57+3.19i	5.57-3.19j	0.047	1.69+2.08j	1.69-2.08j	0.308	3.194
Sandy Loam 1.5%	3.226	-0.174	0.437	1.955	-0.094	0.167	1.152	0.148	1.417
Sandy Loam 3%	3.161	0.607	-0.167	1.954	0.163	-0.337	1.156	0.440	0.455
Sandy Loam 6%	4.175	4.871	2.97-5.08j	2.97+5.08j	0.292	0.56+0.45j	0.56-0.450j	2.024	7.677
Silt Loam 2.5%	2.679	-0.068	0.274	1.490	-0.149	0.155	1.116	0.196	1.274
Silt Loam 5%	3.246	1.514	1.40+0.92j	1.40-0.92j	0.239	0.32+1.31j	0.32-1.31j	4.362	4.657
Clay Loam 1%	2.977	0.133	-0.089	1.045	0.112	-0.142	0.948	0.181	1.488
Clay Loam 3%	2.677	0.227	0.669	4.060	0.075	0.390	4.377	0.291	0.601
Clay Loam 6%	3.915	6.626	-0.45-2.50j	-0.45+2.50j	0.322	0.34+0.33j	0.34-0.33j	3.048	10.252
Clay 1%	2.692	0.178	-0.064	1.074	0.116	-0.178	0.996	0.150	0.895
Clay 3.5%	3.202	1.213	0.81+0.58j	0.81-0.58j	0.294	-0.055+1.10j	-0.055-1.10j	7.010	2.661
Clay 7%	4.098	0.14 +0.22j	0.14-0.22j	8.062	0.059 +0.16j	0.059-0.16j	0.998	2.882	9.492

REFERENCES

[1] Y.-K. Hue, "Analysis of Electromagnetic Well-Logging Tools," *Dissertation*, Department of Electrical Engineering, Ohio State University, 2006.

[2] F. L. Teixeira, W. C. Chew, M. Straka, M. L. Oristaglio, and T. Wang, "Finite-difference time-domain simulation of ground penetrating radar on dispersive, inhomogeneous, and conductive soils," *IEEE Transactions on Geo-science and Remote Sensing*, vol. 36, no. 6, Nov. 1998.

[3] F. L. Teixeira and W. C. Chew, "Finite-difference computation of transient electromagnetic waves for cylindrical geometries in complex media," *IEEE Transactions on Geoscience and Remote Sensing*, vol. 38, no. 4, pp. 1530, July 2000.

[4] A. Z. Elsherbeni and V. Demir, *The Finite-Difference Time-Domain Method for Electro-magnetics with MATLAB Simulations*, Second edition, ACES Series on Computational Electro-magnetics and Engineering, SciTech Publishing, an Imprint of IET, Edison, NJ, 2016.

[5] S. Caldwell and C. McCoy, *Monitoring Movement of the Saltwater Transition Zone Beneath the Virginia Eastern Shore by Electromagnetic (EM)-Induction Logging*, United States Geological Survey (USGS), 2019.

[6] S.-C. Kong, "ADE-FDTD scattered-field formulation for dispersive materials," *IEEE Microwave and Wireless Components Letters*, vol. 18, no. 1, pp. 4, Jan. 2008.

[7] A. Velasco, M. F. Hadi, A. Z. Elsherbeni, and J. E. Diener, "Debye coefficients for low frequency FDTD dispersive soils analysis," *2019 International Applied Computational Electromagnetics Society Symposium - China (ACES)*, Nanjing, China, 2019.

[8] O. P. Gandhi, B.-Q. Gao, and J.-Y. Chen, "A frequency-dependent finite-difference time-domain formulation for general dispersive media," *IEEE Transactions on Microwave Theory and Techniques*, vol. 41, no. 4, pp. 658-665, May 1993.

[9] M. Loewer snd J. Igel, "FDTD simulation of GPR with a realistic multi-pole debye description of lossy and dispersive media," *2016 16th International Conference on Ground Penetrating Radar (GPR)*, June 2016.

[10] C. A. Brau, *Modern Problems in Classical Electrodynamics*, Oxford University Press, 2004.

[11] M. A. Eleiwa and A. Z. Elsherbeni, "Debye constants for biological tissues from 30 Hz to 20 GHz," *Applied Computational Electromagnetics Society Journal*, vol. 16, no. 3, pp. 202, Nov. 2001.

[12] M. Mrozowski and M. A. Stuchly, "Parameterization of media dispersive properties for FDTD," *IEEE Transactions on Antennas and Propagation*, vol. 45, no. 9, pp. 1438, Sep. 1997.

[13] I. F. Almog, M. S. Bradley, and V. Bulovic, "The Lorentz Oscillator and its Applications," Massachusetts Institute of Technology, *Lecture Notes*, Mar. 2011.

[14] R. L. Jesch, "Dielectric Measurements of Five Different Soil Textural Types as Functions of Frequency and Moisture Content," *Electro-magnetic Fields Division Center for Electronics and Electrical Engineering*, National Bureau of Standards, October 1978.

[15] F. Krewer, F. Morgan, and M. O'Halloran, "Development of accurate multi-pole Debye functions for electromagnetic tissue modelling using a genetic algorithm" *Progress in Electro-magnetics Research Letters*, vol. 43, pp. 137-147, 2013.

Andres Velasco received his B.S. degree in Engineering Physics from Colorado School of Mines, Golden, CO, United States, in 2020. He is currently pursuing his M.S degree in Electrical Engineering at the Colorado School of Mines. His research interests include wave propagation, dispersive materials, dielectric measurements, and computational electromagnetics in cylindrical coordinate systems.

Atef Z. Elsherbeni received an honor B.Sc. degree in Electronics and Communications, an honor B.Sc. degree in Applied Physics, and a M.Eng. degree in Electrical Engineering, all from Cairo University, Cairo, Egypt, in 1976, 1979, and 1982, respectively, and a Ph.D. degree in Electrical Engineering from Manitoba University, Winnipeg, Manitoba, Canada, in 1987. He started his engineering career as a part time Software and System Design Engineer from March 1980 to December 1982 at the Automated Data System Center, Cairo, Egypt. From January to August 1987, he was a Post-Doctoral Fellow at Manitoba University. Elsherbeni joined the faculty at the University of Mississippi in August 1987 as an Assistant Professor of Electrical Engineering. He advanced to the rank of Associate Professor in July 1991, and to the rank of Professor in July 1997. He was the Associate Dean of the College of Engineering for Research and Graduate Programs from July 2009 to July 2013 at the University of Mississippi. He then joined the Electrical Engineering and Computer Science (EECS) Department at Colorado School of Mines in August 2013 as the Dobelman Distinguished Chair Professor. He was appointed the Interim Department Head for (EECS) from 2015 to 2016 and from 2016 to 2018 he was the Electrical Engineering Department head. In 2009 he was selected as Finland Distinguished Professor by the Academy of Finland and TEKES. Elsherbeni is a Fellow member of IEEE and ACES. He is the Editor-in-Chief for ACES Journal, and a past Associate Editor to the Radio Science Journal. He was the Chair of the Engineering and Physics Division of the Mississippi Academy of Science, the Chair of the Educational Activity Committee for IEEE Region 3 Section, the General Chair for the 2014 APS-URSI Symposium, the President of ACES Society from 2013 to 2015, and the IEEE Antennas and Propagation Society (APS) Distinguished Lecturer for 2020-2022.

Joseph E. Diener received his Masters' degree in Electrical Engineering from the Colorado School of Mines in 2017. Currently he is a Ph.D. student at the Colorado School of Mines studying Electrical Engineering. His research interests include finite difference time domain methods, antennas, microwave measurements, and phased arrays.

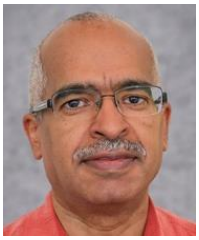

Mohammed F. Hadi received the B.Sc. degree in Electrical Engineering from Kuwait University, in 1988, and the M.Sc. and Ph.D. degrees from the University of Colorado at Boulder in 1992 and 1996, respectively. He was a Professor with the Electrical Engineering Department and an Associate Dean at Kuwait University until 2014. He was a Visiting Research Scholar with Duke University during 2007 to 2008, and with the Colorado School of Mines from 2014 to 2016. He was also an Adjunct Professor with the University of Colorado at Boulder from 2012 to 2018. He has been a Research Professor at Colorado School of Mines since 2016. Hadi was recognized as a Consulting Expert with the Kuwait's Court of Appeals since 2007. He has over ten years of experience in governmental work and consultations in the areas of engineering training, higher education planning, and Kuwait's labor profile studies. His current research interests include FDTD development for modeling electrically large structures as well as FDTD algorithm optimizations in curvilinear coordinates. Hadi served as a Board Member of the Kuwait Fund for Arab Economic Development's prestigious National Engineers Training Program for several years. He held membership and chair positions in several high-level governmental inquiries at the Kuwait's Ministries of Defense, Trade and Industry, Energy, and Higher Education, including the membership of Kuwait's Private Universities Executive Office and the Counselor for the Minister of Trade and Industry. He also served on the Technical Program Committees for several conferences by the IEEE and the Applied Computational Electromagnetics Society.

Finite-Difference Time-Domain Simulation of Arbitrary Impedance using One Port S-Parameter

Joshua M. Kast and Atef Z. Elsherbeni

Department of Electrical Engineering
Colorado School of Mines, Golden, CO 80401, USA
jkast@mines.edu, aelsherb@mines.edu

Abstract ─ Many modern radio-frequency devices comprise both lumped-element components and complex geometries. Simulation of such a device requires modeling the electromagnetic interactions with both geometric features and lumped components. We present a method for including arbitrary lumped-element components into finite-difference time-domain (FDTD) simulations. The lumped-element components, which are described by their scattering parameters, are modeled in the Yee grid as dependent voltage sources. The mathematical formulation is described, along with its implementation into a FDTD simulator. For verification, simulation results of resistive, capacitive, and inductive loads are presented, and are compared to simulation results from previous lumped-element FDTD methods. This represents a first-step in modeling multiport networks described by their scattering parameters.

Index Terms ─ Circuit analysis, computational electromagnetics, fast Fourier transform, finite-difference time-domain (FDTD), linear lumped circuit, scattering parameters, stripline circuit.

I. INTRODUCTION

The finite-difference time-domain (FDTD) technique is used to simulate the behavior of electric and magnetic fields in regions comprising arbitrary materials and geometries. In addition to modelling basic materials and geometries, the FDTD technique has been extended to model voltage and current sources, lumped-elements [1], active devices [2], and arbitrary impedances [3]. Such extensions to the fundamental FDTD method increase its utility in modelling real-world electronic devices. In this work, we present a new approach to the simulation of arbitrary impedances based on their S-parameter representation.

Several descriptions exist for the representation of S-parameter defined loads in the FDTD grid [4]–[8], which utilize a transformation from S-parameters to admittance (Y) parameters. The method we describe here is most similar to the voltage-source based approaches described by Kuo et al. [9], which describes a network through its impedance (Z) parameters, and uses a dependant voltage source to simulate the arbitrary impedance. We extend the technique of [9] by providing a model which easily integrates into an existing FDTD code [1], and naturally extends to the simulation of networks spanning multiple cells. An impedance-based formulation was selected because it allows for the use of a current probe and dependent voltage source, two commonplace FDTD simulation elements, without the need to write a specialized electric field updating equation.

Commonly available commercial and open-source FDTD packages implement varying capabilities for simulation of arbitrary impedances. While formulations for arbitrary one- and two-port impedances are described in the literature, these are not commonly implemented in FDTD packages. The commercial packages Remcom's XFDTD [10] and Keysight's EMPro [11] allow the embedding of RLC impedances into a domain, but not arbitrary S-Parameters. Similarly, CEMS software [12] allows the incorporation of RLC impedances as well as diodes into FDTD domains. The open-source MEEP [13] and OpenEMS [14] packages do not have support for embedding either S-parameter nor RLC impedances into FDTD domains.

The formulation we describe in this paper is applicable to situations where an FDTD simulation domain contains a one-port passive circuit element which is defined by its S-parameter representation. In this case, the S-parameters may be applied directly to the simulation, without a need to approximate the circuit component with a combination of lumped-elements or geometric features.

II. FORMULATION

In the FDTD time-marching loop, electric fields are updated by means of the Maxwell's equation for magnetic field:

$$\nabla \times \vec{H} = \epsilon \frac{\partial \vec{E}}{\partial t} + \sigma^e \vec{E} + \vec{J}_i. \tag{1}$$

Submitted On: February 25, 2020
Accepted On: July 19, 2020

https://doi.org/10.47037/2020.ACES.J.350902

Calculated magnetic fields are in-turn used to update electric fields:

$$\nabla\times\vec{E}=-\mu\frac{\partial\vec{H}}{\partial t}-\sigma^{m}\vec{H}-\vec{M}_{i}. \tag{2}$$

Here, $\vec{E}$ and $\vec{H}$ represent the electric and magnetic fields, respectively, as vector quantities. We denote the electrical conductivity of the medium as σ^{e}, and the induced current as $\vec{J}_{i}$. The value for magnetic current, M_{i} need not be considered in the simulations below.

By expanding the curl ($\nabla\times$) operator, we may separate (1) and (2) into 6 separate equations. Taking equation (1) and considering the calculation for only the Z component of the electric field, we get the equation:

$$\frac{\partial E_{z}}{\partial t}=\frac{1}{\epsilon_{z}}\left(\frac{\partial H_{y}}{\partial x}-\frac{\partial H_{x}}{\partial y}-\sigma_{z}^{e}E_{z}-J_{iz}\right). \tag{3}$$

The FDTD method requires that equations be discretised for computation in a 3D rectangular grid. Following the formulation of [1], we re-formulate (3) with spatial coordinates discretised to cell indices *i*, *j*, and *k*, and time discretised into time-steps denoted as *n*. With this modification, the derivatives are translated into central differences. For a Z-directed electric field at time-step $n+1/2$, we get:

$$\begin{aligned}E_{z}\big|_{i,j,k}^{n+1}=&\frac{2\epsilon_{z}\big|_{i,j,k}-\Delta t\,\sigma_{z}^{e}\big|_{i,j,k}}{2\epsilon_{z}\big|_{i,j,k}+\Delta t\,\sigma_{z}^{e}\big|_{i,j,k}}E_{z}\big|_{i,j,k}^{n}\\&+\frac{2\Delta t\left(H_{y}\big|_{i,j,k}^{n+\frac{1}{2}}-H_{y}\big|_{i-1,j,k}^{n+\frac{1}{2}}\right)}{\Delta x\left(2\epsilon_{z}\big|_{i,j,k}+\Delta t\,\sigma_{z}^{e}\big|_{i,j,k}\right)}\\&-\frac{2\Delta t\left(H_{x}\big|_{i,j,k}^{n+\frac{1}{2}}-H_{x}\big|_{i,j-1,k}^{n+\frac{1}{2}}\right)}{\Delta y\left(2\epsilon_{z}\big|_{i,j,k}+\Delta t\,\sigma_{z}^{e}\big|_{i,j,k}\right)}\\&-\frac{2\Delta t}{2\epsilon_{z}\big|_{i,j,k}+\Delta t\,\sigma_{z}^{e}\big|_{i,j,k}}J_{iz}\big|_{i,j,k}^{n+\frac{1}{2}}.\end{aligned} \tag{4}$$

Equation (4) generally describes the updating of the electric field within the FDTD grid. However, a specific behavior is required for a region defined by an S-parameter. Specifically, we create a region which exerts a voltage in response to the current passing through it in the Z direction. The measurement of this current, calculation of the voltage, and application to the FDTD cell are presented below.

For a region designated as a voltage source with voltage V_{s} at time $n+1/2$, we may write the conducted current J_{iz} as:

$$J_{iz}\big|_{i,j,k}^{n+\frac{1}{2}}=\frac{I_{z}\big|_{i,j,k}^{n+\frac{1}{2}}}{\Delta x\Delta y}=\frac{\Delta V+V_{s}\big|_{i,j,k}^{n+\frac{1}{2}}}{R_{s}}, \tag{5}$$

where ΔV is the potential difference which may already exist across the cell, which is calculated by:

$$\Delta V=\Delta z\frac{E_{z}\big|_{i,j,k}^{n+1}+E_{z}\big|_{i,j,k}^{n}}{2}. \tag{6}$$

In (6), we use the time average of two electric field values, because the electric field at time-step *n* is not precisely known. Combining (6) with (5) and (4), we get a general equation for a cell containing a voltage source:

$$\begin{aligned}E_{z}\big|_{i,j,k}^{n+1}=&\\&\frac{2\epsilon_{z}\big|_{i,j,k}-\Delta t\,\sigma_{z}^{e}\big|_{i,j,k}-\dfrac{\Delta t\Delta z}{R_{s}\Delta x\Delta y}}{2\epsilon_{z}\big|_{i,j,k}+\Delta t\,\sigma_{z}^{e}\big|_{i,j,k}+\dfrac{\Delta t\Delta z}{R_{s}\Delta x\Delta y}}E_{z}\big|_{i,j,k}^{n}\\&-\frac{2\Delta t\,V_{s}\big|_{i,j,k}^{n+\frac{1}{2}}}{R_{s}\Delta x\Delta y\left(2\epsilon_{z}\big|_{i,j,k}+\Delta t\,\sigma_{z}^{e}\big|_{i,j,k}+\dfrac{\Delta t\Delta z}{R_{s}\Delta x\Delta y}\right)}\\&+\frac{2\Delta t\left(H_{y}\big|_{i,j,k}^{n+\frac{1}{2}}-H_{y}\big|_{i-1,j,k}^{n+\frac{1}{2}}\right)}{\Delta x\left(2\epsilon_{z}\big|_{i,j,k}+\Delta t\,\sigma_{z}^{e}\big|_{i,j,k}+\dfrac{\Delta t\Delta z}{R_{s}\Delta x\Delta y}\right)}\\&-\frac{2\Delta t\left(H_{x}\big|_{i,j,k}^{n+\frac{1}{2}}-H_{x}\big|_{i,j-1,k}^{n+\frac{1}{2}}\right)}{\Delta y\left(2\epsilon_{z}\big|_{i,j,k}+\Delta t\,\sigma_{z}^{e}\big|_{i,j,k}+\dfrac{\Delta t\Delta z}{R_{s}\Delta x\Delta y}\right)}.\end{aligned} \tag{7}$$

In the case of this work, a voltage source with internal resistance is generally not needed. By taking the limit of (7) as R_{s} approaches zero, we get the formulation for a hard voltage source:

$$E_{z}\big|_{i,j,k}^{n+1}=-E_{z}\big|_{i,j,k}^{n}-\frac{2}{\Delta z}V_{s}\big|_{i,j,k}^{n+\frac{1}{2}}. \tag{8}$$

We attempt to simulate a linear lumped network by means of this voltage source. Therefore, we must calculate the value of V_{s} at each time-step, in response to the current through the network. The frequency response of a one-port RF network may be defined by its reflection coefficient Γ, which is obtained from the S-parameter S_{11}. For a network excited by a sinusoidal voltage at frequency f ($\tilde{V}(f)$), the relationship between voltage and current at a given frequency is described as [15]:

$$Z(f)=\frac{\tilde{V}(f)}{\tilde{I}(f)}=Z_{0}\frac{1+S_{11}(f)}{1-S_{11}(f)}. \tag{9}$$

For clarity, we may rewrite (9) as:

$$\tilde{V}(f)=\tilde{I}(f)Z_{11}(f). \tag{10}$$

Equation (10) describes the relationship of frequency-domain quantities of voltage and current. However, for FDTD simulation, we require voltage to be calculated in the time-domain. Taking the inverse Fourier transform of (10), we find that the operation of multiplication has transformed into convolution of

current and impedance:

$$V(t) = I(t) * \mathbb{F}^{-1}\{Z_{11}(f)\}. \quad (11)$$

While other methods [4-6], [8-9] make use of polynomial approximations of the circuit impedance, the use of convolution allows truly arbitrary impedances to be simulated, at a moderate cost in computation time. We will define the symbol $\hat{z}_{11}(t)$ as the inverse Fourier transform of $Z_{11}(f)$, giving:

$$V(t) = I(t) * \hat{z}_{11}(t). \quad (12)$$

To calculate voltage, it is necessary to measure the current through the cell at each time-step. This is accomplished by the integral form of Ampere's law:

$$I_{\text{free}} = \oint \vec{H} \cdot dl. \quad (13)$$

Applied to the Yee grid, (13) becomes:

$$I_z\Big|_{is:ie,\, js:je,k}^{n+\frac{1}{2}} = \Delta x \sum_{i=is}^{ie} \left(H_x\Big|_{i,\, js-1,k}^{n+\frac{1}{2}} - H_x\Big|_{i,\, je,k}^{n+\frac{1}{2}} \right) + \Delta y \sum_{j=js}^{je} \left(H_y\Big|_{ie,\, j,k}^{n+\frac{1}{2}} - H_y\Big|_{is-1,\, j,k}^{n+\frac{1}{2}} \right). \quad (14)$$

For accurate calculation of the current through the cell, the values of *is*, *js*, *ie*, and *je* are chosen to bound the cell containing the hard voltage source, with an additional margin of 1 cell in each direction. At each time-step, (14) is evaluated and the result saved in an array with current values for previous time-steps, enabling the convolution in (12) to be computed:

$$V_s\Big|_{i,\, j,k}^{n+\frac{1}{2}} = \sum_{m=1}^{n} I_s\Big|_{is:ie,\, js:je,k}^{m+\frac{1}{2}} \hat{z}_{11}\left(\left(n - m + \frac{1}{2} \right) \Delta t \right). \quad (15)$$

The complete updating equation for the S-parameter defined cell may now be written as:

$$E_z\Big|_{i,\, j,k}^{n+1} = -E_z\Big|_{i,\, j,k}^{n} - \frac{2}{\Delta z} \sum_{m=1}^{n} I_s\Big|_{is:ie,\, js:je,k}^{m+\frac{1}{2}} \hat{z}_{11}\left(\left(n - m + \frac{1}{2} \right) \Delta t \right). \quad (16)$$

It is important to note that the notation $I_s\Big|_{is:ie,\, js:je,k}^{m+\frac{1}{2}}$ in (16) refers to the array containing all computed values of current from the beginning of the simulation to the current time-step.

III. SIMULATION CONFIGURATION

To test this formulation, an FDTD simulation was created using the MATLAB codes presented in [1], with modifications to support a voltage-source controlled by the formulation described in Section II. The configuration of the computational domain is illustrated in Fig. 1.

The circuit comprises a 20 mm length of conductive stripline suspended in a dielectric material with a permittivity of $\epsilon_r = 3.2$. Above and below the dielectric material are thin sheets modelled as perfect electric conductors. The stripline width of 1.2 mm, and the separation between the top and bottom PEC plates of 2.0 mm, was optimized in previous FDTD simulations to give an 50Ω characteristic impedance for the transmission line.

For simulation, a uniform cell size of $\Delta x = \Delta y = \Delta z = 0.1\text{mm}$ was chosen. The simulation was performed with a time step of $\Delta t = 173.325$ fs, and the domain was excited with a Gaussian pulse chosen to give a minimum of 40 cells per wavelength. For all simulations, 20000 time-steps were carried out. The domain is excited by a single voltage source in the plane of the stripline conductor, producing a Gaussian pulse of with a 1V amplitude.

IV. SIMULATION RESULTS

For the resistive circuit described below, a simulation was carried out using the lumped-element (LE-FDTD) formulation described in [1], [16], [17]. For capacitive (RC) and inductive (RL) circuits, the appropriate formulation described in [3] was simulated using the CEMS software [12].

Then the LE-FDTD, RL, or RC representation of the circuit component was replaced with a voltage source, which was updated at each time-step according to the formulation in Section II. For each simulation, voltage and current were recorded at points indicated in Fig. 1. These values are plotted in the time and frequency domain for comparison.

A. Resistive 50Ω load

To test the formulation described in Section II a simulation was carried out using an ideal 50Ω load terminating the stripline shown in Fig. 1. For a structure with $Z_0 = 50\Omega$, terminated in a 50Ω load, the S_{11} is expected to be 0 for all frequencies. Using (9), we find $Z_{11} = 50\Omega$ across all frequencies. The simulated S- parameter defined load was compared to a LE-FDTD simulated 50Ω resistor in place of the 1 port S_{11} element.

Time domain results from the simulation are plotted in Fig. 2 as voltage and current through the probes illustrated in Fig. 1. At the beginning of the simulation, the Gaussian pulse excitation pulse may be seen followed by several reflections. There is a good agreement both in magnitude and timing between the S-parameter defined load (port) of Section II and of the LE-FDTD simulation.

The time-domain results were converted to frequency-domain S-parameters for comparison, as plotted in Fig. 3. As with the time-domain results, we see good agreement between the S-parameters, both in magnitude and in phase.

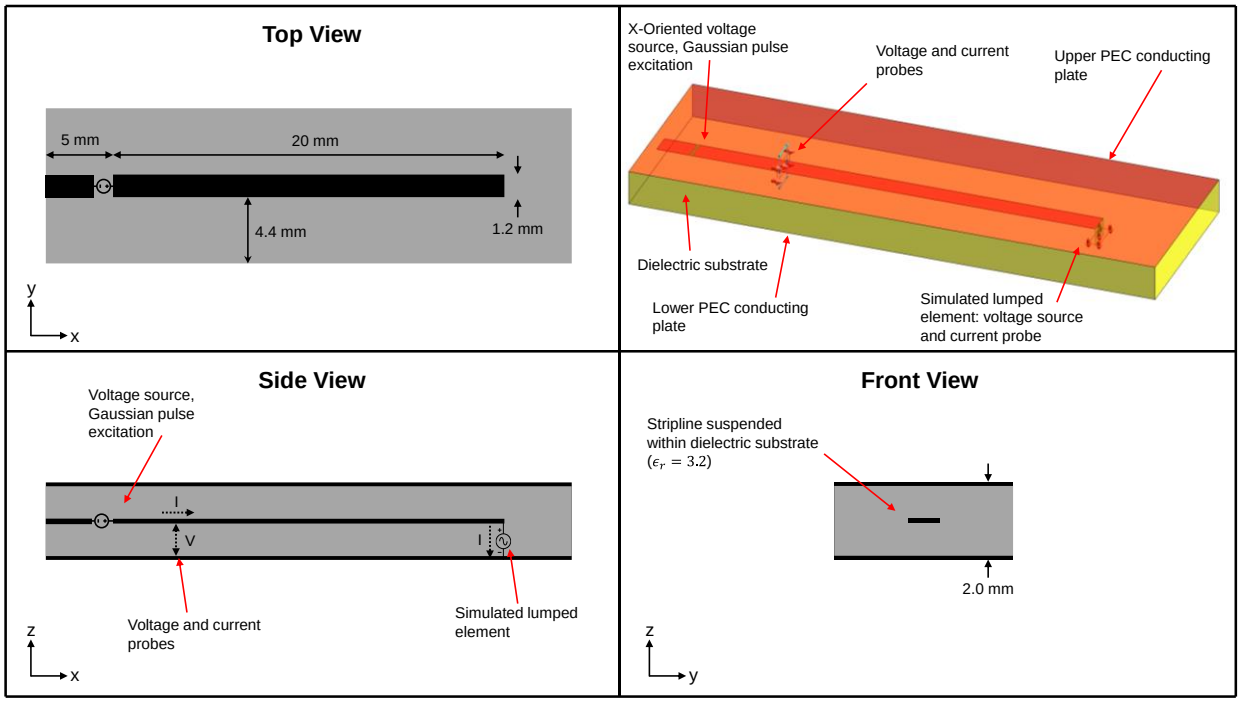

Fig. 1. Stripline configuration for FDTD simulation.

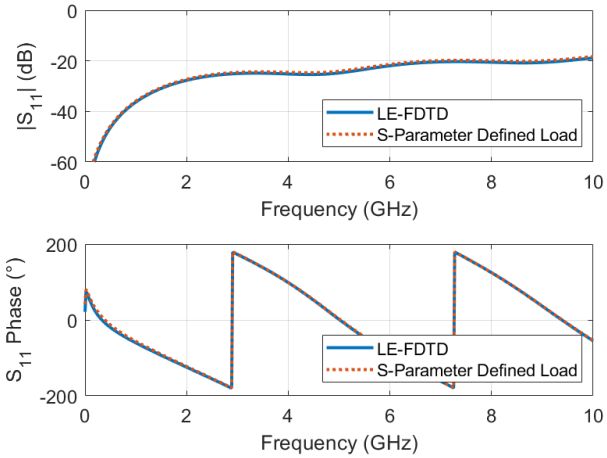

Fig. 2. Computed time-domain voltage and current based on results for lumped-element and S-parameter simulation with 50Ω resistive load.

B. Capacitive (RC) load

To further test the simulation, a lumped-load comprising a 10 µF capacitor in parallel with a 50 Ω resistor was simulated using both the S-parameter defined load and the LE-FDTD method. The S-parameters for this configuration were calculated as described in [18].

Time-domain results from this simulation are plotted in Fig. 4. As with the resistive 50Ω load case, good agreement is seen between the S-parameter defined load (port) and the LE-FDTD representations of the RC circuit. Similarly, the frequency-domain results plotted in Fig. 5 align well: at low frequencies, the impedance of the capacitor is large, and the effect of the 50Ω load dominates. At higher frequencies, the impedance of the capacitor decreases, and the reflection of the RC load decreases.

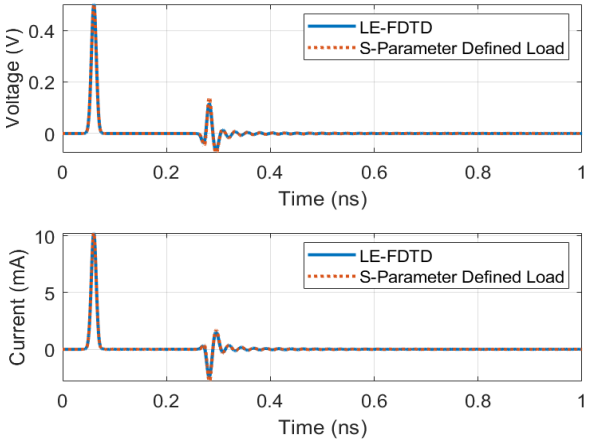

Fig. 3. Frequency-domain results from the resistive load simulation.

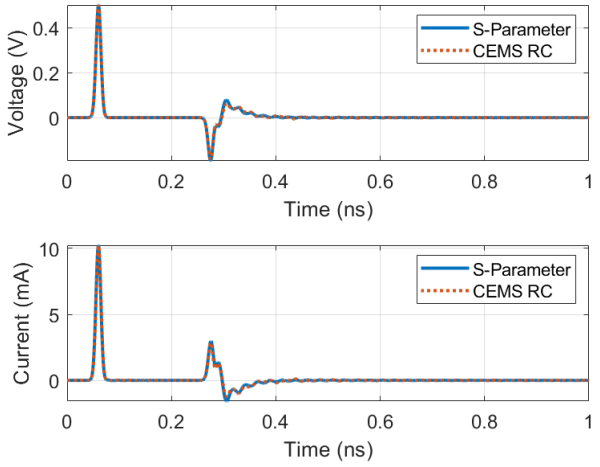

Fig. 4. Time-domain results from the RC load simulation.

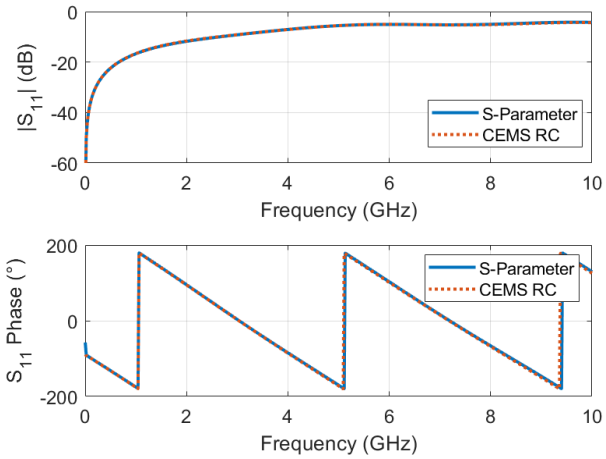

Fig. 5. Frequency-domain results from the RC load simulation.

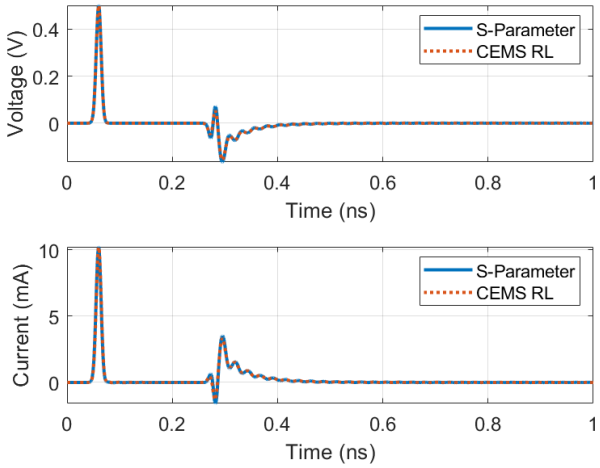

Fig. 6. Time-domain results from the RL load simulation.

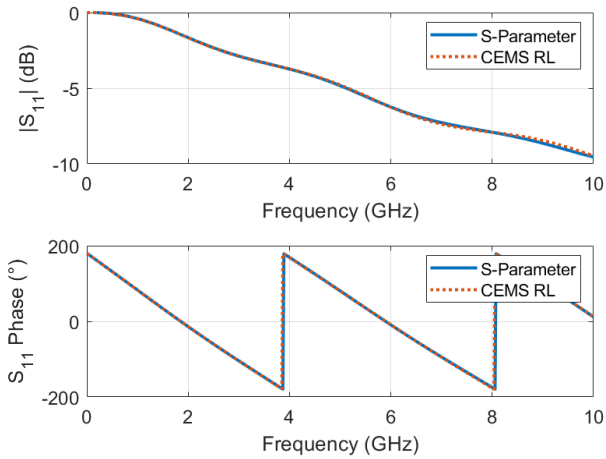

Fig. 7. Frequency domain results from the RL load simulation.

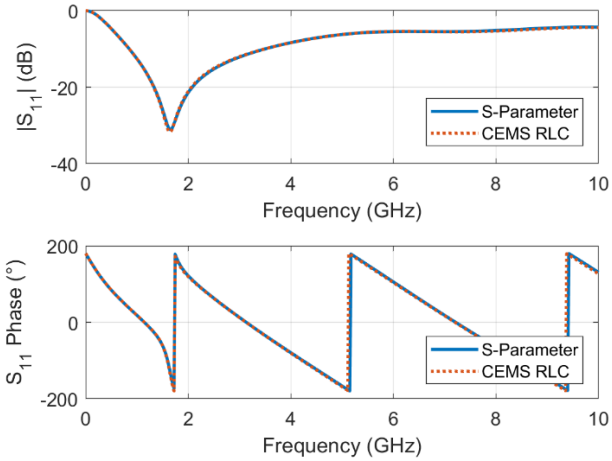

Fig. 8. Frequency-domain results from parallel RLC circuit.

C. Inductive (RL) load

An RL load comprising 50Ω resistor in parallel with a 10 nH inductor was simulated. As in the previous simulations, an LE-FDTD model was compared with an S-parameter defined load. The results from this simulation are plotted in Fig. 6 and transformed to frequency domain in Fig. 7. From the frequency-domain results, we observe the effect of the RL circuit: as frequency is increased, it becomes increasingly well-matched as the impedance of the inductor decreases.

D. Resonant (Parallel RLC) load

As a final test of the formulation, the stripline was terminated with a network comprising a 50Ω resistor, 10 nH inductor, and a 1 pF capacitor connected in parallel. Frequency-domain results from this simulation are plotted in Fig. 8. Again good agreement is obtained from the LE-FDTD model and the S-parameter simulation based on

the formulation described in this paper.

V. DISCUSSION

The formulation developed in this paper for a one port S-parameter model is used to represent resistive, capacitive, inductive, and RLC loads as terminations for a stripline transmission line FDTD simulation. These simulation results were compared to LE-FDTD simulations of the same geometries, where existing formulations for resistive capacitive, and inductive networks were used [1,3]. In all cases, good agreement is observed from the two different model simulations.

It is important to note that the agreement between the simulation results did not diminish when the complexity of the network was increased. The parallel RLC network contains two reactive components: an inductor and capacitor. This suggests that this technique may be applicable even for passive loads comprising many components in different configurations.

VI. CONCLUSION

In this work, we present an application of voltage sources and current probes, widely implemented in FDTD packages, to model arbitrary loads defined by S-parameters. By converting S-parameters to time-domain Z (impedance) parameters, it is possible to simulate the arbitrary impedance as a dependant voltage source within the FDTD grid. The method described in this paper therefore allows for embedding of an arbitrary one-port impedance into an FDTD domain, where the impedance is described in the form of its S-parameters.

REFERENCES

[1] A. Z. Elsherbeni and V. Demir, "The finite-difference time-domain method for electromagnetics with Matlab simulations," *Raleigh: The Institution of Engineering and Technology*, 2016.

[2] K. Elmahgoub and A. Z. Elsherbeni, "FDTD implementations of integrated dependent sources in full-wave electromagnetic simulations," *Applied Computational Electromagnetics Society (ACES) Journal*, vol. 29, no. 12, pp. 1093-1101, Dec. 2014.

[3] V. Demir, "Formulations for modeling voltage sources with RLC impedances in the FDTD method," *Applied Computational Electromagnetics Society (ACES) Journal*, vol. 31, no. 9, pp. 1020-1027, Sep. 2016.

[4] Y. Wang and S. Langdon, "FDTD simulation of real lumped components and RF devices," in *2016 10th European Conference on Antennas and Propagation (EuCAP)*, pp. 1-4, 2016.

[5] T.-L. Wu, S.-T. Chen, and Y.-S. Huang, "A novel approach for the incorporation of arbitrary linear lumped network into FDTD method," *IEEE Microw. Wirel. Compon. Lett.*, vol. 14, no. 2, pp. 74-76, Feb. 2004.

[6] X. Ye and J. L. Drewniak, "Incorporating two-port networks with S-parameters into FDTD," *IEEE Microw. Wirel. Compon. Lett.*, vol. 11, no. 2, pp. 77-79, Feb. 2001.

[7] J. Zhang and Y. Wang, "FDTD analysis of active circuits based on the S-parameters [microwave hybrid ICs]," in *Proceedings of 1997 Asia-Pacific Microwave Conference*, vol. 3, pp. 1049-1052 1997.

[8] H. E. A. El-Raouf, W. Yu, and R. Mittra, "Application of the Z-transform technique to modelling linear lumped loads in the FDTD," *Antennas Propag. IEE Proc. - Microw.*, vol. 151, no. 1, pp. 67-70, Feb. 2004.

[9] C.-N. Kuo, R.-B. Wu, B. Houshmand, and T. Itoh, "Modeling of microwave active devices using the FDTD analysis based on the voltage-source approach," *IEEE Microw. Guid. Wave Lett.*, vol. 6, no. 5, pp. 199-201, May 1996.

[10] *XFDTD*, State College, PA: Remcom, 2020.

[11] *EMPrio.* Santa Rosa, CA: Keysight, 2020.

[12] V. Demir and A. Elsherbeni, "Computational Electromagntics Simulator (CEMS)," Software Package Version 4, Aug. 2020.

[13] A. Oskooi, D. Roundy, M. Ibanescu, P. Bermel, J. D. Joannopoulos, and S. G. Johnson, "MEEP: A flexible free-software package for electromagnetic simulations by the FDTD method," *Computer Physics Communications*, vol. 181, pp. 687-702, 2010

[14] T. Liebig, A. Rennings, S. Held, and D. Erni, "openEMS – A free and open source equivalent-circuit (EC) FDTD simulation platform supporting cylindrical coordinates suitable for the analysis of traveling wave MRI applications," *International Journal of Numerical Modelling: Electronic Networks, Devices and Fields*, vol. 26, no. 6, pp. 680-696, 2013.

[15] D. A. Frickey, "Conversions between S, Z, Y, H, ABCD, and T parameters which are valid for complex source and load impedances," *IEEE Trans. Microw. Theory Tech.*, vol. 42, no. 2, pp. 205-211, Feb. 1994.

[16] W. Sui, D. A. Christensen, and C. H. Durney, "Extending the two-dimensional FDTD method to hybrid electromagnetic systems with active and passive lumped elements," *IEEE Trans. Microw. Theory Tech.*, vol. 40, no. 4, pp. 724-730, Apr. 1992.

[17] M. Piket-May, A. Taflove, and J. Baron, "FD-TD modeling of digital signal propagation in 3-D circuits with passive and active loads," *IEEE Trans. Microw. Theory Tech.*, vol. 42, no. 8, pp. 1514-1523, Aug. 1994.

[18] D. M. Pozar, *Microwave Engineering*, 4th Edition. Hoboken, NJ: Wiley, 2011.

Joshua M. Kast is a Ph.D. candidate at Colorado School of Mines, Department of Electrical Engineering. He received his Bachelor of Science degree in Chemistry, and Master of Science degree in Electrical Engineering in 2011 and 2017 respectively, both from Colorado School of Mines. His current areas of research include computational electromagnetics with emphasis on the finite-difference time-domain method, and measurement of nonlinear microwave devices.

Atef Z. Elsherbeni received an honor B.Sc. degree in Electronics and Communications, an honor B.Sc. degree in Applied Physics, and a M.Eng. degree in Electrical Engineering, all from Cairo University, Cairo, Egypt, in 1976, 1979, and 1982, respectively, and a Ph.D. degree in Electrical Engineering from Manitoba University, Winnipeg, Manitoba, Canada, in 1987. He started his engineering career as a part time Software and System Design Engineer from March 1980 to December 1982 at the Automated Data System Center, Cairo, Egypt. From January to August 1987, he was a Post-Doctoral Fellow at Manitoba University. Elsherbeni joined the faculty at the University of Mississippi in August 1987 as an Assistant Professor of Electrical Engineering. He advanced to the rank of Associate Professor in July 1991, and to the rank of Professor in July 1997. He was the Associate Dean of the college of Engineering for Research and Graduate Programs from July 2009 to July 2013 at the University of Mississippi. He then joined the Electrical Engineering and Computer Science (EECS) Department at Colorado School of Mines in August 2013 as the Dobelman Distinguished Chair Professor. He was appointed the Interim Department Head for (EECS) from 2015 to 2016 and from 2016 to 2018 he was the Electrical Engineering Department Head. In 2009 he was selected as Finland Distinguished Professor by the Academy of Finland and TEKES. Elsherbeni is a Fellow member of IEEE and ACES. He is the Editor-in-Chief for ACES Journal, and a past Associate Editor to the Radio Science Journal. He was the Chair of the Engineering and Physics Division of the Mississippi Academy of Science, the Chair of the Educational Activity Committee for IEEE Region 3 Section, the general Chair for the 2014 APS-URSI Symposium, the president of ACES Society from 2013 to 2015, and the IEEE Antennas and Propagation Society (APS) Distinguished Lecturer for 2020-2022.

Non-quasi-static Effects Simulation of Microwave Circuits based on Physical Model of Semiconductor Devices

Ke Xu, Xing Chen, and Qiang Chen

College of Electronics and Information Engineering
Sichuan University, Chengdu, Sichuan 610065, China
xingc@live.cn

Abstract ─ This work explores analyzing the non-quasi-static effects of a microwave circuit by employing a physical model-based field-circuit co-simulation method. Specifically, it uses the semiconductor physical model to characterize the semiconductor devices, and simulates the lumped circuit by cooperating semiconductor physical equations into Kirchhoff's circuit equations. Then the lumped circuit simulation is hybridized with the finite-difference time-domain (FDTD) simulation by interfacing EM (electromagnetic) field quantities with lumped-element quantities at each timestep. Taken a microwave limiter circuit as an example, the simulation results agree well with the measured results, which prove that this method can characterize non-quasi-static effects well. As a comparison, the equivalent circuit model-based co-simulation cannot characterize the non-quasi-static effects accurately.

Index Terms ─ Full-wave simulation, non-quasi-static effects, PIN microwave limiter, semiconductor physical model.

I. INTRODUCTION

To analyze the microwave circuit and evaluate its electromagnetic compatibility characteristics, the field-circuit co-simulation method is widely used [1]. It solves Maxwell's equations and Kirchhoff's equations simultaneously to characterize interactions between electromagnetic waves and active/passive circuit elements. In the field-circuit co-simulation method, semiconductor devices' nonlinear characteristics play an important role [2]. Especially as the operating frequency increases, the nonlinear non-quasi-static effects of semiconductor devices cannot be ignored anymore [3]. Because in the quasi-static effects, the channel charge is assumed to be equilibrium once biases are applied, thus the finite charging time of the carriers in the inversion layer is ignored [3]. This gives erroneous simulation results for signals with a working time period comparable to or smaller than the channel transit time [3]. Hence, more and more researchers aim at modeling and simulating the non-quasi-static effects of microwave circuits [3-6].

By now, the non-quasi-static effects of microwave circuits are mainly simulated by the equivalent circuit model-based field-circuit co-simulation method [3-6]. For example, non-quasi-static models of the Tunneling FETs [4] and MOSFET [5,6] are proposed, which all belong to the equivalent circuit model. However, the equivalent circuit models still do not have enough accuracy, because the models are obtained with an approximation to the physical equations [5]. Moreover, the parameters within the models are not easy to be determined [6]. And in those cases, the physical model of semiconductor devices is of great advantage and highly desirable, which is based on the physical equations of the semiconductor devices and highly accurate [7].

Furthermore, the current studies on physical model-based simulation of circuits mainly don't involve the electromagnetic computation [8-11] or rarely explored simulating non-quasi-static effects of circuits working at high frequencies [12-15]. One of the reasons is that the complicated physical model-based simulation needs to solve not only the semiconductor physical equations but also Maxwell's equations [7]. Moreover, constructing a previse model and extracting precise physical parameters of semiconductor devices are crucial in the simulation of circuits working at high frequencies [16]; as some extracted parameters usually work well at low frequencies but badly at high frequencies. Hence, current investigations on physical simulation of circuits at high frequency don't involve electromagnetic computation, or they are limited to special self-designed semiconductor devices with known physical parameters rather commercial semiconductor devices [8-11].

Hence, this work focuses on analyzing the non-quasi-static effects of a microwave circuit by the physical model-based field-circuit co-simulation. In this method, the semiconductor physical equations are cooperated into Kirchhoff's equations to obtain node voltages and branch currents of a lumped circuit, then this circuit simulation is coupled with FDTD simulation

Submitted On: April 15, 2020
Accepted On: May 24, 2020

https://doi.org/10.47037/2020.ACES.J.350903

by interfacing quantities between them. Moreover, a commercial PIN diode limiter circuit is taken as an example, which shows strongly non-quasi-static effects, because the length of the base region is thin enough. The limiter circuit is simulated by the physical model-based field-circuit co-simulation, and the accuracy of this method in simulating non-quasi-static effects is validated by comparing it with the measured results.

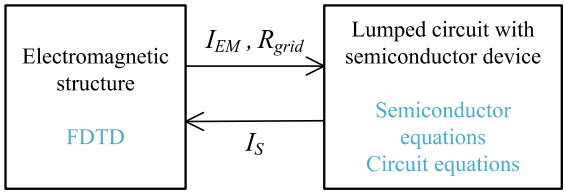

Fig. 1. The division and interfacing principle of the field-circuit hybrid system.

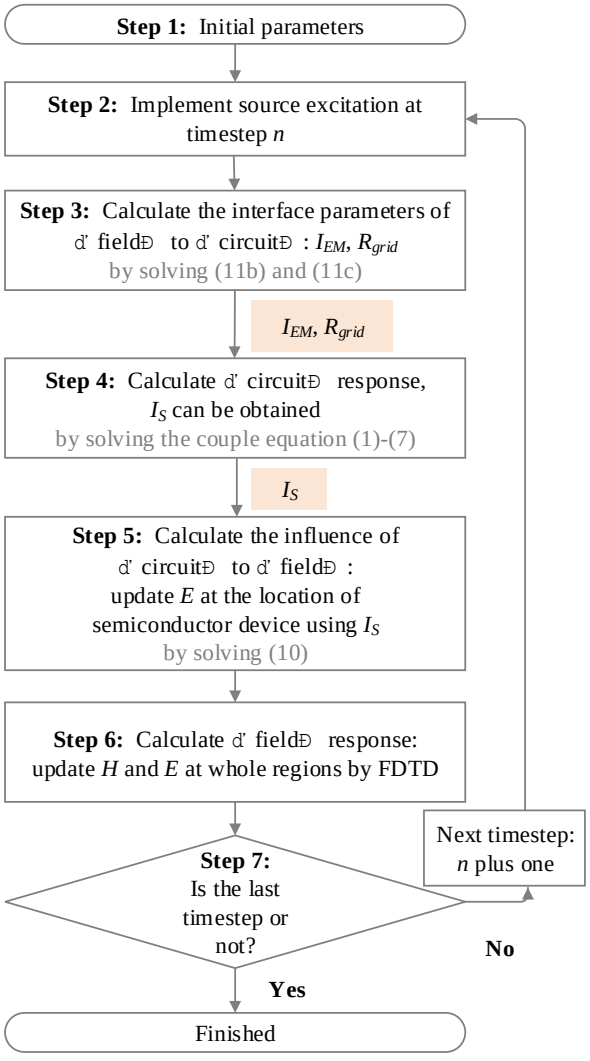

Fig. 2. The physical model-based field-circuit co-simulation procedure.

II. SIMULATION METHOD

In the co-simulation method, the filed-circuit hybrid system is divided into two parts [17]: (1) the distributed electromagnetic structure, which is characterized by Maxwell's equations; (2) the lumped circuit comprising with semiconductor devices, which is characterized by semiconductor equations and Kirchhoff's equations. The two parts are coupled by interfacing lumped circuit quantities U and I, with electromagnetic-field quantities $\boldsymbol{E}$ and $\boldsymbol{H}$, as shown in Fig. 1.

The simulation flowchart is shown in Fig. 2. At each timestep, after implementing source excitation, the key four steps are step 3-6: Step 4 and 6 calculate "circuit" and "field" response, respectively; step 3 and step 5 calculate the interface parameters I_{EM}, R_{grid} and I_s between the "field" and "circuit" parts. After these steps, it will march to the next timestep. These key steps will be introduced as follows.

A. Step 4: The physical model-based lumped circuit simulation

The lumped circuit is solved by using Kirchhoff's current equation. In a lumped circuit, assume that a lumped element is located between $(k\text{-}1)^{th}$ and k^{th} node, the relationship between its current I_j and node voltage U_k and U_{k-1} is described in (1). According to the Kirchhoff's current equation [17], the sum of all currents leaving a node is zero, as (2):

$$I_j = \psi(U_k, U_{k-1}), \tag{1}$$

$$\sum I_j = 0. \tag{2}$$

After substituting (1) to (2), (2) is solved by the Newton-Raphson iteration method [17]. Hence, the transient voltage and current of the lumped circuit can be obtained.

For a lumped circuit element, such as a resistor or a capacitance, the relationship described in (1) can be obtained by analytic equations.

For a specific semiconductor device, it is modeled by the drift-diffusion physical model, which can characterize the non-quasi-static effects well, as the equation group (3-7) [18]:

$$\boldsymbol{J}_{\mathrm{n}} = qD_{\mathrm{n}}\nabla n_{\mathrm{e}} - q\mu_{\mathrm{n}} n_e \nabla\varphi, \tag{3}$$

$$\boldsymbol{J}_{\mathrm{p}} = -qD_{\mathrm{p}}\nabla p - q\mu_{\mathrm{p}} p\nabla\varphi, \tag{4}$$

$$\partial n_{\mathrm{e}}/\partial t = q^{-1}\nabla\cdot\boldsymbol{J}_{\mathrm{n}} + G - R, \tag{5}$$

$$\partial p/\partial t = -q^{-1}\nabla\cdot\boldsymbol{J}_{\mathrm{p}} + G - R, \tag{6}$$

$$\nabla\cdot(\varepsilon_{\mathrm{s}}\nabla\varphi) = q(n_{\mathrm{e}} - p + N_A - N_D). \tag{7}$$

Equation (3) and (4) are current equations for electrons and holes in a semiconductor, equation (5) and (6) are continuity equations for electron and hole, equation (7) is Poisson's equation, where J_n and J_p are the electron and hole current densities, q is the electronic charge, D_n and D_p are the hole and electron diffusion coefficients, n_e and p are the electron and hole density respectively, μ_n and μ_p are the hole and electron mobility

respectively, φ is the electric potential, t is time, ε_s is the permittivity of the semiconductor material, R is electron-hole recombination rate, G is electron-hole generation rate, N_A is acceptor impurity concentration, and N_D is donor impurity concentration.

Discrete (3-7) on the mesh of the semiconductor device chip's 1D physical model, and solve the discrete equations in time domain by the finite difference method [19], the relationship between voltage and current of the semiconductor device can be obtained.

In conclusion, the characteristics of the lumped circuit comprising with semiconductor devices can be obtained by solving the coupled equations (1-7).

B. Step 6: The FDTD method

In the filed-circuit co-simulation method, the electromagnetic structure part is simulated by Maxwell's equations (8-9) by the FDTD method [20]:

$$\nabla \times \mathbf{E} = -\mu \frac{\partial \mathbf{H}}{\partial t}, \tag{8}$$

$$\nabla \times \mathbf{H} = \mathbf{J} + \varepsilon \frac{\partial \mathbf{E}}{\partial t}, \tag{9}$$

where $\boldsymbol{E}$ is the electric field, $\boldsymbol{H}$ is the magnetic intensity, ε is the permittivity, μ is the permeability, $\boldsymbol{J}$ is the current density.

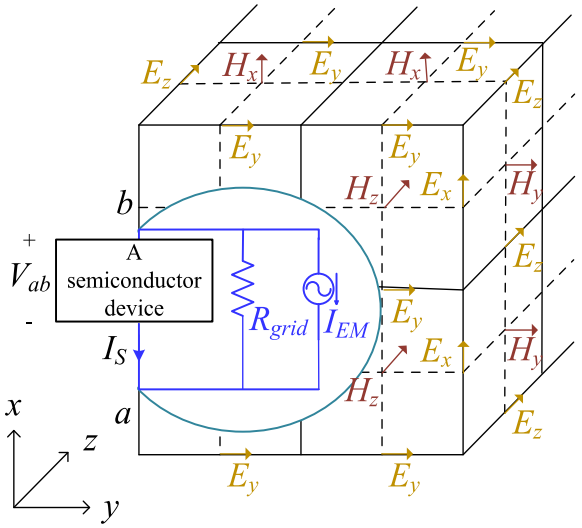

Fig. 3. A semiconductor device is located on the Yee grid of a distributed electromagnetic structure.

C. Step 3, 5: The field-circuit interfacing method

At the location where the semiconductor device is located, the electric field $\boldsymbol{E}$ and magnetic intensity $\boldsymbol{H}$ need to be specially treated to interface "field" and "circuit" parts, which is shown as follows.

Assume that a semiconductor device is located along the x-axis from a point to b point on the Yee grid, as shown in Fig. 3. The current through the semiconductor device is I_s. On the Yee grid from a point to b point, we assume that the permittivity ε and mesh are uniform for simplicity, equation (9a) can be discretized to (10a) [17], the discretization can also be generalized to the ununiform situation:

$$E^{n+1}_{x(i+\frac{1}{2},j,k)} = \mathrm{K}^{n+1}_{xijk} - \Gamma^{n+1}_{xijk} \cdot I^{n+1}_{sx}, \tag{10a}$$

where

$$\Gamma^{n+1}_{xijk} = \frac{dt}{\varepsilon dydz}, \tag{10b}$$

$$\mathrm{K}^{n+1}_{xijk} = E^{n}_{x(i+\frac{1}{2},j,k)} + \Gamma^{n+1}_{xijk} \cdot [(H^{n+\frac{1}{2}}_{z(i+\frac{1}{2},j+\frac{1}{2},k)} - H^{n+\frac{1}{2}}_{z(i+\frac{1}{2},j-\frac{1}{2},k)}) \cdot dz - (H^{n+\frac{1}{2}}_{y(i+\frac{1}{2},j,k+\frac{1}{2})} - H^{n+\frac{1}{2}}_{z(i+\frac{1}{2},j,k-\frac{1}{2})}) \cdot dy], \tag{10c}$$

where Γ and K are intermediate variables, the subscript index i, j, k indicate the location on Yee grid at x, y, z direction, respectively; the superscript index n indicates the timestep; dx, dy, and dz are cell sizes at corresponding directions.

Assume that the voltage across the semiconductor device is V_{ab}, which can be obtained by integrating the electric field from a point to b point, hence (10a) is integrated to (11a) [17]:

$$V^{n+1}_{ab} = [(I^{n+1}_{x})_{EM} - I^{n+1}_{sx}](R^{n+1}_{x})_{grid}, \tag{11a}$$

where

$$(R^{n+1}_{x})_{grid} = \sum_{(i_a,j_a,k_a)}^{(i_b,j_b,k_b)} \Gamma^{n+1}_{xijk} dx, \tag{11b}$$

$$(I^{n+1}_{x})_{EM} = \frac{\sum_{(i_a,j_a,k_a)}^{(i_b,j_b,k_b)} \mathrm{K}^{n+1}_{xijk} dx}{(R^{n+1}_{x})_{grid}}. \tag{11c}$$

In (11a), I_{EM}, R_{grid}, and I_s can equivalently form a parallel lumped circuit, as shown in Fig. 3. By this equivalent circuit, the "field" and "circuit" parts are interfaced. In this parallel circuit, I_s is the current through the semiconductor device; I_{EM} and R_{grid} are equivalent circuit model of the distributed electromagnetic structure at timestep $(n+1)$.

Hence in the flowchart, I_{EM} and R_{grid} are calculated by (11a) and (11b) in step 3, which characterize the effect of the "field" to "circuit". Then they are passed to step 4, the formed parallel circuit is calculated by the physical model-based lumped circuit simulation, and the current through the semiconductor device I_S can be obtained. I_S characterizes the influence of the "circuit" to "field"; then in step 5, the electric field is updated by (10a) using I_S at the location where the semiconductor device is located [17]. In this way, the physical-model circuit simulation and FDTD field simulation are integrated into a unified scheme.

III. RESULTS

To verify the feasibility and accuracy of this simulation method in simulating the non-quasi-static effects of a microwave circuit, a microwave limiter circuit is taken as an example and simulated.

A commercial PIN diode SMP1330 is selected as the limiter diode, because this diode shows strongly non-quasi-static effects at microwave frequencies. The length of this PIN diode base region X_B = 2 um [21], and its transit time frequency f_T is about 325 MHz. The transit time frequency f_T of a PIN diode in megahertz can be calculated by (12) [22]:

$$f_T \approx \frac{1300}{X_B^2}. \tag{12}$$

The working frequency range of the limiter is 0.5-2.5 GHz, which is higher than the transit time frequency, and the non-quasi-static effects dominate its electric characteristics [23].

A. Simulation model

The configuration of the limiter circuit is in Fig. 4. The limiter diode is connected between the center of microstrip and a grounding via. The left and right end of the microstrip is input port 1 and output port 2, respectively.

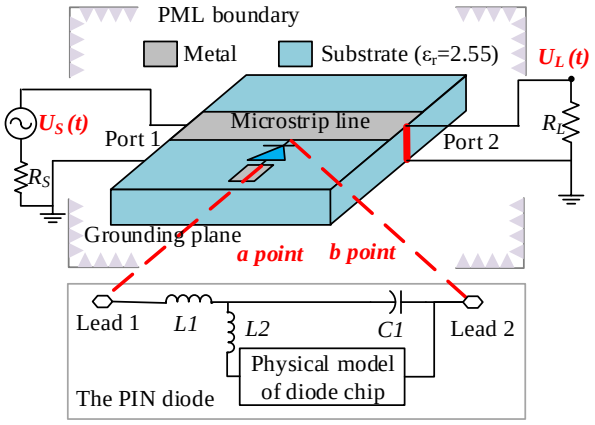

Fig. 4. The configuration and simulation model of the PIN limiter circuit.

The simulation model is also shown in Fig. 4, the main issues arising with the modeling will be explained:

1) The model is divided into two parts: the electromagnetic structure which is within the PML boundary and the lumped circuit which is within the grey solid rectangle.

2) Source and load. The discrete Thévenin source is added to port 1 to characterize the signal source, it consists of a time-varying voltage source $U_S(t)$ and an input resistance R_S of 50 ohms. Moreover, a lumped load resistance R_L of 50 ohms is added to port 2 to characterize the load. The voltage across R_L is $U_L(t)$.

3) The simulation model of the PIN diode is comprised of two parts: the physical model of chip and the equivalent circuit model of the semiconductor package. The physical model of the diode chip is characterized by its doping profile, which can be obtained from the physical parameters of the chip [24]. A GA-based curve fitting approach is applied to extract the physical parameters from the measurement results, and its doping profile is shown in Fig. 5.

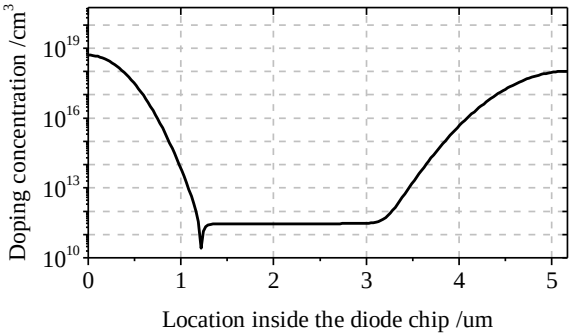

Fig. 5. The doping concentration profile of the diode chip physical model.

Using the simulation model described above, the limiter circuit is simulated by the physical model-based field-circuit co-simulation method.

To compute the scatting parameters of the limiter, a unit amplitude modulated Gaussian pulse is injected to the input port 1 as excitation, the reflection waveform at input port 1, and transmitter voltage waveform at output port 2 are calculated to obtain S11 and S21 respectively.

The output power vs input power curve of the limiter can be calculated. The input signal $U_S(t)$ is defined as a sine wave with an amplitude of A at working frequency f, as in (13). Hence the input power can be obtained, as in (14):

$$U_S = A \cdot \sin(2\pi f), \tag{13}$$

$$P_{input} = 0.125 \cdot A^2 / R_S. \tag{14}$$

The output power defines as the power that is being consumed on the load R_L, which presents the power "delivered to" the following circuit connected to the limiter. The output voltage waveform $U_L(t)$ can be calculated by the physical-model simulation method, hence the output power can be calculated by integrating transient power over a time period:

$$P_{output} = \int_{t=0}^{t=T} \frac{U_L(t)^2}{R_L} dt. \tag{15}$$

By calculating the relationship between input power and output power with the input power increases, the output power vs input power curve can be obtained.

B. Measure method

Figure 6 shows the measure setup of the output

power vs input power curve. By coaxial lines and SMA connectors, the two ports are connected to signal source and power meter respectively. The signal source is characterized by the voltage source $U_S(t)$ and internal resistance R_S; the power meter is characterized by the load resistance R_L in the simulation model of Fig. 4. The displayed output power of the signal source is the input power of the limiter, the displayed input power of the power meter is the output power of the limiter. Hence, the output power vs input power curve can be measured.

The measured output power vs input power curve is shown in Fig. 8. It can be observed that, the output power is equal to input power when the input power is less than 7 dBm, which means that there is no attenuation at this input power range. However, with the input power increases, the output power attenuation increases. There is nearly 8.99 dB attenuation when the input power is 23 dBm, which means that 87.38% of the input power is reflected to the signal source. Because the impedance of the limiter diode is small due to the non-quasi-static effects when the large signal inputs [23].

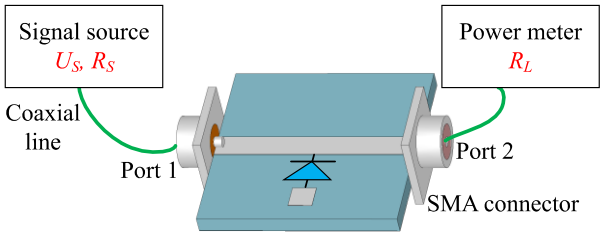

Fig. 6. The measure setup of the output power vs input power curve.

C. Simulation results

The simulated and measured scattering parameters of the limiter are shown in Fig. 7. From the figure, the physical model-based field-circuit co-simulation method can characterize the small-signal scattering parameters well. There is hardly any loss at 500 MHz; but the loss increases with the working frequency increasing, and the S11 is 0.5 dB at 2.5 GHz. The loss generates from both the microstrip structure and the diode itself.

The simulated and measured power limiting characteristics, namely the output power vs input power curve at 1 GHz is shown in Fig. 8. As mentioned above, this power characteristic is dominated by the non-quasi-static effects. As shown in the figure, the simulated results agree well with the measured results. The output power is equal to the input power when the input power is less than 7 dBm. Both the simulated and measured results show that the 1dB compression point is 8 dBm. The measured attenuation of the output power is nearly 8.99 dB when the input power is 23 dBm; the simulated attenuation is 9.11 dB, which means the simulation results are accurate. Meanwhile, it means that the limiter begins to limit the output power when the input power is large enough. Moreover, from the results of Fig. 8, the limiter shows non-linear effects with the power increases. To analyze it more clearly, the output voltage waveforms $U_L(t)$ are simulated when the input power is 4 dBm, 10 dBm, 16 dBm, and 22 dBm respectively, as shown in Fig. 9. At the four input power, the amplitude A of the input voltage $U_S(t)$ is 1 V, 2 V, 4 V, and 8 V, which increase doubly. However, the maximum output voltage value of $U_L(t)$ at the four power is 0.49 V, 0.69V, 0.95 V, and 1.33 V respectively, which do not increase doubly. The increased percentage than the previous one is 41%, 38%, and 40% respectively. It demonstrates the decrease of the limiter impedance, which is due to the accumulated carriers in the base of the diode [23], namely the non-linear non-quasi-static effects dominate the phenomenon.

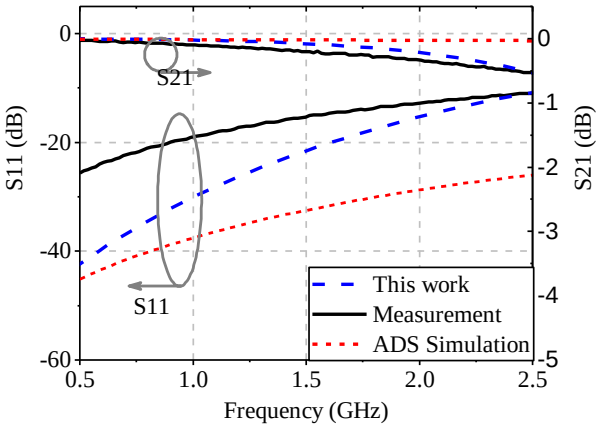

Fig. 7. The scattering parameters of the limiter.

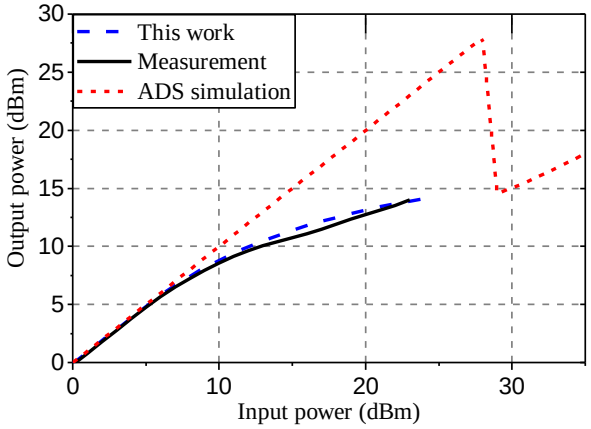

Fig. 8. The output power vs input power curve at 1 GHz of the limiter circuit.

The power limiting characteristic is also simulated by ADS using the equivalent circuit model, which is provided by the semiconductor manufacturer [21]. The results are also shown in Fig. 8. It is obvious that there

is a large divergence between the measured results and the equivalent circuit simulation results. The reason is that the inaccuracy of the equivalent circuit model in characterizing the non-quasi-static effects of the semiconductor device.

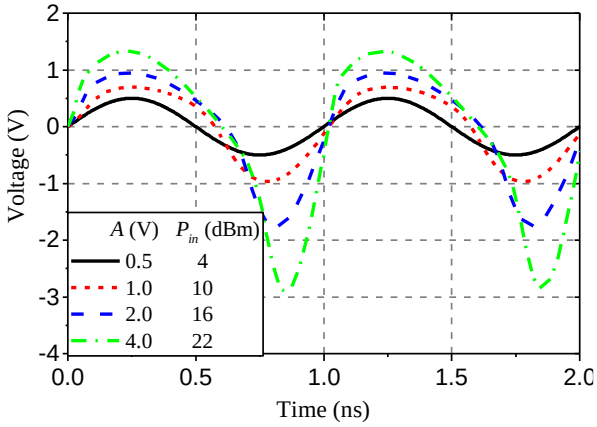

Fig. 9. The output voltage waveforms at different input power of 1 GHz.

VI. CONCLUSION

The non-quasi-static effects of the microwave circuits are analyzed by the physical model-based simulation method. In this method, the semiconductor physical equations are cooperated into the Kirchhoff's circuit equations to obtain voltages and currents of a lumped circuit, then this circuit simulation is coupled with FDTD simulation by interfacing quantities between them.

The results show that, the simulation method in this work is largely more accurate compared with the equivalent circuit model-based simulation method. This simulation method is an attractive candidate in the simulating and predicting non-quasi-static effects of the microwave circuits.

ACKNOWLEDGMENT

This work was supported by the Fund of Ministry of Education of China under Grant 6141A0202504.

REFERENCES

[1] S. Chen, D. Ding, Z. Fan, and R. Chen, "Nonlinear analysis of microwave limiter using field-circuit coupling algorithm based on time-domain volume-surface integral method," *IEEE Microwave and Wireless Components Letters*, vol. 27, no. 10, pp. 864-866, Oct. 2017.

[2] K. ElMahgoub and A. Z. Elsherbeni, "FDTD implementations of integrated dependent sources in full-wave electromagnetic simulations," *Applied Computational Electromagnetics Society Journal*, vol. 29, no. 12, 2014.

[3] M. Chan, K. Y. Hui, C. Hu, and P. K. Ko, "A robust and physical BSIM3 non-quasi-static transient and AC small-signal model for circuit simulation," *IEEE Transactions on Electron Devices*, vol. 45, no. 4, pp. 834-841, Apr. 1998.

[4] B. Lu, Z. Lv, H. Lu, and Y. Cui, "A non-quasi-static model for tunneling FETs based on the relaxation time approximation," *IEEE Electron Device Letters*, vol. 40, no. 12, pp. 1996-1999, Dec. 2019.

[5] H. Wang, T. Chen, and G. Gildenblat, "Quasi-static and nonquasi-static compact MOSFET models based on symmetric linearization of the bulk and inversion charges," *IEEE Transactions on Electron Devices*, vol. 50, no. 11, pp. 2262-2272, Nov. 2003.

[6] Y. Cao, W. Zhang, J. Fu, Q. Wang, L. Liu, and A. Guo, "A complete small-signal MOSFET model and parameter extraction technique for millimeter wave applications," *IEEE Journal of the Electron Devices Society*, vol. 7, pp. 398-403, 2019.

[7] F. Filicori, G. Vannini, and V. A. Monaco, "A nonlinear integral model of electron devices for HB circuit analysis," *IEEE Transactions on Microwave Theory and Techniques*, vol. 40, no. 7, pp. 1456-1465, July 1992.

[8] J. Grajal, V. Krozer, E. Gonzalez, F. Maldonado, and J. Gismero, "Modeling and design aspects of millimeter-wave and submillimeter-wave Schottky diode varactor frequency multipliers," *IEEE Transactions on Microwave Theory and Techniques*, vol. 48, no. 4, pp. 700-711, Apr. 2000.

[9] D. B. Ameen and G. B. Tait, "Convolution-based global simulation technique for millimeter-wave photodetector and photomixer circuits," in *IEEE Transactions on Microwave Theory and Techniques*, vol. 50, no. 10, pp. 2253-2258, Oct. 2002.

[10] D. Pardo, J. Grajal, C. G. Pérez-Moreno, and S. Pérez, "An assessment of available models for the design of Schottky-based multipliers up to THz frequencies," *IEEE Transactions on Terahertz Science and Technology*, vol. 4, no. 2, pp. 277-287, Mar. 2014.

[11] J. V. Siles and J. Grajal, "Physics-based design and optimization of Schottky diode frequency multipliers for Terahertz applications," *IEEE Transactions on Microwave Theory and Techniques*, vol. 58, no. 7, pp. 1933-1942, July 2010.

[12] X. Chen, J. Q. Chen, K, Huang, and X. B. Xu, "A circuit simulation method based on physical approach for the analysis of Mot_bal99lt1 p-i-n diode circuits," *IEEE Trans. Electron. Devices*, vol. 58, no. 9, pp. 2862-2870, Sept. 2011.

[13] A. Subbiah and O. Wasynczuk, "Computationally efficient simulation of high-frequency transients in power electronic circuits," *IEEE Transactions on Power Electronics*, vol. 31, no. 9, pp. 6351-6361,

Sept. 2016.
[14] B. Allard, H. Garrab, T. B. Ben Salah, H. Morel, K. Ammous, and K. Besbes, "On the role of the N–N+ junction doping profile of a PIN diode on its turn-off transient behavior," *IEEE Transactions on Power Electronics*, vol. 23, no. 1, pp. 491-494, Jan. 2008.
[15] A. T. Bryant, X. Kang, E. Santi, P. R. Palmer, and J. L. Hudgins, "Two-step parameter extraction procedure with formal optimization for physics-based circuit simulator IGBT and p-i-n diode models," *IEEE Transactions on Power Electronics*, vol. 21, no. 2, pp. 295-309, Mar. 2006.
[16] T. Ren, Y. Zhang, and Z. Jin, "A 340-400 GHz zero-biased waveguide detector using an self-consistent method to extract the parameters of Schottky barrier diode," *Applied Computational Electromagnetics Society Journal*, vol. 30, no. 12, 2015.
[17] W. Sui, *Time-Domain Computer Analysis of Nonlinear Hybrid Systems*. CRC Press, 2018.
[18] S. M. Sze and K. K. Ng, *Physics of Semiconductor Devices*. Hoboken, NJ: John Wiley & Sons, 2006.
[19] S. Selberherr, *Analysis and Simulation of Semiconductor Devices*. Springer Science & Business Media, 2012.
[20] A. Taflove, "A perspective on the 40-year history of FDTD cmputational electrodynamics," *Applied Computational Electromagnetics Society Journal*, vol. 22, no. 1, 2007.
[21] Skyworks Solutions, Inc. "SMP1330 Series: Plastic Packaged Limiter Diodes," 2016.
[22] J. F. White, *Microwave Semiconductor Engineering*. Van Noslrand Reinhold Company, New York, 1982.
[23] M. E. Clarke and S. Rahim, "A non quasi-static empirical model of the power PIN diode for circuit simulation," *The International Journal for Computation and Mathematics in Electrical and Electronic Engineering*, 1994.
[24] M. Kurata, "Design considerations of step recovery diodes with the aid of numerical large-signal analysis," *IEEE Transactions on Electron Devices*, vol. 19, no. 11, pp. 1207-1215, Nov. 1972.

Ke Xu received the B.S. degree in Electronics and Information Engineering from Sichuan University, Chengdu, China, in 2013. She is currently pursuing the Ph.D. degree in Radio Physics at the same university. Her research interests include computational electromagnetics and semiconductor device numerical simulation.

Xing Chen received the M.S. degree in Radio Physics and the Ph.D. degree in Biomedical Engineering from Sichuan University, Sichuan, China, in 1999 and 2004, respectively. In 1991, he joined as a Teaching Staff and is currently a Professor with the College of Electronics and Information Engineering, Sichuan University. His research interests include antenna, microwave imaging, global optimization, numerical methods applied in electromagnetics, and parallel computation. Chen is a Senior Member of the Chinese Institute of Electronics.

Qiang Chen Provide received the B.S. degree in Electronic Information Engineering and the M.S. degree in Radio Physics from Sichuan University, Sichuan, China, in 2014 and 2017, respectively. He is currently pursuing the Ph.D. degree in Radio Physics at Sichuan University. His research interests include antenna design, multi-physics computation and microwave rectifier design.

Application of Spectral Extrapolation Technique to Stepped-Frequency RCS Measurement

C. F. Hu [1], N. J. Li [1], and C. H. Fang [2]

[1] Science and Technology on UAV Laboratory
Northwestern Polytechnical University, Xi'an, 710072, China
huchufeng@nwpu.edu.cn, linanjing76@163.com

[2] Science and Technology on Electromagnetic Compatibility Laboratory
China Ship Development and Design Centre, Wuhan, 430000, China
27634073@qq.com

Abstract **—** "Time domain gating" used in the stepped-frequency radar cross section (RCS) measurement causes the inaccurate frequency domain data, especially at two ends of the band. This paper proposes a spectral extrapolation method for improving the measured RCS at two ends of the band more exactly. The core idea is: the measured frequency domain data are extrapolated to obtain the unknown value out of band with an auto-regressive model (AR model). The parameter in the AR model is calculated by the maximum entropy spectral estimation algorithm. Therefore, the span of the original band is extended, and both ends of frequency on the original band are inside the range of the new band. If the time domain gating is adding to the new band, the precision at two ends of the original band can be greatly improved. The simulation and experimental results show that more effective frequency domain data near the two ends of the band can be predicted by using the spectral extrapolation method, and the maximum error at the ends of the original band is less than 1dB after extrapolation, so it can ensure the accuracy of RCS measurement over the whole frequency band.

Index Terms **—** Auto-regressive model, maximum entropy spectral estimation, spectral extrapolation, stepped-frequency RCS measurement.

I. INTRODUCTION

So far, the stepped-frequency RCS measurement method is widely used in indoor's scattering measurement [1,2]. It uses a vector network analyzer to transmit and receive with variable frequency signals to measure S21 of the target. To obtain RCS of the target, another target with the known RCS (usually a metal ball) is measured. Compared with the traditional continuous wave RCS measurement method, wideband data composed of many discrete frequencies can be obtained in a very short time by the stepped-frequency RCS measurement. However, some of the transmitted signals will be coupled into the received signal due to the receiving antenna is put near the transmitting antenna, which will affect the accuracy of measurement. Besides, the background clutter also has a greater impact on the accuracy of measurement[3].

To eliminate the influence of background clutter and antenna coupling signals, a "time domain gating" technique is commonly used [4,5], which changes the frequency domain data to the time domain response with inverse fast Fourier transformation (IFFT) and then selects the target's signal (the location of the target in the time domain response is known in advance), thus the interference between the antenna coupling signals and background clutter outside the target area are eliminated. However, the gating also has a great impact when the time domain response of the target was changed back to the frequency domain data with fast Fourier transformation (FFT). The original frequency domain data will be contaminated, which is called the "Gibbs effect", that is, the two ends of the frequency band will have a fluctuation, and the range of gating is smaller, the fluctuation at two ends of the frequency band is larger. Normally, we are not concern about the impact of this "edge effect", but when the test frequency is low (such as the L-band), the span of frequency domain data is narrow for the radiation performance of the antenna, the accurate RCS data after gating become very limited.

To reduce the influence of time domain gating, we try to obtain more information on the spectrum. The spectrum estimation methods mainly appears in the field of super-resolution imaging [6-9] and computational electromagnetics [10,11]. However, the applicability of these methods in the field of RCS measurement has not been verified. Reference [12] gives a method of using low-frequency RCS data to predict high-frequency RCS data. The method supposes that the response is a linear

Submitted On: April 29, 2020
Accepted On: June 14, 2020

https://doi.org/10.47037/2020.ACES.J.350904

time-invariant system, and the RCS data is regarded as the far-field power spectral function, then the extrapolation is performed by using the rational function, but the prediction error of this method is large and only simulation data is used for verification. Recently, reference [13] has proposed a basis pursuit (BP) L1 optimization method to eliminate the impact of data errors caused by limited bandwidth through compressed sensing, but it assumes that the original signal has sparse characteristics.

The linear prediction method has been widely used in high-resolution spectrum estimation of discrete data, especially when the sequence is short, a higher resolution than the Fourier spectrum can be obtained. Therefore, the paper presents a spectral extrapolation method based on linear prediction to extend the span of the original band and the two ends of frequency on the original band are inside the range of the new band. Therefore, despite the time domain gating reduces the effective frequency domain data, the precision at two ends of the original band will also be greatly improved. In this paper, which is an expansion submitted to the 2020 ACES Proceedings paper, more detail of the method is described. The simulation and experimental results are given to show that the spectral extrapolation method can ensure the accuracy of stepped-frequency RCS measurement over the whole frequency band.

II. THE SPECTRAL EXTRAPOLATION OF STEPPED-FREQUENCY SIGNAL

As shown in Fig. 1, the target's time domain response multiplied with a gating is equivalent to convolving the original band with a sinc function, resulting in fluctuations on the frequency domain data, especially at two ends of the band. If the original band is extrapolated by the linear prediction, then the span of the original band is increased. Although the new frequency domain data will also fluctuate after gating, but the two ends of frequency on the original band are inside the range of the new band, thus the measurement errors at two ends of the original band will be greatly reduced.

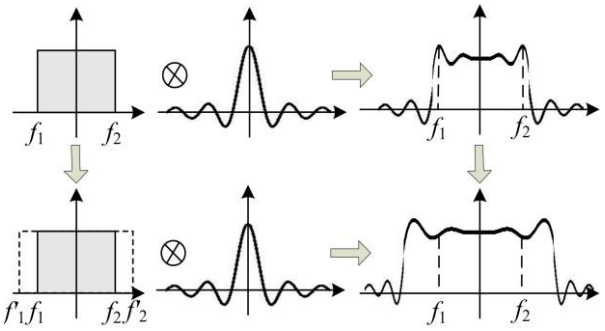

Fig. 1. The principle of spectral extrapolation.

The spectral extrapolation method is based on the auto-regression model (AR model) in the modern spectral estimation theory [14,15]. The AR model is a kind of linear prediction. The model parameters are calculated by Burg algorithm. For example, the N points data are known, the data before or after N points can be predicted by the model, which is similar to the interpolation. The AR model is recursive by N points, and the interpolation is derived from two points (or a few points), both of them are to increase effective data. Since the predicted data has the same autocorrelation function as the known data, so the predicted data contains the information of known data. It has proved that the extrapolated sequence has the largest entropy, and then the maximum information of the unknown spectrum is obtained. The detailed procedures are as follows:

According to the definition of the auto-regressive model, the current data x (n) can be represented by a linear combination of previous data x (n-1), x (n-2) ... x (n-m):

$$x(n) = -\sum_{i=1}^{m} a_m(i)\, x(n-i) + e(n), \tag{1}$$

where, $\hat{x}(n) = -\sum_{i=1}^{m} a_m(i)\, x(n-i)$ is prediction data of x(n), $e(n)$ is prediction error, $a_m(i)$ is the coefficient of linear combination.

For the forward prediction, the prediction data $\hat{x}^f(n)$, the forward prediction error $e^f(n)$, the forward prediction error power ρ^f are as following:

$$\hat{x}^f(n) = -\sum_{i=1}^{m} a_m(i)\, x(n-i), \tag{2}$$

$$e^f(n) = x(n) - \hat{x}^f(n), \tag{3}$$

$$\rho^f = \frac{1}{N-m}\sum_{n=m}^{N-1} \left| e^f(n) \right|^2 . \tag{4}$$

For the backward prediction, the prediction data $\hat{x}^b(n-m)$, the backward prediction error $e^b(n)$, the backward prediction error power ρ^b are as following:

$$\hat{x}^b(n-m) = -\sum_{i=1}^{m} a_m^*(i)\, x(n-m+i), \tag{5}$$

$$e^b(n) = x(n-m) - \hat{x}^b(n-m), \tag{6}$$

$$\rho^b = \frac{1}{N-m}\sum_{n=m}^{N-1} \left| e^b(n) \right|^2 . \tag{7}$$

The coefficients $a_m(i)$ are calculated by the following recursion formulas:

$$a_m(i) = a_{m-1}(i) + k_m a_{m-1}^*(m-i), \tag{8}$$

$$a_m(m) = k_m, \tag{9}$$

where, k_m is the recursion coefficient, and i = 1, 2,..., m-1.

According to the recursion formulas, The relationship of e^f(n) and e^b(n) are given by the following formulas:

$$e_m^f(n) = e_{m-1}^f(n) + k_m e_{m-1}^b(n-1), \quad (10)$$

$$e_m^b(n) = e_{m-1}^b(n-1) + k_m^* e_{m-1}^f(n), \quad (11)$$

$$e_0^f(n) = e_0^b(n) = x(n). \quad (12)$$

Let the sum of forward and backward prediction error power is:

$$\rho^{fb} = \frac{1}{2}\left[\rho^f + \rho^b\right]. \quad (13)$$

ρ^{fb} is only the function of k_m, and let $\partial\rho^{fb}/\partial k_m=0$, we have:

$$k_m = \frac{-2\sum_{n=m}^{N-1} e_{m-1}^f(n) e_{m-1}^{b*}(n-1)}{\sum_{n=m}^{N-1}\left|e_{m-1}^f(n)\right|^2 + \sum_{n=s}^{N-1}\left|e_{m-1}^b(n-1)\right|^2}, \quad (14)$$

where, m= 1, 2,..., p, and p is the model order.

The steps of the spectral extrapolation method using original frequency domain data are as follows:

Step 1: the initial condition $e_0^f(n) = e_0^b(n) = x(n)$ is given, then k_1 is estimated by (14);

Step 2: the model coefficient $a_1(1) = k_1$ is obtained for m = 1;

Step 3: $e_1^f(n)$ and $e_1^b(n)$ are obtained by k_1 and (10) - (12), then k_2 is estimated by (14);

Step 4: The model coefficients $a_2(1)$ and $a_2(2)$ for m = 2 are calculated by (8) and (9);

Step 5: Repeat step 2 to step 4 until m = p, all of the model coefficients are obtained. Then the forward and backward prediction data can be calculated by the coefficients.

III. RESULTS

A. Simulation results

The effect of time domain gating on the spectrum is simulated. The span of the frequency band is from 8GHz to 12GHz, and the corresponding range of a resolution unit is 0.0375m. Assume that the spectrum without time domain gating is a regular straight line, and then the width of gating with 10 resolution units (0.375 m) and 20 resolution units (0.75 m) are added to the original spectrum respectively. The spectrum after gating is shown in the Fig. 2. From the figure we can see that the time domain gating causes a large fluctuation at two ends of the frequency domain response, and as the width of gating becomes narrower, the range of fluctuation in the frequency band is larger, so if we want to remove more background clutter, a narrow gating should be used, but frequency domain data at two ends of the band will be inaccurate.

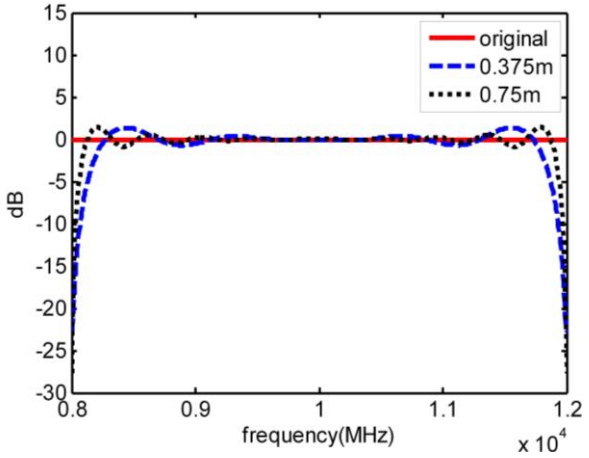

Fig. 2. The frequency domain response with different time domain gatings.

To validate the spectral extrapolation method, the simulation data are shown in Fig. 3. The original data (the red solid line) are combined by the amplitude and phase related to two signals at different distance and a random signal. The purpose is to make the original data have a certain signal-to-noise ratio, which is closer to the actual measured signal. The sectional data in the middle of the original data are selected to extrapolate. The extrapolated data are shown with the blue dashed line. It can be seen from the figure that compared with the original data, parts of extrapolated data near the sectional data are agreed with the original data. So the results validate that more effective data can be obtained by the spectral extrapolation method to increase the band width.

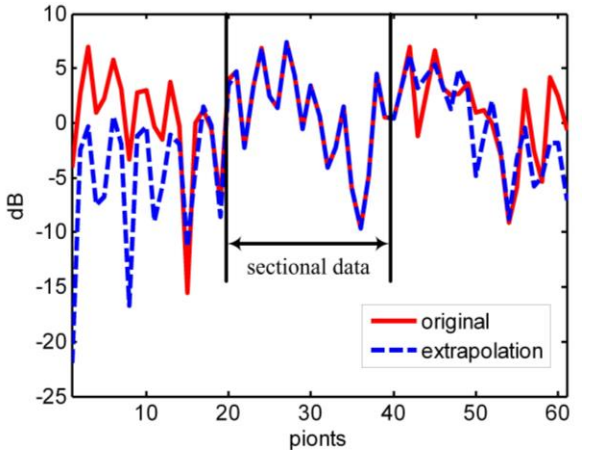

Fig. 3. The compare of original and extrapolated data.

From the results of the simulation, the extrapolation error is determined by the model order p. In general, the model order p is not known in advance, and a large value needs to be selected at first and determined during

recursion. The appropriate model order is selected when the error power is essentially constant. As can be seen from the Fig. 4, when the order is greater than 6, the variation of error power is small, so the model order is 6.

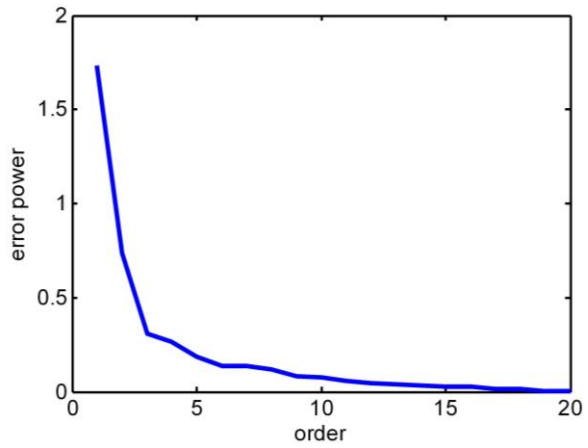

Fig. 4. The error power changed with the model order.

B. Experimental results

Two PEC spheres were measured in the anechoic chamber of Northwestern Polytechnical University. The theoretic frequency domain data of the sphere whose value is known that can be used to compare with measured value to verify the effectiveness of the spectral extrapolation method. One of the spheres with 150mm diameter is used as the calibration target and another sphere with 75mm diameter is regarded as the target to be measured, seen in Fig. 5 and Fig. 6 respectively. A vector network analyzer connected with two horn antennas is used to transmit and receive the stepped frequency signals. The test frequency range is from 8GHz to 12GHz, and the frequency interval is 5MHz. The spheres are put on the center of the turntable, and the test distance from the antenna to the sphere is about 18 meters. The turntable has turned a circle with 1 degree interval.

Fig. 5. 150mm sphere.

Fig. 6. 75mm sphere.

Figure 7 shows the curve of the target changed with angles at three different frequencies without the time domain gating. It can be seen that the curves have large fluctuations at all frequencies, and the measurement error is about 5dB at 10GHz. The main reason is that the echo of the target is rather weak, which is greatly influenced by the clutter.

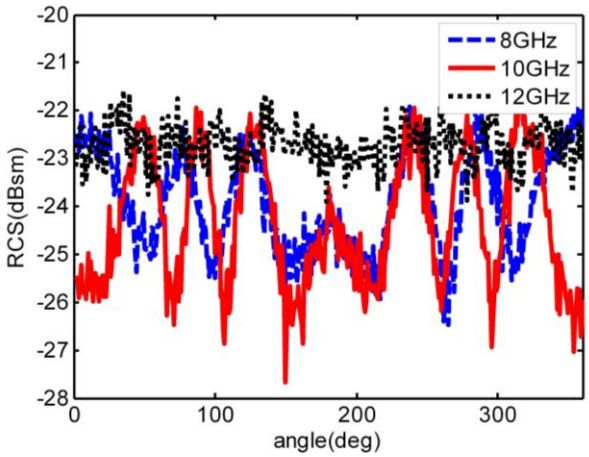

Fig. 7. The RCS results at different frequencies without time domain gating.

In order to eliminate the clutter outside the target area, the frequency domain data of the target is transformed into the time domain response, as shown in Fig. 8. The curve is also represented as the range profile of the target. For the reason that the diameter of the sphere is small, which is in the resonance region at the frequency range. Therefore, in addition to the direct reflection, the backscatter of the target also has diffraction, thus the width of the time domain gating is 0.4 meter.

After adding a time domain gating, the RCS at three frequencies are shown in Fig. 9. From the figure, we can see that the measurement error at 10 GHz is less than 1dB, which means that the impact of clutter is very little. But the measurement error at 8GHz and 12GHz

are larger, which can reach to 8dB. The fluctuations at two ends of the band are both increased for the influence of the time domain gating.

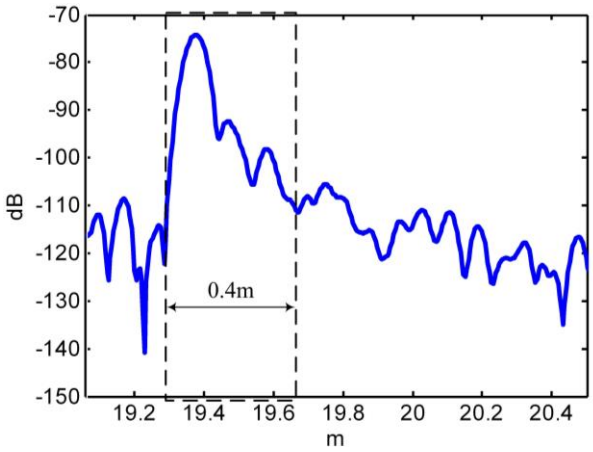

Fig. 8. The time domain response of the target.

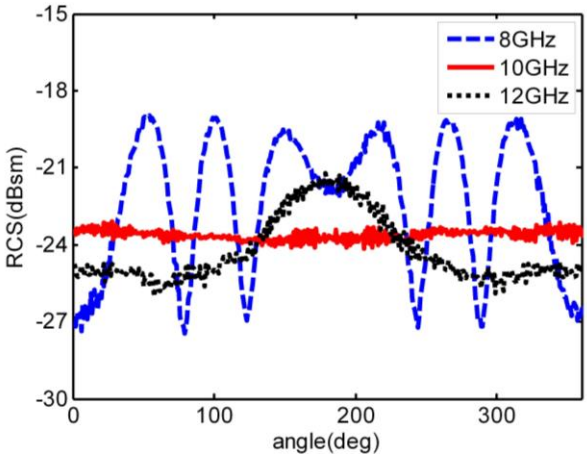

Fig. 9. The RCS results at different frequencies with the time domain gating.

The frequency domain data are extrapolated by the spectral extrapolation method, then the same time domain gating is used to the new frequency band from 7GHz to 13GHz, so the precision at 8GHz and 12GHz on the original band can be greatly improved, as shown in Fig. 10. Compared with the theoretic value, the maximum error is less than 1dB at all frequencies.

The RCS results of three frequencies at different angles after extrapolation are shown in Fig. 11. After extrapolation, the RCS errors at different angles of 8GHz and 12GHz are less than 1dB, which is nearly equal to the errors at 10GHz in the band. It can be seen that the precision on two ends of the frequency band can be greatly improved by using the spectral extrapolation method, and the RCS values near the out of band can be predicted.

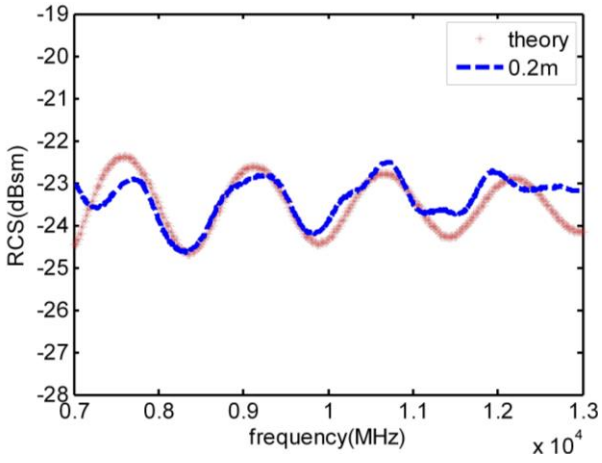

Fig. 10. The RCS results at 7GHz to 13GHz after the extrapolation.

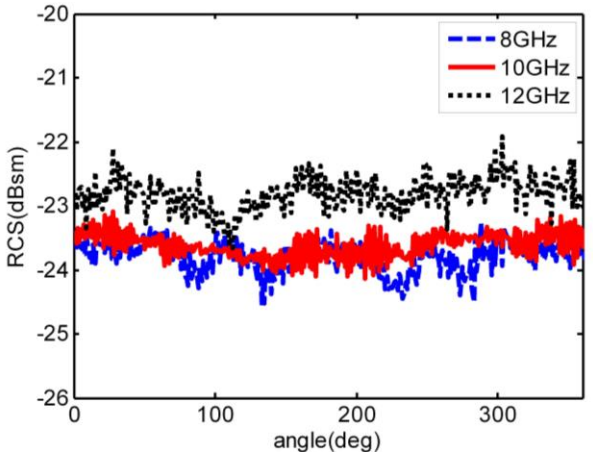

Fig. 11. The RCS results at different angles after extrapolation.

VI. CONCLUSION

The stepped-frequency RCS measurement method has high efficiency and accuracy, but it has a low precision on two ends of the frequency band when a time domain gating is used. This paper presents a spectral extrapolation method which is experimentally demonstrated to be effective. After extrapolation, the two ends of frequency on the original band are inside the range of the new band, so that the measurement precision at the original band can be improved. Moreover, RCS values near the out of band can be predicted by using the spectral extrapolation method. The method can not only be applied to the stepped-frequency RCS measurement but also may be used to other broadband measurements.

ACKNOWLEDGMENT

This work was supported by the National Natural Science Foundation of China (No. 61871323) and the Aeronautical Science Foundation of China (No. 2018ZD53048).

REFERENCES

[1] L. Sevgi, Z. Rafiq, and I. Majid, "Radar cross section (RCS) measurements," *IEEE Trans. Antennas Propagat Mag.*, vol. 55, no. 6, pp. 277-291, Dec. 2013.

[2] C. Larsson and M. Gustafsson, "Wideband measurements of the forward RCS and the extinction cross section," *Applied Computational Electromagnetic Society Journal*, vol. 28, no. 12, pp. 1145-1152, Dec. 2013.

[3] A. Bati, L. To, and D. Hilliard, "Advanced radar cross section clutter removal algorithms," *IEEE Conference on Antennas and Propagation*, Barcelona, Spain, Apr. 2010.

[4] R. A. M. Mauermayer and T. F. Eibert, "Time gating based on sparse time domain signal reconstruction from limited frequency domain information," *Symposium of the Antenna Measurement Techniques Association*, Texas, USA, Oct. 2016.

[5] R. Phumvijit, P. Supanakoon, and S. Promwong, "Measurement scheme of radar cross section with time gating," *International Conference on Electrical Engineering/Electronics, Computer, Telecommunications and Information Technology*, Phuket, Thailand, June 2017.

[6] I. J. Gupta, "High-resolution radar imaging using 2-D linear prediction," *IEEE Trans. Antennas Propagat.*, vol. 42, no. 1, pp. 31-37, Jan. 1994.

[7] Y. X. Wang and H. Ling, "A frequency-aspect extrapolation algorithm for ISAR image simulation based on two-dimensional ESPRIT," *IEEE Trans. Geosci. Remote Sensing*, vol. 38, no. 4, pp. 1743-1747, July 2000.

[8] C. M. Tong, P. W. Yan, Z. G. Huang, and F. Z.Geng, "Simultaneous extrapolation of RCS of a radar target in both angular and frequency domains based on bivariate pad é approximant technique," *Asia-Pacific Microwave Conference Proceedings*, Suzhou, China, Dec. 2005.

[9] I. Erer, S. Kent, and M. Kartal, "High resolution radar imaging from incomplete data," *IEEE Radar Conference*, Rome, Italy, May 2008.

[10] J. Ling, S. X. Gong, X. Wang, B. Lu, and W. T. Wang, "A novel two-dimensional extrapolation technique for fast and accurate radar cross section computation," *IEEE Trans. Antennas Propagat Letters.*, vol. 9, pp. 244-247, 2010.

[11] G. G. Zeng, Z. Feng, and S. Y. Li, "The application of genetic algorithm on the frequency extrapolation method using current density from the MOM," *International Conference on Business Management and Electronic Information*, Guangzhou, China, May 2011.

[12] K. Seol, W. Cho, G. Kang, and J. Koh, "RCS at high frequency band using rational functions," *IEEE International Symposium on Antennas and Propagation*, Boston, MA, USA, July 2018.

[13] I. J. LaHaie and G. D. Dester, "Application of L1 minimization to image-based near field-to-far field RCS transformations," *European Conference on Antennas and Propagation*, Krakow, Poland, Mar. 2019.

[14] S. M. Alessio, *Digital Signal Processing and Spectral Analysis for Scientists: Concepts and Applications*, Springer, Berlin, Germany, 2016.

[15] V. K. Nguyen, M. D. E. Turley, and G. A. Fabrizio, "A new data extrapolation approach based on spectral partitioning," *IEEE Signal Processing Letters*, vol. 23, no. 4, pp. 454-458, Apr. 2016.

C. F. Hu received B.Sc. in 2004 and M.Sc. in 2007 both from Northwestern Polytechnical University, and obtained Ph.D. from Northwestern Polytechnical University in 2010. Now he is a Vice Professor in Science and Technology on UAV Laboratory, Northwestern Polytechnical University. His research interests including RCS measurement and radar imaging and microwave remote sensing.

N. J. Li received B.Sc. in 1998 and M.Sc. in 2001 both from Northwestern Polytechnical University, and obtained Ph.D. from Northwestern Polytechnical University in 2006. Now he is a Vice Professor in Science and Technology on UAV Laboratory, Northwestern Polytechnical University. His research interests including RCS measurement and radar imaging.

Chonghua Fang was born in Hubei Province, China, in 1980. He received the B.S. degree in Physics from Jianghan University, Wuhan, China, in 2002 and the M.S. degree in Materials Physics and Chemistry from Huazhong University of Science and Tech-

nology, Wuhan, China, in 2005 and the Ph.D. degree in Design and Construction of Ship and Marine Structure from China Ship Development and Design Center, Wuhan, China, in 2009. From 2009 to 2017, he was a Senior Engineer with the Science and Technology on Electromagnetic Compatibility Laboratory. He is the author of more than 50 articles, and more than 10 inventions. His research interests include classic radar scattering and quantum radar scattering, electromagnetic compatibility, electromagnetic environment, computational electromagnetics.

Skeletonization Accelerated Solution of Crank-Nicolson Method for Solving Three-Dimensional Parabolic Equation

Hafiz Faiz Rasool, Chen Jun, Xiao-Min Pan*, and Xin-Qing Sheng

Center of Electromagnetic Simulation, School of Information and Electronics
Beijing Institute of Technology, Beijing, 100081, People's Republic of China
hafiz@bit.edu.cn, chenjun_11@foxmail.com, xsheng@bit.edu.cn, *xmpan@bit.edu.cn

Abstract ─ Parabolic equation models discretized with the finite difference method have been extensively studied for a long time. However, several explicit and implicit schemes exist in the literature. The advantage in explicit schemes is its simplicity, while its disadvantage is conditional stability. On the other hand, implicit schemes are unconditionally stable but require special treatment for a fast and accurate solution such as the Crank-Nicolson (CN) method. This method becomes computationally intensive for problems with dense meshes. The resulting matrix from the CN in two and three-dimensional cases requires high computational resources. This paper applies hierarchical interpolative factorization (HIF) to reduce the computational cost of the CN method. Numerical experiments are conducted to validate the proposed HIF acceleration.

Index Terms ─ Alternating direction implicit method, Crank-Nicolson method, hierarchical interpolative factorization, interpolative decomposition, Shur complement.

I. INTRODUCTION

The mathematical model of an electromagnetic problem is usually obtained in terms of partial differential equations (PDEs), integral equations, or integro-differential equations derived from Maxwell's equations. Numerical methods apply a sort of discretization which yields a linear system of algebraic equations (i.e., a matrix equation). The development of powerful computers and fast solution methods for linear systems like the multi-grid/multi-level methods has made the numerical solution of electromagnetic (EM) problems viable [1-3]. The extensive use of wireless communication speeds up the research in EM wave propagation in outdoor and indoor environments. The methods that have been traditionally used to model EM wave propagation in indoor environments (i.e., tunnels) are modal analysis, geometrical optics, and the parabolic equation (PE) approximation. The modal analysis method and the geometrical optics method both have unacceptable limitations and their applicability is limited to specific geometries. The parabolic equation method has been shown to provide a better balance between accuracy and efficiency [2].

Several numerical techniques are available to solve parabolic type equations such as the split-step parabolic equation (SSPE) method [1, 2, 6], the finite element method (FEM) [3], and the finite difference method (FDM) [4, 7, 15-17]. Among these, the finite-difference approaches are more popular because of their simplicity, flexibility, and capability to handle complex boundary conditions (BCs) at short-range propagation problems [8].

The Crank-Nicolson method has been widely used to model wave propagation in tunnels [15], [16]. The high computational cost is a serious obstacle to use the CN scheme in practice. The alternating direction implicit (ADI) methods were developed to address the problem of computational efficiency, but the application of these methods to the problems that vary in time or space encounters serious problems due to the necessity of initial and boundary conditions evaluation at the intermediate steps [7], [9], [10], [11-14]. The trade-off is the loss of accuracy.

In this paper, we improve the efficiency of the CN method by employing the HIF algorithm to make the methods based on 3DPE be potentially capable for problems that vary in time and space simultaneously. Several numerical experiments revealed substantial evidence that HIF can accurately approximate differential and integral operators in a variety of settings with high practical efficiency [18-22]. However, the performance of the HIF in accelerating the parabolic equation in our scenarios is still unclear. In order to answer the question and to find a remedy for the computational efficiency issue for the CN scheme, HIF fast solver has been employed. In order to establish a basis of comparison, the traditional rectangular waveguide model is chosen, as the analytical solution is available for this problem [16]. Secondly, a particular bended-waveguide model is considered to check the validity of the proposed method.

II. THE CN METHOD FOR 3DPE

A 3DPE can be obtained from the Helmholtz

Submitted On: March 27, 2020
Accepted On: June 5, 2020

https://doi.org/10.47037/2020.ACES.J.350905

equation in Cartesian coordinates (x, y, z) as [15]:

$$\left[\frac{\partial^2}{\partial x^2}+\frac{\partial^2}{\partial y^2}+\frac{\partial^2}{\partial z^2}+k_0^2\right]\varphi(x,y,z)=0, \qquad (1)$$

where φ is either the electric or magnetic field and $k_0 = 2\pi/\lambda$ is the free space wavenumber (λ is the wavelength). Assuming that, the direction of propagation is along the *z*-axis. A reduced function $\varphi(x,y,z) = e^{ik_0 z}u(x,y,z)$ is used to separate the rapidly varying phase term in Eq. (1) [15, 16]:

$$\left|\frac{\partial^2 u}{\partial z^2}\right| \ll k_0\left|\frac{\partial u}{\partial z}\right|, \qquad (2)$$

which physically corresponds to paraxial propagation, and substituting Eq. (2) into (1), a 3DPE can be obtained as [16]:

$$\frac{\partial u}{\partial z} = -\frac{1}{2ik_0}\left(\frac{\partial^2}{\partial x^2}+\frac{\partial^2}{\partial y^2}\right)u. \qquad (3)$$

In the following, Eq. (3) is numerically discretized by the CN method using a square grid (*xy*-plane), forwarding in the *z*-direction [4]. The grid points in *x*, *y*, and *z*-directions are denoted by ($i\Delta x$, $j\Delta y$, $n\Delta z$), where, $i = 0,1,2...N_x$, $j = 1,2,...N_y$, and $n = 1,2...N_z$. The transverse and longitudinal discretization's $\Delta x = \frac{x_{\max}}{N_x - 1}$, $\Delta y = \frac{y_{\max}}{N_y - 1}$, and $\Delta z = \frac{z_{\max}}{N_z - 1}$ are referred to as the incremental step sizes in *x*, *y*, and *z* directions, respectively. Consequently, the CN discretization of 3DPE mentioned in Eq. (3) can be written as:

$$r_x\left(u_{i+1,j}^{n+1}+u_{i-1,j}^{n+1}\right)+r_y\left(u_{i,j-1}^{n+1}+u_{i,j+1}^{n+1}\right)+\left(1-2r_x-2r_y\right)u_{i,j}^{n+1}$$
$$=-r_x\left(u_{i+1,j}^{n}+u_{i-1,j}^{n}\right)-r_y\left(u_{i,j-1}^{n}+u_{i,j+1}^{n}\right)+\left(1+2r_x+2r_y\right)u_{i,j}^{n}, \qquad (4)$$

where $r_x = \frac{\Delta z}{4ik_0\Delta x^2}$ and $r_y = \frac{\Delta z}{4ik_0\Delta y^2}$ are the mesh ratios.

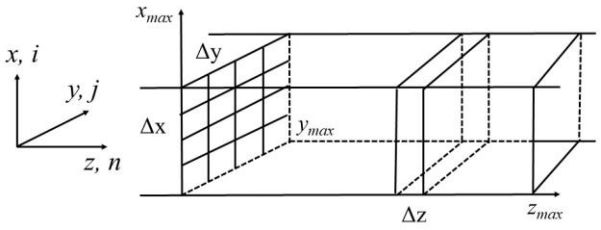

Fig. 1. The geometry of a three-dimensional rectangular waveguide model.

The two-dimensional (2D) cuts of the transverse plane are obtained along the propagation axis inside a rectangular tunnel's cross-section with perfectly conducting walls. The field is discretized at the plane of propagation into a mesh net and is evaluated at spatial steps along the direction of propagation, as illustrated in Fig. 1.

III. THE HIF ALGORITHM

Most recently, hierarchical interpolative factorization (HIF) has been proposed to efficiently and accurately solve a sparse matrix system of linear equations obtained by the discretization of finite difference or finite element methods in the form of $\mathbf{A}\cdot\boldsymbol{u} = \boldsymbol{f}$ [18]. The HIF factorization is based on the approximate decomposition where a recursive reduction strategy is employed to reduce the computational cost. An approximate representation of the original matrix is firstly obtained and then is used to compute the inverse. A threshold control to the reduction scheme is employed to reach the balance between the accuracy and the efficiency of the factorization. HIF works both for symmetric and general sparse matrices. In this work, we only focus on the HIF in terms of a symmetric matrix as the matrix arising from the CN scheme is symmetric. The recursive implementation of HIF is based on the commonly used octree [19]. According to the geometric coordinates, the HIF groups unknown degrees of freedom (DOFs) into the blocks using an octree available at https://github.com/klho/FLAM/. The HIF uses well known Shur complement and interpolative decomposition (ID) numerical tools for elimination and sparsification [18]. The elimination process is based on skeletonization which is divided into volumetric, face, and edge elimination. As discussed in Section II, a 3DPE is transformed into a series of 2D transverse planes propagating in the *z*-direction. So, for simplicity, we can solve a series of 2D problems to obtain the solution of a 3D problem. Consequently, the volumetric skeletonization is skipped in our discussion.

A. Overview of geometric factorization

In the solution process of partial differential equations (PDEs) and their application in a real problem, the partition of the domain is often necessary and convenient. Figures 2 (a)-(g) illustrate the idea of a domain partition, sparsification, and elimination processes based on Shur complement and skeletonization. Black dots correspond to the active DOFs for each level. The partition naturally induces a block representation of **A** proceeding in a hierarchical fashion. Figure 2 (a) shows the discretized domain transformation into a square grid and then splits the square domain into sixteen patches called "leaves" (they will be organized in a tree) [18]. During HIF factorization, the boundary points are selected as active points according to the skeletonization. As a result, the interior DOFs within all sixteen patches are eliminated, as shown in Fig. 2 (b). After the Shur complement sparsification, as discussed in [18], the interactions among the redundant interior DOFs are

represented by the active DOFs, namely, the boundary points on the edges of nearby patches. Figure 2 (c) shows the elimination of DOFs selected in Fig. 2 (b), placed on the edges of nearby cells. Merging cells and organizing the domain in a tree of patches, as shown in Fig. 2 (d). The alternative processes between Shur complement for cells and skeletonization for edges (Figs. 2 (e)-(f)), reduce the problem size into a reasonable size, as illustrated in Fig. 2 (g). This procedure is repeated for each cell up to the coarsest level based on hierarchical domain decomposition.

The resulting factorization allows the rapid application of the matrix inverse, which provides a fast direct solver or preconditioner, depending on the accuracy and specified relative precision (ε) of the ID. The relative precision of the ID is a specified positive real number used to control the accuracy of the HIF algorithm [18].

B. Skeletonization

Skeletonization figures out the redundant points according to the low-rank property of the matrix based on ID. To conduct skeletonization, the original symmetric matrix $\mathbf{A}$ is written as:

$$\mathbf{A} = \begin{bmatrix} \mathbf{A}_{CC} & \mathbf{A}_{CK}^{T} \\ \mathbf{A}_{CK} & \mathbf{A}_{KK} \end{bmatrix}, \tag{5}$$

where C collects the DOFs in a box at a given level and K denotes the rest of the DOFs. Generally, $\mathbf{A}_{CK}^{T}$ and $\mathbf{A}_{CK}$ are numerically low-rank matrices. HIF then conducts the ID on $\mathbf{A}_{CK}$ and obtains,

$$\begin{aligned} \mathbf{A}_{CK} &= \begin{bmatrix} \mathbf{A}_{RK} & \mathbf{A}_{SK}, \end{bmatrix} \approx \begin{bmatrix} \mathbf{T}_{C} \cdot \mathbf{A}_{SK} & \mathbf{A}_{SK} \end{bmatrix}, \\ \mathbf{A}_{CC} &= \begin{bmatrix} \mathbf{A}_{RR} & \mathbf{A}_{SR}^{T} \\ \mathbf{A}_{SR} & \mathbf{A}_{SS} \end{bmatrix}, \end{aligned} \tag{6}$$

where $\mathbf{T}_{C}$ is the interpolation matrix associated with the active unknowns, having indices $C = S \cup R$. Here, S denote the skeleton point set, and R is the redundant point set [18].

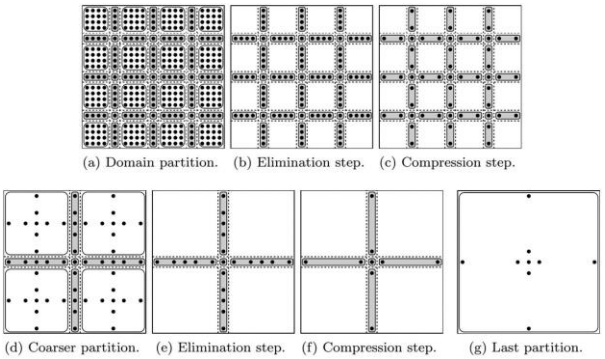

Fig. 2. Illustration of active DOFs at each level of HIF in the factorization process in a hierarchical fashion.

C. Schur complement sparsification

After the skeletonization, HIF obtains $\mathbf{A}_{RR}$ which represents self-interaction to the redundant point set R. By making use of the skeleton point set S, HIF eliminates the redundant points. Mathematically, $\mathbf{A}_{RR}$ is eliminated from $\mathbf{A}$ and a size-reduced form of $\mathbf{A}$ is obtained. When moving to a next active cell, the size-reduction of $\mathbf{A}$ takes place for the original matrix $\mathbf{A}$.

The detailed deduction and implementation, including a comprehensive accuracy control of the HIF algorithm, can be found in [18,19].

IV. SIMULATION RESULTS

Numerical simulations are performed on Intel (R) Core (TM) i3-4005U CPU @ 1.70 GHz, 8 GB RAM. First, the obtained results of the CN and ADI methods are verified via the analytical. The rectangular waveguide's cross-section dimensions are $(40\lambda \times 40\lambda)$ operating at 3 GHz frequency, where $\Delta x = \Delta y = 0.8\lambda$, and $\Delta z = 1\lambda$. A 2D Gaussian source is placed at the center of the waveguide at $(x_s, y_s, z_s) = (20\lambda, 20\lambda, 0)$ with a beamwidth of $\theta_{bw} = 4.34^{\circ}$, under Dirichlet boundary conditions applied on the walls of the rectangular waveguide.

We begin with the validation of the proposed method. Figures 3 (a-c) and (d-f) show the field distributions of a source with un-tilted $(x_{elv}, y_{elv}) = (0^{\circ}, 0^{\circ})$ and tilted $(x_{elv}, y_{elv}) = (-0.5^{\circ}, 0.5^{\circ})$ patterns in the *xy*-plane as a function of width-height variations at z = 100 m. As observed, CN and ADI methods agree with the analytical solution, where the error difference generated by both methods is about 1%. Figures 4 (a)-(c) show the resources used by the HIF factorization including factorization time (t_f), memory used in factorization (m_f), and the solution time (t_s), respectively. The overall solution time t_s includes the factorization construction time t_f and the time required for the HIF solver to evaluate the inverse of the given matrix.

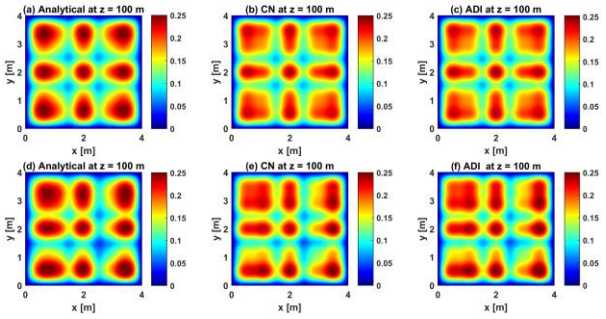

Fig. 3. The 2D field distribution as a function of width-height variations at z = 100 m by the analytical, CN,

and ADI methods, $\theta_{bw} = 4.34^\circ$, $\Delta x = \Delta y = 0.8\lambda$, and $\Delta z = 1\lambda$; TM polarization. (a-c): $(x_{elv}, y_{elv}) = (0^\circ, 0^\circ)$, (d-f): $(x_{elv}, y_{elv}) = (-0.5^\circ, 0.5^\circ)$.

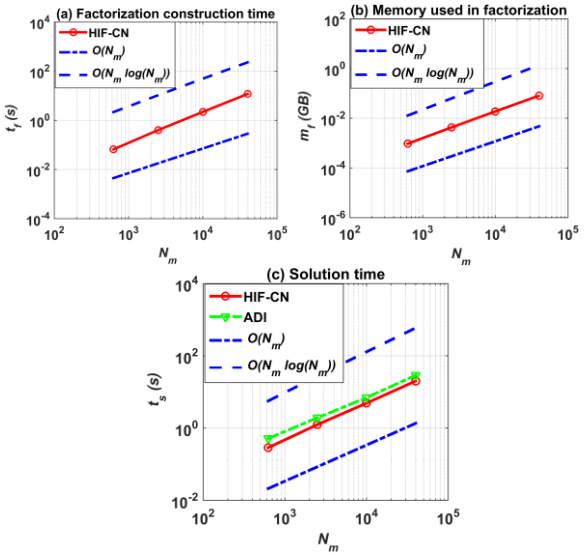

Fig. 4. Scaling results for the HIF-CN model for a PEC straight rectangular waveguide model. (a) Factorization construction time, (b) memory used in factorization, and (c) solution time of HIF-CN and ADI models, $\varepsilon = 10^{-9}$, and *occ* = 64. The data used in these figures are summarized in Table 1.

In this work, both the CN and ADI methods are designed to solve a matrix corresponding to the *xy*-plane. Hence, the overall matrix size corresponding to the *xy*-plane remains the same and can be compared for the given numerical tests. Here, N_m denotes the total number of DOFs solved by both models in the *xy*-plane corresponding to the tunnel's cross-section, while $O(N_m)$ and $O(N_m \log(N_m))$ are the extrapolated values which represent the reference scaling to estimate the efficiency of the algorithm. As the factorization is taking place on the *xy*-transverse plane, hence, t_f and m_f are only depending on the grid size. Furthermore, the size of the errors introduced by finite difference approximation of 3DPE can be controlled by the selection of the discretization intervals Δx and Δy. In order to avoid the aliasing effects, Nyquist's theorem restricts the transverse discretization's intervals $(\Delta x, \Delta y)$, to be less than 1.9λ [15]. The selection of the range increment Δz also depends on the accuracy requirements; it should be chosen as small as necessary to overcome numerical oscillation problems. It should be noted that the overall storage cost to store the field matrices by both models may also depend on the discretization points along the propagation axis, and similarly, the solution time t_s is also depending on: (i) the discretization points along the *z*-axis (ii) the time required for applying factorization *F* or F^{-1} (iii) the time required for solving multiple right-hand sides (iv) the time required for constructing octree, hence, $t_s > t_f$ [18]. The data used in these figures are summarized in Table 1.

Table 1: Factorization and matrix application results for the HIF-CN application in a straight rectangular waveguide model

ε	N_m	N_r	t_f (s)	t_s (s)	m_f (GB)	Error
10^{-6}	25^2	141	0.05	0.27	9.7e-4	1.3e-16
	50^2	651	0.30	1.21	4.3e-3	9.9e-8
	100^2	2775	2.1	3.91	1.8e-2	8.8e-7
	200^2	11439	10.4	18.4	7.9e-2	7.7e-7
10^{-9}	25^2	141	0.06	0.2	9.7e-4	4.6e-16
	50^2	651	0.40	1.24	4.3e-3	1.3e-10
	100^2	2775	2.2	4.8	1.9e-2	4.1e-10
	200^2	11439	11.8	20.0	8.2e-2	7.7e-10
10^{-12}	25^2	141	0.06	0.38	9.7e-4	5.4e-16
	50^2	651	0.46	1.58	4.4e-3	4.3e-14
	100^2	2775	2.6	6.2	1.9e-2	1.2e-12
	200^2	11439	18.6	21.2	8.6e-2	5.5e-13

The total cost of mf, tf, and ts is very close to $O(N_m)$. As can be seen in Table 1, the error generated by the HIF algorithm and the computational resources depends on the relative precision of ID (ε), as well as at the total number of DOFs. The remaining number of active DOFs (N_r) at the highest level are also shown for different N_m at tree occupancy parameter (*occ* = 64). The tree occupancy parameter (*occ*) shows the maximum number of points at each leaf node in a hyper-octree, as each nonempty node in hyper-octree is recursively subdivided until it contains at most *occ* points. As discussed in Section III, the HIF algorithm using a matrix sparsification technique called skeletonization, which facilitates the efficient inversion of the discretized operator obtained by the CN method and thus reduces the overall computational cost for the CN resulting matrix. It can be seen that for the given numerical example, the solution time of HIF-CN is sufficiently reduced when compared with the ADI method for the same problem size, as shown in Fig. 4 (c). The ADI methods are suitable for smooth and straight geometries, the application of theses method would result in the introduction of errors if the boundary conditions are varying rapidly, as significant energy coupling on the sloping terrain boundary between the two transverse directions can

occur within a single marching step. Thus, the marching of the vertical and horizontal field planes must be done simultaneously [7].

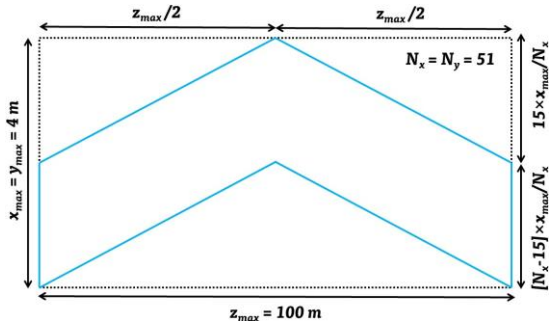

Fig. 5. The geometry of a typical bended-waveguide model.

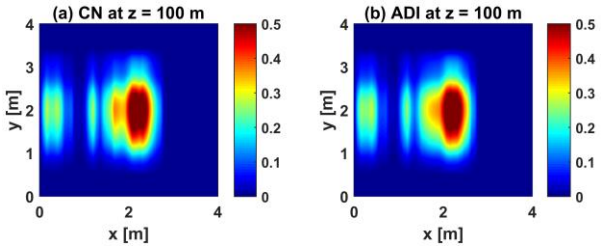

Fig. 6. The two-dimensional cross-sectional field distribution of the (a) CN and (b) ADI methods inside the bended-waveguide model as a function of width-height variation at z = 100 m.

The second test is related to the numerical solution of a bended-waveguide model, as illustrated in Fig. 5. Figures 6 (a) and (b) show the 2D field plots obtained at z = 100 m with un-tilted and tilted patterns of the radiating field. The 2D cuts of field plots are mostly good for visualization purposes. For precise validation, one-dimensional field plots are also obtained along the direction of propagation to check the accuracy of both models against the analytical solution, as shown in Fig. 7. The operational parameters are listed in Fig. 7 inset. The simulation results obtained from the proposed method for a bended-waveguide model are validated with the ADI method, as the analytical solution is not available for this problem in the available literature. A good agreement is observed between the two methods as most of the energy propagating through the simple geometries is contained inside the parabolic margin, the repeated application of the boundary condition at the inner fields converges the correct solution for the ADI method also. However, the overall accuracy would be reduced for the ADI method for modeling complex geometries or in the presence of an obstacle [9], [10].

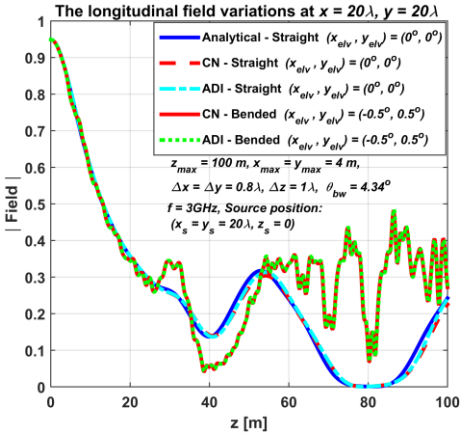

Fig. 7. The longitudinal field variations along the center of the bended-waveguide model according to the geometry shown in Fig. 5.

V. CONCLUSION

In this paper, the HIF based Crank-Nicolson (CN) method is proposed for the solution of a three-dimensional parabolic equation (3DPE). The traditional straight rectangular and particular bended-waveguide models are used for numerical tests. The simulation results are compared with the ADI method as well as against the analytical solution. The proposed work would help in reducing the computational cost of the CN method.

ACKNOWLEDGMENT

This work was supported in part by the National Natural Science Foundation of China (NSFC) under Grant No. 61771053, 61421001, the Key Laboratory for Information Science of Electromagnetic Waves under Grant EMW201908.

REFERENCES

[1] M. Levy, *Parabolic Equation Methods for Electromagnetic Wave Propagation*. London, IEE Institution of Electrical Engineers, 2000.

[2] G. Apaydin and L. Sevgi, *Radio Wave Propagation, and Parabolic Equation Modeling*. Wiley-IEEE Press, 2017.

[3] Ö. Ö. M. Kuzuoğlu, *MATLAB-based Finite Element Programming in Electromagnetic Modeling*. CRC Press, 2019.

[4] J. C. Strikwerda, *Finite Difference Schemes and Partial Differential Equations*. 2nd ed., Philadelphia, PA: SIAM, 2004.

[5] A. Hrovat, G. Kandus, and T. Javornik, "A survey of radio propagation modeling for tunnels," *IEEE Commun. Surveys Tuts.*, vol. 16, no. 2, pp. 658-669, 2nd Quarter, 2014.

[6] H. F. Rasool, X. M. Pan, and X. Q. Sheng, "A fourier split-step based wide-angle three-dimensional vector parabolic wave equation algorithm predicting the field strength over flat and irregular forest environments," *Applied Computational Electromagnetic Society Journal*, vol. 34, no. 6, pp. 874-881, June 2019.

[7] C. A. Zelly and C. C. Constantinou, "A three-dimensional parabolic equation applied to VHF/ UHF propagation over irregular terrain," *IEEE Trans. Antennas Propag*., vol. 47, pp. 1586-1596, Oct. 1999.

[8] Z. He, T. Su, H. C. Yin, and R. S. Chen, "Wave propagation modeling of tunnels in complex meteorological environments with parabolic equation," *IEEE Trans. Antennas Propag*., vol. 66, no. 12, pp. 6629-6634, 2018.

[9] P. Angot, J. Keating, and P. D. Minev, "A direction splitting algorithm for incompressible flow in complex geometries," *Computer Methods in Applied Mechanics and Engineering*, vol. 217-220, pp. 111-120, 2012.

[10] T. A. Dauzhenka and I. A. Gishkeluk, "Quasilinear heat equation in three dimensions and Stefan problem in permafrost soils in the frame of alternating directions finite difference scheme," *Proc. WCE*-London, UK, 2013.

[11] E. L. Tan, "Efficient algorithms for Crank-Nicolson-based finite-difference time-domain methods," *IEEE Transactions on Microwave Theory and Techniques*, vol. 56, no. 2, pp. 408-413, Feb. 2008.

[12] A. V. Londersele, D. D. Zutter, and D. V. Ginste, "Provably stable local application of Crank-Nicolson time integration to the FDTD method with nonuniform gridding and subgridding," *2018 Intl. App. Comp. Electromagnetics Society Symposium (ACES)*, Denver, CO, USA, Mar. 25-29, 2018.

[13] N. Feng, Y. Zhang, Q. Sun, J. Zhu, W. T. Joines, and Q. H. Liu, "An accurate 3-D CFS-PML based Crank–Nicolson FDTD method and its applications in low-frequency subsurface sensing," *IEEE Trans. Antennas Propag*., vol. 66, no. 6, pp. 2967-2975, June 2018.

[14] S. G. Garcia, T.-W. Lee, and S. C. Hagness, "On the accuracy of the ADI-FDTD method," *IEEE Antennas and Wave Propag. Letter*, vol. 1, pp. 31-34, 2002.

[15] R. Martelly and R. Janaswamy, "An ADI-PE approach for modeling radio transmission loss in tunnels," *IEEE Trans. Antennas Propag*., vol. 57, no. 6, pp. 1759-1770, June 2009.

[16] G. Apaydin and L. Sevgi, "Calibration of three-dimensional parabolic equation propagation models with the rectangular waveguide problem," *IEEE Antennas Propagat. Mag*., vol. 54, no. 6, pp. 102-116, Dec. 2012.

[17] X. Zhang, N. Sood, and C. D. Sarris, "Radio-wave propagation modeling in tunnels with a hybrid vector parabolic equation/waveguide mode theory method," *IEEE Trans. Antennas Propag.*, vol. 66, no. 12, pp. 6540-6551, June 2018.

[18] K. L. Ho and L. Ying, "Hierarchical interpolative factorization for elliptic operators: Differential equations," *Comm. Pure Appl. Math*., vol. 69, no. 8, 2016.

[19] K. L. Ho and L. Ying, "Hierarchical interpolative factorization for elliptic operators: Integral equations," *Comm. Pure Appl. Math*., vol. 69, pp. 1314-1353, no. 7, 2016.

[20] Y. N. Liu, X. M. Pan, and X. Q. Sheng, "Skeletonization accelerated MLFMA solution of volume integral equation for plasmonic structures," *IEEE Trans. Antennas Propag.*, vol. 66, no. 3, pp. 1590-1594, Mar. 2018.

[21] S. L. Huang, W. Song, Y. Z. Wang, Y. M. Wu, X. M. Pan, and X. Q. Sheng, "Efficient and accurate electromagnetic angular sweeping of rough surfaces by MPI parallel randomized low-rank decomposition," *IEEE Journal of Selected Topics in Applied Earth Observations and Remote Sensing*, vol. 13, no. 1, pp. 1752-1760, 2020.

[22] D. Wu, Y. N. Liu, Y. M. W. Wu, X. M. Pan, and X.-Q. Sheng, "Skeletonization improved calculation of electric fields by the impedance matrix of MoM," *IEEE Antennas and Wireless Propag. Lett*., Accepted, 2020.

Design and Finite Element Analysis of a Novel Permanent Magnet Assisted Reluctance Synchronous Motor

Xianming Deng, Ran Li, Lei Hao, Ankang Zhang, and Junhong Zhou

Jiangsu Province Laboratory of Mining Electric and Automation, China University of Mining and Technology
Xuzhou, 221116, China
xmdengcumt@126.com, marchliran@163.com

Abstract ─ In this paper, a permanent magnet assisted synchronous reluctance machine (PMASRM) with optimized permanent magnet width and asymmetric rotor structure is proposed. A typical PMASRM is selected as the reference motor (Pre-optimized PMASRM). In order to reduce the large torque ripple of conventional PMASRM, an optimization method to design the permanent magnet width is investigated and the Optimized Magnet-width PMASRM is proposed. On this basis, an asymmetric flux barriers structure is proposed to further reduce the torque ripple. Some electromagnetic characteristics including air-gap flux density, no-load back EMF and motor efficiency are examined by Finite Element Analysis (FEA). The simulation results show that the proposed PMASRM can not only decrease the harmonic component of no-load back EMF obviously, but also reduce the torque ripple in steady-state operation, which proves the rationality of the motor structure.

Index Terms ─ Asymmetric flux barriers, Finite Element Analysis (FEA), magnet width, PMASRM, torque ripple.

I. INTRODUCTION

The typical structure of PMASRM is to put the permanent magnet in the proper position of the flux barrier in the synchronous reluctance machine (SRM). In order to obtain higher torque density and improve power factor, the ferrite permanent magnet material which is slightly weaker than rare earth permanent magnet but more widely sourced and cheaper is usually used [1]. So ferrite PMASRM is widely used in industry because of its high cost performance, good thermal stability, wide speed range and no over voltage risk. Measures to achieve high torque density, low torque ripple, high power factor, low iron loss and high mechanical strength were summarized [2], and the problem of demagnetization of ferrite is also discussed [3]. A PMASRM by using one step or more than two axially laminate rotors with asymmetric flux-barrier is proposed which can reduce the torque ripple but not to decrease the average torque [4]. Methods to improve torque ripples and cogging torque of SRM are investigated and proposed [5]. Flux barriers are asymmetrically designed so that the relative position relation between outer edge of flux barriers and teeth may not be in agreement, which reduces torque ripple dramatically [6]. In addition, two ferrite PMASRM using asymmetric rotor structure with shifted flux barriers and enlarged opening angle of flux barrier respectively are also proposed to improve the motor performance, which have a greater improvement in efficiency and torque ripple [7, 8].

Torque of PMASRM is consisted by two parts: basic torque by the interaction between the rotor permanent magnet field and the stator magnetic field, which is called the permanent magnet torque; as well as the second one donating reluctance torque caused by the unequal reluctance of d-axis and q-axis [9]. When reluctance torque plays a greater role than permanent magnet torque, the motor exhibits higher salient polarity. In order to obtain higher saliency, PMASRM is usually designed as a multi-layer flux barrier structure. Nowadays, the widely used PMASRM structures include "U" type flux barrier, arc type flux barrier, V type flux barrier and hybrid type flux barrier [10-13] as shown in Fig. 1.

The most important disadvantage of PMASRM is that the inherent torque ripple is large and the harmonic content of no-load back EMF is not easy to filter [14]. Aiming at these shortcomings of PMASRM, a novel design method of PMASRM is proposed in this paper. Firstly, a PMASRM with "U" type magnetic barrier is selected as the Pre-optimized PMASRM and its shortcomings are analyzed by finite element simulation. Then, without changing the size of the motor and the consumption of permanent magnets, two optimization schemes are proposed and simulated by FEA. Finally, this paper compares the two optimized motors with the Pre-optimized PMASRM. The simulation results show that the performance of the optimized motor is better than that of the former motor, which proves the rationality of the design.

Submitted On: June 22, 2019
Accepted On: June 29, 2020

https://doi.org/10.47037/2020.ACES.J.350906

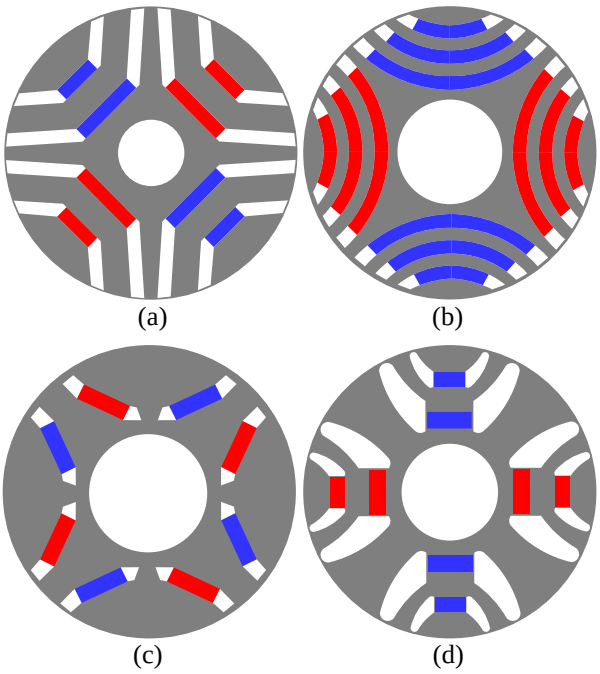

Fig. 1. (a) 'U' type flux barrier, (b) arc type flux barrier, (c) 'V' type flux barrier, and (d) hybrid type flux barrier.

II. PRINCIPLE AND CHARACTERISTIC ANALYSIS OF PRE-OPTIMIZED PMASRM

A. Basic parameters design of motor

Basic parameters include the main size of motor, the size and working point of permanent magnet, slot and stator winding. If the slot type is not suitable or load is not satisfied, it is necessary to adjust the size of permanent magnet and its correspondence parameters to meet design requirements and technical and economic indicators.

Table 1: Main parameters of the motor

Parameters	Value
Rated power/W	550
Rated speed/rpm	1000
Rated line voltage/V	380
Frequency/Hz	50
Stator outer diameter/mm	62.5
Stator inner diameter/mm	38.75
Core length/mm	85
Number of poles	6
Stator slot number	36
Height of magnet/mm	2
Ferrite magnet type	FB9B
Steel type	D2350

The main dimensions of the motor are the inner and outer diameters of stator and rotor, the length of stator core and the effective length of air-gap, etc. The main dimensional relationship of the induction motor can be approximated by using to derive the main size relations of the motor. Selected main parameters of motors are shown in Table 1 below.

The decision to select FB9B as the ferrite permanent magnet material is based on its basic performance, which is better than several similar permanent magnets.

B. Design of rotor structure

Considering the processing cost affected by the shape of the rotor and the permanent magnet, the 'U' type flux barrier structure is adopted for the rotor of the Pre-optimized PMASRM. Furthermore, the maximum output torque of one-layer, two-layer and three-layer flux barrier structures increases obviously as the number of layer increases. However, the maximum output torque of four-layer flux barrier structure and five-layer flux barrier structure does not increase significantly compared with three-layer flux barrier structure, on the contrary, that will increase its torque ripple [15]. Considering the above facts comprehensively, this paper chooses three-layer 'U' flux barrier structure rotor as the Pre-optimized PMASRM rotor, and chooses three-layer permanent magnets in equal width and height to insert into the flux barriers. The section diagram of the Pre-optimized PMASRM is shown in Fig. 2.

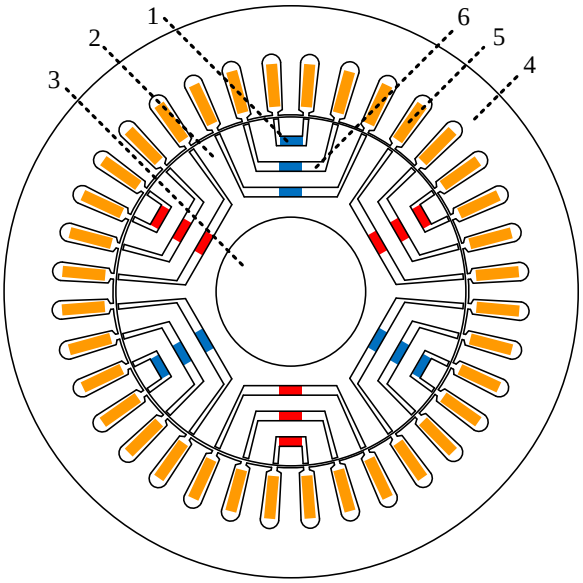

1-Permanent magnet, 2-Rotor core, 3-Shaft,
4-Stator core, 5-Stator winding, 6-Flux barrier

Fig. 2. FEA model of the pre-optimized PMASRM.

C. FEA of pre-optimized PMASRM

In this paper, Maxwell FEA software is used to establish the model of the Pre-optimized PMASRM and the FEA is carried out. The air-gap flux density curve, no-load back EMF waveform, power angle

characteristics and rated load operation performance of the Pre-optimized PMASRM are obtained and its shortcomings are analyzed.

FEA was used to analyze the Pre-optimized PMASRM. The air-gap flux density and no-load back EMF were solved by Ansoft field calculator. Fourier analysis and harmonic content comparison of air-gap flux density waveform and no-load back EMF waveform were carried out and the THD of no-load back EMF waveform was calculated.

From Fig. 3 (b) and Fig. 4 (b), the harmonic component of the air-gap flux density waveform of the Pre-optimized PMASRM is large. Similarly, the harmonic component of the no-load back EMF is also large, especially the third harmonic component accounts for a large proportion. The THD is 48.38%.

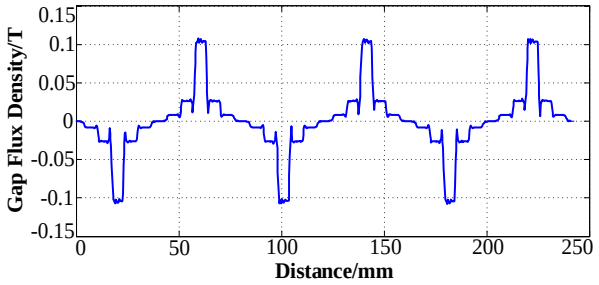

(a)

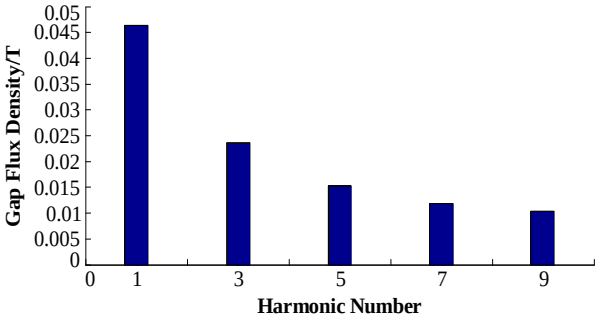

(b)

Fig. 3. (a) Air-gap flux density waveform of the pre-optimized PMASRM, and (b) harmonic analysis results of air-gap flux density for pre-optimized PMASRM.

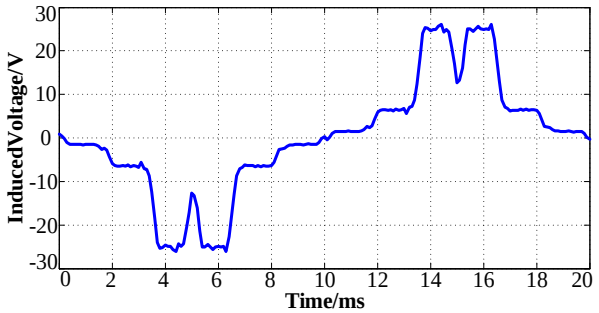

(a)

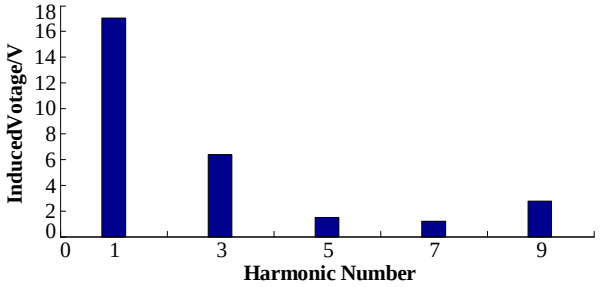

(b)

Fig. 4. (a) No-load back EMF waveform of the pre-optimized PMASRM, and (b) harmonic analysis results of no-load back EMF for the pre-optimized PMASRM.

D. Analysis of power angle characteristics

In order to obtain the power angle characteristics of Pre-optimized PMASRM, it is necessary to calculate the torque. By setting different power angles in Maxwell software and calculating the corresponding torque values of different power angles through FEA, the power angle characteristics of permanent magnet synchronous motor are obtained. Usually, the resistance of stator winding is small, so its influence is neglected. The torque of PMASRM is given by [16]:

$$T_{em}=m\frac{E_0U}{X_d\Omega_s}\sin\delta+m\frac{U^2}{2\Omega_s}\left(\frac{1}{X_q}-\frac{1}{X_d}\right)\sin 2\delta, \quad (1)$$

where m is phase number, E_0 is no-load EMF, U is power supply voltage, Ω_s is mechanical angular velocity, δ is power angle, X_d and X_q are d-axis and q-axis reactance, respectively.

It can be seen from (1) that the torque consists of two parts: basic torque by the interaction between the rotor permanent magnet field and the stator magnetic field, which is called the permanent magnet torque; as well as the second one donating reluctance torque caused by the unequal reluctance of d-axis and q-axis. Figure 5 is the torque component diagram of the ferrite PMASRM. The main component of torque is reluctance torque, so the maximum output torque occurs when the power angle is greater than 90 degrees, while in a certain range before 90 degrees, the torque is negative [17]. Figure 6 is the power angle characteristics of Pre-optimized PMASRM.

III. ELECTROMAGNETIC DESIGN OF OPTIMIZED MAGNET-WIDTH PMASRM

In order to solve the problems of large harmonic component of air-gap flux density waveform and THD of no-load back EMF of Pre-optimized PMASRM, a novel motor structure designed by optimizing the width of multi-layer permanent magnet is proposed, which is called Optimized Magnet-width PMASRM in the following. It makes the harmonic component of air-gap

flux density waveform and no-load back EMF waveform less, so that the waveforms are closer to sinusoidal wave.

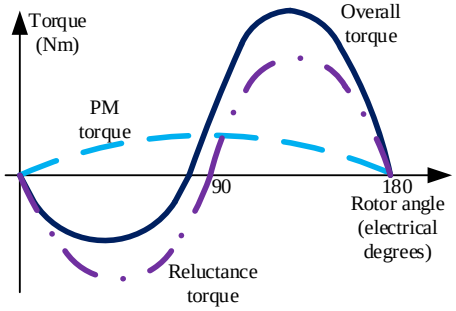

Fig. 5. Torque component of the ferrite PMASRM.

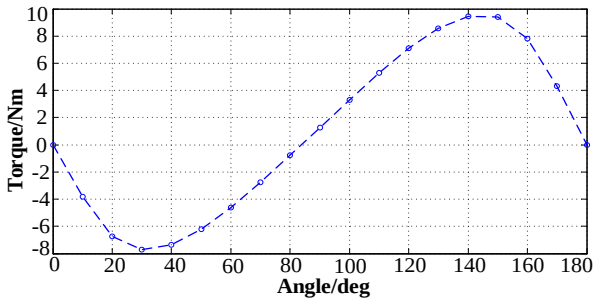

Fig. 6. Power angle characteristics of pre-optimized PMASRM.

A. Calculation of magnetic circuit

Ignoring the stator core magnetoresistance and the rotor core magnetoresistance, an equivalent magnetic circuit diagram of the magnetic circuit for Pre-optimized PMASRM can be obtained [18], as shown in Fig. 7.

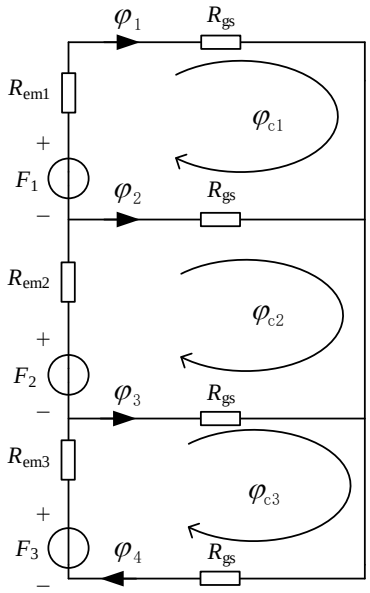

Fig. 7. Equivalent magnetic circuit.

In Fig. 7 F_1, F_2 and F_3 are magnetic motive force of PM1, PM2 and PM3, respectively; R_{em1}, R_{em2} and R_{em3} are reluctance of PM1, PM2 and PM3, respectively; R_{gs} is the reluctance of air-gap; $\phi_1, \phi_2, \phi_3, \phi_4$ are branch flux; $\phi_{c1}, \phi_{c2}, \phi_{c3}$ are loop flux.

From Fig. 7, because the thickness of the permanent magnet is much larger than the air-gap width of the motor and the thickness of three layers of permanent magnets is equal, this paper assumes that:

$$R_{em1} = R_{em2} = R_{em3} = \alpha R_{gs}. \tag{2}$$

In (2), α>1.

Similar to the principle of superposition in electric circuits, the principle of superposition can also be used in magnetic circuits. For a linear system, the response of any branch of a bilateral linear magnetic circuit with multiple independent sources equals the algebraic sum of the response of each independent source acting alone, at which time all other independent sources are replaced by their respective impedance. Because the ferrite permanent magnet is chosen, the core is far from saturated, so it can be approximated as a linear system. When only one magnetic motive force of F_1 acts on the whole magnetic circuit, the equivalent magnetic circuit can be obtained as follows.

In Fig. 8,

$$\begin{aligned} R_* &= \frac{(R_{em3}+R_{gs})R_{gs}}{R_{em3}+2R_{gs}} + R_{em2} \\ &= \alpha + (\frac{1+\alpha}{2+\alpha})R_{gs} \gg R_{gs} \end{aligned}. \tag{3}$$

A and B are inversely proportional to the reluctance of their magnetic branches, so,

$$\frac{\varphi_1}{\varphi_{*1}} = \frac{R_*}{R_{gs}} = \frac{\alpha + (\frac{1+\alpha}{2+\alpha})R_{gs}}{R_{gs}} = \alpha + \frac{1+\alpha}{2+\alpha}. \tag{4}$$

Therefore, φ_1>>φ_{*1}, the flux lines stimulated by F_1 mostly pass through φ_1 to form a loop, and the very small part of them pass through φ_{*1} to form a loop. So, φ_1 can be regarded as all the flux lines stimulated by F_1. Similarly, φ_2 and φ_3 can be seen as all the flux lines stimulated by F_2 and F_3, respectively.

From Fig. 3 (a), the air-gap flux density waveform of the Pre-optimized PMASRM waveform is closer to the rectangular waveform because the magnetic lines passing through L_2 and L_3 are almost zero. Because $\varphi_{l1} \approx \varphi_{l2}$, so,

$$\varphi_2 = \varphi_{l2} - \varphi_{l1} \approx 0. \tag{5}$$

Similarly,

$$\varphi_3 = \varphi_{l3} - \varphi_{l2} \approx 0. \tag{6}$$

If the waveform of air-gap flux density is expected to be closer to sinusoidal waveform, then it is necessary to make φ_2>0. On the premise of keeping the motor size and rotor core unchanged, that is, R_{gs} and R_{emi} (i = 1, 2,

3) unchanged, only F_2 can be increased to make $F_2 > F_1$; similarly, F_3 should be increased to make $F_3 > F_2$. So in total: $F_3 > F_2 > F_1$.

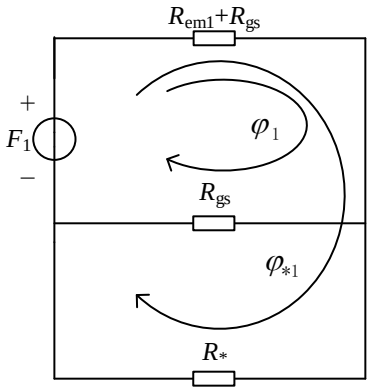

Fig. 8. Equivalent magnetic circuit with F_1 working alone.

B. Optimization strategy of optimized magnet-width PMASRM

According to the special multi-layer flux barrier structure of PMASRM, the outer surface of the rotor can be divided into several parts. As shown in Fig. 9, taking the three-layer flux barrier structure as an example, the outer surface of the rotor can be divided into four parts, namely L_1, L_2, L_3 and L_4.

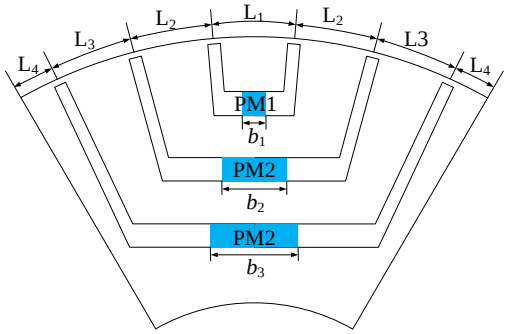

Fig. 9. The rotor model for single pole.

The flux path of motor without load is observed by FEA. In Fig. 10, distribution of flux lines under no-load is shown and three representative routes of magnetic lines are marked. It is found that the flux line which goes through L_3 is generated by PM3; which goes through L_2 is generated by PM2 and PM3; which goes through L_1 is generated by PM1, PM2 and PM3. Therefore, the amount of magnetic lines going through L_1, L_2, L_3 and L_4 can be adjusted by properly distributing the volumes of PM1, PM2 and PM3, so that the waveform of air-gap flux density is closer to sinusoidal wave.

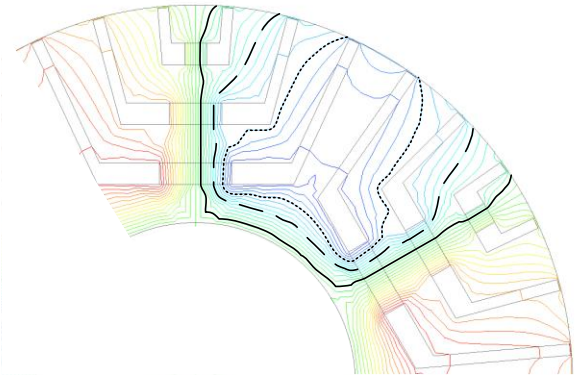

Fig. 10. Distribution of flux lines of two poles under no-load.

This paper assumes that the magnetic line φ_3 passing through L_3 is generated by more parts of PM3 than PM2. Similarly, the magnetic line φ_2 passing through L_2 is generated by more parts of PM2 than PM1. α_1, α_2, α_3 and α_4 are the angles crossed by L_1, L_2, L_3 and L_4, respectively. Therefore, after the rotor flux barrier structure is determined, which means after the determination of α_1, α_2, α_3 and α_4, there is an optimal distribution of the width of PM1, PM2 and PM3, which makes the harmonic component of the air-gap flux density waveform smaller under no-load condition. Figure 11 shows the distribution of air-gap flux density curve under one magnetic pole. B_{g3} is produced by PM3, B_{g2} is produced by PM3 and PM2 together, B_{g1} is produced by PM1, PM2 and PM3.

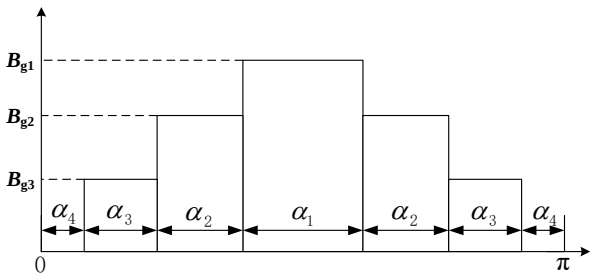

Fig. 11. Distribution of air-gap flux density of single pole under no-load condition.

C. Calculation of the width of permanent magnet basic

As it can be seen in Fig. 10, **the magnetic flux density** generated by the permanent magnet is proportional to the width of the permanent magnet. Under the premise that the angle of the flux barrier of the motor remains unchanged, the area equivalent principle (that is, the area of the corresponding part of the air-gap flux density waveform is proportional to the width of the permanent magnet) is used to calculate.

Comprehensively considering the manufacturing cost of rotor punching and permanent magnets, the magnetic barrier height of each layer is h=2mm, the rotor core length is l=85mm, and the amount of permanent magnets per pole is V=7584mm^3. According to the model in Fig. 2, the angle α_1=10° crossed by the first layer of magnetic barrier corresponds to the electrical angle $\beta_1=p\alpha_1$=30° (p is the number of pole pairs). Similarly, the electrical angles crossed by the second and third layers of magnetic barrier are B_2 = 90° and β_3 = 150°, respectively. In Fig. 11, the area of the ideal sinusoidal flux waveform corresponding to the electrical angle crossed by the first layer of magnetic barrier is:

$$S_1=\int_{90°-\frac{\beta_1}{2}}^{90°+\frac{\beta_1}{2}}\sin x\mathrm{d}x=0.518. \tag{7}$$

Similarly, the area corresponding to the second and third layer of magnetic barrier are:

$$S_2=\int_{90°-\frac{\beta_2}{2}}^{90°+\frac{\beta_2}{2}}\sin x\mathrm{d}x=1.415, \tag{8}$$

$$S_3=\int_{90°-\frac{\beta_3}{2}}^{90°+\frac{\beta_3}{2}}\sin x\mathrm{d}x=1.933. \tag{9}$$

Therefore, the width of the permanent magnet in the first layer of magnetic barrier is calculated by:

$$b_1=\frac{V}{3hl}\frac{S_1}{\sum_{i=1}^{3}S_i}=2\text{mm}. \tag{10}$$

Similarly, the widths of the second and third layer of magnetic barrier permanent magnets b_2 and b_3 are 5.4mm and 7.4mm, respectively. The structure of the Optimized Magnet-width PMASRM is shown in Fig. 12.

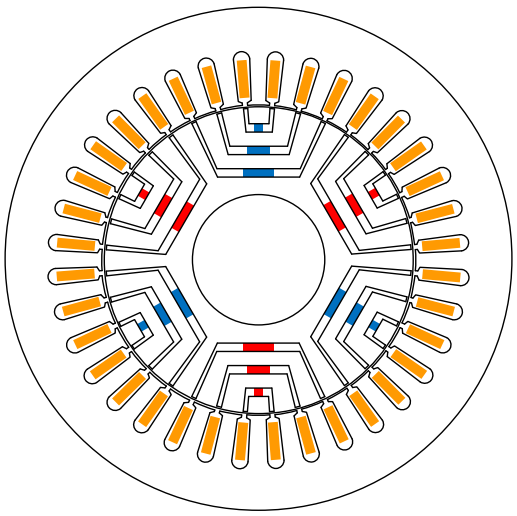

Fig. 12. FEA model of the optimized magnet-width PMASRM.

D. FEA of the optimized magnet-width PMASRM

Similar to the Pre-optimized PMASRM, the FEA of the Optimized Magnet-width PMASRM was carried out by Maxwell software. The air-gap flux density waveform and the harmonic content of Fourier analysis, no-load back EMF waveform, harmonic content, distortion rate and torque ripple under rated conditions were analyzed.

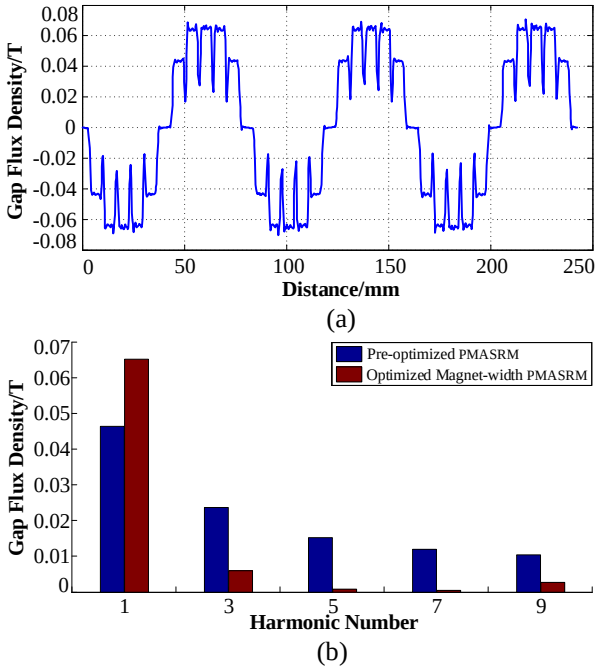

Fig. 13. (a) Air-gap flux density waveform of optimized magnet-width PMASRM, and (b) hanalysis results of no-load back EMF for two kinds of motors.

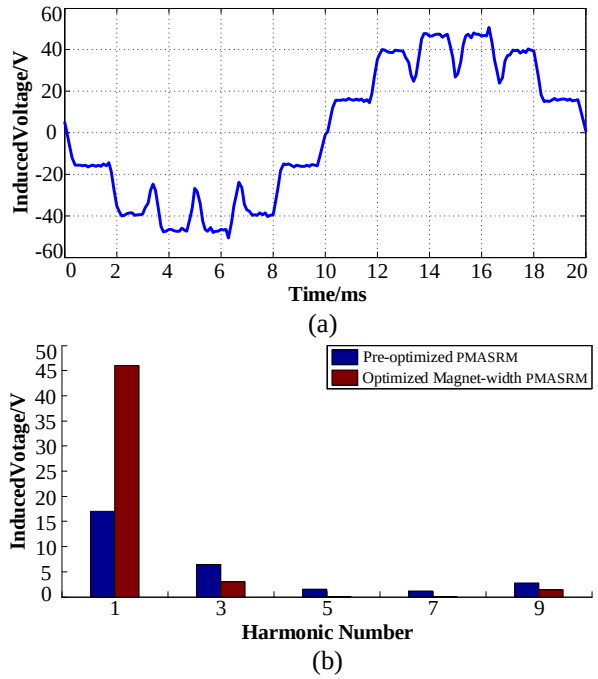

Fig. 14. (a) No-load back EMF waveform of optimized magnet-width PMASRM, and (b) harmonic analysis results of no-load back EMF for two kinds of motors.

By comparing and analyzing the harmonics of air-gap flux density harmonics in Fig. 13 and no-load back EMF harmonics of Optimized Magnet-width PMASRM in Fig. 14, the no-load back EMF and the fundamental wave content of air-gap flux density of Optimized Magnet-width PMASRM increase significantly compared with the Pre-optimized PMASRM. Besides, the fifth, seventh and ninth harmonics have been reduced. Moreover, THD of no-load back EMF is reduced from 48.38% to 18.52%. Therefore, the Optimized Magnet-width PMASRM reduces the harmonic component, making the induction EMF waveform and air-gap flux density waveform closer to sinusoidal waveform.

This paper uses Maxwell software and FEA. The three-phase symmetrical rated voltage is applied to the three-phase stator windings of the Pre-optimized PMASRM and the motor with Pre-optimized PMASRM. Both motors have rated loads. The current distortion and torque ripple of the two motor structures under rated loads are observed in Fig. 15 (in this paper, the torque ripple is defined as peak to peak torque values).

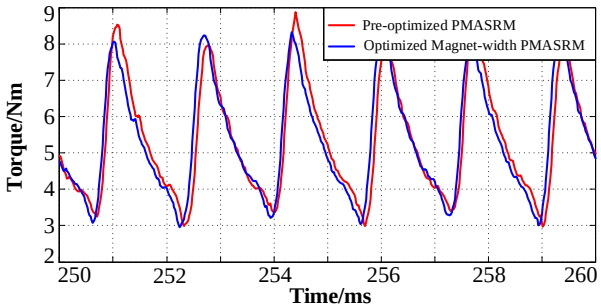

Fig. 15. Torque ripple for two kinds of motors.

The simulation results show that, with the same load, compared with the Pre-optimized PMASRM, the torque ripple of Pre-optimized PMASRM decreases from 5.89Nm to 5.51Nm. Because these two structures have same core structure of the motor, that is to say, the torque ripple caused by reluctance torque is not weakened. The weakening part of the torque ripple is due to the optimization of permanent magnet torque. Because the reluctance torque accounts for a large proportion in the ferrite motor, it is necessary to optimize the structure of the rotor core in order to optimize the torque ripple to a large extent. Considering that the torque ripple of the Pre-optimized PMASRM is still slightly larger, in the following sections, an optimization scheme of asymmetric flux barrier rotor structure is proposed to further weaken the torque ripple.

IV. ELECTROMAGNETIC DESIGN OF ASYMMETRIC FLUX BARRIER PMASRM

In order to further weaken the torque ripple and minimize the harmonic distortion rate of no-load back EMF on the basis of Pre-optimized PMASRM, the design optimization of the rotor core are investigated.

Because the PMASRM exhibits high anisotropy, the salient polarity of the rotor leads to serious torque ripple. Generally, there are two sources of torque ripple in PMASRM: one is the interaction between stator and rotor magnet motive potentials, the other is the uneven change of reluctance caused by slotting between stator and rotor.

A. The design strategy of Asymmetric PMASRM

At present, the most effective way to solve the torque ripple is to use asymmetric rotor structure, In order to solve this problem, a novel asymmetric flux barrier structure is proposed in this paper. The structure is shown in the Fig. 16. This structure can not only weaken the torque ripple obviously, but also retain the advantage of low harmonic component of no-load back EMF.

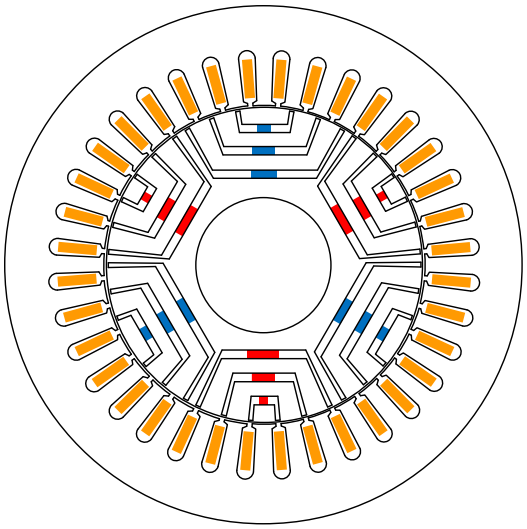

Fig. 16. FEA model of asymmetric PMASRM.

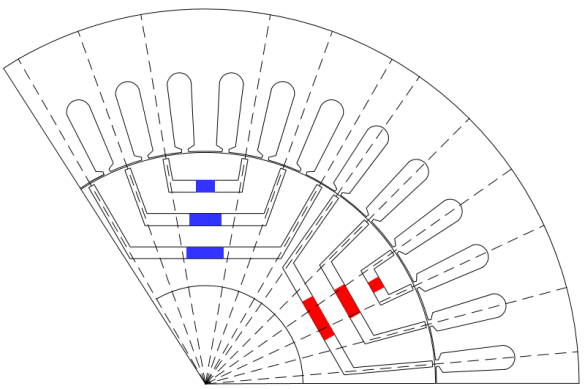

Fig. 17. Design of flux barriers of asymmetric PMASRM.

All the ends of flux barriers of N-pole are aligned with the teeth of the stator, and all the ends of flux

barriers of S-pole are aligned with the slots of the stator, as shown in the Fig. 17. When the motor rotates, half of the ends of the magnetic barrier aligns with the teeth, and the other half aligns with the slot. The rotor magnetic barriers are regarded as virtual slots and the rotor core as virtual teeth. By using this method, the cogging effect between stator and rotor can be weakened and the torque ripple can be further weakened.

The width of permanent magnet needs to be redefined due to the change of the original angle of magnetic barrier, i.e. the magnitude of α_1, α_2, α_3 and α_4. According to the method of optimizing the width of permanent magnets mentioned above, the widths of N-pole permanent magnets PM1N, PM2N and PM3N are 3.2mm, 5.4mm and 6.2mm, respectively; the widths of S-pole permanent magnets PM1S, PM2S and PM3S are 2 mm, 5.4mm and 7.4mm, respectively.

B. FEA of theasymmetric PMASRM

Similar to the Pre-optimized PMASRM, the FEA of Asymmetric PMASRM is carried out by Maxwell software. The air-gap flux density waveform and the harmonic content of Fourier analysis, no-load back EMF waveform, harmonic content, distortion rate and torque ripple under rated conditions are analyzed.

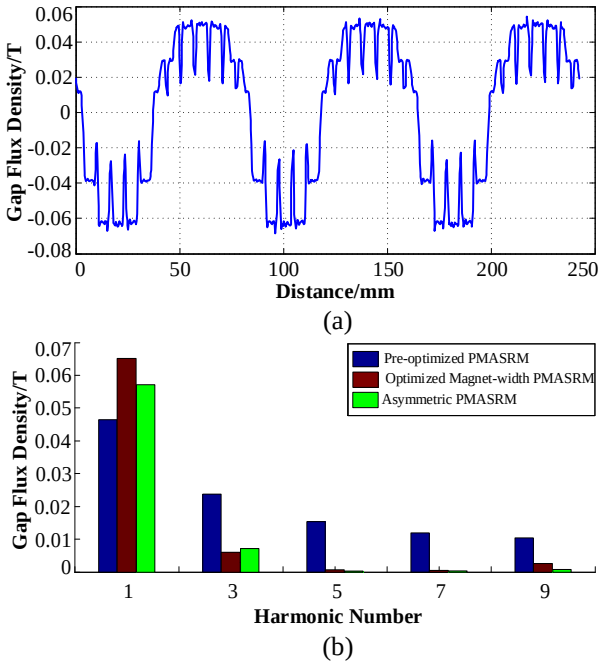

Fig. 18. (a) Air-gap flux density waveform of asymmetric PMASRM, and (b) harmonic analysis results of no-load back EMF for three kinds of motors.

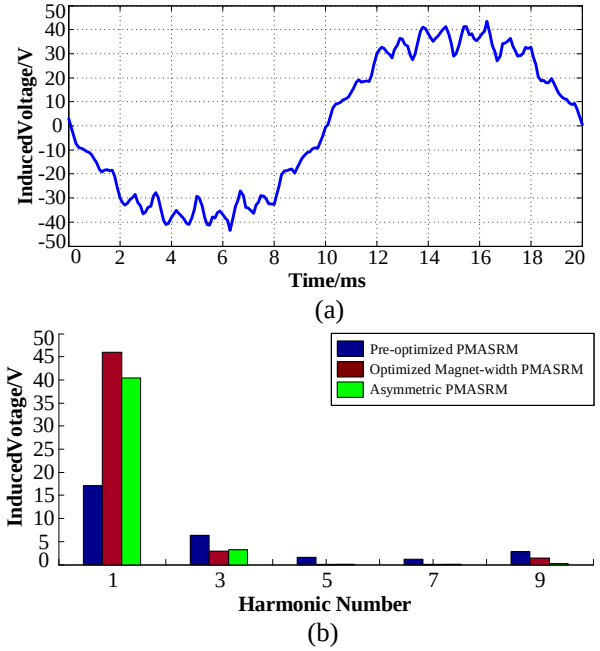

Fig. 19. (a) No-load back EMF waveform of asymmetric PMASRM, and (b) harmonic analysis results of no-load back EMF for three kinds of motors.

According to the analysis results in Fig. 18, it can be seen that the air-gap flux density waveform is asymmetrical because of the unsymmetrical magnetic barriers. The fundamental wave of the air-gap flux density waveform decreases and the harmonic component increases. The FFT and THD of no-load back EMF waveform are analyzed in Fig. 19. Although the fundamental wave decreases, the higher harmonic does not change significantly, and the THD of no-load back EMF waveform changes from 18.52% to 9.72%. Therefore, the Asymmetric PMASRM can further decrease the harmonic component of no-load back EMF, making it closer to the sinusoidal wave.

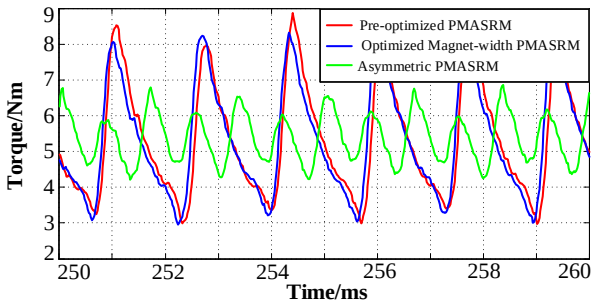

Fig. 20. Torque ripple for three kinds of motors.

As can be seen from Fig. 20, the torque ripple of Asymmetric PMASRM is further reduced compared with the former two motors, from 5.85Nm and 5.51Nm to 2.64Nm, which reduces the torque ripple significantly.

C. Motor efficiency at rated load

Efficiency is an important index of motor. Because the PMASRM exhibits high anisotropy, the harmonic content of stator and rotor flux density is serious [19]. Reducing the iron loss of motor is a key problem in optimizing the design of PMASRM. In this paper, the iron and copper losses of three kinds of structural motors in synchronous operation are obtained by FEA, and the results are present in Table 2 below.

Table 2: Efficiency of three kinds of motor under rated load

	Pre-Optimized PMASRM	Optimized Magnet-width PMASRM	Asymmetric PMASRM
Iron loss (W)	7.27	7.14	7.68
Copper loss (W)	69.10	66.79	64.46
Output power (W)	560	559.4	557.53
Efficiency	88%	88.32%	88.54%

From Table 2, it can be seen that the efficiency of the three kinds of structure motors is very similar, and all of them are above 88%, which fully meets the requirements of the design of PMASRM. It shows that the design of Asymmetric PMASRM with magnetic barrier is reasonable and feasible.

V. CONCLUSION

In this paper, a PMASRM with optimized permanent magnet width is proposed, and then an improved PMASRM with asymmetric magnetic barriers is proposed. The two-dimensional models of three kinds of PMASRM with different rotor structures are established and analyzed by FEA. The air-gap flux density waveforms, no-load back EMF waveforms and their harmonic analysis of the three kinds of motors are obtained, and the torque ripple under rated load is compared. The results show that the air-gap flux density waveform, induction electromotive force waveform and current waveform of Optimized Magnet-width PMASRM and Asymmetric PMASRM are closer to sinusoidal distribution than those of conventional PMASRM with the same amount of permanent magnet, and the torque ripple of Asymmetric PMASRM decreases significantly under the same load. It proves the rationality of optimizing the design of permanent magnet width motor and asymmetric magnetic barrier motor.

ACKNOWLEDGMENT

This work was supported by the Natural Science Foundation of Jiangsu Province Grant No. BK20190634.

REFERENCES

[1] M. De Gennaro, J. Jürgens, A. Zanon, J. Gragger, E. Schlemmer, A. Fricassè, L. Marengo, B. Ponick, E. T. Olabarri, J. Kinder, A. Cavallini, P. Mancinelli, M. Hernandez, and M. Messagie, "Designing, prototyping and testing of a ferrite permanent magnet assisted synchronous reluctance machine for hybrid and electric vehicles applications," *Sustainable Energy Technologies & Assessments*, vol. 31, pp. 86-101, Jan. 2019.

[2] J. X. Shen, "Analysis and design of synchronous reluctance machines PART I: An overview," *Microwaves*, vol. 44, no. 10, pp. 72-79, Oct. 2016.

[3] X. Liu, Y. Li, Z. Liu, T. Ling, and Z. Luo, "Optimized design of a high-power-density PM-assisted synchronous reluctance machine with ferrite magnets for electric vehicles," *Archives of Electrical Engineering*, vol. 66, no. 2, pp. 279-293, 2017.

[4] K. Wang, Z. Q. Zhu, G. Ombach, M. Koch, S. Zhang, and J. Xu, "Torque ripple reduction of synchronous reluctance machines: using asymmetric flux-barrier", *COMPEL - The International Journal for Computation and Mathematics in Electrical and Electronic Engineering*, vol. 34, no. 1, pp. 18-31, Jan. 2015.

[5] T. Mohanarajah, J. Rizk, A. Hellany, M. Nagrial and A. Klyavlin, "Torque ripple improvement in synchronous reluctance machines," *2018 2nd International Conference on Electrical Engineering (EECon)*, Colombo, pp. 44-50, Sept. 2018.

[6] M. Sanada, K. Hiramoto, S. Morimoto, and Y. Takeda, "Torque ripple improvement for synchronous reluctance motor using an asymmetric flux barrier arrangement," *38th IAS Annual Meeting on Conference Record of the Industry Applications Conference*, vol. 1, pp. 250-255, Oct. 2003.

[7] M. Davoli, C. Bianchini, A. Torreggiani, and F. Immovilli, "A design method to reduce pulsating torque in PM assisted synchronous reluctance machines with asymmetry of rotor barriers," *2016 42nd Annual Conference of the IEEE Industrial Electronics Society* (*IECON)*, pp. 1566-1571, Oct. 2016.

[8] M. Xu, G. Liu, and Q. Chen, "Torque ripple improvement for ferrite-assisted synchronous reluctance motor by using asymmetric flux-barrier arrangement," *International Journal of Applied Electromagnetics & Mechanics*, pp. 1-10, 2019.

[9] N. Bianchi, E. Fornasiero, and W. Soong, "Selection of PM flux linkage for maximum low-speed torque rating in a PM-assisted synchronous

reluctance machine," *IEEE Transactions on Industry Applications*, vol. 51, no. 5, pp. 3600-3608, 2015.
[10] N. Bianchi, S. Bolognani, D. Bon, and M. Dai Pre, "Rotor flux-barrier design for torque ripple reduction in synchronous reluctance and PM-assisted synchronous reluctance motors," *IEEE Transactions on Industry Applications*, vol. 45, no. 3, pp. 921-928, 2009.
[11] N. Bianchi, S. Bolognani, D. Bon, and M. Dai PrÉ, "Torque harmonic compensation in a synchronous reluctance motor," *IEEE Transactions on Energy Conversion*, vol. 23, no. 2, pp. 466-473, June 2008.
[12] H. Cai, B. Guan, and L. Xu, "Low-cost ferrite PM-assisted synchronous reluctance machine for electric vehicles," *IEEE Transactions on Industrial Electronics*, vol. 61, no. 10, pp. 5741-5748, Oct. 2014.
[13] F. Xing, W. Zhao, and B. Kwon, "Design of a novel rotor structure for PM-assisted synchronous reluctance machines to improve torque characteristics," *2016 IEEE Conference on Electromagnetic Field Computation (CEFC)*, Miami, FL, pp. 1-1, 2016.
[14] R. Rouhani, S. E. Abdollahi, and S. A. Gholamian, "Torque ripple reduction of a synchronous reluctance motor for electric vehicle applications," *2018 9th Annual Power Electronics, Drives Systems and Technologies Conference (PEDSTC)*, Tehran, pp. 386-391, 2018.
[15] B. Boazzo, A. Vagati, G. Pellegrino, E. Armando, and P. Guglielmi, "Multipolar ferrite-assisted synchronous reluctance machines: A general design approach," *IEEE Transactions on Industrial Electronics*, vol. 62, no. 2, pp. 832-845, Feb. 2015.
[16] X. Zhang, L. Zeng, and R. Pei, "Designing and comparison of permanent magnet synchronous reluctance motors and conventional motors in electric vehicles," *2018 21st International Conference on Electrical Machines and Systems (ICEMS)*, Jeju, pp. 202-205, 2018.
[17] R. T. Ugale and B. N. Chaudhari, "A new rotor structure for line start permanent magnet synchronous motor," *2013 International Electric Machines & Drives Conference*, Chicago, IL, pp. 1436-1442, 2013.
[18] H. Huang, Y. Hu, Y. Xiao, and H. Lyu, "Research of parameters and anti-demagnetization of rare-earth-less permanent magnet assisted synchronous reluctance motor," 2015 *IEEE International Magnetics Conference (INTERMAG)*, Beijing, pp. 1-1, 2015.
[19] N. Bianchi and M. Barcaro, "Iron losses reduction in synchronous motors with anisotropic rotor," *2008 34th Annual Conference of IEEE Industrial Electronics*, Orlando, FL, pp. 1258-1263, 2008.

Xianming Deng was born in Sichuan, China. He received his B.S., M.S., and Ph.D. in Electrical Engineering from China University of Mining and Technology, Jiangsu, China. He is currently a Professor in the School of Electrical and Power Engineering of China University of Mining and Technology. His current research fields include power electronics and motor drive.

Ran Li was born in Shanxi, China. He received his B.S. in Electrical Engineering from Shandong University of Technology, Shandong, China. He is currently receiving a Master education at China University of Mining and Technology. His current research interests include power electronics and motor drive.

Lei Hao was born in Shandong, China. He received his B.S. in Electrical Engineering from Shandong University of Technology, Shandong, China. He is currently receiving a Master education at China University of Mining and Technology. His current research interests include power electronics and motor drive.

Ankang Zhang was born in Jiangsu, China. He received his B.S. in Electrical Engineering and Intelligent Control from Nantong University, Jiangsu, China. He is currently receiving a Master education at China University of Mining and Technology. His current research interests include Motor control and transformer design.

Junhong Zhou was born in Hunan, China. He received his B.S. in Information Engineering from China University of Mining and Technology, Jiangsu, China. He is currently receiving a Master education at China University of Mining and Technology. His current research interests include power electronics and motor drive.

A Hybrid Approach on Metamaterial-Loaded Fractal Antenna Design

D. Prabhakar [1], C. H. Rajendra Babu [2], V. Adinarayana [3], and V. V. K. D. V. Prasad [1]

[1] Department of ECE, Gudlavalleru Engineering College (A)
Seshadri Rao Knowledge Village, Gudlavalleru, Andhra Pradesh, India
prabhakar.dudla@gmail.com, varaprasadvvkd@gmail.com

[2] Department of CSE, Andhra Layola Institute of Engineering and Technology, Andhra Pradesh, India
chikkalarajendra@gmail.com

[3] Department of ECE, Avanthi Institute of Engineering &Technology (AIET), Andhra Pradesh, India
joy.adi2011@gmail.com

Abstract – The paper provides the interoperable hybrid Grasshopper–Grey Wolf optimization (GHGWO) of the Square Split-Ring Resonator (SRR) metamaterial unit cell. This paper discusses the complex phase strategies of the electric and magnetic interplay of the charged microstrip line of the split ring resonator (SRR). Optimized unit of metamaterial cells for their bandwidth enhancement is packed into a new square fractal antenna. In the interim period of dual band efficiency, a new design is introduced for a microstrip line-feeding square fractal antenna with a faulty ground composition. In the second stage, a quasi-static SRR model is being used to streamline its structural parameters in an effort to reinforce the bandwidth so that optimized composition resonates at the required intensity area. In the GHGWO hybrid algorithm, SRR unit cell size limitations should be optimized and the convergence actions of the algorithm improved. Certain evolutions termed modified hybrid BF-PSO classical BFO, chaos PSO and IWO are being tested for efficiency of the Hybrid GHGWO algorithm. In the final stage, optimized SRR unit cells are stacked into a square fractal antenna that provides bandwidth output suited to wireless usages with upper and lower band. The prototype square fractal antenna without and with SRR unit cells is efficiently evaluated by trial results.

Index Terms – Grasshopper–Grey Wolf Optimisation (GHGWO), metamaterial unit cell, quasi-static SRR model and microstrip line, Split-Ring Resonator (SRR).

I. INTRODUCTION

An antenna is known as a broadband unless its impendence or configuration varies considerably over about one octave or more [5]. In contemporary wireless transmission networks the miniaturization of antenna layout focused on fractal geometry is of significant importance [1].

In this study, we are proposing a new model of a three-step square fractal antenna. The bandwidth of the planned fractal antenna is increased by partial ground plane on the reverse side of a substratum. Secondly, we prioritize bandwidth in the built fractal antenna with the use of MTM unit cells with optimized split-ring resonator. A hybrid Grass Hopper [2], and grey wolf optimization [2] (GHGWO) algorithm are used to optimize structural variables in split ring resonant unit cells. However, a disadvantage of these techniques is the extensive amount of CPU times utilized in determining the numerical solution compared to the fully explicit methods for the same selection of values. Thus if we were to write them in matrix form, the coefficient matrix would be penta diagonal. The rest of paper is structured as follows: Section II discusses the brief review of hybrid GHGWO algorithm is proposed, Section III comprises of experimental results, and Section IV gives a brief conclusion.

Bilal Babayigit et al. [3] developed a Taguchi Method (TM) to model a non-side lobe level deletion (SLL) optimization for the CAA (non-uniform circular antenna array). TM, a rigorous design strategy, incorporated the numerical nature of experiments as a signal to noise ratio and orthogonal array devices. Such methods decrease the design parameters rather than complete factor evaluation, thus increased the rate of convergence and produced more precise solutions. TM's high output in achieving reduced SLLs was demonstrated by experimental results.

Although the methods mentioned above often focus on the problem of the fractal antenna design more effectively for various kinds of problems, there exist some obvious shortages when compared with other algorithms.

Submitted On: January 4, 2020
Accepted On: June 25, 2020

https://doi.org/10.47037/2020.ACES.J.350907

II. PROPOSED METHODOLOGY

A. Fractal antenna functionality

An antenna that utilizes fractal and self-similar layout to improve the perimeter (internal and external) of the equipment that can send data or obtain electromagnetic radiation inside a particular surface area or velocity may be outlined as a fractal antenna. Up to the third cycle, the process is continued, resulting in new fractal geometry as shown in Fig. 1. Two unit cells (MTM) of the metamaterial are placed on both sides of the feed line above the support to increase the bandwidth of the designed antenna for broadband enhancement [4].

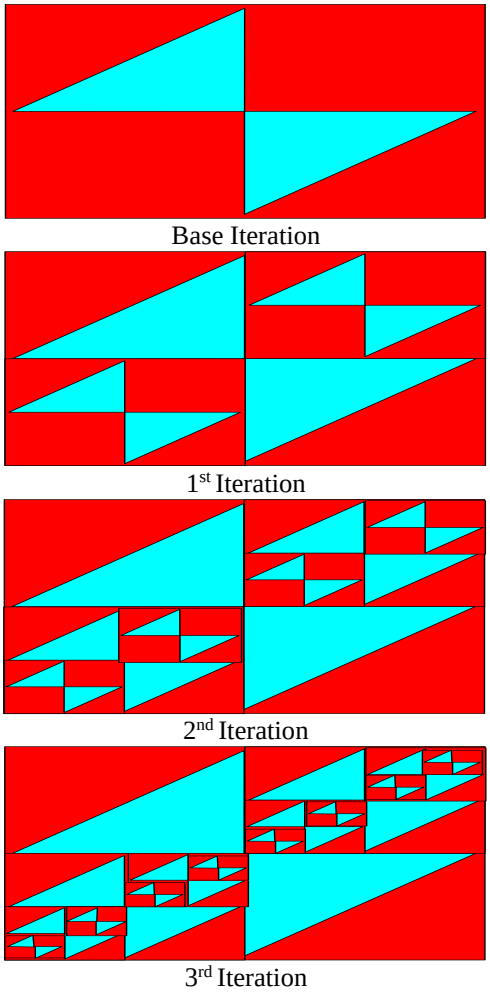

Fig. 1. Proposed square fractal geometry with different iterations (0^{th} (base iteration), 1st, 2nd and 3rd).

The model for the proposed fractal antenna is shown in Fig. 2 (a), while Fig. 2 (b) portrays the partial ground layer on the backside of substrate.

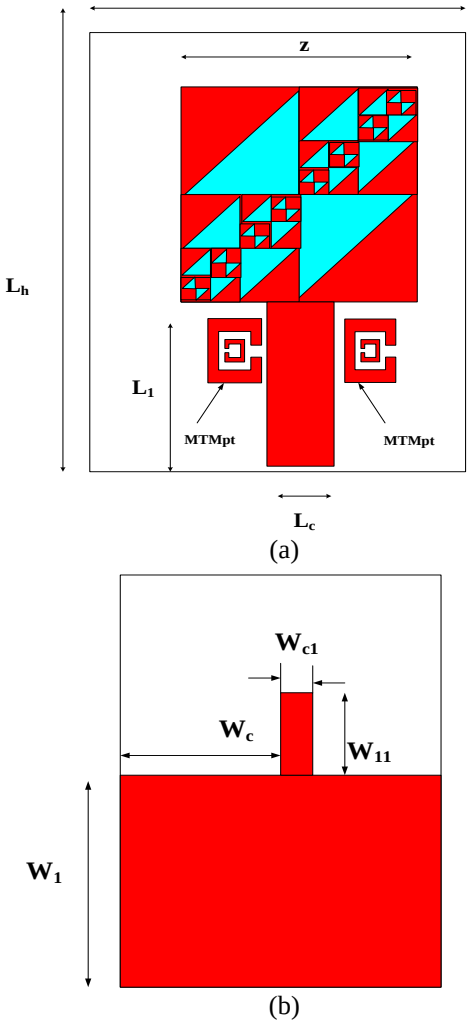

Fig. 2. (a) Top view of optimized fractal antenna. (b) Bottom view of optimized fractal antenna.

B. Hybridizing GHGWO

Hybridizing Grasshopper (GH) with Grey Wolf Optimization (GWO) to counteract early convergence and long computation time, entangled in large space with local minimums.

The computational modelling used to precisely evaluate the swarming activities of grasshoppers is shown as defines:

$$A_S = C_S + D_S + E_S, \quad (1)$$

where, A_s Dictates the position of the s^{th} grasshopper, C_s is the social interaction, D_s is the gravity force and E_s defines the wind advection.

To provide random behaviour, the equation can be written as $A_s = rd_1C_s + rd_2D_s + rd_3E_s$, where rd_1, rd_2 and rd_3 are random numbers in [0, 1]:

$$C_s = \sum_{\substack{v=1 \\ v\neq 1}}^{p} g(e_{sv}) e_{sv}, \quad (2)$$

where, e_{sv} is the distance between s[th] and the v[th] grasshopper, computed as $e_{sv} = |d_1 - d_2|$, g is a function to state the strength of social forces, as shown in Eq. (3), and $e_{sv} = (d_1 - d_2)/e_{sv}$ is a unit vector from the s[th] grasshopper to the v[th] grasshopper.

The g function, which defines the social forces, is calculated as follows:

$$g(rd) = Pe^{-rd/k} - e^{-rd}, \quad (3)$$

where, P denotes the intensity of attraction and k is the length scale. The shape of the function g have D component and is computed as:

$$D_s = -qy_q, \quad (4)$$

where, q is the gravitational constant and y_q shows a unity vector towards the centre of earth.

The E component is computed as follows:

$$E_s = kh_b, \quad (5)$$

where, k is a constant drift and h_b is a unity vector in wind direction.

The first component of the Eq. (6) will apparently elucidate the location of the present grasshoppers concerning other grasshoppers:

$$P_x^h = z\left(\sum_{\substack{y=1 \\ y\neq 1}}^{p} z\frac{u_h - l_h}{2} w\left(\left|k_y^h - k_x^h\right|\right)\frac{k_y - k_x}{h_{xy}}\right) + Q_h. \quad (6)$$

In Eq. (6), the first x from the left has the same weight as inertial (w) in GH. It minimizes grasshopper's movements throughout the goal. Exploration and exploitation of the whole prey balances the parameter. The second x decreases the attraction zone, comfort zone, and repulsion zone between grasshoppers. By using the element $z\frac{u_h - l_h}{2} w(|k_y - k_x|)$, $z\frac{u_h - l_h}{2}$ linearly diminishes the space that the grasshoppers should explore and exploit. The element $w(|k_y - k_x|)$ implies if a grasshopper should be repelled from (exploration) or attracted to (exploitation) the target. The z internal contributes to a decrease of the repulsion or attraction between grasshoppers proportionally to the number of iterations, and the z external decreases the search covers around the target with the rise of the iteration count. In short, Eq. (6) first expression, the sum takes into account the role of other grasshoppers and applies the fragility of the grasshopper's relationship [6,7]. The second term Q_h, facilitates their tendency to travel towards the food source. The parameter h also facilitates the change in momentum of grasshoppers that evaluate and subsequently consume the source of food. The coefficient c minimizes the comfort space in proportion to the number of iterations and computed as defines:

$$h = h\max - a\frac{h\max - h\min}{A}, \quad (7)$$

where, $h$max is the maximum value, $h$min is the minimum value, a indicates the current iteration, and A is the maximum number of iterations.

In GHGWO, a search medium upgrades its position by using alpha and beta as shown in Eq. (8):

$$P(t+1) = P + f1 * rand * ((P_1 - P) + (P_2 - P))/2. \quad (8)$$

A further mural for the upgrade of the alpha and beta direction is not upgraded by all people of the population, but by alpha only in the GHGWO proposed to maintain their workforce homogeneity. The proposed algorithm acts as a declining strategy to avoid the local optimum:

$$P(t+1) = P + f1 * rand * (P_1 - P). \quad (9)$$

Chaos is known for non-linear probabilistic systems as a computational pseudorandom phenomenon. One-dimensional pseudo-invertible maps can produce chaotic motion. This paper uses a well-known chaotic map called a logistic map that depends sensibly on its initial condition. The logistic map is depicted as:

$$p_{t+1} = \mu \cdot p_t(1 - p_t), \quad (10)$$

where, p_t is a variable, and μ is usually set to four, thus for any p_t located in [0, 1], the equation can generate a deterministic chaotic sequences recursively.

A chaotic search strategy was formulated subject to the logistic map. Chaotic search techniques can be interpreted as:

$$lp_t^{q+1} = \mu \cdot lp_t^q(1 - lp_t^q), \quad (11)$$

where, p_t^q represents the chaotic variable and q denotes the iteration number.

C. Split-ring resonator MTM cell configuration

Two concentric conductor circles with divisions in direction opposite to one another comprise of a square split-ring resonator. The magnitudes are much lower than the operational wavelength of these metallic resonant additions and thus, quasi-static theory can be very well implemented in predicting its electromagnetic attitudes using the appropriate RLC resonant model. The integration of SRR with the quasi-static electric system counterpart is shown in Fig. 3 (a) and Fig. 3 (b) represents the equivalent circuit model. The capacitance between the two conductor rings (G12) of the resulting current and voltage distribution is in series in the first half of SRR with a capacitance in the second half of the circle. It is presumed that rings of wavelength "*wd*" and split length "*sl*" are the same in both SRR rings for the derivation of the corresponding inductance A_d and capacitance B_d. The SRR framework shall be etched

with a thickness of 1.575 mm on a FR4 epoxy substratum. The inductance interpretation A_d is specified as:

$$A_d = \frac{\mu_0}{2}\frac{h_{avg}}{4}4.86\left[In\left(\frac{0.98}{\rho}\right)+1.84\rho\right], \quad (12)$$

where, μ_0 is free-space permeability and h_{avg} is the average strip length of both rings, computed as defies:

$$h_{avg} = 4[rl-(wd+sl)], \quad (13)$$

Rl is the length of outer ring, *wd* is the width of each ring and *sl* is the separation between both rings.

'ρ' being the filling ratio is given as below:

$$\rho = \frac{wd+sl}{[rl-wd+sl]}. \quad (14)$$

The expression for effective capacitance 'B_d' is computed as:

$$B_d = \frac{B_{12}}{4} = \left[rl-\frac{(wd+sl)}{2}\right]B_0, \quad (15)$$

where, 'B_0' is the per-unit length capacitance between two conductor rings in the presence of dielectric substrate of height '*ht*' and dielectric constant 'ε_a', presented as follows:

$$B_0 = \varepsilon_0\varepsilon_b^t\frac{H(\sqrt{1-m^2}}{H(m)}. \quad (16)$$

Here, ε_0 is free-space permittivity and H is the complete elliptic integral of first type:

$$m = \frac{sl}{sl+wd}. \quad (17)$$

The ε_b^t, effective relative permittivity, of dielectric substrate is given as:

$$\varepsilon_b^t = 1+\frac{2}{\pi}arctg\left[\frac{ht}{2\pi(wd+sl)}\right](\varepsilon_t-1). \quad (18)$$

The resonant intensity for the RLC models is generated by A_d and B_d (as in Eq. (19)). This is additionally based on geometrical parameters of SRR, i.e., '*rl*' outer ring length, '*wd*' ring width and '*sl*' separation of both rings:

$$fq_t = \frac{1}{2\pi\sqrt{A_d B_d}}. \quad (19)$$

The goal is to optimize SRR layout so that the optimized unit cell resonates at an appropriate resonance frequency by tuning its geometric parameters (*rl*, *wd*, *sl*). Given this goal, the cost function is derived as observes for optimization as:

$$fq_{ct} = fq_{dr} - fq_{cr}. \quad (20)$$

The ideal frequency of resonance is 'fq_{dr}' and the resonant frequency of 'fq_{cr}' is determined using the RLC method. Resonant intensity fq_t and resonant frequency fq_{cr} are related to the built fractal antenna is designed to simulate and observationally tested without metamaterial cells in order to acquire the double band output at 3.68 GHz. When evaluating the data, the signal transmission is interrupted at a 4.4 GHz narrow band which makes the intensity band inoperable.

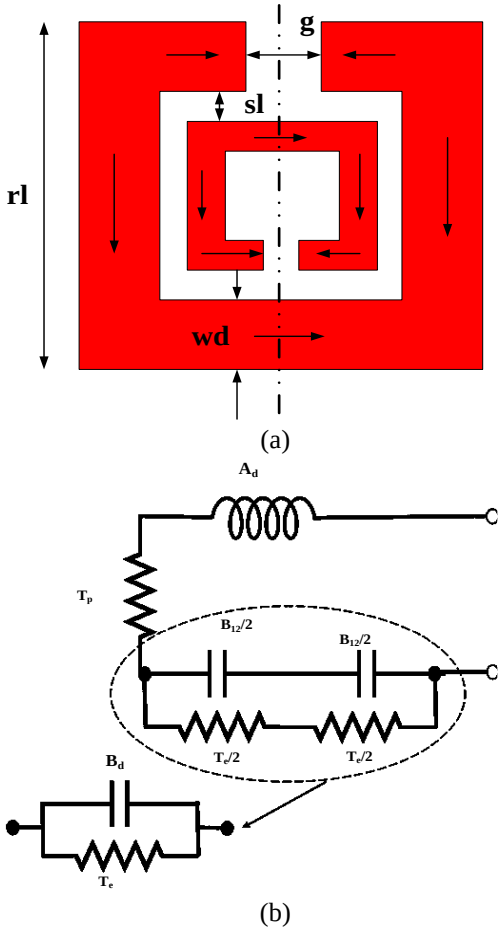

Fig. 3. (a) Structural dimensions of split-ring resonator. (b) Its quasi-debilitated frequency range into usable band, the desired static equivalent circuit model.

D. Selection of parameters for optimization algorithms

A wide selection of parameter settings associated with the specific optimization algorithm strongly influences the performance of optimization. For proposed hybrid GHGWO, A_s Dictates the position of the grasshopper, C_s is the social interaction, D_s is the gravity force and E_s defines the wind advection.

For original BFO techniques and hybrid BF-PSO, highest possible chemical count 'N_c', reproductive count 'N_{re}' and removal and neutralization count 'N_{ed}' are perceived to be 50, 4 and 4, respectively.

III. EXPERIMENTAL RESULTS

The fitness chart is shown in Fig. 4, the convergence graph. As shown in the graph, the GHGWO, BF-PSO output is close to that of chaos PSO. Nonetheless, the conversion rate is slow compared to other algorithms, while the IWO-classical BFO is compatible with the peak iteration termination requirements.

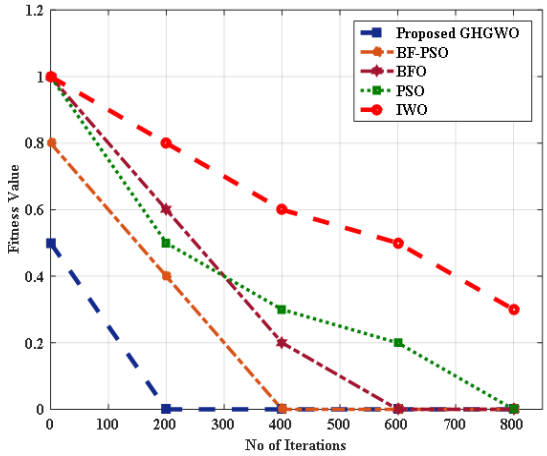

Fig. 4. Convergence plot for proposed GHGWO, modified BF-PSO, classical BFO, PSO and IWO algorithms.

In Table 1 the proposed GHGWO algorithm is obviously efficient in comparison with other algorithms. In this optimizing task, the mean value and standard deviation achieved in the GHGWO algorithm is better than in other algorithms [8, 9]. PSO and modified BF-PSO results are also identical to the GHGWO algorithm:

$$j = \pm\sqrt{\frac{(1+Q_{11})^2 - Q_{21}^2}{(1-Q_{11})^2 - Q_{21}^2}}, \tag{21}$$

$$c^{ik_0 b} = \frac{Q_{21}}{1 - Q_{11}\dfrac{j-1}{j+1}}, \tag{22}$$

$$p = \frac{1}{r_0 b}\left[\left\{\left[In\left(c^{ik_0 b}\right)\right]' + 2w\pi\right\} - s\left[In\left(c^{ik_0 b}\right)\right]\right], \tag{23}$$

where, $\left[In\left(c^{ik_0 b}\right)\right]$ represents imaginary components, and $\left[In\left(c^{ik_0 b}\right)\right]'$ represents real components of complex number Q_{11} and Q_{21} are derived correspondingly, p and j represent both refractive index and product impedance, r_0 for wave events in free room shows wave number, b for peak cell length and w for periodical functions typical of sinusoidal structure. The cell of the MTM unit has a homogenous effective index and impedance, because the optimized size of the external ring (rl) is $\frac{\lambda}{12}$ for the optimal resonant frequency of 4.4 GHz. It makes the simple branch ($w = 0$) to be used for continuous refractive index. Active permeability and permeability are extracted from the corresponding refractive index and impedance:

$$\varepsilon = \frac{p}{j}, \tag{24}$$

$$\mu = pj. \tag{25}$$

Figures 5 (a), (b) applies to a Q-parameter (Q11 and Q21) magnitude and stage Chart derived from HFSS simulation of optimized SRR design. The real and imaginary portions of derived complex permeability and permittivity are shown in figure 5c d, accordingly. It's evident from the Fig. 5 (c), (d), that in frequency ranges from 3.9 up to 4.5 GHz both permittivity and permeability are negative and hence have dual-negative metamaterial properties in target frequency range. Therefore, the framework used to forecast costs is efficiently using a quasi-static analogous model.

In Fig. 6 displays retarded loss functionality, reflecting an increase of the bandwidth in the newly designed fractal antenna after charging optimized SRR unit cells. From the figure, the fractal antenna contributes to dual-band output at 3.68 GHz and 4.72 GHz without metamaterial unit cells. In the frequency range between 4.2 and 4.5 GHz the signal transmission is limited, so this band felt the impact.

Figure 7 contrasts simulated and measured coefficient outcomes with MTM unit cells, respectively for modelled fractal antenna without charging.

The data are collected from the bench top vector network analyzer with a frequency between 10MHz and 20GHz.

Table 1: Comparative performance of proposed GHGWO algorithm with various methods

Criteria	Proposed GHGWO	Modified BF-PSO	Classical BFO	PSO	IWO
Best solution	0.000001	0.000002	0.000005	0.000002	0.00003
Mean solution	0.054213	0.528061	0.492478	0.517842	0.440051
Worst solution	0.691249	0.741507	0.870005	0.782456	0.880102
Standard deviation	0.354328	0.381412	0.454483	0.418753	0.463854
Average time(T)	4.018	4.546	9.411	4.587	11.151

For optimized antennas loaded with SRR, Fig. 8 shows simulated and measured VSWR performance. VSWR is an important parameter that indicates a signal feed location corresponding impedance.

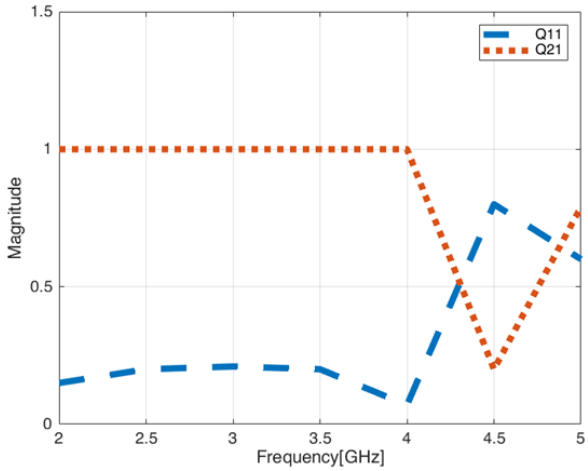

(a)

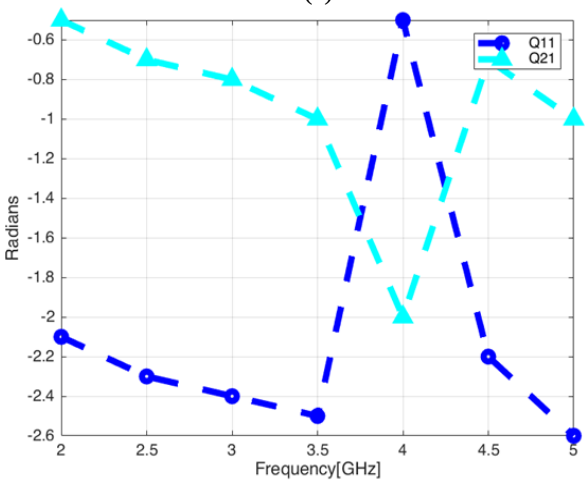

(b)

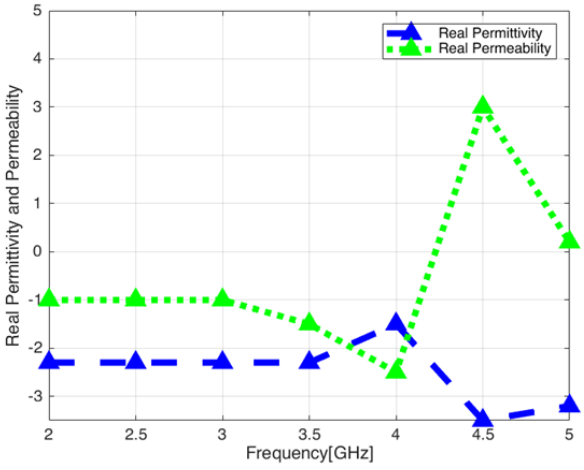

(c)

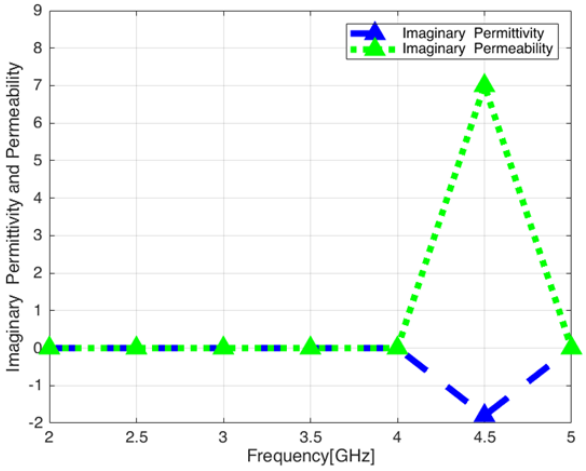

(d)

Fig. 5. (a) Extracted magnitude of Q11 and Q21 for optimized SRR. (b) Extracted phase (radians) of Q11 and Q21 for optimized SRR. (c) Real components of permittivity and permeability. (d) Imaginary components of permittivity and permeability.

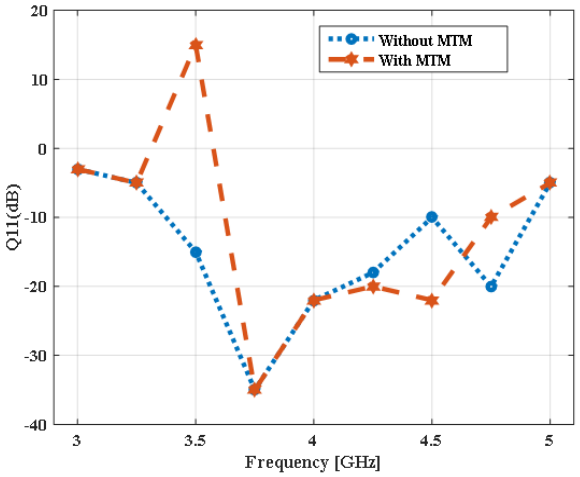

Fig. 6. Antenna without MTM and with MTM performance comparison.

The antenna gain vs. frequency plot for an integrated fractal antenna equipped with SRR shown in Fig. 9. The optimistic strong gain in the small frequency range between 3.44 and 4.85 GHz can be seen. At 4 GHz, the peak frequency is 13.8 dB, and the lowest at 4.4 GHz is 3.2 dB.

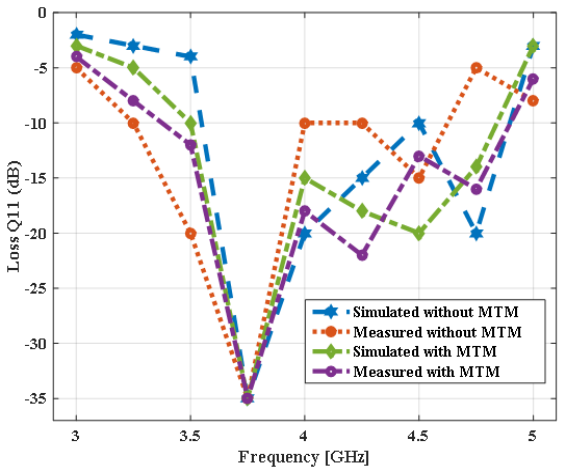

Fig. 7. Return loss properties simulated and measured for fractal antenna cells without and with MTM unit cells.

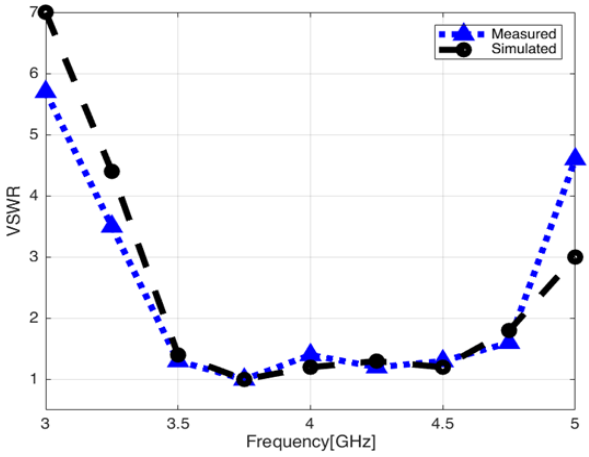

Fig. 8. VSWR for configured SRR-loaded fractal antenna simulated and measured.

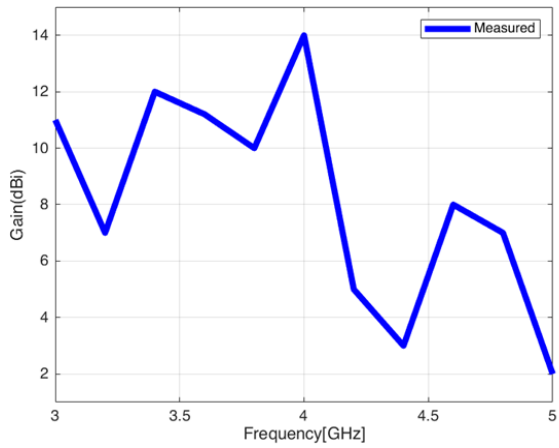

Fig. 9. Measured antenna gain versus frequency track for SRR-presented antennas optimized.

IV. CONCLUSION

The paper envisages the new design of a partial-ground square fractal microstrip line-fed antenna. Enhanced rectangular band on a partial plane increases capacitance stability, leading to a double-band output of 3.68 GHz and 4.72 GHz. The GHGWO hybrid algorithm is proven superior to other algorithms due to its stronger mean solution, the lowest standard deviation and substantially lower time. Two square split-ring resonators, a common metamaterial unit cell, are charged after an optimization close to the micro-line feed of the formulated fractal antenna. Upon processing of the antenna with optimized SRR structures, dual band response from the built fractal antenna is converted into bandwidth efficiency (3.49–4.73 GHz). For the conceptual testing of simulation effects the modelled fractal antenna without and with metamaterial mounting is generated. The enhanced findings show that an optimisation in the antenna design and engineering of the SRR metamaterial unit Cell for the throughput progression of the designed fractal antenna.

REFERENCES

[1] D. Werner, R. Haupt, and P. Werner, "Fractal antenna engineering: The theory and design of fractal antenna arrays," *IEEE Antennas and Propagation Magazine*, vol. 41, no. 5, pp. 37-58, 1999.

[2] E. Ekmekci, K. Topalli, T. Akin, and G. Turhan-Sayan, "A tunable multi-band metamaterial design using micro-split SRR structures," *Optics Express*, vol. 17, no. 18, pp. 16046-16058, 2009.

[3] D. Srivastava, A. Khanna, and J. Saini, "Design of a wideband gap-coupled modified square fractal antenna," *Journal of Computational Electronics*, vol. 15, no. 1, pp. 239-247, 2015.

[4] B. Babayigit and E. Senyigit, "Design optimization of circular antenna arrays using Taguchi method," *Neural Computing and Applications*, vol. 28, no. 6, pp. 1443-1452, 2016.

[5] P. Mishra, S. Pattnaik, and B. Dhaliwal, "Square-shaped fractal antenna under metamaterial loaded condition for bandwidth enhancement," *Progress In Electromagnetics Research C*, vol. 78, pp. 183-192, 2017.

[6] M. Dorostkar, R. Azim, and M. Islam, "A novel Γ-shape fractal antenna for wideband communications," *Procedia Technology*, vol. 11, pp. 1285-1291, 2013.

[7] R. Bojanic, V. Milosevic, B. Jokanovic, F. Medina-Mena, and F. Mesa, "Enhanced modelling of split-ring resonators couplings in printed circuits," *IEEE Transactions on Microwave Theory and Techniques*, vol. 62, no. 8, pp. 1605-1615, 2014.

[8] Y. Choukiker and S. Behera, "Modified Sierpinski square fractal antenna covering ultra-wide band application with band notch characteristics," *IET Microwaves, Antennas & Propagation*, vol. 8, no. 7, pp. 506-512, 2014.

[9] A. Numan and M. Sharawi, "Extraction of material parameters for metamaterials using a full-wave simulator [Education Column]," *IEEE Antennas and Propagation Magazine*, vol. 55, no. 5, pp. 202-211, 2013.

Design and Analysis of EBG Antenna for Wi-Fi, LTE, and WLAN Applications

Pronami Bora, P. Pardhasaradhi, and B. T. P. Madhav

Antennas and Liquid Crystals Research Center, Department of ECE
Koneru Lakshmaiah Education Foundation, Andhra Pradesh, 522502, India
pronamiz@gmail.com

Abstract ─ A non-planar electromagnetic band gap (EBG) structured antenna is proposed in this paper for wireless communication applications. The proposed design consists of coplanar waveguide (CPW) fed square patch antenna embedded with triangular EBG backing on FR-4 substrate material for 2.4 GHz (Wi-Fi, LTE) and 5.2 GHz (WLAN) applications. Gain is improved from 2.8 dB to 13.9 dB by adding EBG structure in the proposed antenna and the parametric analysis is done for optimizing the antenna performance characteristics. The proposed antenna provides a maximum efficiency of 82.5% in the resonating frequencies. The prototyped antenna is having good correlation with the simulation results obtained from Finite Element Method (FEM) based Anyss-HFSS. High Frequency Structure Simulator is used to analyze the antenna parameters and the simulated and measured results are correlating well with each other with a slight change in frequencies.

Index Terms ─ Coplanar waveguide, EBG, high frequency structure simulator, long term evolution, wireless fidelity, wireless LAN.

I. INTRODUCTION

Over the past few years EBG structures are gaining much attention in the research activities for their ability to achieve compact size antennas than the conventional antennas by controlling the electromagnetic properties of the antenna [1]. EBG structures are artificial periodic structures which resists the electromagnetic waves in a particular frequency band. EBGs find applications in microwave filters, gratings, amplifiers and microstrip devices [2]. These structures exhibit the ability to vary the electromagnetic behavior and this unique property is incorporated in antennas to achieve enhanced gain, improved radiation pattern and thereby increasing the performance and efficiency of the antenna. The concept of EBG structures is based on the principle of total internal reflection realized by periodic structures. EBGs generate reflected and source waves in same direction which enables improvement in the radiation pattern and gain enhancement and can be used to increase the overall performance of an antenna [3]. The use of EBG structures provides improved capability of suppressing the surface waves and reducing the mutual coupling compared to other traditional approaches [4]. EBGs are basically of 3 types: one dimensional (1D) EBG, two dimensional (2D) and three dimensional (3D) electronic band gap structures. 1D EBG structures are periodic in one dimension only and as a result the band gaps are limited to that particular direction only. This limits the use of 1D EBG structures. 2D EBG structures are homogenous in one dimension and periodic in two directions which make them beneficious for achieving compactness and stability. 3D EBG structures are periodic in all dimensions and have a remarkable feature of blocking the electromagnetic waves in all directions due to its periodic nature but it is difficult to fabricate and analyze. Several researchers incorporated EBG structures in antenna to enhance the directivity and the bandwidth of the antenna [5-6]. Various EBG structures have been incorporated in wearable antennas for reducing SAR and efficient transmission [7-9]. The advantages of using EBGs in microwave applications have been reported in [10]. Various shapes of EBG structure like spiral, E shape, fork like, mushroom, woodpile for providing compactness have been investigated [11]. In this paper, we propose a 2D EBG structured antenna to enhance the gain and bandwidth by suppressing the surface waves. The 2D EBG structures are more valuable than 3D EBG due to their ease of fabrication and their capability of maintaining similar control like 3D structures on the wave propagation. The benefits of EBG structures have motivated us to design our proposed antenna which is a CPW fed square patch antenna embedded with triangular EBG backing with 0.4 depth of trench on FR-4 substrate material having dielectric conductivity of 4.4. This design provides an improvement in gain and efficiency by providing a maximum gain of 13.9 dB with an efficiency of 82.5%.

II. ANTENNA DESIGN

The antenna parameter performances are changed according to various shapes of EBG cells. In this work, we have considered sixteen different antenna

Submitted On: January 7, 2020
Accepted On: June 25, 2020

https://doi.org/10.47037/2020.ACES.J.350908

configurations by varying the EBG structures and the patch structures. Basic design structures consisting of rectangular, square, triangular and circular patches are presented. Similarly, the different EBG structures including square EBG, rectangular EBG, circular EBG and square EBG are considered. Figure 1 represents the groups of 4 different model designs considered. The antenna parameters of all the structures can be calculated from the standard expressions available in literature [12]. All the EBG structures are incorporated with trenches of depth of 0.4mm from the substrate. The four different patch structures with square EBG where each unit cell dimension is 37x37mm^2 is shown in Fig. 1 (a) and the corresponding reflection coefficient curves for all the four combinations is shown in Fig. 2. Figure 1 (b) shows the four different patch structures with rectangular EBG where each unit cell dimension is 37x15 mm^2 and the corresponding reflection coefficient curves can be observed in Fig. 3. Similarly Fig. 1 (c) and 1 (d) shows the four different patch structures with circular EBG where each unit cell dimension of radius 17.5 mm and four different patch structures with triangular EBG respectively. The corresponding reflection coefficient curves are shown in Figs. 4 and 5 respectively

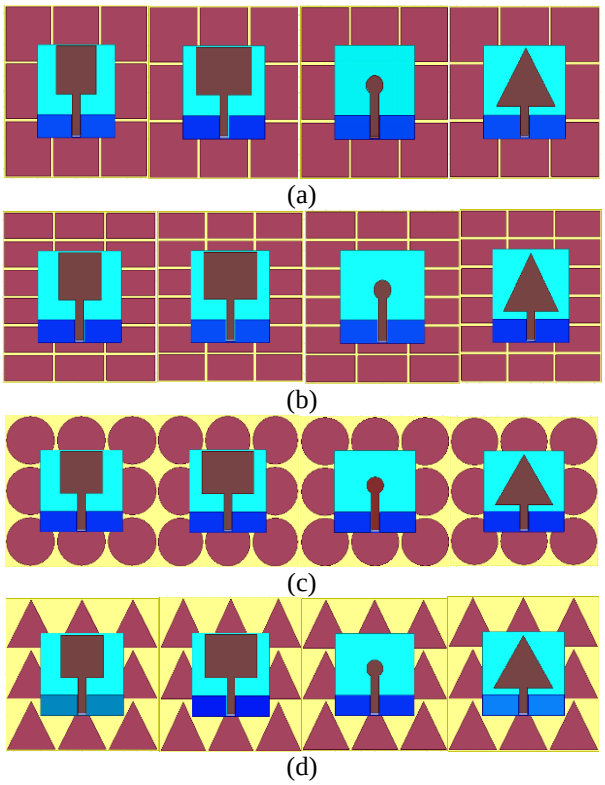

Fig. 1. Different EBG structures with variations in patch: (a) square EBG with different patch structures, (b) rectangular EBG with different patch structures, (c) circular EBG with different patch structures, and (d) triangular EBG with different patch structures.

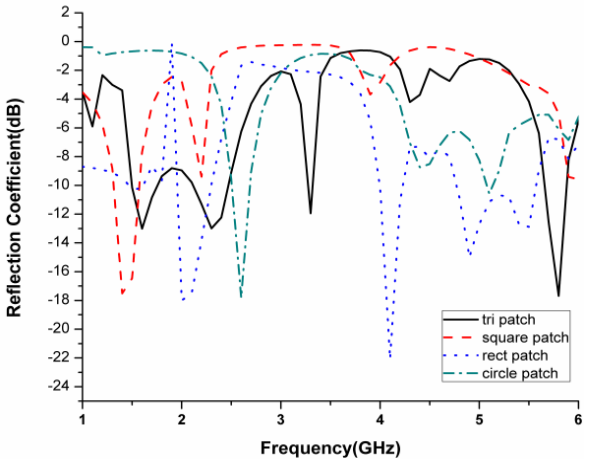

Fig. 2. Simulated reflection coefficient for square EBG with different patch structure.

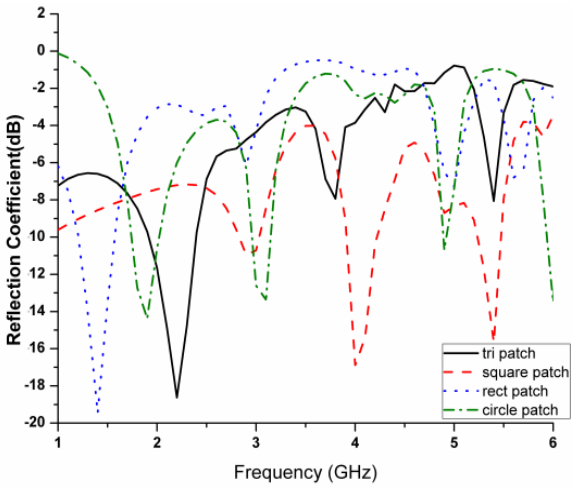

Fig. 3. Simulated reflection coefficient for rectangular EBG with different patch structure.

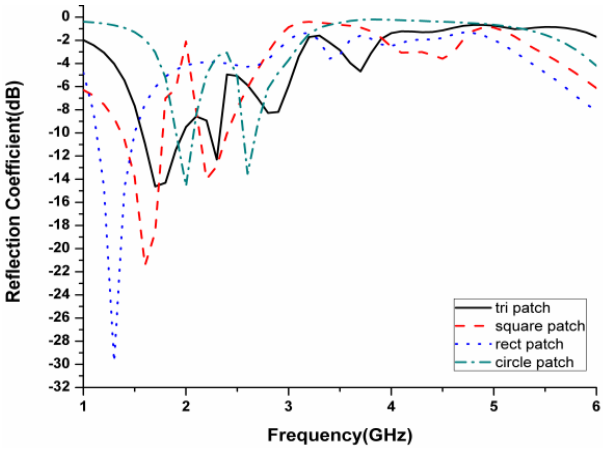

Fig. 4. Simulated reflection coefficient for circular EBG with different patch structure.

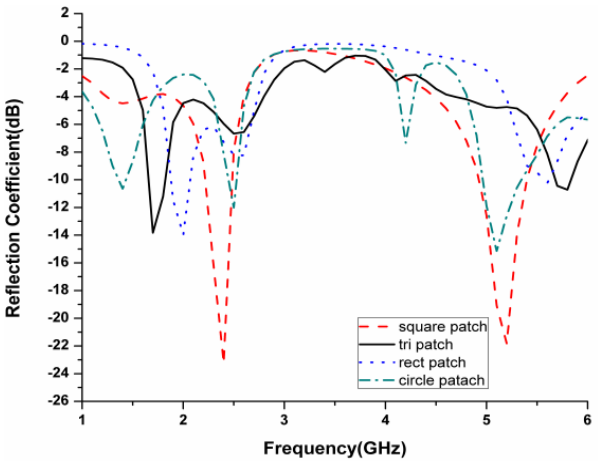

Fig. 5. Simulated reflection coefficient for triangular EBG with different patch structure.

From the analyses and observations implemented in this paper, it can be seen that the square patch antenna with triangular EBG structures gives the effective result in the desired frequency range which can be witnessed from the reflection coefficient curves of other models in Figs. 2, 3, 4 and 5 respectively. It is observed that out of the sixteen different designs, seven designs have satisfactory results in our desired range. The antenna parameters like gain, VSWR and reflection co-efficient of the seven models were compared with each other given in Table 1 and the analyses proved that the optimized result is given by our proposed design.

Table 1: Antenna parameters

Model	Reflection Coefficient (dB)	VSWR	Max Gain (dB)
Square EBG Circle Patch	-17	<2	4
Square EBG Triangular Patch	-13,-16	<2	8.1
Rectangular EBG Triangular Patch	-18	<1.5	4.5
Circular EBG Circle Patch	-13,-14	>2	4
Triangular EBG Square Patch	**-23,22**	**<1.5**	**13.9**
Triangular EBG Rectangular Patch	-12	<2	6.4
Triangular EBG Circle Patch	-14	<2.5	0.8

III. PROPOSED DESIGN AND RESULTS

The proposed CPW fed microstrip antenna with 3D EBG backing is shown in Fig. 6 (a). The antenna is mounted on FR-4 substrate which is one of the most commonly available materials with a relative permittivity of 4.4 and loss tangent of 0.005. The substrate thickness is 1.6 mm with trenches of 0.4 mm. Thickness of the substrate reduces the size of antenna and surface radiations. The bottom plane consists of periodically distributed triangular electronic band gap structures. The patch antenna is fed by a co-planar waveguide which is 6 mm in width and dimension of the feed length is 29.9 mm. A second substrate of height 1.6 mm is incorporated above the EBG surface with a gap of 1.4 mm. The other dimensions of the design are given in Table 2.

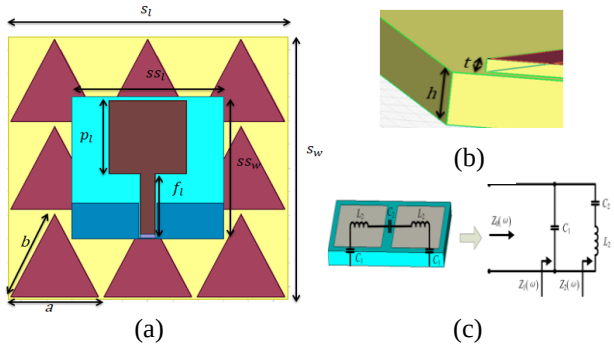

Fig. 6. Triangular EBG square patch antenna: (a) top view, (b) side view, and (c) equivalent circuit of EBG cell.

The side view of the model to show the dimension of the trenches and the equivalent circuit of a conventional EBG cell of the triangular structure is shown in Figs. 6 (b) and 6 (c) respectively.

Where C_1 is the capacitance between unit cells, C_2 arise as a result of gap between unit cells, and ground and L_2 represents the inductance of EBG. The input impedance can be given as:

$$Z_o(w) = Z_1(w)/Z_2(w),$$

$$Z_o(w) = \frac{j(1-w^2C_1L_2)}{W(C_1C_2L_2W^2-C_1-C_2)}.$$

As a result, the resonating frequency expression can be given as:

$$f_r = \frac{1}{2\pi}\sqrt{\frac{C_1+C_2}{L_1C_1C_2}}.$$

It can be seen from the expression of resonating frequency that if we reduce the size of the unit cell then there is no effect in capacitance between the adjacent cells, however C_1 reduces and the overall inductance increases resulting in decrease in the resonating frequency. This can be further observed with the reflection co-efficient curves for square and triangular EBG structures as shown in Fig. 7.

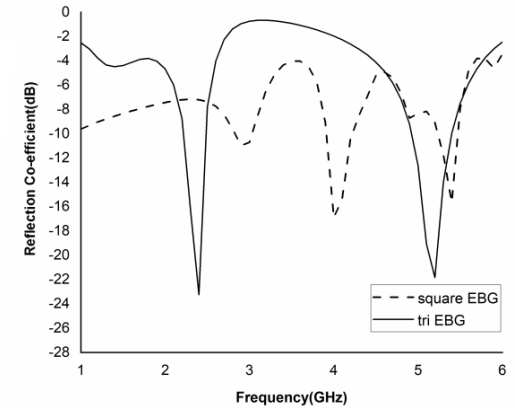

Fig. 7. Effect of cutting EBG.

Table 2: Antenna dimensions

Dimensions	s_l	s_w	ss_l	ss_w	p_l	f_l	a	b
mm	111	111	60	60	29.44	29.9	35	35

Reflection coefficient of the antenna is improved significantly with the use of the EBG structures and gain is also increased to a considerable extent which is evident from Figs. 8 and 9 for both the operating frequency.

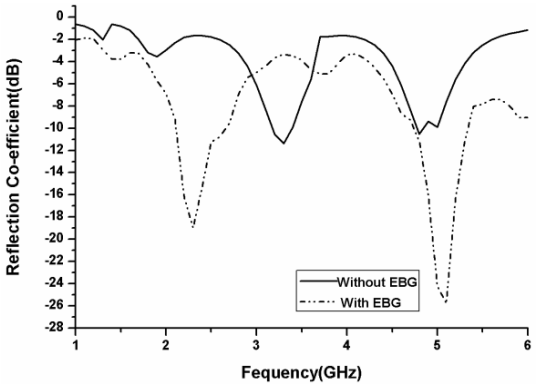

Fig. 8. Measured reflection coefficient with and without EBG for square patch.

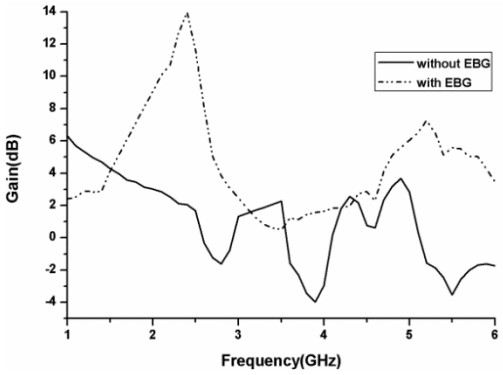

Fig. 9. Gain with EBG without EBG.

The fabricated antenna is shown in Fig. 10. Optimization of all parameters has been done for the best possible performance.

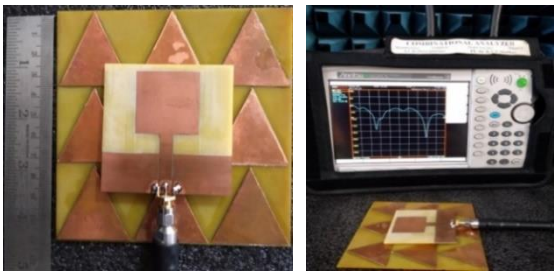

(a) (b)

Fig. 10. Fabricated antenna and measurement setup: (a) fabricated model and (b) measurement setup.

Ansoft High Frequency Structure Simulator (HFSS) version 13.0 is used for carrying out simulations of the proposed design and the measured results were carried out in Vector Network Analyzer manufactured by ANRITSU. The model number is MS2073C offering a frequency range from 5 kHz to 15 GHz and 350 μs/data point sweep speed.

A. Reflection coefficient

Figure 11 shows the measured and the simulated reflection coefficient for the proposed antenna. The proposed antenna is providing return loss greater than 18 dB and VSWR of less than 1.5 at the operating frequencies.

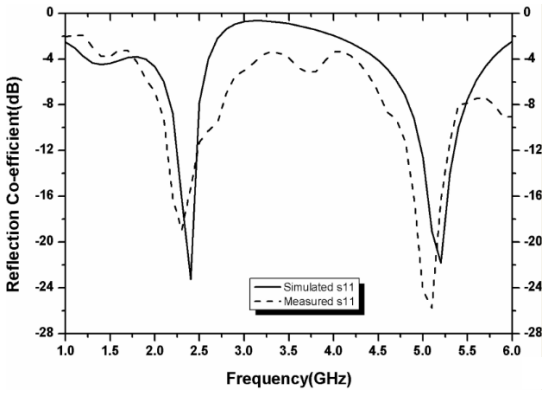

Fig. 11. Simulated and measured reflection coefficient.

It is visible from the figures that the measured and the simulated results are well matched with each other with slight change in frequencies.

B. Radiation pattern

Figures 12 and 13 shows the radiation patterns for both the H and E plane respectively for the two operating frequencies. The radiation pattern of the proposed antenna maintains good performance in both the resonating frequencies.

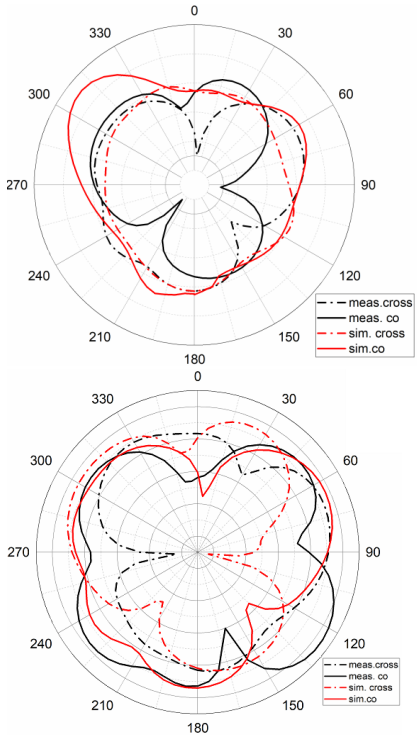

Fig. 12. Measured and simulated E and H plane radiation patterns for antenna at frequency 2.4 GHz.

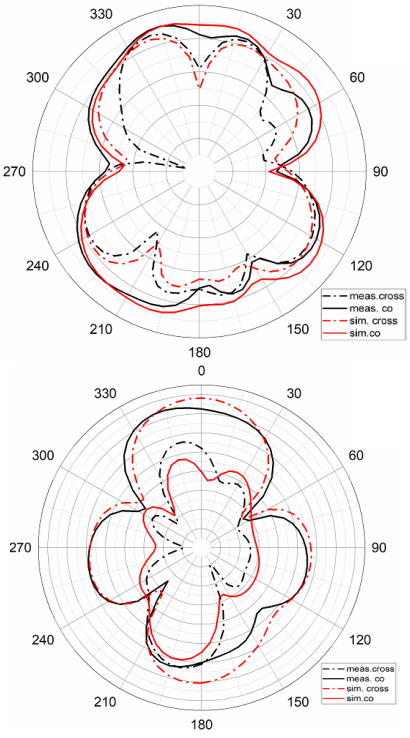

Fig. 13. Measured and simulated E and H plane radiation patterns for antenna at frequency 5.2 GHz.

It is observed that for every operating state of the antenna co-polarization is greater than X-polarization in the H plane. Thus, the antenna is having better transmission and reception efficiency. The gain versus efficiency plot is shown in Fig. 14.

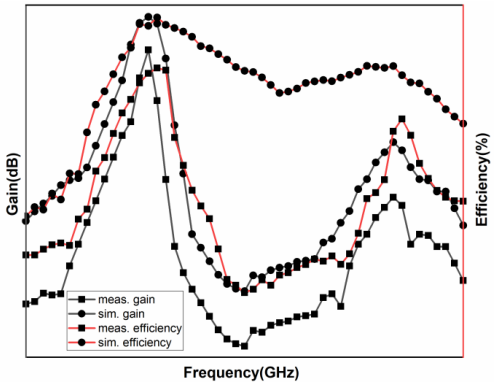

Fig. 14. Gain vs efficiency plot of proposed design.

The proposed design has a maximum gain of 13.9 dB and efficiency at 2.4 GHz resonating frequency in 82.5%. Another resonating frequency is obtained at 5.2 GHz with a gain of 7.2 dB and efficiency of 67%.

IV. PARAMETRIC ANALYSIS

To achieve the best possible performance, several physical parameters of the proposed design are varied to observe the changes in the reflection coefficient which are discussed in this section. The original dimensions used in the proposed model gives the optimized results which is visible from the observations.

A. Variation in width of feed

The antenna is CPW fed with a 50 ohm transmission line. The variations in the feed width were evaluated by changing the width to 5 mm and 7 mm and our proposed design gives the optimized result as shown in Fig. 15.

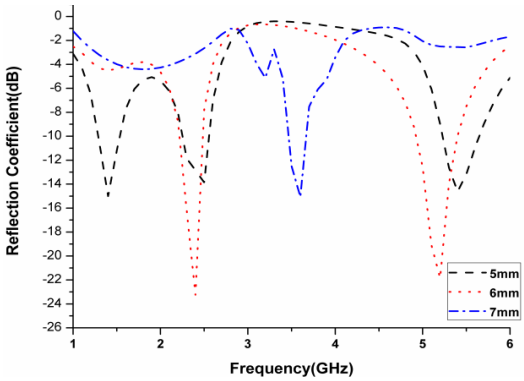

Fig. 15. Simulated reflection coefficient by changing feed width.

B. Variation in distance between EBG and antenna

Reflection coefficient is observed by changing the distance of the triangular EBG structures and the CPW antenna to 1 mm and 1.8 mm. The distance of 1.4 mm of our proposed design is gives the best results as evident from Fig. 16.

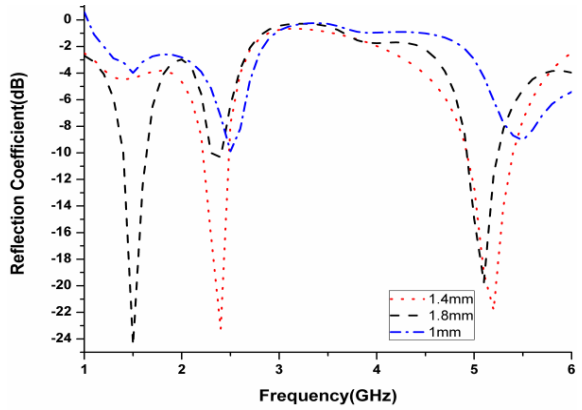

Fig. 16. Simulated reflection coefficient by changing the spacing between EBG and CPW antenna

Table 3 shows the comparison of size, bandwidth, gain and resonating frequencies of other antennas available in literature with the proposed design for wireless applications. It can be observed that the overall gain and bandwidth have been improved with our proposed design. Moreover, the size of our proposed design is also the optimized one with reflection coefficient > 20dB. Numerical results demonstrate that the proposed antenna is advantageous in terms of bandwidth, gain, low weight and cost of fabrication.

Table 3: Comparison with other antenna models

Ref. No.	Size (mm)	Resonance Frequency (GHz)	Gain (dB)	Bandwidth (GHz)
[13]	140x80	2.4	8.7	2.4-2.57
[14]	60x60	2.4	2.4	2.4-2.5
[15]	60x60	2.44	5.39	2.3-2.435
[16]	68x40	5.8	8.4	5.4-5.8
[17]	218x53x73	3.5	4.7	3.5
[18]	100x100	1.57 and 2.3	3.2	1.57-1.65, 2.2-2.4
This paper	60x60	2.4 and 5.2	13	2.2-2.5, 4.8-5.3

V. CONCLUSION

In this paper, triangular EBG structured CPW fed square patch antenna is proposed. Due to the transmission characteristics of EBG structures and the use of CPW feeding, the overall size of this patch antenna is smaller than the conventional patch antennas. The back lobes and mutual coupling are reduced to a greater extent and considerable gain has been obtained.

Proposed antenna will serve some of the S-band and C-band applications covering WiFi, WIMAX and LTE. The proposed antenna provides a gain improvement of around 10 dB with 82.5% efficiency and the resonating frequencies of 2.4 GHz and 5.2 GHz with good impedance matching makes the proposed antenna suitable for Wi-Fi, LTE and WLAN applications.

REFERENCES

[1] M. Abu, S. A. M. Ali, H. Hassan, and I. M. Ibrahim, "Characterization of artificial magnetic conductor, electromagnetic band gap and frequency selective surface," *Journal of Telecommunication, Electronic and Computer Engineering*, vol. 10, 2018.

[2] J. Gomez, A. Tayebi, J. R. Almagro, I. Gonzalez, and F. Catedra, "Design and optimization of an EBG antenna with an efficient electromagnetic solver," *International Journal of Antennas and Propagation*, Article ID 427178, 2012.

[3] M. A. B. Abbasi, S. S Nikolaou, M. A. Antoniades, M. N. Stevanović, and P. Vryonides, "Compact EBG-backed planar monopole for BAN wearable applications," *IEEE Transactions on Antennas and Propagation*, vol. 65, iss. 2, pp. 453-463, Feb. 2017.

[4] H. F. Shaban, H. A. Elmikaty, and A. A. Shaalan, "Study the effects of electromagnetic band-gap (EBG) substrate on two patches microstrip antenna," *Progress In Electromagnetics Research B*, vol. 10, pp. 55-74, 2008.

[5] A. R. Weily, K. P. Esselle, T. S. Bird, and B. C. Sanders, "Dual resonator 1-D EBG antenna with slot array feed for improved radiation bandwidth," *IET Microwaves, Antennas and Propagation*, vol. 1, no. 1, pp. 198-203, 2007.

[6] G. K. Palikaras, A. P. Feresidis, and J. C. Vardaxoglou, "Cylindrical electromagnetic bandgap structures for directive base station antennas," *IEEE Antennas and Wireless Propagation Letters*, vol. 3, no. 1, pp. 87-89, 2004.

[7] R. Pei, M. Leach, E. G. Lim, Z. Wang, C. Song, J. Wang, W. Zhang, Z. Jiang, and Y. Huang, "Wearable EBG-backed belt antenna for smart on-body applications," *IEEE Transactions on Industrial Informatics*, Apr. 2020.

[8] M. El Atrash, A. A. A., and S. S. Abd-Alwahab, "An ultra-thin compact highly efficient Π-section CRLH–EBG based antenna for ISM applications," *IEEE International Symposium on Antennas and Propagation and USNC-URSI Radio Science Meeting*, pp. 1595-1596, 2019.

[9] P. Sambandam, M. Kanagasabai, S. Ramadoss, R. Natarajan, M. G. N. Alsath, S. Shanmuganathan, and M. Sindhadevi, "Compact monopole antenna backed with fork slotted EBG for wearable

applications," *IEEE Antennas and Wireless Propagation Letters*, 2019.
[10] Y. Rahmat-Samii, "The marvels of electromagnetic band gap (EBG) structures," *ACES Journal*, vol. 18, no. 4, Nov. 2003.
[11] S.-R. Kiom, G.-Y. Lee, T. U. Nouyen, and K.-J. Jong, "Performance improvement of MIMO antenna with 1D EBG ground structures for wideband applicatio," *IEEE Antennas and Wireless Propagation Letters*, vol. 12, pp. 168-1571, 2013.
[12] C. A. Balanis, *Antenna Theory: Analysis and Design*. 3rd ed., NJ: Wiley, 2005.
[13] A. Khidre, K.-F. Lee, F. Yang, and A. Z. Elsherbeni, "Circular polarization reconfigurable wideband E-shaped patch antenna for wireless applications," *IEEE Transactions on Antennas and Propagation*, vol. 61, iss. 2, Feb. 2013.
[14] D. N. Vaishnavi, G. Vanaja, G. Jayasree, and S. Mounika, "Design and analysis of metamaterial antenna with EBG loading," *Far East Journal of Electronics and Communications*, ISSN: 0973-7006, vol. 14, no. 2, pp. 127-136, 2015.
[15] N. A Malek, A. M. Ramly, A. Sidek, and S. Y Mohamad, "Characterization of acrylonitrile butadiene styrene for 3D printed patch antenna," *Indonesian Journal of Electrical Engineering and Computer Science*, vol. 6, no. 1, pp. 116-123, Apr. 2017.
[16] K.V. Prasad, M. V. S. Prasad, M. S. Kumar, and B. Alekhya, "Surface wave suppression in patch arrays using EBG structures," *IEEE Conference on Signal Processing And Communication Engineering Systems*, vol. 6, pp. 100-104, 2018.
[17] I. Kim and Y. Rahmat-Samii, "Beam-tilted dipole EBG array antenna for future base station applications," *Proc. IEEE Antennas Propag. Soc. Int. Symp*., pp. 1224-1225, 2013.
[18] S. Jun, B. Sanz-Izquierdo, J. Heirons, C. X. Mao, S. Gao, D. Bird, and A. McClelland, "Circular polarised antenna fabricated with low-cost 3D and inkjet printing equipment," *Electronics Letters*, vol. 53, no. 6, pp. 370-371, Mar. 16, 2017.

Pronami Bora received U.G. and P.G. degree from Gauhati University and Assam Don Bosco University, Assam. Presently working as an Assistant Professor in Dept. of ECE, KLEF, A.P. Research interest includes antennas and wireless communications.

P.Pardha Saradhi received U.G., P.G. and Ph.D. degrees from Acharya Nagarjuna University, A.P., India. He is working as Professor in Dept. of ECE, KLEF, A.P. and has published more than 67 papers in International Journals and Conferences. He is Reviewer for many journals including Elsevier, Taylor and Francis and is a life member of IACSIT, IAENG and UACEE.

B T P Madhav working as Professor in ECE and Associate Dean R&D at KLEF. He has published more than 248 Scopus/SCI papers in International, National Journals and is a reviewer for several International Journals including IEEE, Elsevier, Wiley, Springer and Taylor and Francis. His research interests include antennas, liquid crystals applications and wireless communications. He is a member of IEEE and life member of ISTE, IACSIT, IRACST, IAENG, UACEE and Fellow of IAEME.

Design of Reconfigurable Patch Antenna in Frequency, Pattern, and Switchable Polarization

Yan Zhang [1], Da Sun [1], Tao Dong [2], and Jie Yin [2]

[1] School of Electronic and Information Engineering
Beihang University, Beijing, 100191, China
yanzhang@buaa.edu.cn, sunda_buaa@163.com

[2] State Key Laboratory of Space-Ground Integrated Information Technology
Beijing Institute of Satellite Information Engineering, Beijing, 100095, China
dongtaoandy@163.com, kingjack333333@126.com

Abstract ─ In this paper, a circularly polarized frequency, pattern, and polarization switching antenna is proposed. The antenna consists of an octagonal patch, a narrow octagonal ring and four diamond-shaped parasitic patches on the top layer. Two feed points of the radiating patch are connected to a Wilkinson power divider loaded with the phase reconfigurable transmission lines on the bottom layer. Reconfiguration of the polarization and pattern is realized by using PIN diodes as switching components. By controlling the bias voltage across the varactors, various narrow frequency bands can be achieved. The proposed antenna operates at a frequency tuning range from 1.96 to 2.03 GHz. The radiation pattern can be switched among five cases in yoz-plane and xoz-plane, with the switchable polarization between left- and right-hand circular polarization. In addition, these three types of reconfiguration can be controlled independently.

Index Terms ─ Beam switching, frequency reconfigurable, patch antenna, switchable polarization.

I. INTRODUCTION

With the rapid development of modern wireless communication, people have a strong demand for the higher speed and quality of information transmission. Thus, antennas in modern applications must be multifunctional and adaptable with the system requirements in the varying electromagnetic environment. Reconfigurable antennas, also known as the tunable antenna, have attracted much attention.

Frequency reconfigurable antennas are realized by using PIN diodes [1-3], varactors [4-6] and MEMS [7] as the RF switches to change the size of the radiating patch or using liquid crystal [8] and metasurface [9]. Polarization reconfigurable antennas can be achieved by controlling the states of the PIN diodes to change the structure of the feeding network [10,11] and adjust the radiation structure of the antenna [12,13]. Pattern reconfiguration or beam scanning based on PIN diodes, parasitic stubs and metamaterial structure are introduced in [14-16]. In the recent years, some efforts have been done to realize arbitrary combination of two of three reconfigurable characteristics, including frequency and polarization reconfigurable antenna [17], pattern and polarization reconfigurable antenna [18] and so on. Furthermore, some antennas with frequency, pattern reconfiguration and polarization switching have been also reported in [19,20]. However, most of reconfigurable antennas combined two or three types of reconfiguration are unable to control the antenna parameters independently.

Therefore, a novel reconfigurable patch antenna is designed to achieve three types of reconfiguration independently in this paper. By controlling the bias voltage across the varactors and PIN diodes, the three types of reconfiguration can be realized, and characteristic parameters of the antenna can be controlled independently.

II. ANTENNA DESIGN

The geometry of the proposed reconfigurable antenna is shown in Fig. 1. On the top layer of the upper substrate, an octagonal patch, as shown in Fig. 1 (a), is located at the center and surrounded by four diamond-shaped parasitic patch elements. The center radiating patch with a cross-shaped slot is fed by the Wilkinson power divider with the phase reconfigurable transmission lines.

In order to realize the frequency reconfiguration, eight varactors (D1 to D8) are located between the octagonal patch and octagonal ring. In addition, four PIN diodes are placed across the slot of parasitic patch for pattern reconfiguration. On the bottom layer of the lower

Submitted On: April 22, 2020
Accepted On: June 11, 2020

https://doi.org/10.47037/2020.ACES.J.350909

substrate, the feed network, as shown in Fig. 1 (c), consists of a Wilkinson power divider and the phase reconfigurable transmission lines with six PIN diodes (S11, S12, S21, S22, S31 and S32) providing the required phase shift along two output branch lines for different polarizations.

Two pieces of substrates with the dielectric constant ε_r (2.9), have a thickness of h1 (4.5 mm) and h2 (1.5 mm), as shown in Fig. 1 (b). The ground plane is located on the top layer of the lower substrate. And the output ports of the feed network (Port 1 and 2) are connected to the octagonal radiating patch via two probes. Detailed dimensions of the proposed antenna are listed in Table 1.

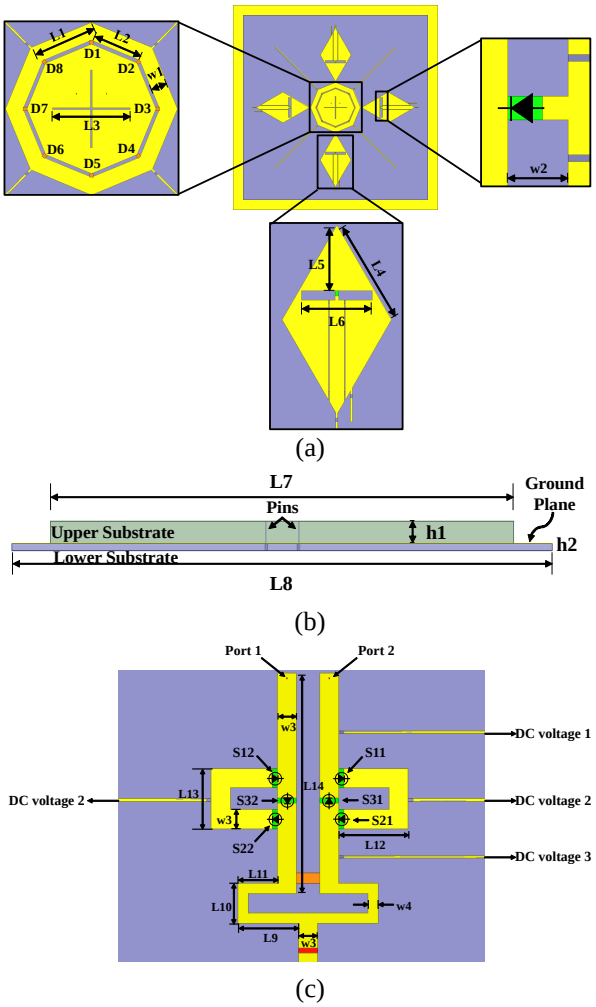

Fig. 1. Geometry of the proposed antenna: (a) top view, (b) side view, and (c) bottom view.

Table 1: Dimensions of the proposed antenna

Parameter	Value/mm	Parameter	Value/mm
L1	18.7	L11	7.9
L2	14.8	L12	13.2
L3	22	L13	12
L4	30	L14	44.1
L5	17.9	w1	5
L6	19.5	w2	2.6
L7	160	w3	3.8
L8	180	w4	2.1
L9	12.1	h1	4.5
L10	8.1	h2	1.5

III. SIMULATION AND ANALYSIS

In this section, the reconfiguration mechanism of the antenna is described in detail and the performance of the proposed antenna is simulated by using HFSS.

A. Frequency reconfiguration

The frequency reconfiguration is achieved by controlling the reverse bias voltage of the varactors, MA2S372, (D1 to D8 shown in Fig. 1 (a)) connected between the radiating patch and the octagonal ring. Under different capacitance values, the radiating patch with an octagonal ring provides several frequency bands. The equivalent capacitance of varactors at different bias voltages are listed in Table 2.

Table 2: Capacitance values of the varactor

Bias Voltage/V	Equivalent Capacitance/pF
4.5	10
6	8
9	6
13.5	4
30	2

Figure 2 shows the simulated results at different reverse bias voltages for RHCP. As the reverse bias voltage increases from 4.5 to 30 V, the resonant frequency of antenna shifts from 1.96 to 2.03 GHz, as shown in Fig. 2 (a). From Figs. 2 (b)-(c), the antenna gain is higher than 7.68 dBi and the axial ratio is below 3 dB at resonant frequency for different reverse bias voltages, which indicates good circular polarization (CP) performance during frequency reconfiguration.

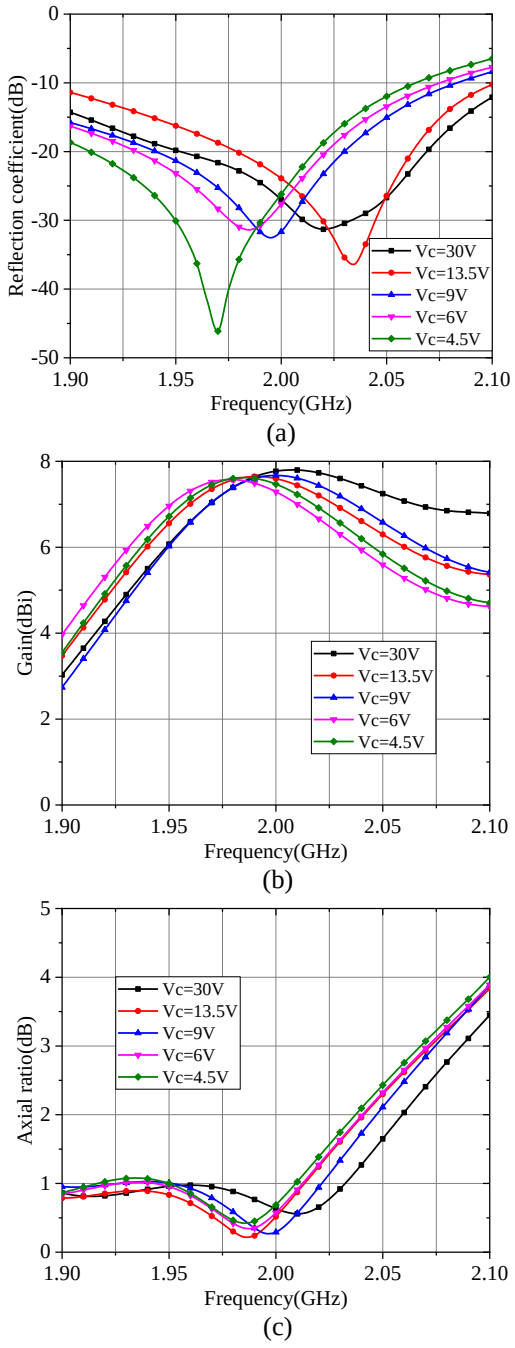

Fig. 2. Simulated results at different reverse bias voltage for RHCP: (a) reflection coefficient, (b) realized gain, and (c) axial ratio.

B. Polarization reconfiguration

The polarization reconfiguration of antenna can be realized by the Wilkinson power divider and phase reconfigurable transmission lines. By controlling the ON/OFF state of the PIN diodes, the left-hand (LH) and right-hand circular polarization (RHCP) of antenna can be chosen.

By controlling the DC voltage 1, 2 and 3 (V1 < V2 < V3), the diodes S12, S22, S31 are in ON state, and all the other diodes are OFF. In this case, a 90°-delay transmission line is inserted into the left branch and LHCP is realized. The transmission path of the signal and the simulated radiation patterns are shown in Figs. 3 and 4.

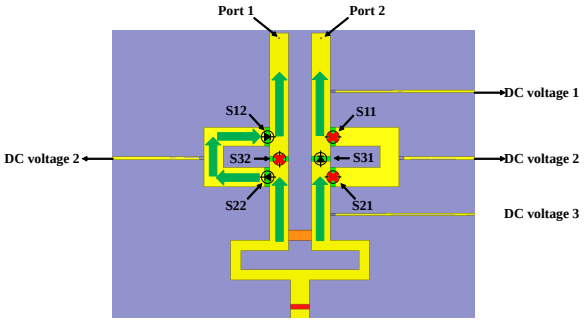

Fig. 3. Transmission path of the signal at V1 < V2 < V3.

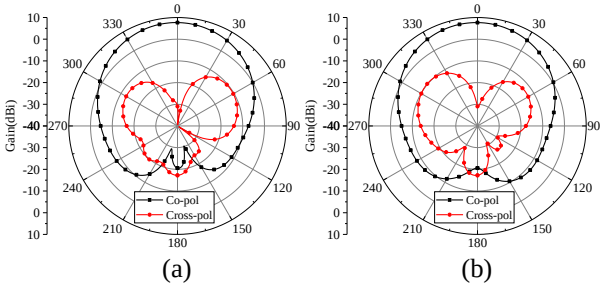

Fig. 4. Simulated LHCP radiation patterns of the antenna at 2 GHz: (a) yoz-plane and (b) xoz-plane.

It can be seen from Fig. 4 that the antenna gain is 7.68 dBi and the cross-polarization level is less than -20 dB for LHCP state.

Similarly, as the diodes S11, S21, S32 are in ON state (V1 > V2 > V3) and all the other diodes are switched OFF, the transmission path of the signal is shown in Fig. 5. At this time, the antenna establishes the RHCP. The simulated results are shown in Fig. 6.

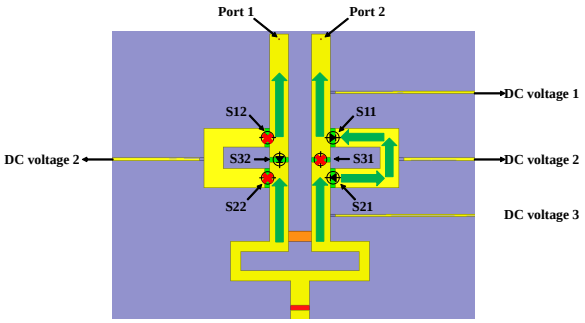

Fig. 5. Transmission path of the signal at V1 > V2 > V3.

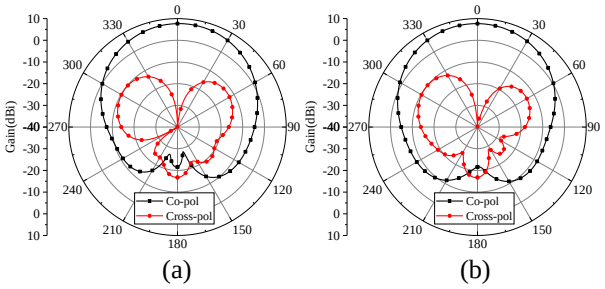

Fig. 6. Simulated RHCP radiation patterns of the antenna at 2 GHz: (a) yoz-plane and (b) xoz-plane.

From Fig. 6, the antenna gain is 7.66 dBi with the cross-polarization less than -20 dB for RHCP state. In addition, the axial ratio (AR) versus frequency of the proposed antenna for LHCP and RHCP cases is also presented in Fig. 7.

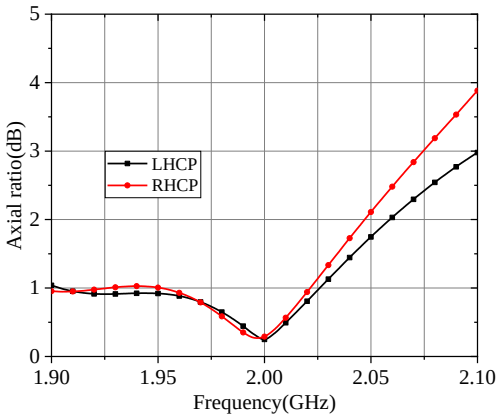

Fig. 7. Simulated axial ratio of the proposed antenna in two CP states for LHCP and RHCP.

It can be seen from Fig. 7 that the AR is 0.3 dB at 2 GHz. Compared with Figs. 2 (a) and (c), good CP performance (AR<1dB) can be observed in the whole of reconfigure frequency range from 1.96 to 2.03 GHz.

C. Pattern reconfiguration

The pattern reconfiguration is achieved by changing the OFF/ON state of the PIN diodes (S1 to S4) on the parasitic patch A, B, C and D, as shown in Fig. 8.

The surface current distributions on the radiating and parasitic patches for three cases are shown in Fig. 9.

As S1-S4 are in ON state, the surface current is mainly located at the radiating patch, as shown in Fig. 9 (a). As S1 is in OFF state, the surface current on the parasitic patch A, where S1 is located, increased significantly, as shown in Fig. 9 (b). And the main beam tilts toward +y direction. Similarly, the main beam tilts toward -y direction as S2 is in OFF state, as shown in Fig. 9 (c). The information on the state of four PIN diodes for five cases is listed in Table 3.

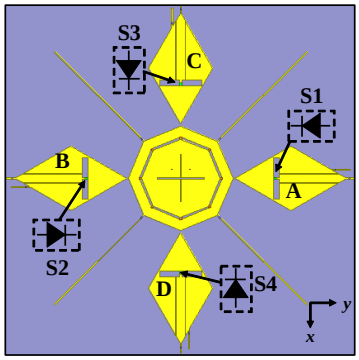

Fig. 8. Structure of the pattern reconfiguration module.

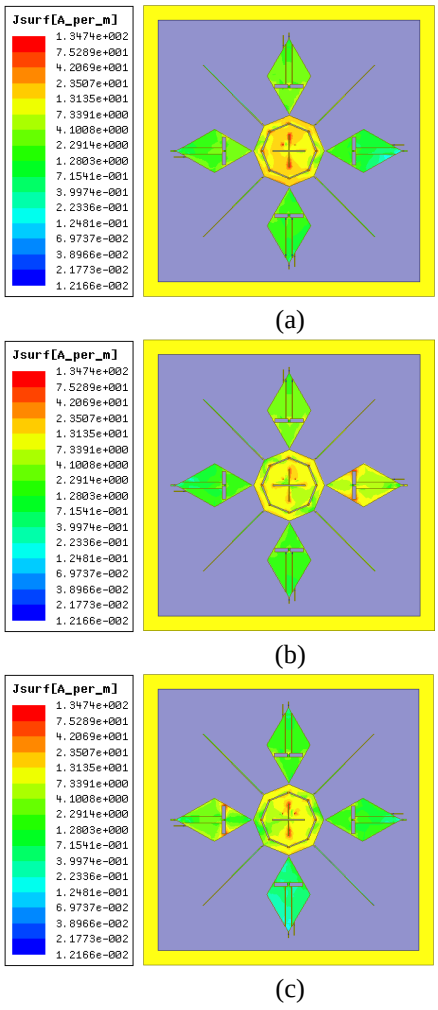

Fig. 9. Simulated surface current distributions at 2 GHz in different cases: (a) S1-S4 are ON, (b) S1 is OFF, and others are ON, (c) S2 is OFF, and others are ON.

Table 3: The state of four PIN diodes for five cases

Case	S1	S2	S3	S4	Pattern Mode
1	ON	ON	ON	ON	Boresight
2	OFF	ON	ON	ON	+y-direction tilted
3	ON	OFF	ON	ON	-y-direction tilted
4	ON	ON	OFF	ON	-x-direction tilted
5	ON	ON	ON	OFF	+x-direction tilted

Taking the polarization state of RHCP as an example, when the bias voltage across the varactor D1 to D8 is 9V, the resonance frequency of the antenna is 2GHz. In order to evaluate the impedance characteristics of antenna for these four pattern reconfiguration cases, the simulated reflection coefficients are provided in Fig. 10.

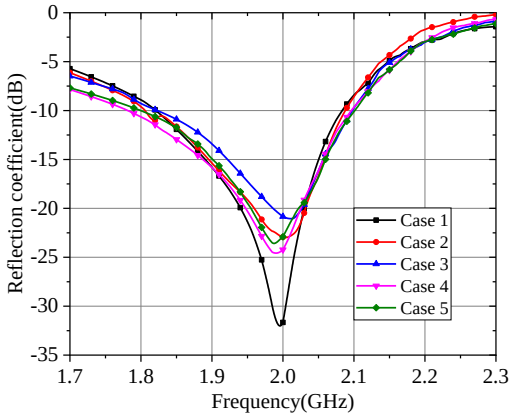

Fig. 10. Simulated reflection coefficient for five cases (Vc=9V).

It is noticed from Fig. 10 that the antenna operates in the frequency band of 1.82-2.09 GHz with reflection coefficient of less than -10 dB for different cases. Detailed information on simulation results is listed in Table 4.

Table 4: Impedance characteristics for five cases

Case	Center Frequency/ GHz	Bandwidth/ %	-10dB Band Range/GHz
1	1.96	13.8	1.82~2.09
2	1.95	14.4	1.81~2.09
3	1.96	14.3	1.82~2.10
4	1.94	15.5	1.79~2.09
5	1.95	15.4	1.80~2.10

The simulated radiation efficiency of the proposed antenna for five cases is shown in Fig. 11.

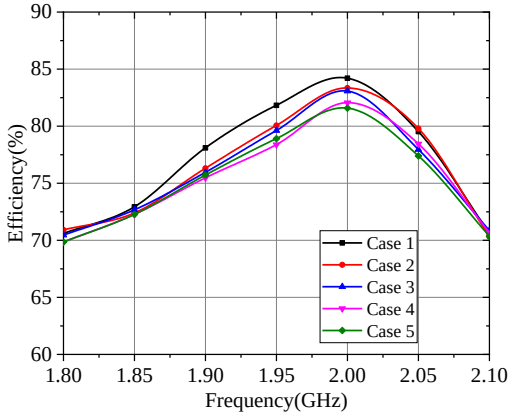

Fig. 11. Simulated radiation efficiency of the proposed antenna in different cases for Vc=9V.

From Fig. 11, results of the simulation indicate that the proposed antenna features a good efficiency, being greater than 70% in the whole operating frequency range for five cases. Meanwhile, the simulated RHCP radiation patterns at 2GHz for five cases are shown in Fig. 12.

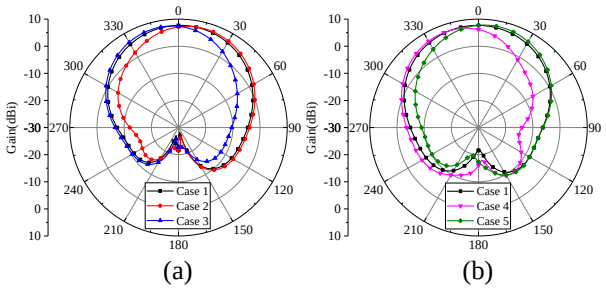

Fig. 12. Simulated RHCP radiation patterns of the antenna for five cases at 2 GHz: (a) yoz-plane and (b) xoz-plane.

It can be seen from Fig. 12 that: 1) the main beam could tilt toward five directions for pattern reconfiguration; 2) the beamwidth becomes narrower as the main beam tilts.

For the comparison purpose, the simulated LHCP radiation patterns at 2 GHz for five cases are also shown in Fig. 13. And detailed simulation results of radiation characteristics are listed in Table 5 and 6.

It can be seen from Table 5 and 6, for LHCP in Case 1, the main beam direction is at -1° in yoz-plane with a 3dB beamwidth from -40.6° to 37°. Therefore, the main beam direction of the proposed antenna can be pointed to approximate 10° and -10° in yoz-plane for Case 2 and Case 3, respectively, with the realized gain around 7.62-7.64 dBi. Similarly, when the diodes operate in Case 4 and Case 5, the main beam of the pattern can be pointed to -15° and 10° in xoz-plane with the realized gain around 7.27-7.84 dBi. In addition, when the antenna operates in

RHCP, the main beam direction of the proposed antenna can be pointed to approximate 1°, 13°, -13° in yoz-plane and -17°, 10° in xoz-plane for Case 1 to Case 5. The difference of the radiation patterns in yoz-plane and xoz-plane is mainly due to the asymmetry of the feed network.

The peak gain and axial ratio at the main beam for five cases are presented in Fig. 14.

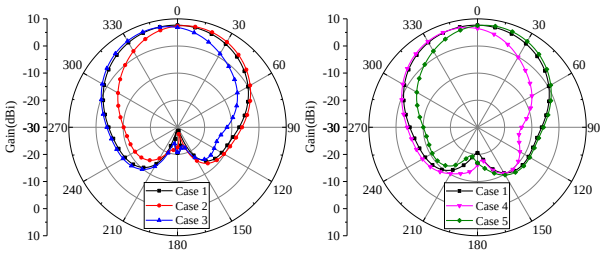

Fig. 13. Simulated LHCP radiation patterns of the antenna for five cases at 2 GHz: (a) yoz-plane and (b) xoz-plane.

Table 5: Radiation characteristics of the proposed antenna in yoz-plane

Case	Polarization	Gain/ dBi	Beam Direction	3dB Beam Range
1	LHCP	7.67	-1°	-40.6°~37°
	RHCP	7.70	1°	-40.5°~36°
2	LHCP	7.64	10°	-19.8°~42°
	RHCP	7.68	13°	-16.5°~46°
3	LHCP	7.62	-10°	-41.3°~20°
	RHCP	7.53	-13°	-46.3°~15°

Table 6: Radiation characteristics of the proposed antenna in xoz-plane

Case	Polarization	Gain/ dBi	Beam Direction	3dB Beam Range
1	LHCP	7.66	0°	-40.7°~37°
	RHCP	7.68	0°	-41.0°~37°
4	LHCP	7.27	-15°	-46.7°~13°
	RHCP	7.09	-17°	-48.7°~10°
5	LHCP	7.84	10°	-18.8°~42°
	RHCP	7.95	10°	-21.7°~41°

From Fig. 14 (a), it can be observed that the peak gain in yoz-plane is about 7.68 dBi with 0.05 dB and 0.17 dB variation along the beam direction for LHCP and RHCP, respectively. In Fig. 14 (b), the peak gain at 0° has a variation of 0.39 dB and 0.59 dB along the beam direction in xoz-plane for LHCP and RHCP. In addition, the axial ratio along the main beam direction for five cases is less than 3dB for CP reconfiguration.

In order to demonstrate that the radiation pattern of the antenna in CP state can be switched among five cases within the frequency reconfigurable range from 1.96 to 2.03 GHz, the simulated results are provided in Fig. 15 and Fig. 16.

Figure 15 and Fig. 16 present the co-polarization and cross-polarization radiation patterns for RHCP in different cases at 1.96 GHz (Vc=4.5V) and 2.03GHz (Vc=30V), respectively.

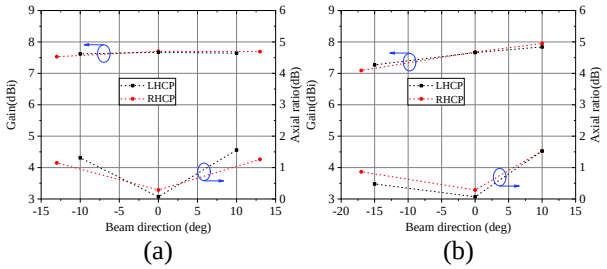

Fig. 14. Simulated peak gain and axial ratio versus the beam direction angles at 2 GHz: (a) yoz-plane and (b) xoz-plane.

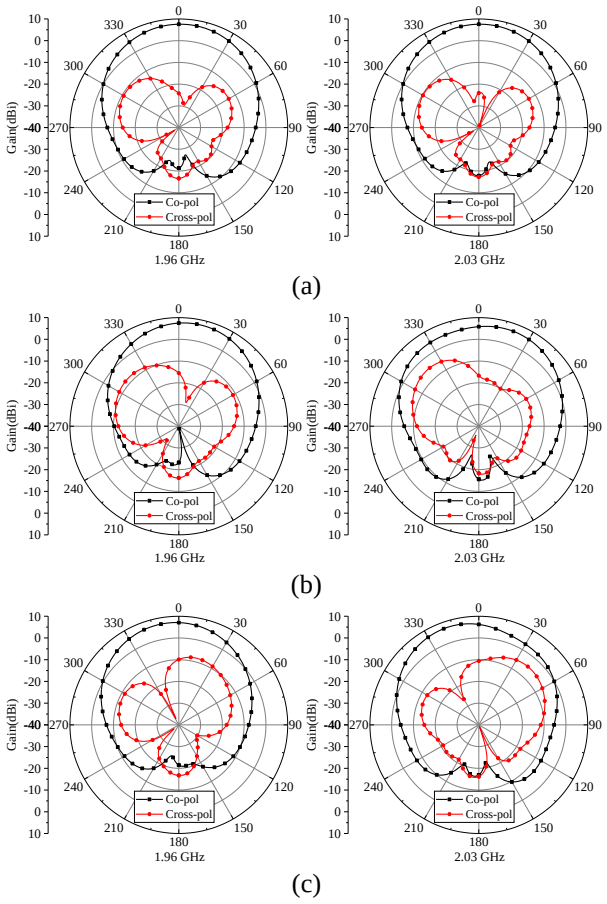

Fig. 15. Simulated RHCP radiation patterns in yoz-plane at 1.96 GHz and 2.03 GHz: (a) Case 1, (b) Case 2, and (c) Case 3.

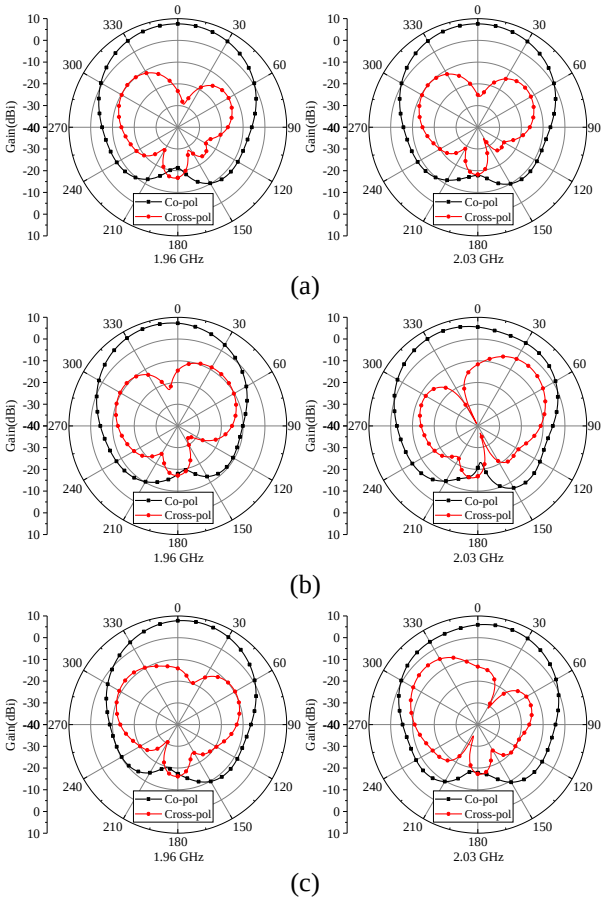

Fig. 16. Simulated RHCP radiation patterns in xoz-plane at 1.96 GHz and 2.03 GHz: (a) Case 1, (b) Case 4, and (c) Case 5.

The main beam direction of the pattern can be pointed to approximate 0°, 10°, -6° in yoz-plane and -1°, -10°, 7° in xoz-plane with cross-polarization levels less than −15 dB at 1.96 GHz. Similarly, when the antenna operates at 2.03 GHz, the beam direction can be pointed to approximate 3°, 17°, -16° in yoz-plane and -1°, -19°, 14° in xoz-plane with cross-polarization levels less than −10 dB. All the above simulated results indicate that the proposed antenna can realize pattern reconfiguration in LHCP and RHCP during the reconfigure frequency range.

IV. MEASUREMENT RESULTS AND DISCUSSION

An antenna prototype is fabricated and tested for impedance and radiation characteristics of the proposed design. A photo of the fabricated antenna prototype is shown in Fig. 17.

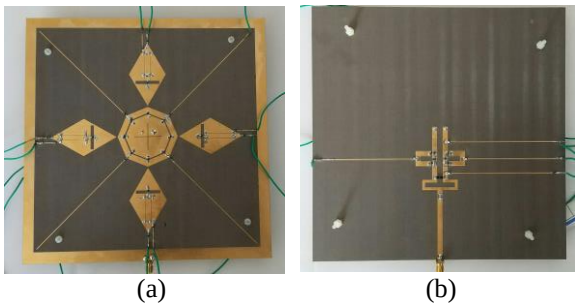

Fig. 17. Photographs of the proposed antenna: (a) top view and (b) bottom view.

The measured reflection coefficient of the antenna is presented in Fig. 18.

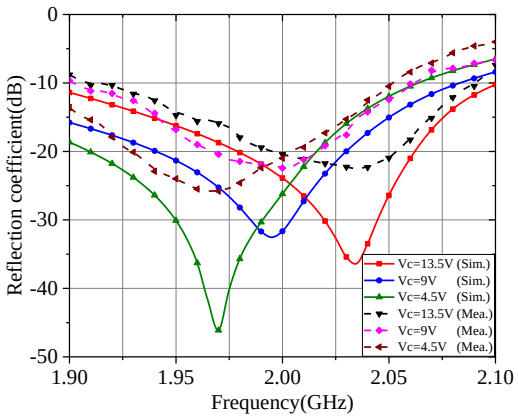

Fig. 18. Simulated and measured reflection coefficient at different reverse bias voltage.

From Fig. 18, it can be seen that the resonant frequency ranges from 1.96 to 2.03 GHz as the bias voltage increases from 4.5 to 13.5V. The differences between the measured and simulated data may be related to the mismatch caused by external connectors, the deviation of the substrate dielectric constant, and the processing error of the structure.

The measured radiation performance of the antenna is shown in Fig. 19.

Figure 19 shows that the agreement between the simulation results and the measured data is reasonably good.

Compared with the existing designs of reconfigurable antennas listed in Table 7, the proposed work has the advantages of low profile, high efficiency, and multiple functions, which is very attractive in mobile communication.

Table 7: Compared with the reported reconfigurable antennas

Ref.	Type	Reconfiguration	Actuators	η (%)	Size (λ_0)
[21]	Patch	Frequency and polarization	12 Varactors	60	0.62×0.62×0.03
[22]	Patch	Frequency and pattern	4 PIN diodes	78	0.67×0.67×0.02
[23]	Slot	Polarization and pattern	9 PIN diodes	75	4.5×1.1×0.08
[19]	Patch and pixel layer	Frequency, polarization and pattern	60 PIN diodes	53	2.1×1.1×0.07
[20]	Slot	Frequency, polarization and pattern	48 PIN diodes	49	0.86×0.78×0.01
This work	Patch	Frequency, polarization and pattern	10 PIN diodes and 8 Varactors	70	1.2×1.2×0.04

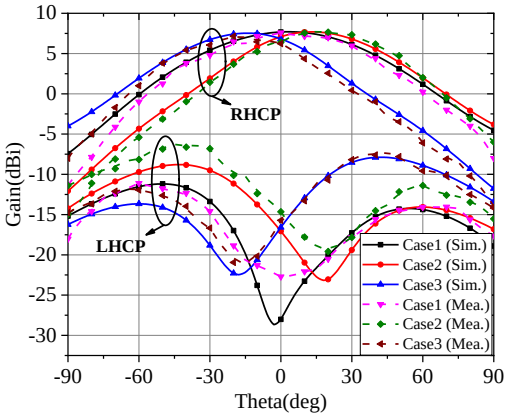

(a)

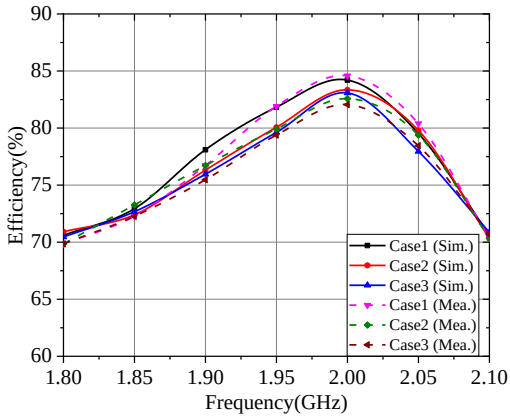

(b)

Fig. 19. Simulated and measured RHCP results of the proposed antenna for Vc=9V: (a) radiation patterns in the yoz-plane (at 2 GHz), and (b) radiation efficiency.

V. CONCLUSION

A novel patch antenna design for frequency, pattern, and polarization reconfiguration has been presented in this paper. By using varactors and PIN diodes, these three kinds of characteristics of the antenna could become reconfigurable independently. Simulations about impedance and radiation characteristics of the antenna have been carried out for different cases. To validate this antenna design, a S-band patch antenna is fabricated and measured as an example. It is found that the polarization (LHCP/RHCP), resonant frequency (1.96 to 2.03 GHz) and radiation pattern reconfiguration can be realized independently. With the multiple functions and a low-profile structure, the proposed antenna could be applied to mobile communication, satellites communication and telemetry systems. Besides, it can also improve signal-to-noise ratio and increase the spectrum utilization of the wireless communication by dynamically adjusting frequency, polarization or radiation characteristics. In the future, methods of adaptive adjustment will be further investigated to better meet the communication needs in different scenarios.

ACKNOWLEDGMENT

This work was supported in part by the CAST Innovation Fund (China Academy of Space Technology), in part by the Aerospace Science and Technology Innovation Fund (China Aerospace Science and Technology Corporation), in part by the Open Research Fund of State Key Laboratory of Space-Ground Integrated Information Technology under grant NO. 2015_SGIIT_KFJJ_TX_01.

REFERENCES

[1] M. Shirazi, J. Huang, T. Li, and X. Gong, "A switchable-frequency slot-ring antenna element for designing a reconfigurable array," *IEEE Antennas and Wireless Propag. Lett.*, vol. 17, no. 2, pp. 229-233, Feb. 2018.

[2] L. Pazin and Y. Leviatan, "Reconfigurable slot antenna for switchable multiband operation in a wide frequency range," *IEEE Antennas and Wireless Propag. Lett.*, vol. 12, pp. 329-332, 2013.

[3] T. Li, H. Zhai, X. Wang, L. Li, and C. Liang, "Frequency-reconfigurable bow-tie antenna for bluetooth, WiMAX, and WLAN applications," *IEEE Antennas and Wireless Propag. Lett.*, vol. 14, pp. 171-174, 2015.

[4] B. Babakhani and S. Sharma, "Wideband frequency tunable concentric circular microstrip patch antenna with simultaneous polarization reconfiguration," *IEEE Antennas and Propagation Magazine*, vol. 57,

no. 2, pp. 203-216, Apr. 2015.

[5] S. Honda, S. Saito, and Y. Kimura, "Frequency control of a varactor-loaded dual-band single-layer shorted multi-ring microstrip antenna fed by an L-probe with reduced patch area in half," *2019 International Symposium on Antennas and Propagation (ISAP)*, pp. 1-3, 2019.

[6] M. W. Young, S. Yong, and J. T. Bernhard, "A miniaturized frequency reconfigurable antenna with single bias, dual varactor tuning," *IEEE Trans. Antennas Propag.*, vol. 63, no. 3, pp. 946-951, Mar. 2015.

[7] A. Zohur, H. Mopidevi, D. Rodrigo, M. Unlu, L. Jofre, and B. A. Cetiner, "RF MEMS reconfigurable two-band antenna," *IEEE Antennas and Wireless Propag. Lett.*, vol. 12, pp. 72-75, 2013.

[8] Y. Zhao, C. Huang, A. Qing, and X. Luo, "A frequency and pattern reconfigurable antenna array based on liquid crystal technology," *IEEE Photonics Journal*, vol. 9, no. 3, pp. 1-7, June 2017.

[9] B. Majumder, K. Krishnamoorthy, J. Mukherjee, and K. P. Ray, "Frequency-reconfigurable slot antenna enabled by thin anisotropic double layer metasurfaces," *IEEE Trans. Antennas Propag.*, vol. 64, no. 4, pp. 1218-1225, Apr. 2016.

[10] S. M. Kumar and Y. K. Choukiker, "Frequency and polarization reconfigurable microstrip antenna with switching feed configuration," *2018 IEEE Indian Conference on Antennas and Propogation (InCAP)*, Hyderabad, India, pp. 1-4, 2018.

[11] S. W. Lee and Y. J. Sung, "Simple polarization-reconfigurable antenna with T-shaped feed," *IEEE Antennas and Wireless Propaga. Lett.*, vol. 15, pp. 114-117, 2016.

[12] P. Pan and B. Guan, "A wideband polarization reconfigurable antenna with six polarization states," *2018 12th International Symposium on Antennas, Propagation and EM Theory (ISAPE)*, Hangzhou, China, pp. 1-4, 2018.

[13] J. Row and Y. Wei, "Wideband reconfigurable crossed-dipole antenna with quad-polarization diversity," *IEEE Trans. Antennas Propag.*, vol. 66, no. 4, pp. 2090-2094, Apr. 2018.

[14] G. Yang, J. Li, D. Wei, S. Zhou, and R. Xu, "Pattern reconfigurable microstrip antenna with multidirectional beam for wireless communication," *IEEE Trans. Antennas Propag.*, vol. 67, no. 3, pp. 1910-1915, Mar. 2019.

[15] M. Jusoh, T. Aboufoul, T. Sabapathy, A. Alomainy, and M. R. Kamarudin, "Pattern-reconfigurable microstrip patch antenna with multidirectional beam for WiMAX application," *IEEE Antennas and Wireless Propag. Lett.*, vol. 13, pp. 860-863, 2014.

[16] S. Yan and G. A. E. Vandenbosch, "Radiation pattern-reconfigurable wearable antenna based on metamaterial structure," *IEEE Antennas and Wireless Propag. Lett.*, vol. 15, pp. 1715-1718, 2016.

[17] L. Tan, R. Wu, and Y. Poo, "Magnetically reconfigurable SIW antenna with tunable frequencies and polarizations," *IEEE Trans. Antennas Propag.*, vol. 63, no. 6, pp. 2772-2776, June 2015.

[18] W. Yang, W. Che, H. Jin, W. Feng, and Q. Xue, "A polarization-reconfigurable dipole antenna using polarization rotation AMC structure," *IEEE Trans. Antennas Propag.*, vol. 63, no. 12, pp. 5305-5315, Dec. 2015.

[19] D. Rodrigo, B. A. Cetiner, and L. Jofre, "Frequency, radiation pattern and polarization reconfigurable antenna using a parasitic pixel layer," *IEEE Trans. Antennas Propag.*, vol. 62, no. 6, pp. 3422-3427, June 2014.

[20] L. Ge, Y. Li, J. Wang, and C. Sim, "A low-profile reconfigurable cavity-backed slot antenna with frequency, polarization, and radiation pattern agility," *IEEE Trans. Antennas Propag.*, vol. 65, no. 5, pp. 2182-2189, May 2017.

[21] N. Nguyen-Trong, L. Hall, and C. Fumeaux, "A frequency- and polarization-reconfigurable stub-loaded microstrip patch antenna," *IEEE Trans. Antennas Propag.*, vol. 63, no. 11, pp. 5235-5240, Nov. 2015.

[22] Y. P. Selvam, M. Kanagasabai, M. G. N. Alsath, S. Velan, S. Kingsly, S. Subbaraj, Y. V. Ramana Rao, R. Srinivasan, A. K. Varadhan, and M. Karuppiah, "A low-profile frequency- and pattern-reconfigurable antenna," *IEEE Antennas and Wireless Propag. Lett.*, vol. 16, pp. 3047-3050, 2017.

[23] S. Chen, D. K. Karmokar, P. Qin, R. W. Ziolkowski, and Y. J. Guo, "Polarization-reconfigurable leaky-wave antenna with continuous beam scanning through broadside," *IEEE Trans. Antennas Propag.*, vol. 68, no. 1, pp. 121-133, Jan. 2020.

Yan Zhang received the B.S. and Ph.D. degrees in Electromagnetic Field and Microwave Technology from the Beijing University of Aeronautics and Astronautics (BUAA), Beijing, China, in 2002 and 2006, respectively. From 2007 to 2008, he was a Post-Doctoral Researcher with the Communication, Navigation, Surveillance/Air Traffic Management (CNS/ATM) Laboratory, Civil Aviation Administration of China (CAAC), BUAA. He is currently an Associate Professor of Electronics and Information Engineering with BUAA.

He has authored over 40 papers. His research interests include antenna, electromagnetic surface and antenna array. Zhang was the recipient of the Outstanding Doctoral Dissertation Award and the Outstanding Post-Doctoral Researcher Award presented by BUAA in 2008.

Da Sun received the degree in Electronics and Information Engineering in 2018. He is currently pursuing the M.S. degree in Electronic Science and Technology, School of Electronics and Information Engineering, Beihang University, Beijing, China. His research interests include antenna, electromagnetic surface and antenna array.

Tao Dong received the B.S. and Ph.D. degrees in Electronics Science and Technology from Beijing Institute of Technology in 1999 and 2004, respectively. He is currently a Professor with State Key Laboratory of Space-Ground Integrated Information Technology, Beijing Institute of Satellite Information Engineering. His research interests include antenna, phased array and optoelectronic devices.

Jie Yin received the B.S. and Ph.D. degrees in Electronics Science and Technology from Beijing University of Posts and Telecommunications (BUPT) in 2005 and 2010, respectively. He is currently a Senior Engineer in State Key Laboratory of Space-Ground Integrated Information Technology, Beijing Institute of Satellite Information Engineering. His research interests include free space optical communication, space optical networks and microwave photonics.

A SIW Horn Antenna without Broad Wall Loaded with Trapezoidal Air Slot

Mingxi Zhang [1,2], Wei Li [1], Shaobin Liu [1], Xiaochun Liu [1,2], Chen Wu [1], and Junyu Deng [1]

[1] College of Electronic and Information Engineering
Nanjing University of Aeronautics and Astronautics, Nanjing, 211106, China
plrg@nuaa.edu.cn, 1452882408@qq.com, lsb@nuaa.edu.cn, liuxiaochun637@sina.com,
wuchen199701@163.com, 870086946@qq.com

[2] The Aeronautical Science Key Laboratory for High Performance Electromagnetic Windows
Jinan, 250023, China
plrg@nuaa.edu.cn, liuxiaochun637@sina.com

Abstract ─ In this paper, a SIW horn antenna without broad wall loaded with trapezoidal air slot is proposed, processed, and tested. Based on the SIW horn antenna, this antenna strips off the wide wall at the horn diameter, introduces surface waves on the surface of the dielectric substrate, and improves the impedance matching between the antenna and free space. Further, trapezoidal air slots are loaded on the exposed dielectric substrate, gradually changes the dielectric constant of the dielectric substrate, so that the dielectric constant of the dielectric substrate can get closer to which of air, and the working bandwidth can be further expanded. The actual measurement results show that the working bandwidth of the antenna is 15.2-38GHz, the relative bandwidth reaches to 85.7%, and the maximum gain in the band is 9.1dBi.

Index Terms ─ Broadband antenna, horn antenna, impedance matching, substrate integrated waveguide.

I. INTRODUCTION

The horn antenna is a widely used in microwave antenna. The traditional horn antenna is gradually expanded from the terminal of the metal waveguide. It has the advantages of simple structure, wide frequency bandwidth, large power capacity, and convenient adjustment and use [1]. But there are also significant disadvantages such as: high profile, large volume, and high processing cost. With the introduction of substrate integrated waveguide technology (SIW), horn antennas based on SIW technology entered our field of vision [2]. This horn antenna has a lower profile and cheaper processing cost, which solves the shortcomings of the traditional metal waveguide horn antenna. However, due to the different dielectric constants of the dielectric substrate and the free space, electromagnetic waves emitted from the dielectric substrate to the free space may have an impedance mismatch, which leads to a narrow working bandwidth of the antenna.

In order to solve this problem, a horn antenna loaded with a dielectric plate was proposed [3-4]. A semi-circular or rectangular dielectric substrate was extended in the front section of the horn antenna as an impedance transformer of the antenna, which expanded the horn the bandwidth of the antenna. Further, on the dielectric substrate of the antenna extension, air holes of different sizes are punched to further increase the bandwidth of the horn antenna [5]. In addition, the method of introducing additional resonance frequency by loading metal blocks on the extended dielectric substrate has also been proposed [6-7]. This method requires a thinner horn antenna and a lower antenna profile.

A corrugated horn antenna has been proposed [8]. The corrugated structure is adopted at the horn diameter. The antenna has a good bandwidth expansion in low frequency bands. The antenna is integrated on a single-layer dielectric substrate, which is easy for planar circuit integration. Several non-planar horn antennas have also been reported [9-10]. Loading the traditional SIW horn antenna with an inhomogeneous-polarizer or using a pyramid-type horn antenna based on coupled feed can enhance the radiation performance of the antenna but cannot meet the requirements of single layer, low profile antenna.

In order to further miniaturize the horn antenna, a horn antenna without a wide wall has entered our field of vision [11-12]. Based on the traditional SIW horn antenna, the metal broad wall at the horn diameter is stripped off, and a plane wave is introduced on the antenna surface to improve the impedance matching between the antenna and free space. Further, air holes are punched on the exposed dielectric substrate to expand the bandwidth of the antenna.

Other forms of wideband antennas also offer inspiration. A simple method is proposed for enhancement in bandwidth and gain of the self complementary Bowtie antenna. Using this simple method, by making variation

Submitted On: April 29, 2020
Accepted On: May 30, 2020

https://doi.org/10.47037/2020.ACES.J.350910

of the single dimension of the structure of the antenna, the bandwidth is improved by 21% and return loss S11 is also improved of whole of the band of interest [15]. A novel printed monopole antenna with defective ground structure is proposed. The initial design is further modified to enhance the impedance bandwidth and gain by employing a defective ground structure in the co-planar ground plane of the monopole patch [16]. Several high-performance Sierpinski fractal antennas have been reported, among which the feeding position has become a key factor [17,19].

In this article, we propose a SIW horn antenna without broad wall loaded with trapezoidal air slot. On the basis of the traditional horn antenna, the metal wide wall at the horn diameter is stripped off. And on the bare dielectric substrate, trapezoidal air slots are punched. Without enlarging the size of the antenna, the broadband operation of the antenna is realized. This antenna has a simple structure and low processing cost, and will have a good application prospect in the actual working environment.

II. ANTENNA STRUCTURE AND OPTIMIZATION

A. Antenna structure

The antenna is a single-layer dielectric substrate, the material of which is FR-4. Its dielectric constant is 4.3, and the loss tangent is 0.025.

The structure of the antenna is shown in Fig. 1, which is successively divided into microstrip line part, SIW part and horn caliber part. The impedance of the microstrip line is 50 ohms, which can be well matched with the SMA connector. The surface metal, medium substrate, bottom metal plate and metal vias form the SIW structure. To avoid energy leakage, the diameter d of all metal vias is 0.4mm, and the spacing x between the metal vias is 0.7mm.

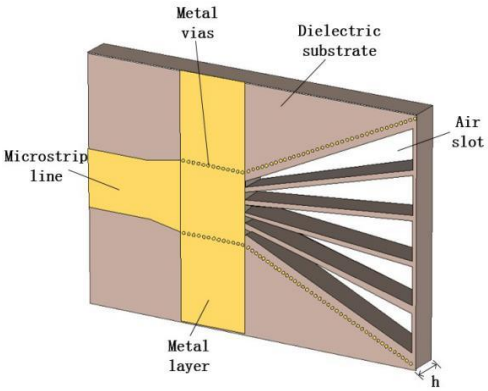

(a) 3-D view

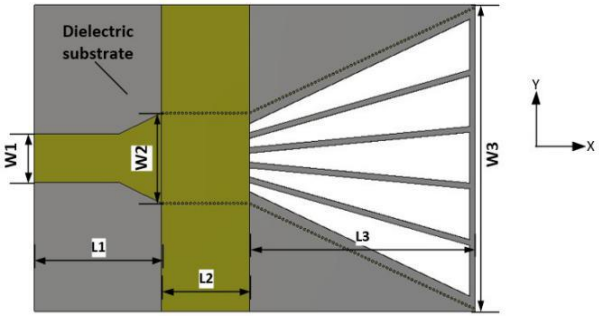

(b) Top view

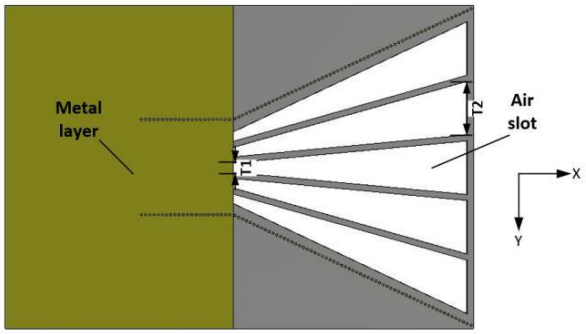

(c) Bottom view

Fig. 1. Antenna structure.

Electromagnetic waves are fed into the SIW cavity by means of microstrip feeding. The main mode of transmission is transformed from the TEM mode on the coaxial cable to the TE mode in the SIW cavity. Starting at the junction of the rectangular SIW cavity and the horn diameter, the metal wide wall was stripped, and the surface wave was added to the TE mode, which greatly improved the impedance matching between the antenna and the free space.

B. Antenna design principles and optimization

The data in Fig. 1 is shown in Table 1. W1 is the width of the microstrip line, and its value is to comply with the impedance matching of 50 ohms. Because we know that the main mode transmitted in the SIW cavity is TE_{10} mode, according to formula (1) we can calculate the width W2 of the SIW cavity:

$$W2 = \frac{c_0}{f_{c(TE_{10})}\sqrt{\varepsilon_r}} + \frac{d^2}{1.1x} + \frac{d^3}{6.6x^2}, \quad (1)$$

where d and x are the diameter of the metallized via and the distance between the vias, f_c is the cutoff frequency corresponding to the TE_{10} mode, and c_0 is the speed of light in free space.

Table 1: The specific value of the parameter (unit:mm)

W1	W2	W3	L1	L2	L3
8.6	15.9	54	22.5	15.5	40
h	**T1**	**T2**	**d**	**x**	
4.3	1.6	8.97	0.4	0.7	

Further, in the simulation software CST2015, we establish an antenna model and set the width of the SIW cavity to the calculated value w2. It can be seen that the antenna has a very wide bandwidth, as shown in Fig. 2, which proves that our calculation is reasonable. For 38GHz and above, the gain of antenna is too low at this time, we do not regard this as our working bandwidth. The definition of dBi is the antenna gain db value obtained by using the ideal point source omnidirectional antenna as reference.

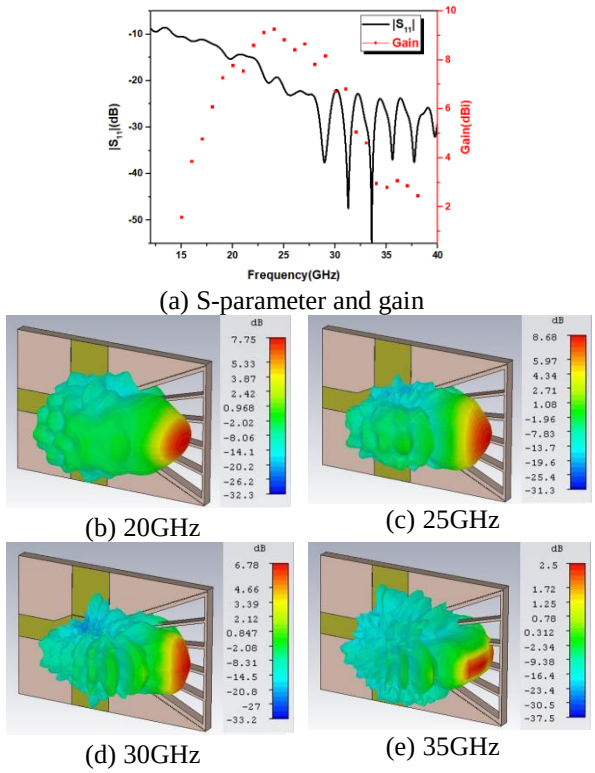

(a) S-parameter and gain

(b) 20GHz (c) 25GHz

(d) 30GHz (e) 35GHz

Fig. 2. Simulated S-parameter curve and gain.

The lengths of the upper and lower sides of the trapezoidal air gap are T1 and T2. The setting of these two values must first consider the level of processing technology. In order to ensure the stability of the structure of antenna, the minimum distance between two adjacent slots should be greater than 1mm. The following is the formula (2) for changing the dielectric constant of the dielectric substrate by drilling and other methods. In the case of our trapezoidal slot, the specific formula (3) is proposed. It can be seen that our scheme has nothing to do with frequency, and is also available for broadband transmission:

$$\varepsilon_{reff} = \frac{\varepsilon_r \ S_a - S_w \ + S_w}{S_a}, \tag{2}$$

$$\varepsilon_{reff} = \frac{\varepsilon_r \left[\ W_2 + W_3 \ - N \ T_1 + T_2 \ \right] + N \ T_1 + T_2}{W_2 + W_3}, \tag{3}$$

where S_a is the area of the dielectric plate at the entire horn diameter, S_w is the total area which is dug by punching or other methods, and N is the number of trapezoidal slots.

When the FR-4 substrate works at 20GHz or above, the medium loss is too large and it is difficult to obtain a high gain. In our design, due to the introduction of trapezoidal air slot, the medium loss of FR-4 was reduced to a certain extent. The antenna can still get high gain at 20-25GHz. To verify this view, we compare the gain of the antenna under without slot and different size slots. The results are shown in Fig. 3. It can be seen that the larger the slot area is higher the gain at high frequencies. However, the slot size has an upper limit. Oversize slot will lead to the instability of the structure of antenna and the rapid change of dielectric constant.

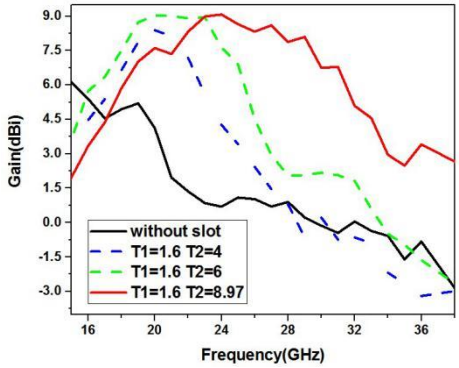

Fig. 3. Antenna gain of different sizes of slot.

Synthesizing the factors above, the values of T1 and T2 are finally set, at this time the dielectric constant of the dielectric substrate is slowly changed from 2.64 to 1.56, reducing the mismatch caused by the sudden change of the dielectric constant.

III. SIMULATED AND MEASURED RESULTS

On the basis of the above scheme, we have established a model in the electromagnetic simulation software CST2015 and optimized the parameters. In order to further verify the performance of the antenna, we prototyped the proposed antenna. The S-parameters of the antenna were tested using a vector network analyzer and compared with our simulated results. The specific data is shown in Fig. 4.

It can be seen that the simulated and measured results of the antenna match well, which is due to the simple structure of the antenna, and the influence of processing accuracy is considered in the design. The antenna we proposed achieves broadband transmission from 15.2GHz to 38GHz without increasing the size of the antenna, which is very rare.

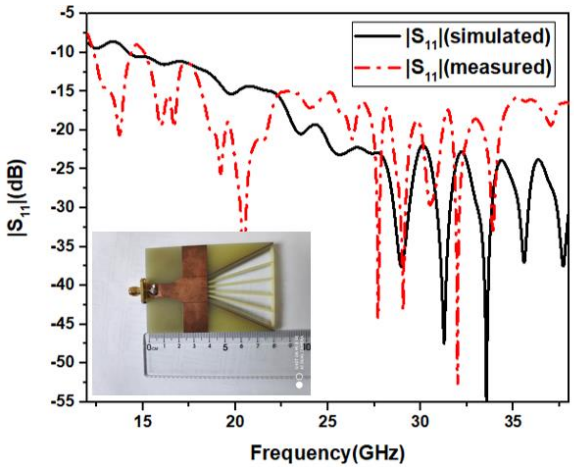

Fig. 4. Antenna simulated and measured S-parameter comparison.

In the microwave dark room, the radiation pattern and antenna gain of the antenna were tested. The simulated and measured gain of the antenna are shown in Fig. 5. It can be seen that the two are basically consistent. In particular, the high-gain region of the antenna belongs to 18GHz to 32GHz. When the antenna works in the low-frequency region, the lower the frequency is, the longer the wavelength is. For such wavelengths, the size of the antenna is relatively small, so the overall gain is small. When the antenna works in the high-frequency region, combined with the above-mentioned formula (1), the main mode of the antenna transmission is no longer the standard TE_{10} mode, which affects the radiation of antenna to a certain extent, resulting in a decrease in gain.

The comparison of the radiation pattern of the simulated and measured of the antenna is shown in Fig. 6. We selected four frequency points for comparison. The simulated and measured results are not only agree, but also have good radiation characteristics for the horn antenna. In order to better reflect the advantages of our proposed antenna, we compared with the previous work. The results are shown in Table 2. The compared items include size, maximum gain in band, and operating frequency. It can be seen that our antenna achieves broadband transmission without increasing the size of the antenna, and with high gain at the same time.

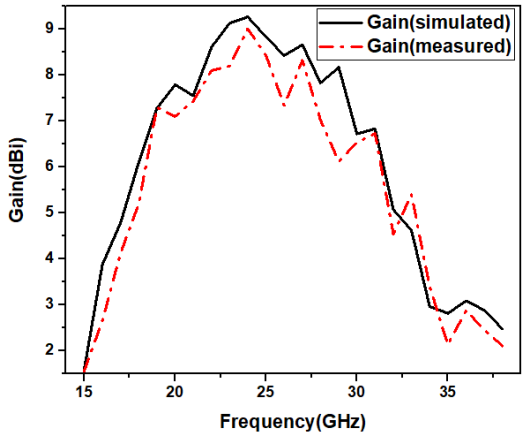

Fig. 5. Comparison of simulated and measured gain.

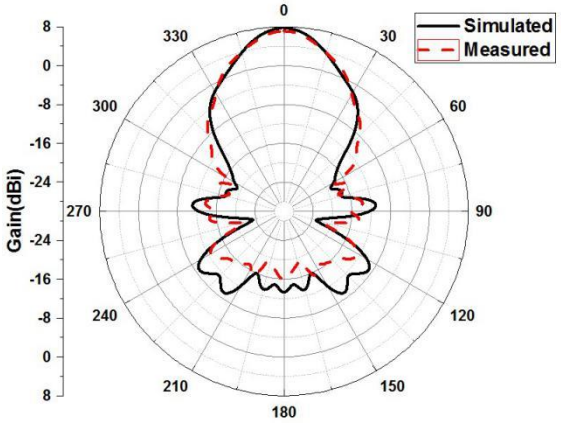

(a) 20GHz

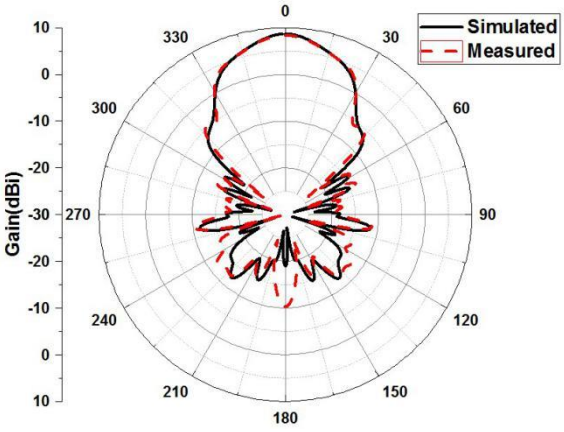

(b) 25GHz

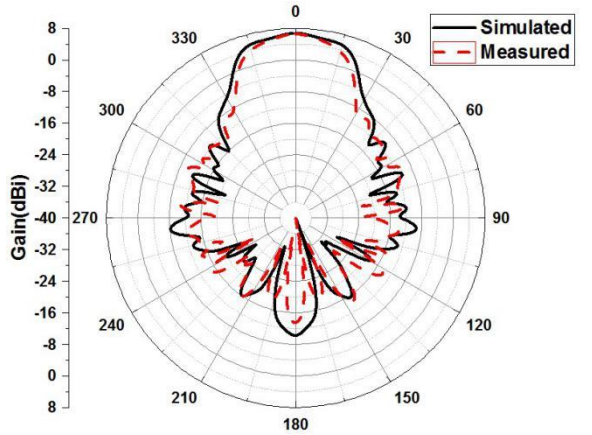

(b) 30GHz

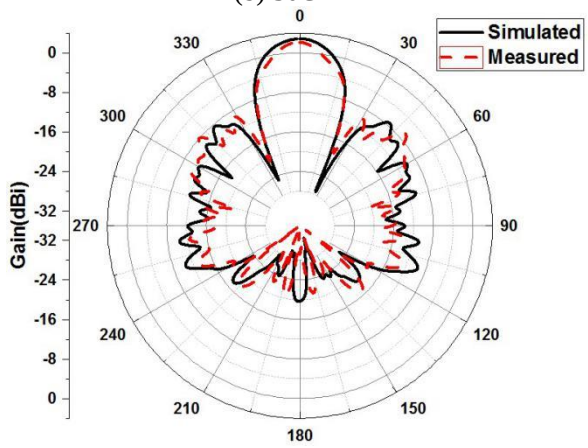

(c) 35GHz

Fig. 6. Simulated and measured direction diagram of each frequency point.

Table 2: Antenna performance comparison

Ref.	Frequency (GHz)	Band-width	Maximum Gain (dBi)	Single Layer
[11]	17.7-26.7	40.5%	9.2	yes
[12]	19.1-27.4	35.7%	8.9	yes
[13]	26.7-29.1	8.6%	6.54	yes
[14]	31-58	60.7%	19	no
Proposed	15.2-38	85.7%	9.1	yes

IV. CONCLUSION

In this paper, a SIW horn antenna without broad wall loaded with trapezoidal air slot is proposed, processed, and tested. Based on the SIW horn antenna, the impedance bandwidth of the antenna is improved by stripping the wide metal wall at the horn aperture and etching the air slot on the exposed dielectric plate. Furthermore, the air slot reduces the medium loss of the antenna and improves the gain of the antenna when it works at high frequencies. The physical size of the antenna is 78mm*54mm*4.3mm, the measured impedance bandwidth is 15.2-38GHz, and the maximum gain in the band is 9.1dBi. This horn antenna is simple in structure and low in cost, which has a good application prospect in practical engineering.

REFERENCES

[1] T.-C. Lin, C.-H. Lee, J.-L. Dong, C.-N. Chiu, D.-B. Lin, and H.-P. Lin, "A new uniformity-enhanced double ridged horn antenna for radiated susceptibility test from 1 GHz to 18 GHz," *IEEE International Symposium on Electromagnetic Compatibility & IEEE Asia-pacific Symposium on Electromagnetic Compatibility IEEE*, 2018.

[2] L. Wang, X. Yin, S. Li, H. Zhao, L. Liu, and M. Zhang, "Phase corrected substrate integrated waveguide H-plane horn antenna with embedded metal-via arrays," *IEEE Transactions on Antennas & Propagation*, part 2, vol. 62, no. 4, pp. 1854-1861, 2014.

[3] W. Che, B. Fu, P. Yao, Y. L. Chow, and E. K. N. Yung, "A compact substrate integrated waveguide H-plane horn antenna with dielectric arc lens," *International Journal of RF and Microwave Computer-Aided Engineering*, vol. 17, no. 5, pp. 473-479, 2007.

[4] H. Wang, D.-G. Fang, B. Zhang, and W.-Q. Che, "Dielectric loaded substrate integrated waveguide (siw) h-plane horn antennas," *IEEE Transactions on Antennas & Propagation*, vol. 58, no. 3, pp. 640-647, 2010.

[5] Y. Cai, Z. P. Qian, Y. S. Zhang, J. Jin, and W. Q. Cao, "Bandwidth enhancement of SIW horn antenna loaded with air-via perforated dielectric slab," *IEEE Antennas Wireless Propag. Lett*., vol. 13, pp. 571-574, Apr. 2014.

[6] M. E. Morote, B. Fuchs, J. F. Zurcher, and J. R. Mosig, "A printed transition for matching improvement of SIW horn antennas," *IEEE Trans. Antennas Propag.*, vol. 61, no. 4, pp. 1923-1930, Apr. 2013.

[7] M. Esquius-Morote, B. Fuchs, J.-F. Zurcher, and J. R. Mosig, "Novel thin and compact H-plane SIW horn antenna," *IEEE Transactions on Antennas and Propagation*, vol. 61, no. 6, pp. 2911-2920, 2013.

[8] Y. Zhao, "Quasi-corrugated substrate integrated waveguide H-plane horn antenna with wideband and low-profile characteristics," *International Journal of RF and Microwave Computer-Aided Engineering*, 2018.

[9] H.-Y. Yu, J. Yu, X. Liu, Y. Yao, and X. Chen, "A wideband circularly polarized horn antenna with a tapered elliptical waveguide polarizer," *IEEE Transactions on Antennas and Propagation*, vol. 67, no. 6, pp. 3695-3703, 2019.

[10] Z. Wang, X. Liang, R. Jin, and J. Geng, "A novel SIW horn antenna with high gain and high efficiency," 2014 *IEEE International Symposium*

on Antennas and Propagation & USNC/URSI National Radio Science Meeting IEEE, 2014.

[11] Y. Cai, Y. Zhang, Z. Qian, W. Cao, and L. Wang, "Design of compact air-vias-perforated SIW horn antenna with partially detached broad walls," *IEEE Transactions on Antennas & Propagation*, vol. 64, no. 6, pp. 2100-2107, 2016.

[12] Y. Cai, Y. Zhang, L. Yang, Y. Cao, and Z. Qian, "A low-profile wideband surface-mountable substrate-integrated waveguide horn antenna," *IEEE Antennas and Wireless Propagation Letters*, vol. 16, pp. 2730-2733, 2017.

[13] S. Lee and J. Choi, "All-textile corrugated ground SIW horn antenna for millimeter-wave WBAN applications," *Journal of Electromagnetic Engineering and Science*, vol. 19, no. 4, pp. 221~226, Oct. 2019.

[14] P. K. Mishra and D. Guha, "Wideband pyramidal ridged horn design by SIW technology," *IEEE Antennas and Wireless Propagation Letters*, vol. 18, no. 7, pp. 1517-1521, 2019.

[15] L. S. Solanki and S. Singh, "Modified wideband bowtie antenna for WLAN and high-speed data communication applications," *Wireless Personal Communication*, vol. 95, no. 3, pp. 2649-2663, Jan. 2017.

[16] A. Singh and S. Singh, "A novel CPW-fed wideband printed monopole antenna with DGS," *International Journal of Electronics and Communication*, vol. 69, no. 1, pp. 299-306, Jan. 2015.

[17] A. Singh and S. Singh, "A modified coaxial probe-fed Sierpinski fractal wideband and high gain antenna," *International Journal of Electronics and Communication*, vol. 69, no. 6, pp. 884-889, June 2015.

[18] A. Singh and S. Singh, "Design and optimization of a modified Sierpinski fractal antenna for broadband applications," *Applied Soft Computing*, vol. 38, pp. 843-850, Jan. 2016.

[19] Y. Kumar and S. Singh, "Microstrip fed multiband hybrid fractal antenna for wireless applications," *Applied Computational Electromagnetics Society Journal*, vol. 31, no. 3, pp. 327-332, Mar. 2016.

Mingxi Zhang, Research Fellow, graduated from Beijing University of Aeronautics and Astronautics in 1982. He is the Chief Expert of Non-metal Structural Materials Technology of China Aviation Industry Corporation. He is currently an Adjunct Professor at Nanjing University of Aeronautics and Astronautics and Jinan University. His current research interests include the research of aircraft electromagnetic window products and functional composite materials.

Wei Li was born in Anhui, China, in 1997. He received the B.Eng. degree in Information Engineering from Hunan University of Technology, Zhuzhou, China, in 2018. Currently studying for a master's degree in Nanjing University of Aeronautics and Astronautics, Nanjing, China. His research focuses on monopulse antenna, horn antenna, microwave passive device based on SIW (Substrate Integrated Waveguide).

Finite Ground CB-CPW Bandpass Filter using Vertically Installed Coupled Open-ended Stubs

Pratik Mondal [1], Susanta Kumar Parui [2], and Rajesh Bera [1]

[1] Department of Electronics and Communication Engineering
Gayatri Vidya Parishad College of Engineering (Autonomous), Madhurawada, Visakhapatnam-530 048, India
pratik665@gmail.com, rajeshkiit12@gmail.com

[2] Department of Electronics & Tele-communication Engineering
Indian Institute of Engineering Science and Technology, Shibpur, Howrah-711103, India
arkapv@yahoo.com

Abstract ─ In this paper, a conductor backed coplanar waveguide (CB-CPW) 3rd order bandpass filter is designed using coupled open-ended stub resonator placed vertically to the signal line. Vertically loaded open ended stubs are designed at quarter wavelength so as to behave like a short circuit at the input terminal thus giving a band-accepted response with lesser metallic area or minimum size. Four such coupled open ended resonators are placed in series and also in closely manner to provide greater field confinement of the proposed bandpass filter. The bandpass filter is designed for a center frequency of 2.5 GHz with FBW of 97.89%, insertion loss of <0.5dB, rising and falling edge selectivity of 30.75 dB/GHz and 27.01dB/GHz respectively with a wide stopband of around 4GHz after the desired passband. Further to validate the design technique six such resonators are placed to obtain 5th order bandpass filter.

Index Terms ─ Bandpass filter, CB-CPW, open-ended, series-stub, vertically installed.

I. INTRODUCTION

Bandpass filter (BPF) is one of the prime components ever for designing any trans-receiver system. Researchers paid much attention on designing of high selective and compact bandpass filter simultaneously in microstrip as well as in Co-planar waveguide (CPW) technology. CPW technology has advantages of easy integration with lumped and active elements. The characteristic impedance of a CPW transmission line is determined by the ratio of w/(w+s), thus unlimited size reduction is possible and the frequency variation of effective permittivity is lower than microstrip which further simplifies broadband circuit design [1]. CPW circuits are low cost, better in performance and easier to fabricate than circuits based on other planar technology. The realization of CPW band pass filter by the discontinuity of the open and short ended stubs has been proposed earlier [2]. Using CPW-structures leaky wave, over moding effect and other undesired modes of propagations are avoided [3]. Conventional CPW has disadvantages of lower thermal dissipation, lower structural strength and experience higher losses compared to microstrip. To solve enormous problems aroused while using conventional CPW with its semi-infinite ground planes, a separate type of coplanar waveguide with electrically narrow ground planes had been developed [4]. This new transmission line which was called conductor backed coplanar waveguide (CBCPW) has several advantages which made it superior for RF and microwave circuit and system design. CB-CPW has an additional lower ground plane which does create a parallel plate waveguide region between the upper and lower ground planes. In a CBCPW circuit, three dominate modes exists; CPW mode, microstrip line (MSL) mode or coplanar microstrip (CPM) [4-5] mode and coupled slot-line mode. These three dominants as well as some higher order modes may be excited and propagate along the structures, thus circuit performance deteriorates. Since the parasitic parallel plate waveguide mode has a lower phase velocity than the CPW mode, power leaks from the CPW mode to the parallel plate waveguide mode [6]. If the top ground planes are wide, then the next higher-order microstrip-like mode may exist and if dielectric substrate is even wider than the structure may support an image-guide-like propagating mode. To solve these problems, several alternatives have been reported earlier including the use of microwave absorbing materials, multiple dielectric layers, metal filled via holes and use of finite ground coplanar (FGC) [5,7]. A thorough and systematic investigation of resonant phenomena in CBCPW and observed that FGC line is better than normal CPW for MMICs and MCMs was reported by Lo et al. [7]. As the ground planes are electrically narrow, spurious resonances created by the CPW ground planes and the metal carrier

Submitted On: January 19, 2018
Accepted On: June 29, 2020
https://doi.org/10.47037/2020.ACES.J.350911

or package base are eliminated and thus, the parallel plate waveguide mode is not established and the problem of spurious resonances is eliminated with improved performances [8-9].

An In this literature, a 3rd order bandpass filter is designed on CB-CPW with major advantage of easy integration with lumped as well as active components with improved performances and higher mechanical strength. The proposed filter is designed and an equivalent resonant circuit for a particular resonant frequency is portrayed. Quarter wavelength vertically loaded open ended stubs are used to provide band-accepted characteristics with smaller design size. The design is optimized in width of the slots to form the discontinuity to achieved the bandwidth of 1-4GHz. Multiple series open ended vertically coupled stub resonators are placed in series to increase the order of the filter and to achieve higher selectivity with low insertion loss. To validate the design technique further six open ended resonators are installed in closed fashion to obtain 5^{th} order bandpass filter. Air bridges are not required due to symmetry of discontinuities [10]. The proposed filter is constructed using FR4 glass epoxy substrate with double side plated CCB.

II. PROPERTIES OF CONDUCTOR BACKED COPLANAR-WAVEGUIDE

The schematic of a CBCPW with finite ground planes in the lateral direction is shown in Fig. 1. Additional lower ground plane provides mechanical strength for a thin and fragile wafer, and acts as a heat sink for circuits with active devices. This configuration of the CPW is known as the conductor-backed coplanar waveguide (CBCPW).

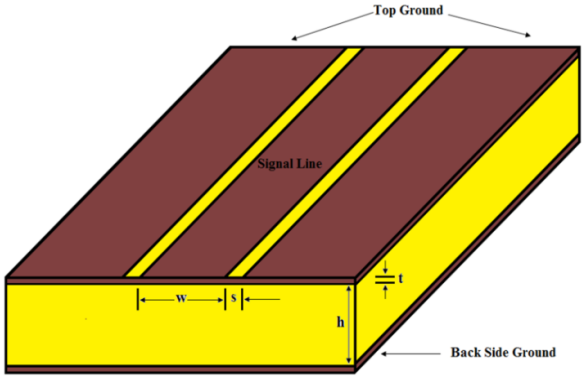

Fig. 1. Schematic of finite ground CB-CPW structure.

A quasi-TEM mode is assumed to propagate on the aforesaid structure. Based on the approximation, Wen's [11] analysis for conventional CPW is extended in [12] to [14] to the CBCPW, analytical expressions as a function of the geometry are expressed as:

$$\varepsilon_{eff} = \frac{1+\varepsilon_r \dfrac{K(k')}{K(k)}\dfrac{K(k_3)}{K(k_3')}}{1+\dfrac{K(k')}{K(k)}\dfrac{K(k_3)}{K(k_3')}}, \quad (1)$$

$$Z_0 = \frac{60\pi}{\sqrt{\varepsilon_{eff}}}\frac{1}{\dfrac{K(k')}{K(k)}+\dfrac{K(k_3)}{K(k_3')}}, \quad (2)$$

where,

$$k = a/b$$

$$k_3 = \tanh(\pi a/2h)/\tanh(\pi b/2h)$$

$$k' = \sqrt{1-k^2}$$

$$k_3' = \sqrt{1-k_3^{\,2}}.$$

K(k) is the elliptic integral function of the first kind. ε_{eff} and Z_0 are the effective permittivity of the substrate and characteristics impedance of transmission line respectively.

III. CHARACTERISTICS OF VERTICALLY INSTALLED COUPLED OPEN STUB

In conventional CPW technology a series stub is designed by creating a discontinuity in the central strip by implementing two slots originating from the edge of the central strip on both sides of the ground such that the slots are connected to each other [10]. In the proposed design of CB-CPW, vertically installed open ended stubs are used and coupled together. This modified in shape stub (vertically loaded) miniaturizes the circuit area in horizontal direct ion along with narrow top ground on both sides of the signal transmission line and electrically small finite bottom ground plane. At the end of the discontinuity an open circuit is created which gives a short circuit at the starting terminal of discontinuity for a length of quarter wavelength of the stub, i.e., $\lambda g/4$, where λg is the guided wavelength and thus provides a band accepted response [13-15].

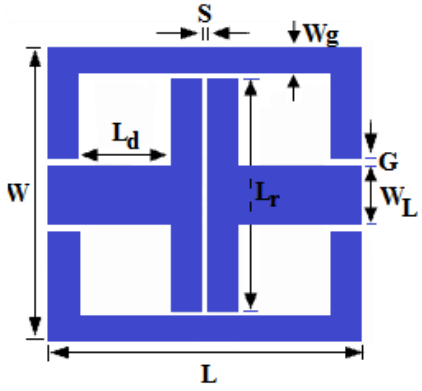

(a)

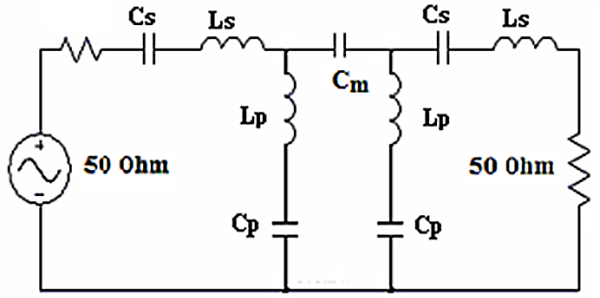

(b)

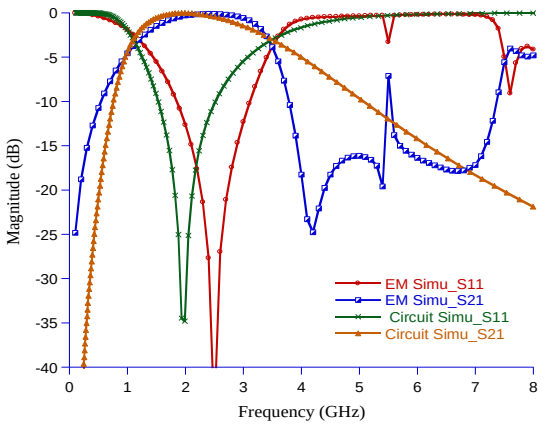

(c)

Fig. 2. (a) Vertically installed coupled series open ended CB-CPW stubs, (b) equivalent circuit model, and (c) comparison between EM and circuit simulated response.

Table 1: Equivalent circuit components

L_s (nH)	C_s (pF)	L_p (nH)	C_p (pF)	C_m (pF)
1.23	3.32	13.514	309.3	0.48

The dimensions of the proposed coupled stub resonator unit is calculated considering quarter wavelength; i.e.; for a substrate having relative permittivity ε_r = 4.4, height of 1.59mm and loss of 0.02, the values of L_r = 16.6mm, WL = 3.8mm, G = 0.2mm, W_r=1mm, W_g = 1mm, W = 18.4mm, L = 18mm and spacing S=0.3mm are chosen for easy fabrication. The characteristic of the CPW circuit primarily depends on the length 'Lr' as depicted in Fig. 2 (a). Now if the length is near to the quarter wavelength (~λ_g/4) then it will behave as a resonant circuit of a resonating frequency of which the quarter-wavelength is considered. Otherwise, if the length is considered to be too large (>λ_g/2) or small (<λ_g/10) then the same component will behave as an equivalent inductance or capacitance respectively [7]. The circuit equivalent of proposed vertically loaded coupled open-ended stub resonator is shown in Fig. 2 (b). From circuit analysis equivalent capacitance and inductance values are calculated and tabulated in Table 1, which are further simulated by Quite Universal Circuit Simulator and simulated plots are overlapped with the EM-Simulated one. The plot shows near similar response between the two as shown in Fig. 2 (c). The simulated result shows a band accepted response with 3dB bandwidth of 2.7GHz ranging from 1.2 GHz to 3.5 GHz with an insertion loss of - 0.017dB. The rising edge and falling edge selectivity are found to be 16.89 dB/GHz and 21.33 dB/GHz respectively.

IV. BPF USING PROPOSED COUPLED OPEN-ENDED RESONATORS

A. Design of 3rd order bandpass filter using four such resonators

In order to increase the order of the filter or sharpness four such series coupled resonators are placed such that the resonators are in close proximity to each other to achieve great field confinement within the circuit than that of other open-ended stub in series or shunt. As the order of the filter is also increased, i.e., numbers of pole increase as the number of series stubs are increased.

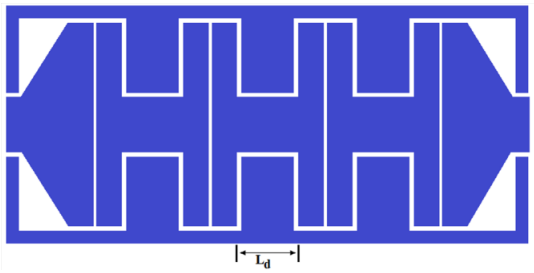

(a)

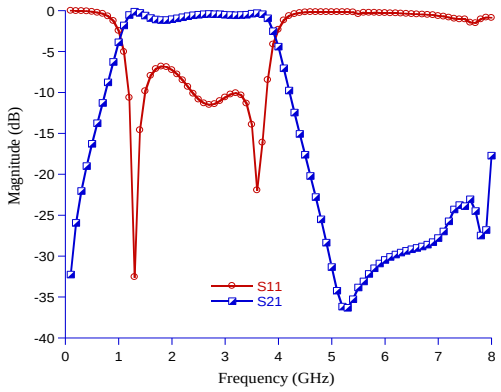

(b)

Fig. 3. (a) Schematic of proposed 3rd order BPF using four vertically loaded coupled open-ended series stubs, and (b) simulates S-parameter responses.

Finally, a 3rd order bandpass filter has been designed with higher selectivity or roll off. The layout design of the filter is given in Fig. 3 (a). The distance between two consecutive resonators are chosen of L_d = 1mm. The simulated results show 3dB bandwidth from 1GHz to 3.9 GHz with an insertion loss of -0.48dB and the selectivity

of 30.75 dB/GHz at the rising edge and 27.01 dB/GHz at the falling edge with a rejection band of around 4GHz after the desired passband as described in Fig. 3 (b).

Figure 4 (a) shows equivalent lumped circuit model for the proposed bandpass filter having four open stubs in symmetric manner. This lumped model has been further simulated with Quite Universal Circuit Simulator and found the results as similar as of simulated responses as sketched in Fig. 4 (b). The EM and circuit simulated responses are found near similar in nature.

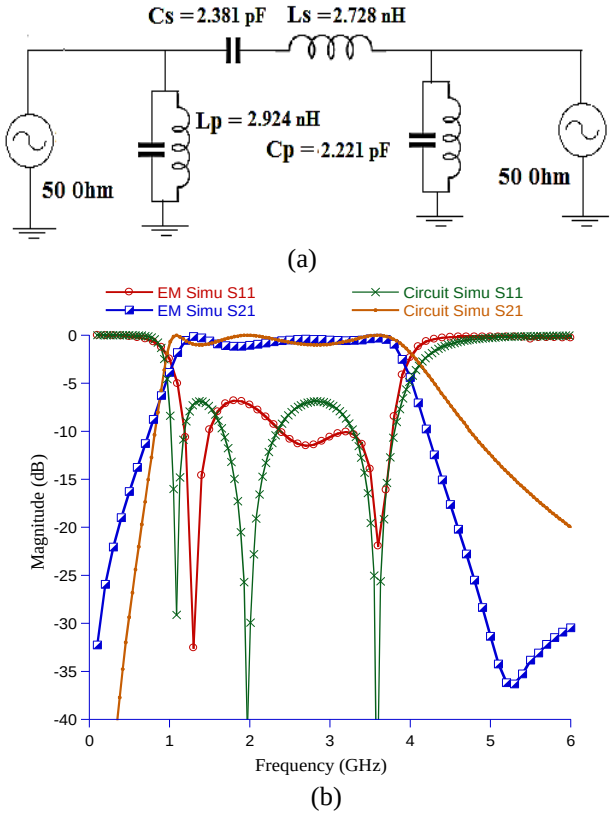

Fig. 4. (a) Circuit equivalent of proposed bandpass filter, and (b) comparison between EM-simulates and circuit simulated S-parameter responses.

Finally, this vertically loaded series coupled open ended stubs-based CB-CPW Band Pass Filter is fabricated using a double side copper plated FR4 substrate having relative permittivity εr = 4.4, height of 1.59mm and loss of 0.02 as portrayed in Fig. 5 (a).

The scattering parameters of fabricated structure are measured by Agilent make Vector Network Analyzer (model N5230A) and obtained results are compared with the simulated responses. It is observed that the measured results have near agreement with the simulated response as shown in Fig. 5 (b). Small deviations in measured results are obtained due to manual fabrication in-accuracy.

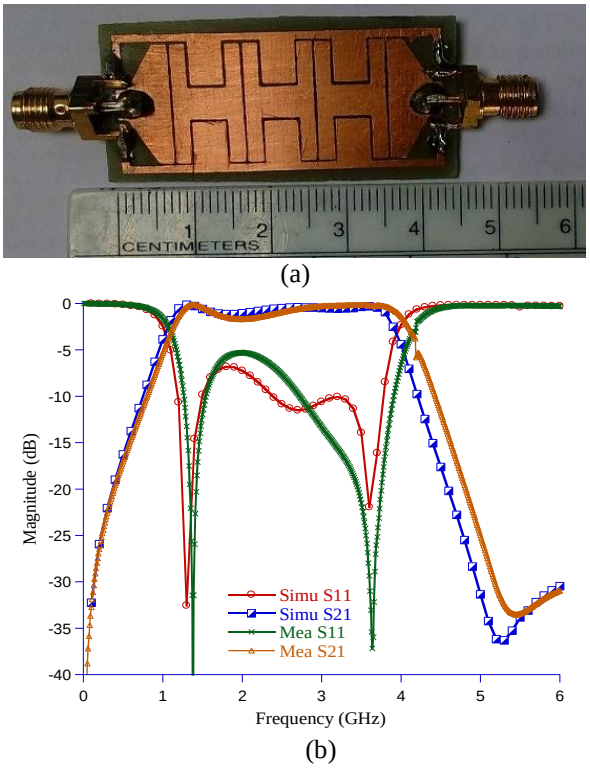

Fig. 5. (a) Fabricated prototype of the proposed bandpass filter, and (b) comparison between simulated and measured S-parameters.

B. 5th Order bandpass filter design

In order to increase further order of the filter, number of vertically installed series open end stubs are also increased.

In a similar manner like the previous design, a 5th order bandpass filter has been realized using EM simulator software. The schematic of the filter is given in Fig. 6 (a). Considering all other design parameters to be same, the new 5th order design is implemented.

The simulated result shows 3dB bandwidth from 1.18 GHz to 3.97 GHz with an insertion loss of -0.62 dB and the selectivity of 58.47 dB/GHz at the rising edge and 56.32 dB/GHz at the falling edge as depicted in Fig. 6 (b). All the five poles of the proposed design are clearly visible and it covers the entire S-band frequency range.

Table 2 shows the comparison of the obtained results of proposed BPFs with some recently reported performance of BPFs. The proposed work has found superior in terms of minimum design complexity and provides adequate performance in every aspects compared in the table includes FBW, insertion loss, selectivity and compactness.

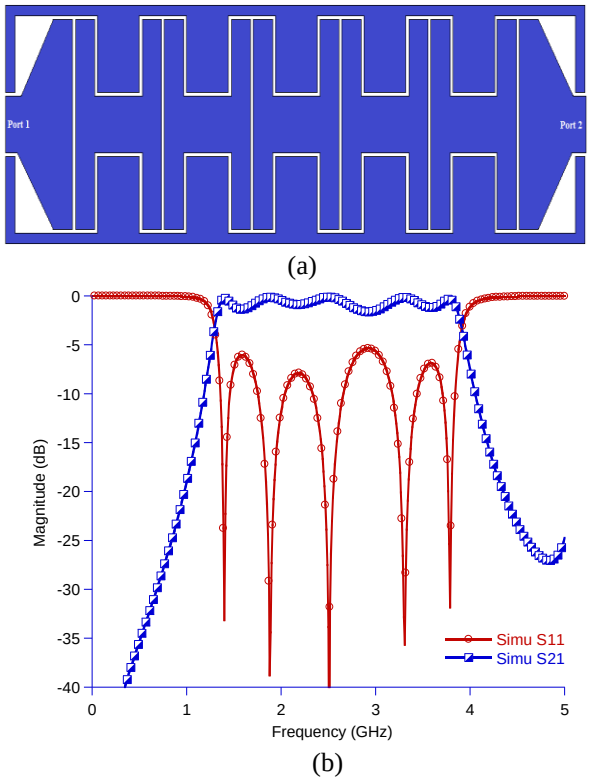

Fig. 6. (a) Schematic of proposed 5th order BPF using four vertically loaded coupled open-ended series stubs, and (b) simulates S-parameter responses

Table 2: Comparison between bandpass filters

Ref. No.	3dB FBW	IL (dB)	Size	Sharpness (R.E. and F.E)	Comments
[8]	110%	1.25	0.5λg ×0.4λg	12 dB/GHz 8.58 dB/GHz	High FBW, high IL, moderate size, poor selectivity
[9]	110%	0.9	0.32λg ×0.12λg	30 dB/GHz 30 dB/GHz	High FBW, high IL, compact size, medium selectivity, return loss <10dB
[14]	29%	1.2	0.38λg ×0.16λg	60 dB/GHz 26.6dB/GHz	Moderate FBW, high IL, compact size, higher selectivity, poor return loss
[15]	66%	0.9	0.64λg ×0.46λg	34.3 dB/GHz 21.3 dB/GHz	High FBW, high IL, medium size, moderate selectivity
Proposed Work [3rd order BPF]	145%	0.48	0.48 λg ×0.23 λg	30.7 dB/GHz 27 dB/GHz	Extreme high FBW, low IL, compact size, moderate selectivity, simple design

VI. CONCLUSION

A bandpass filter is constructed by coupled open ended CB-CPW series stub resonator with vertical placement to signal line. The selectivity and bandwidth of filter has been improved using series arrangement with close proximity and increase of resonating stubs. Multiple series open ended coupled resonators are easy to design and the fabrication requires no via holes or air-bridge as the symmetricity is maintained. The filter also provides a stopband of around 4GHz after the desired pass band.

ACKNOWLEDGMENT

The authors would like to acknowledge IIEST Shibpur for necessary support. The authors are also thankful to all the reviewers for their valuable suggestions.

REFERENCES

[1] R. N. Simons, *Coplanar Wave Guide Circuits, Components, and Systems*. John Wiley & Sons, New York, 2001.

[2] R. N. Simons and G. E. Ponchak, "Modeling of some coplanar waveguide discontinuities," *IEEE Trans. Microwave Theory Tech.*, vol. 36, no. 12, pp. 1796-1803, 1988.

[3] C. C. Tien, C. K. C. Tzuang, S. T. Peng, and C. C. Chang, "Transmission characteristics of finite-width conductor-backed coplanar waveguide," *IEEE Trans. Microwave Theory Tech*., vol. 41, no. 9, pp.1616-1624, Sep. 1993.

[4] G. E. Ponchak, S. Robertson, F. Brauchler, J. East, and L. P. B. Katehi, "Finite width coplanar waveguide for microwave and millimeter-wave integrated circuits," *Int. Symposium on Micro-electronics*, pp. 517-521, 1996.

[5] R. W. Jackson, "Mode conversion at discontinuities in finite-width conductor-backed coplanar waveguide," *IEEE Trans. Microwave Theory Tech.*, vol. 37, pp. 1582-1589, 1989.

[6] A. A. Oliner and K. S. Lee, "The nature of the leakage from higher order modes on microstrip line," *IEEE MTT-S Int. Microwave Symp*. pp. 57-60, 1986.

[7] W. T. Lo, C. Kuang, S. T. Peng, C. C. Chang, J. W. Huang, and C. C. Tien, "Resonant phenomena in conductor backed coplanar waveguides (CBCPW's)," *IEEE Trans. Microwave Theory Tech.*, vol. 41, no. 12, pp. 2099-2108, 1993.

[8] S. N. Wang and N. W. Chen, "Compact, ultra-broadband coplanar waveguide bandpass filter with excellent stopband rejection," *Progress in Electromagnetics Research B*, vol. 17, pp. 15-28, 2009.

[9] D. S. Miguel, J. Bonache, and F. Martín, "Compact wideband CPW bandpass filters with transmission zeros based on stepped impedance resonators (SIR)," *IEEE Microwave and Wireless Components Letters*, vol. 21, no. 12, pp. 664-666, 2011.

[10] P. Mondal and S. K. Parui, "Improvement of stop-band performance of a CPW bandpass filter using

DGS," *Microwave and Optical Technology Letter*, vol. 58, no. 3, pp. 593-597, 2016.

[11] C. P. Wen, "Coplanar waveguide: A surface strip transmission line suitable for nonreciprocal gyromagnetic device applications," *IEEE Trans. Microwave Theory Tech.*, vol. 17, no. 12, pp. 1087-1090, 1969.

[12] G. Ghione and C. U. Naldi, "Coplanar Waveguides for MMIC applications: Effect of upper shielding, conductor backing, finite-extent ground planes, and line-to-line coupling," *IEEE Trans. Microwave Theory Tech.*, vol. 35, no. 3, pp. 260-267, 1987.

[13] T. Moyra, S. K. Parui, and S. Das, "CB-CPW based wide band bandpass filter using open-stub resonator," *Journal of The Institution of Engineers (India): Series B*, vol. 94, no. 1, pp. 13-19, 2013.

[14] J. K. Xiao, N. Zhang, J. G. Ma, and J. S. Hong, "Microstrip/coplanar waveguide hybrid bandpass filter with electromagnetic coupling," IEEE *Microwave and Wireless Components Letters*, vol. 26, no. 10, pp. 780-782, 2016.

[15] V. Gholipour, A. A. Moshiri, and A. Yahaghi, "Highly selective wideband bandpass filter using combined microstrip/coplanar waveguide structure," *IET Electronics Letters*, vol. 52, no. 13, pp. 1145-1147, 2016.

Pratik Mondal received his Bachelor of Engineering degree in Electronics and Communication Engineering from the University of Burdwan, India in 2010. He did his Master of Engineering degree in Electronics & Telecommunication Engineering with specialization in Microwave Communication Engineering from Indian Institute of Engineering Science and Technology, Shibpur, India. He has done his Ph.D. from the same Institute in 2018. Presently, he is associated with Gayatri Vidya Parishad College of Engineeering, Visakhapatnam, India, as an Assistant Professor in the Department of ECE.

His research interests include the Microstrip Planar Circuits, Coplanar Waveguide based Circuits, DGS, DMS, Metamaterials etc. He is an Associate Member of Institution of Engineers, India. He is also a student member of IEEE-MTT Society.

Susanta Kumar Parui received the B.Sc. degree in Physics and B.Tech. degree in Radiophysics and Electronics from the University of Calcutta in the year 1987 and 1990, respectively. He did Master degree in Microwave Communication Engineering from Bengal Engineering College, India, in the year 1993. From 1993 to 2000, he worked as Instrument Engineer. Since 2000, he is associated with the Department of Electronics and Telecommunication Engineering of Indian Institute of Engineering Science and Technology, Shibpur, India and presently holds the post of Associate Professor.

His current research interests include the planar circuits, filters, antenna and EBG. He is a Senior Member of IEEE and also presently holds the post of Vice- Chairman of IEEE-MTT Kolkata Chapter.

Rajesh Bera passed B.Tech. degree in Electronics and Communication Engineering, from Birbhum Institute of Engineering & Technology, West Bengal, India in 2010. He received the M.Tech. and Ph.D. degree from KIIT, Bhubaneswar, India in 2012. Presently, he is attached with Gayatri Vidya Parishad College of Engineeering, Visakhapatnam, India, as an Assistant Professor in the Department of ECE. His research interest includes Array Antenna design, Array parameter optimization and beam-pattern synthesis using Evolutionary Computing Techniques.

An X-Band GaN HEMT Oscillator with Four-Path Inductors

Wen-Cheng Lai [1,2*] and Sheng-Lyang Jang [2]

[1] National Yunlin University of Science and Technology, Taiwan, R. O. C.
*wenlai@yuntech.edu.tw, wenlai@mail.ntust.edu.tw

[2] Dept. of Electronic Eng., National Taiwan University of Science and Technology, Taipei, Taiwan, R. O. C.

Abstract — An X-band GaN HEMT oscillator implemented with the WIN 0.25 μm GaN HEMT technology is proposed. The oscillator consists of a HEMT amplifier with an LC feedback network with four-path inductors. With the supply voltage of V_{DD} = 2 V, the GaN VCO current and power consumption of the oscillator are 10.8 mA and 21.6mW, respectively. The oscillator can generate single-ended signal at 8.82 GHz and it also supplies output power 1.24 dBm. At 1MHz frequency offset from the carrier the phase noise is 124.95 dBc/Hz. The die area of the GaN HEMT oscillator is 2×1 mm^2.

Index Terms — 0.25 μm GaN HEMT, LC oscillator, output power, phase noise.

I. INTRODUCTION

Gallium Nitride (GaN) High Electron-Mobility Transistor (HEMT) devices with high carrier mobility and high breakdown voltage are of great interest because of their suitability for high power RF applications and power switches [1-3]. A GaN power amplifier, if monolithically integrated with a low phase-noise oscillator can provide a flexible high-power signal source, and GaN oscillators are thus indispensable in fully integrated GaN HEMT transceivers. A few GaN HEMT oscillators have been presented in the past. Colpitts oscillator [1]-[3] uses one HEMT and a stub or inductor between the HEMT's source and the ground, providing a positive series feedback to make the HEMT VCO unstable. The second HEMT oscillator uses the common-gate topology with a feedback transmission line element at gate to maximize the device instability [4]-[5]. The resonator circuit is placed at the HEMT device's source side to compensate the opposite sign of reactance from the un-stabilized common-gate device. The third HEMT oscillator uses Hartley topology [6], the source of GaN HMET is grounded. Differential GaN HEMT oscillators [7] are convenient to connect directly to a differential input. The common gate balanced Colpitts oscillator [8]-[10] provides differential outputs and is chosen since it is known for low up-conversion of flicker noise. The above-mentioned oscillators use single-path inductors. This letter presents a GaN oscillator with four-path inductors. Multi-path inductors have been shown to have high-quality factor [11], and are potential for resonator usage and for low phase noise oscillator design. The designed GaN oscillator was manutured with a 0.25 μm GaN on SiC foundry process technology [12].

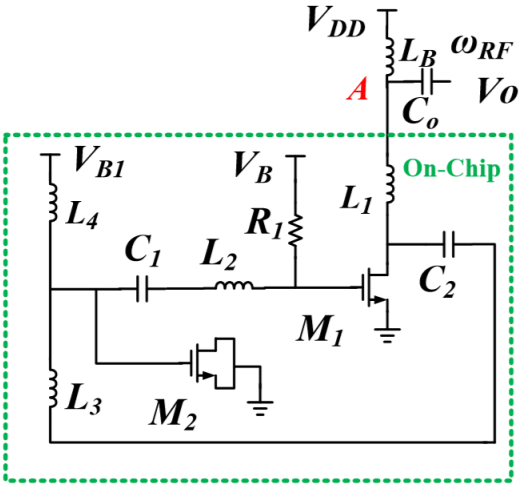

Fig. 1. Schematic of the presented oscillator.

II. DETAIL CIRCUITS DESIGNS

Figure 1 shows the schematic of the designed GaN HEMT oscillator. The oscillator uses an active HEMT, air-bridge interconnects, spiral planar inductors, and metal–insulator–metal (MIM) capacitors. The circuit was designed using Agilent Technologies' Advanced Design System (ADS). The inductor L_1 and HEMT M_1 forms an amplifier and R_1 is gate-biasing resistor. V_B is the gate voltage. V_{DD} is the supply voltage and is connected to the output node A through an RF choke L_B. C_1, C_2 are dc blocking capacitors. HEMT M_2 is used as varactor. V_{B1} is the varactor control voltage using an RF bias inductor L_4. The output is measured at the common node A of L_1 and RF choke. L_3 is used to adjust oscillation frequency and improve the phase noise.

Submitted On: February 9, 2018
Accepted On: July 9, 2020
https://doi.org/10.47037/2020.ACES.J.350912

Inductor L_2, gate-source capacitor of HEMT M_1 and varactor M_2 forms a resonator. L_3 and L_2 are four-path inductors. Inductor L_4 is a symmetric single-path spiral inductor. For simplicity of design guide, authors short A node to the ground, and eliminate M_2 and L_4.

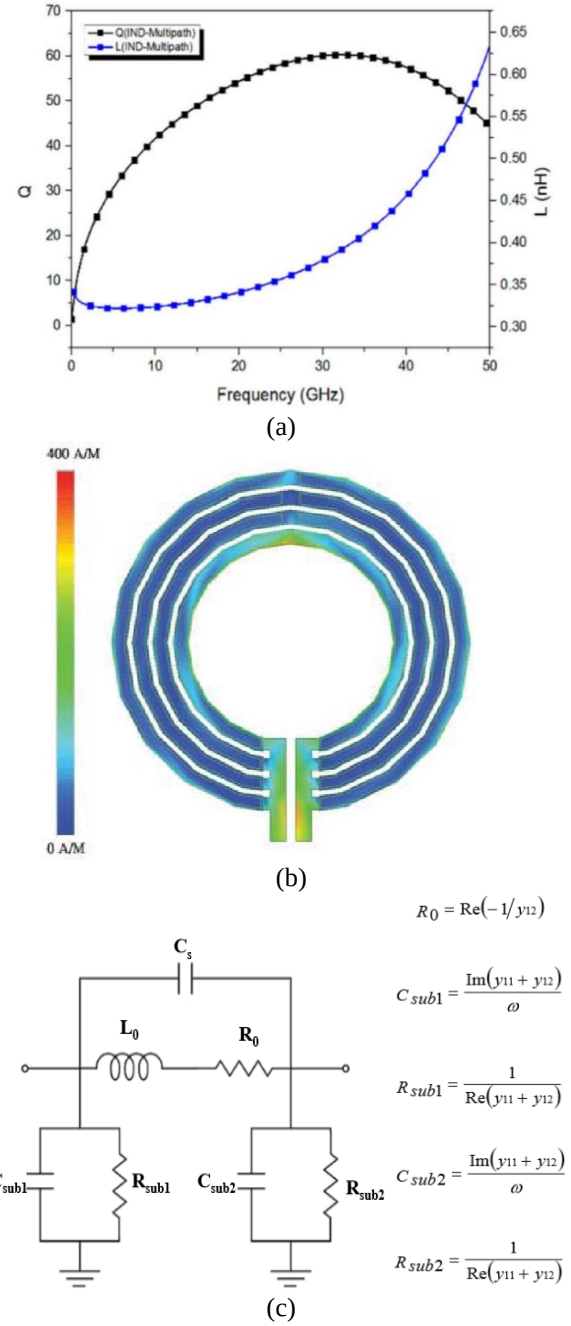

Fig. 2. (a) Chip micrograph for the HEMT oscillator; 2mm×1mm. (b) Simulated current density, simulated *L* and *Q* characteristics of the designed 4-path inductor. (c) A lumped physical model of a circular inductor.

The small-signal model for the oscillator can be built to derive the resonant frequency given by:

$$\omega = \sqrt{\frac{1}{[L_2 + L_3 + L_1]C_{gs}}}. \quad (1)$$

And the equivalent negative resistance used for the resonator is given by:

$$-\mathrm{R} = -\frac{1 - \mathrm{L}_1[\omega^2[L_2 + L_3]\mathrm{C}_{gs}}{\mathrm{g}_m}. \quad (2)$$

Using Leeson's equation as shown in (3), the estimated phase noise improvement is 15 dBc/Hz due to the Q-factor improvement:

$$L(f_m) = 10\log\left[\frac{1}{2}\left(\left(\frac{f_o}{2Q_1 f_m}\right)^2 + 1\right)\left(\frac{f_c}{f_m} + 1\right)\left(\frac{FkT}{P_s}\right)\right]. \quad (3)$$

This article proposes that silicon-on-sapphire (SOS) and micro-electro-mechanical system (MEMS) technologies can be used to proposed high Q-factor inductors operating in X-band. Cgs is the gate-source capacitance and gm is the transconductance of HEMT M_1. –R is used to compensate the loss in the passives and output. Varying V_B to change Cgs is used to tune the oscillation frequency. Figure 2 shows simulated inductance L and Q characteristics of the 4-path L_2 as shown in Fig. 1. Three path inductors have been used previously for low phase noise silicon-based oscillator design [13]. The inductance and quality-factor are extracted from the y parameter. At 10 GHz, the Q-factor is 40 for the designed inductor with L=0.325nH. The self-resonant frequency is about 65 GHz. Figure 2 (c) illustrates the lumped physical model proposed for these suspended inductors. L_0 and R_0 are series inductance and resistance due to conductor losses and dissipation from the induced eddy currents in the substrate. Cs is an inter-turn fringing capacitance and a metal overlap coupling capacitance between the spiral and underpass metal layers. In addition, R_{sub} and C_{sub} are the resistance and parasitic capacitance of the substrate. The inductors parameter of R_0, C_{sub}, R_{sub} and Q-factor are modelled using equations (4). After calculation from equations (4), optimized values of each lump elements determined L_1~L_4 and C_0~C_2 depended on Fig. 2 (c) equivalent circuit in Fig. 1:

$$Q_{factor} = \frac{\omega L_0}{R_0} \cdot \frac{R_{sub}}{R_{sub} + \left[\left(\frac{\omega L_0}{R_0}\right)^2 + 1\right]R_0} \cdot \left[1 - \frac{R_0^2(C_s + C_{sub})}{L_0} - \omega^2 L_0(C_s + C_{sub})\right]$$

$$Q_{factor} = \frac{\mathrm{Im}\left(\frac{1}{y_{11}}\right)}{\mathrm{Re}\left(\frac{1}{y_{11}}\right)}. \quad (4)$$

III. EXPERIMENTALS

The VCOs were designed and fabricated in the WIN 0.25 μm GaN/SiC HEMT process base on simulated and numerical modeling. Figure 3 shows the micrograph of the proposed oscillator with a chip dimension of 2×1 mm^2 including all test pads and dummy metal. Figure 4 shows the measured output voltage waveform of the oscillator. It shows low high-order harmonic. Figure 5 shows the measured output spectrum of the fundamental signal at 8.82 GHz with output power 1.24 dBm. At V_{DD}=2V, the power consumption is 21.6 mW. Figure 6 shows the phase noise performance of VCO. The measured phase noise of VCO is about -124.05 dBc/Hz at 1MHz offset frequency from 8.82 GHz oscillation frequency and has a slope of -30 dB/dec in the frequency offset below 1 kHz the phase noise consists of the $1/f^3$ portion and is due to the flicker noise [14]-[15]. The figure of merit. (FoM) has been defined in Eq. (5) to compare performances of VCOs.

$$FOM = L\{\Delta\omega\} + 10\cdot log(P_{DC}) - 20\cdot log\left(\frac{\omega_o}{\Delta\omega}\right), \qquad (5)$$

where ω_o is the oscillating frequency, $\Delta\omega$ is the offset frequency, $L\{\Delta\omega\}$ is the phase noise at $\Delta\omega$, PDC is DC power consumption of VCOs in mW. By the calculation, the FoM of the proposed VCO is -189.56 dBc/Hz. The FoM is calculated at 1MHz offset frequency and V_{DD}=2V. Figure 7 shows measured phase noise increased with V_{DD}. Increasing V_{DD} can increase voltage swing to enhance S/N ratio ideally, however, when V_{DD} is beyond 2V, this is not guaranteed because the phase noise increases with supply voltage [16]-[18]. Figure 8 shows measured power consumption, output power, and oscillation frequency versus V_B. Maximal output power is measured at V_B=-2.1V. Table 1 shows the performance parameters comparison of the designed GaN HEMT oscillators with others published articles.

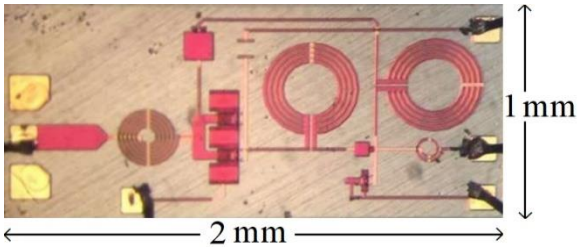

Fig. 3. Chip micrograph for the HEMT oscillator (chip area = 2mm×1mm).

Fig. 4. Measured voltage waveform. V_{DD}=1 V, V_{B1}=0 V, V_B=-2 V. L_{choke}=4.7nH.

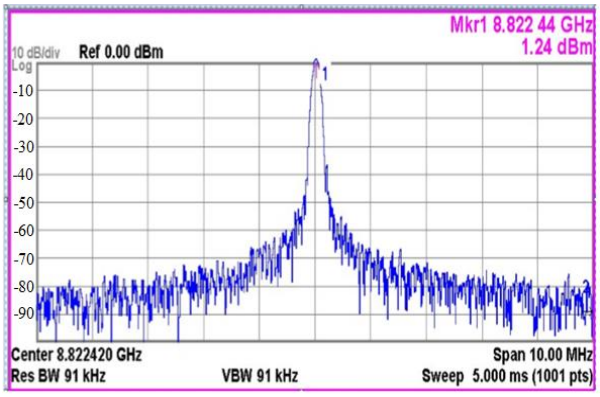

Fig. 5. Measured spectrum. V_{DD}=2V. V_B=-2.0V. V_{B1}=0V.

Fig. 6. Measured phase noise. V_{DD}=2V, V_{B1}=0V, V_B=2V. L_{choke}=4.7nH. A $1/f^3$ guideline is used for reference.

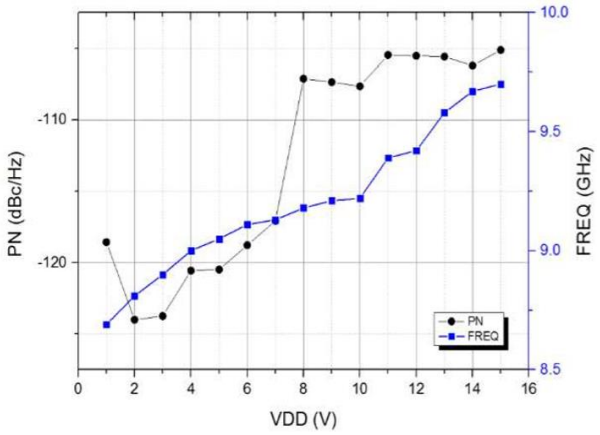

Fig. 7 Measured phase noise and oscillation frequency versus V_{DD}. V_{B1}=-2V. V_T=0 V.

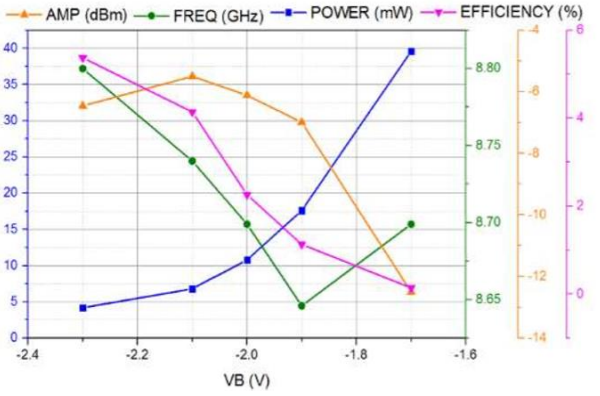

Fig. 8. Measured power consumption, output power, and oscillation frequency versus V_B. V_{DD}=1V. V_{B1}=-2.3~1.7V.

Table 1: Performance comparison of GaN VCOs

Ref.	Proc. (um)	Topol	Vdd(V)/ Pdis(mW)	fo GHz	PN dBc/Hz	FOM dBc/Hz
[10]	0.25	Hartley	28/1456	7.9	-112@ 100KHz	-178
[6]	0.25	Balanced Colpitts	6/180	9.92	-136	-193
[19]	-	Push-push	15/600	9.1	-130	-181
[20]	0.25	Common source	10/600	9.9	-135	-187
[5]	0.25	Common Gate	30/10625	9.55	-115.0	-154.0
This	0.25	Cross-coup	2/21.6	8.8	-124.05	-189.56

VI. CONCLUSION

A 8.8 GHz high power VCO using GaN HEMTs was designed, fabricated, and characterized. At the supply 2V, the output power of the carrier at 8.8 GHz is 1.24 dBm. The measured phase noise of VCO is about 124.05 dBc/Hz at 1MHz offset frequency from the carrier. The phase noise is mainly due to the device flicker current noise. At V_{DD}=2V, the oscillator can supply high output power and low phase noise with the FOM -189.56 dBc/Hz. The power conversion efficiency is 12%. To authors' knowledge, multi-path inductor has been successfully implemented in GaAs process for the first time in literature.

ACKNOWLEDGMENT

The authors would like to thank the Staff of the CIC and *Yung-Han Chang* [2] and *Ji-Shin Chiou* [2] for the help and measurements. This work is support by MOST-105-2221E011124.

REFERENCES

[1] Z. Q. Cheng, Y. Cai, J. Liu, Y. Zhou, K. M. Lau, and K. J. Chen, "A low phase-noise X-Band MMIC VCO using high-linearity and low-noise composite-channel Al 0.3 Ga 0.7N/ Al 0.05 Ga 0.95N HEMTs," *IEEE Trans. Microw. Theory & Tech*., vol. 55, iss. 1, pp. 23-29, 2007.

[2] R. Weber, D. Schwantuschke, P. Bruckner, R. Quay, M. Mikulla, O. Ambacher, and I. Kallfass, "A 67 GHz GaN voltage-controlled oscillator MMIC with high output power," *IEEE Microw. Wireless Compon. Lett.*, vol. 23, pp. 374-376, July 2013.

[3] R. Weber, D. Schwantuschke, P. Bruckner, R. Quay, F. van Raay, and O. Ambacher, "A 92 GHz GaN HEMT voltage-controlled oscillator MMIC," *IEEE MTT-S Int. Microw. Symp. (IMS2014)*, 2014.

[4] H. Chen, X. Wang, X. Chen, L. Pang, W. Luo, B. Li, and X. Liu, "A high power C-band AlGaN/GaN HEMT MMIC VCO," *Int. Workshop on Microw. and Millimeter Wave Cir. and System Tech. (MMWCST)*, 2013.

[5] V. S. Kaper, V. Tilak, H. Kim, A. V., Vertiatchikh, R. M. Thompson, T. R. Prunty, L. F. Eastman, J. and R. Shealy, "High-power monolithic AlGaN/ GaN HEMT oscillator," *IEEE J. Solid-State Cir.*, vol. 38, no. 9, pp. 1457-1461, Sep. 2003.

[6] H. Liu, X. Zhu, C. C. Boon, X. Yi, M. Mao, and W. Yang, "Design of ultra-low phase noise and high-power integrated oscillator in 0.25 μm GaN-on-SiC HEMT technology," *IEEE Microw. Wireless Compon. Lett.*, vol. 24, pp. 120-122, 2014.

[7] C. Sanabria, H. Xu, S. Heikman, and U. K. Mishra, "A GaN differential oscillator with improved harmonic performance," *IEEE Microw. Wireless Compon. Lett.*, vol. 15, pp. 463-465, July 2005.

[8] T. N. T. Do, S. Lai, M. Horberg, H. Zirath, and D. Kuylenstierna, "A MMIC GaN HEMT voltage controlled-oscillator with high tuning linearity and low phase noise," *IEEE Compound Semiconductor Integ. Cir. Symp. (CSICS)*, 2015.

[9] S. Lai, D. Kuylenstierna, M. Horberg, N. Rorsman, I. Angelov, K. Andersson, and H. Zirath, "Accurate phase noise prediction for a balanced Colpitts GaN

HEMT MMIC oscillator," *IEEE Trans. Microw. Theory & Tech.*, vol. 61, no. 11, pp. 3916-3926, Nov. 2013.

[10] S. Lai, D. Kuylenstierna, M. Ozen, M. Horberg, N. Rorsman, I. Angelov, and H. Zirath, "Low phase noise GaN HEMT oscillators with excellent figures of merit," *IEEE Microw. Wireless Compon. Lett.*, vol. 24, no. 6 pp. 412-414, June 2014.

[11] X. Xu, P. Li, M. Cai, and B. Han, "Design of novel high-Q-factor multipath stacked on-chip spiral inductors," *IEEE Trans. Electron Devices*, vol. 59, no. 8, pp. 2011-2018, Aug. 2012.

[12] W. Wohlmuth, M.-H. Weng, C.-K. Lin, J.-H. Du, S.-Y. Ho, T.-Y. Chou, S.-M. Li, C. Huang, W.-C. Wang, and W.-K. Wang, "AlGaN/GaN HEMT development targeted for X band applications," *IEEE Int. Conf. Microw. Communications, Antennas and Electronic Systems*, pp. 1-4. 2013.

[13] S.-L. Jang and Y.-C. Lin, "Low power three-path inductor Class-C VCO without any dynamic bias circuit," *Electronics Lett.*, vol. 53, pp. 1186-1188, 2017.

[14] W.-C. Lai, S.-L. Jang, Y.-Y. Liu, and M.-H. Juang, "A triple-band voltage-controlled oscillator using two shunt right-handed 4th-order resonators," *Journal of Semicond. Tech. and Sci*., vol. 16, no. 4, pp. 1961-1964, Aug. 2016.

[15] S.-L. Jang, Y.-H. Chang, and W.-C. Lai, "A feedback GaN HEMT oscillator," *(ICIMMT)*, 2018.

[16] J.-F. Huang, K.-L. Chen, W. C. Lai, and W.-J Lin, "A fully integrated 5.6 GHz low-phase noise colpitts VCO/QVCO using programmable switched codes," *Microw. and Opt. Tech. Lett.*, vol. 55, no. 7, pp. 1490-1493, Apr. 2013.

[17] S.-L. Jang, Y.-C. Lin, W.-C. Lai, C.-W. Hsue, M.- and H. Juang, "A class-C quadrature VCO using the varactor coupling technique," *Microw. and Opt. Tech. Lett.*, vol. 58, no. 8, pp. 1961-1964, May 2016.

[18] J.-F. Huang, W. C. Lai, and K.-J. Huang, "A 5.6-GHz 1-V low power balanced colpitts VCO in 0.18-um CMOS process," *IEICE Trans. on Electron*, vol. E96-C, no. 6, pp. 942-945, June 2013.

[19] Z. Herbert, L. Szhau, D. Kuylenstierna, J. Felbinger, K. Andersson, and N. Rorsman, "An X-band low phase noise AlGaN-GaN-HEMT MMIC push-push oscillator," *in Proc. IEEE Compound Semicond. Integr. Cir. Symp. (CSICS)*, pp. 1-4, Oct. 16-19, 2011.

[20] G. Soubercaze-Pun, J. G. Tartarin, L. Bary, J. Rayssac, E. Morvan, B. Grimbert, S. L. Delage, J.-C. De Jaeger, and J. Graffeuil, "Design of a X-band GaN oscillator: From the low frequency noise device characterization and large signal modeling to circuit design," *in IEEE MTT-S Int. Dig.*, pp. 747-750, June 11-16, 2006.

Wen-Cheng Lai was born in Taiwan, Republic of China, in 1974. He received Ph.D. degrees in Electronic Engineering from National Taiwan University of Science and Technology in 2015. He joined ASUSTek Computer Inc. in 2015. He joined the Dept. of Electronics, National Penghu Univ. of Sci. and Tech., Taiwan in 2018. In 2020, he is Assistant Professor in National Yunlin University of Science and Technology. He has co-authored more than 200 SCI journal and conference papers in the Radio Frequency circuits design.

Sheng-Lyang Jang was born in Taiwan, Republic of China, in 1959. He received B.S. degree from the National Chiao-Tung University, Hsinchu, Taiwan, in 1981, M.S. degree from the National Taiwan University, Taipei, in 1983, and Ph.D. degree from the University of Florida, Gainesville, in 1989. He joined the Noise Research Laboratory at the University of Florida in 1986. In 1989, he joined the Department of Electronics, National Taiwan University of Science and Technology, Taipei, and became a Full Professor in 1993. He has coauthored more than 240 SCI journal papers in the MOSFET devices and circuits. He also holds 17 US.

Artificial Magnetic Conductor Based Miniaturized Frequency Re-configurable Dielectric Resonator Antenna for 5G and WBAN Applications

Shahid Khan [1], Hazrat Ali [2], Syed Usman Ali Shah [2], Haider Ali [3], and Camel Tanougast [1]

[1] Institut Supérieur d'Électronique et d'Automatique
University De Lorraine, Metz, Lorraine, 57070, France

[2] Department of Electrical and Computer Engineering
COMSATS University Islamabad, Abbottabad, 22060, Pakistan

[3] Department of Electronics Technology, University of Technology, Nowshera, Pakistan
shahid.khan@univ-lorraine.fr, hazratali@cuiatd.edu.pk, syedusman.eng@gmail.com,
haider.ali@uotnowshera.edu.pk, camel.tanougast@univ-lorraine.fr

Abstract — In this work a novel miniaturized frequency reconfigurable Dielectric Resonator antenna using Artificial Magnetic Conductor (AMC) surface is proposed. The prototype is set to work for 5G mid-band frequencies and Wireless Body Area Network (WBAN) applications. The work consists of two parts: firstly, the miniaturization of the prototype using AMC surface and secondly using the same AMC surface to reconfigure the frequency to another wireless application. Using AMC surface, the DR volume is reduced by 85% percent. Connecting the AMC unit cells through ideal switches (micro-trip slabs) re-configures the DR for different frequency. The overall performance observed before switching as well as after switching in both the cases is promising. The design is fabricated for performance analysis. A close agreement is reported between simulated and measured values of the reflection coefficients, radiation pattern, gain and efficiencies. The prototype has stable radiation pattern for both the operating frequencies. The impedance bandwidth values for both the resonance frequencies are 14.2% and 16% respectively. The prototypehas a maximum gain of 6.8dBi and a maximum efficiency of 88%.

Index Terms — 5G, artificial magnetic conductor, dielectric resonator antenna, efficiency, gain, WBAN.

I. INTRODUCTION

Modern communication systems are rapidly evolving. They tend to offer a number of services to the end users without compromising the device compactness. To keep the volume of the device compact, different blocks of the communication systems need to be carefully designed. One important block is the front end including the antenna. Due to limited space availability for the antenna in any communication system, antennas need to be designed carefully so that it may be accommodated easily with the provision of multiple wireless services.

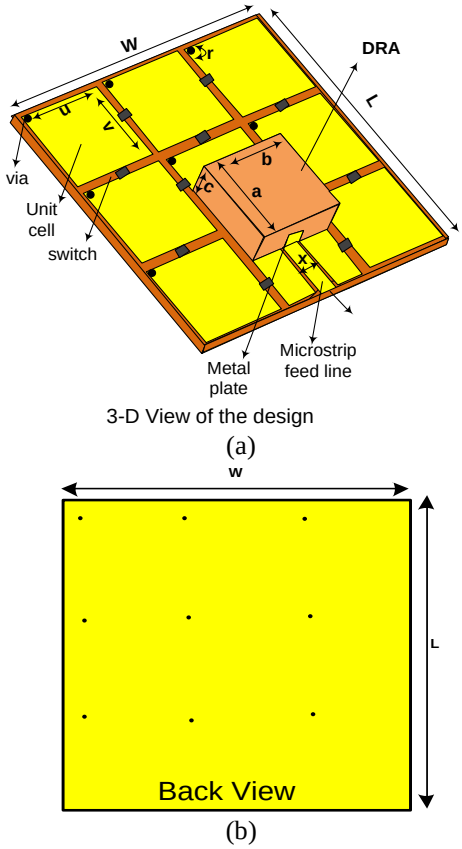

Fig. 1. (a) Represents 3-D front view, and (b) represents the back side of the design.

A number of antenna designs have been proposed for size miniaturization and frequency re-configurability by using different techniques. However, there are very

Submitted On: November 23, 2019
Accepted On: May 3, 2020

https://doi.org/10.47037/2020.ACES.J.350913

few published works which focus simultaneously on both these aspects by using AMC surface. Traditionally, the AMC surface has been in use for different wireless applications. It can be used to excite additional frequencies for different wireless applications [1]. In [2], a low profile circularly polarized meta-surface based antenna is presented, where the meta-surface is used as an independent radiator. In [3], AMC surface is used to enhance the bandwidth of the low profile antenna. Thus, AMC surface enhances the bandwidth, the reflection co-efficient and gain of the antenna. In [4], a compact low profile meta-surface based antenna for medical application is proposed. In this work, addition of the AMC surface with the antenna not only enhances the overall performance of the design but also reduces the specific absorption rate by 95.3%.

Along with the other applications, AMC surface is also useful for the re-configurability of different antenna parameters. With the help of AMC surface, we can perform frequency re-configurability, pattern re-configurability, waveform re-configurability and beam steering. In [5]-[6], AMC surface is used to control re-configurability independently. The active switches and varactor diodes are inserted in the AMC surface [7]. This not only helps to maintain the performance of the design but also performs re-configurability for certain parameters. In all the mentioned examples, the micro-strip patch antennas (MPA) accompany AMC surface. Despite of generating some good results, MPAs have still some shortcomings like narrow bandwidth, low gain, low efficiencies and unstable radiation pattern thus they have enough room for improvement in the overall performance parameters. DRA in combination with the AMC surface can provide good performance parameters like wider bandwidth, stable radiation pattern with good values of gain and efficiencies, as both these independent structures have characteristics of generating good performance results. Therefore, DR can be a good candidate and replacement of MPAs for different wireless applications [8]. However, the DRs have relatively larger size (volume). In the literature very few miniaturized frequency reconfigurable DRAs have been reported. In [9]-[10], different compact and miniaturized DRAs have been reported. In all these examples, the prototypes are either miniaturized or reconfigured separately. There are very few examples, which jointly focus on both the miniaturization and re-configurability aspects. To the best of our knowledge, no work has been reported to miniaturize and re-configure DRAs simultaneously with the help of AMC surface.

In this work, we present a novel re-configurable miniaturized DRA with the help of AMC surface. The AMC surface miniaturizes and re-configures the prototype with overall good performance parameters. The prototype is miniaturized by 85% and re-configured between two operating frequencies for 5G mid-band frequencies and WBAN applications respectively.

II. THEORITICAL BACKGROUND

For the design of the proposed work, the first step is to design DR. For this purpose, a rectangular DR is selected, as it is easy to fabricate and gives more degree of dimension freedom. The initial size of the DR for the 5G mid-band frequency application is designed with the help of the following Dielectric Waveguide model (DWM) [8]-[13]:

$$f_r = \frac{C}{2\pi\sqrt{\epsilon_r}}\sqrt{K_x^2 + K_y^2 + K_z^2}$$
$$K_x = \frac{\pi}{a}\,;\quad K_z = \frac{\pi}{c} \qquad (1)$$
$$K_y \tan\left(K_y \frac{b}{2}\right) = \sqrt{(\epsilon_r - 1)}\left(K_0^2 - K_y^2\right).$$

The three dimensions of the DR calculated with the help of equation (1) are ***a***, ***b*** and ***c*** while K_x, K_y, and K_z are the wave numbers across the three sides of the DR. **C** is the speed of light in free space.

The initial size of the DR gives the target resonance frequency, but the design has a large volume. To address this issue, AMC surface is used. Importantly, each single unit of AMC surface must also have the same resonance frequency. To do this, the AMC surface is carefully designed with the help of following equations [7]:

$$f_r = \frac{1}{2\pi\sqrt{LC}}\,. \qquad (2)$$

Equation (2) defines the resonance frequency of the AMC unit cell. This resonance frequency is dependent on the capacitive and inductive reactance of the AMC surface. The inductance is offered by the metallic vias between the AMC unit cells and ground while capacitances are offered by the gap between the AMC unit cells. To design the AMC unit cells for 3.5GHz resonance frequency, the following equations are incorporated:

$$C = \frac{W\epsilon_0(1+\epsilon_r)}{\pi}\cosh^{-1}\left(\frac{w+g}{g}\right), \qquad (3)$$

$$L = 2 \times 10^{-7} h\left[\ln\left(\frac{2h}{r}\right) + 0.5\left(\frac{2r}{h}\right) - 0.75\right]. \qquad (4)$$

Where, $w = 0.18\lambda_{3.5ghz}$, $g = 0.01\lambda_{3.5ghz}$, and $r = 0.005\lambda_{3.5ghz}$.

The values obtained from Eqs. (3) and (4) are then placed in Eq. (2). The calculations give resonance frequency value in accordance to what we obtain from the DRA. The total number of AMC unit cells are decided from the resonance frequency shift to the same value of the un-miniaturized DRA. Once DR is positioned on the 3×3 arrangement of the AMC unit cells, the current distribution from the AMC surface couples the current distribution inside the DR, thus both the structures resonate at 3.5GHz. Thus, net result is the combined effect of both the structures.

III. ANTENNA DESIGN DISCUSSION

The proposed simple design consists of DR with low permittivity (**ϵ_r= 10**) positioned on FR4 substrate with 1.6mm thickness and 0.002 tangent loss. Both the length and the width of the ground substrate and ground metal

are equal to 60mm. Initially, the DR dimensions are determined by using DWM (Dielectric Waveguide Model) [11]. The three dimensions **a, b,** and **c** are length, width and height of the proposed prototype, which are 20mm, 21mm, 10mm respectively. After determining the initial dimensions of the DR. The DR is fed by a micro-strip line of 3mm width and has a gap of 0.1mm with the neighboring AMC unit cells. A micro-strip patch which is the extended feedline is stacked to the wall of the DR to improve the impedance matching. The design with the initial volume of 4200mm^3 resonates at 3.5GHz. In the next step the volume of the DR is reduced to 605mm^3 by using AMC surface. Figures 1 (a) and (b) explains the top and bottom view of the design in detail. Table 1 represents details of the different dimensions of the proposed design.

A unit cell of the AMC surface was carefully designed at 3.5GHz. The unit cell has a high impedance surface (HIS) characteristic at 3.5GHz. When these AMC unit cells are positioned together, they are then connected to the ground plane with the help of thin metallic vias of 0.4mm radius. Closely analyzing the prototype, it is observed that an RLC resonance circuit is developed. The gap between AMC unit cells introduce capacitances and metallic vias generate inductive effects. Thus the combination of 9 unit cells resonate at 3.5GHz. When the volume of independent DR is reduced to 650mm^3, the frequency moves to 4.3GHz because resonance frequency has an inverse relationship with size of the DR. A decrease in the volume of the DR will shift the resonance frequency of the DR to higher value and vice versa. After doing this, the reduced DR is placed above the array of nine unit cells. As AMC surface act as an independent resonance structure, when the reduced DR couples with AMC surface they both resonate in a single frequency. Due to its metallic nature, the bandwidth is slightly reduced because of the relatively narrow bandwidth response of the AMC surface. In the next phase re-configurability was managed with the help of ideal switches positioned between the AMC cells. These switches are small micro-strip patches of 1×1mm^2. Placement of the ideal switches reduces the capacitance between the AMC unit cells as shown in (2). Reduction of the capacitance between the AMC unit cells causes the shift of resonance frequency to higher frequency thus it resonate the design at 4.2GHz. At both the resonance frequencies the design has stable radiation pattern with the good values of the gain and efficiencies.

During the simulation, the switching circuit was performed with the help of PIN diode, resistors, capacitors and inductors. The equivalent schematic of this switching circuitry was also analysed and both showed great resemblance in terms of simulated results RF PIN diodes BAR 50-02V switch OFF and switch ON the circuit while resistor of 100 Ω limit the current flow to protect the circuit elements and similarly the presence of micro-strip slabs show ON state and their absence show OFF state. The capacitor of 22Pf during the simulation block the flow of DC into input RF port while inductor of 100 pH block the flow of AC current into DC biasing circuit. The above mentioned biasing circuitry during the simulation performs the switching operations. Looking to the close resemblance between the two switching schemes, micro-strip slabs were selected as final switching option as they are easy to simulate and fabricate. There are two switching categories i-e, OFF state and ON state. A total of 12 switches in the form of small micro-strip patches are used for frequency re-configurability. Absence of all the switches makes configuration I (OFF state) and presence of all the switches makes configuration II (ON state). At configuration I antenna resonate at 3.5GHz and at configuration II the prototype is reconfigured to 4.2GHz.

Table 1: Different parameters of the design

Parameters	Without EBG	With EBG
$L_g \times W_g \times H_s$	(60 ×60 ×1.6) mm^3	(50×50×1.6)mm^3
a× b ×c	(20 ×20×12) mm^3	(10 ×10 ×5) mm^3
u × v	-	(15.17×15.7)mm^2
g	-	0.75mm
r	-	0.404mm
L_f	10mm	10mm
W_x	3mm	3.0mm

IV. PARAMETRIC STUDIES

In order to finalize the design for both the miniaturization and re-configurability a number of optimization techniques for different parameters are performed. It includes the effect of attached micro-strip patch to the wall of DR, which is actually the extended feed line. Another important parameter for optimization is the effect of AMC unit cell area on the resonance frequencies. The effect of the number of AMC unit cells on the resonance frequencies are also observed. Lastly, the effect of switches and location of the switches on the frequency re-configurability is also studied.

The extended feedline to the wall of the DR highly effect the impedance matching. Figure 2 shows that as we increase the height of the stacked micro-strip line, the impedance matching improves and a slight increase in the bandwidth is observed because of change in current distribution inside the DR. Thus, maximum matching and relatively wider bandwidth is achieved at 5.22mm height of the extended feedline.

Area of the unit cell also highly affects the resonance frequency. Any increase or decrease in the AMC unit cell area change the high impedance surface (HIS) characteristics, which shifts the resonance frequency. Figure 3 shows that increasing the area of the unit cells shifts the frequency to lower range and vice versa.

It is also clear from the Fig. 3 that an area

of (15.17mm×15.7 mm) gives the required resonance frequency with much better impedance matching. Figure 3 also shows that an increase in the unit cell area has an inverse relationship with the resonance frequency.

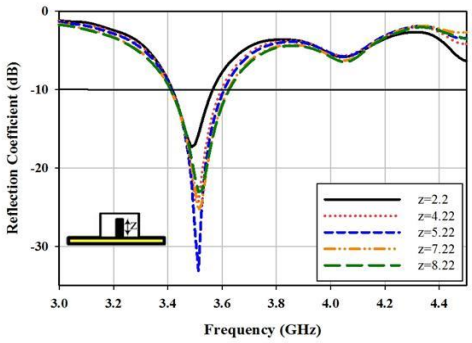

Fig. 2. Effect of the feedline extension.

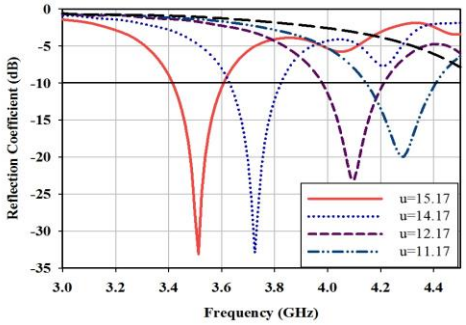

Fig. 3. Effect of AMC unit cell area on S11.

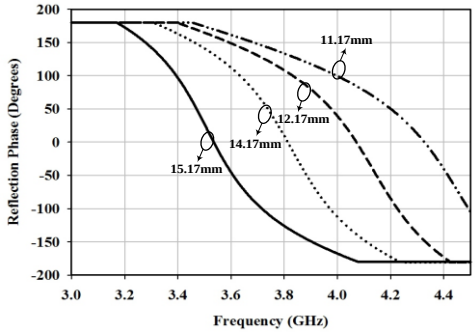

Fig. 4. Phase angle diagram of the Unit Cell.

The phase angle diagram shows that zero crossing of the unit cell has an inverse relationship with the area of the AMC unit cell. Figure 4 shows the effect of changing unit area on the zero crossing of the resonance frequency. Increasing the area of the unit AMC cell causes the shift in zero crossing to low range frequencies and vice versa. (15.17×15.7 mm^2) is the final area of the unit cell at 3.5GHz. Similarly, the number of AMC unit cells also affects the resonance frequency. As AMC surface can act as an independent resonance structure so the number of unit cells can increase or decrease the resonance frequency.

Introduction and location of the switches has also a significant impact on the resonance frequencies. Figure 5 shows the effect of location of switches on the resonance frequencies. The location of the switches were tested on three different points. From Fig. 5, it is clear that with no switches the antenna resonates at 3.5GHz. When the switches are positioned at the top edge of the AMC unit cells, the resonance frequency shifts to higher range but still the required resonance frequency is not achieved. The switches are then tested at bottom position. The location of the switches at this position further shift the resonance frequency but the required resonance frequency is still missing. In order to achieve the required resonance frequency the switches are positioned at the midpoint of the unit cell. From Fig. 5, it is clear that at this position, the antenna resonates at 4.2GHz, which is the required resonance frequency. The final location selected for the position of the switches is the mid-point of the AMC unit cell, which resonates the design at 4.2GHz. The possible reason for the shifting of the resonance frequency to higher frequency is the changing values of the capacitances between the unit cells. It is clear that there is a small gap between the unit cells. This gap actually introduces the capacitances in the overall design. Any change in the capacitance changes the resonance frequency. Introduction of the switches reduces the overall capacitances and thus frequency shift to higher range. The maximum decrease in the equivalent capacitance is observed when switches are positioned at mid of the AMC unit cell. During the simulation process, the switching was performed with the help of micro-strip slabs (ideal switches). In the fabrication of the prototype, they are replaced with a micro-strip line of 1×1mm^2.

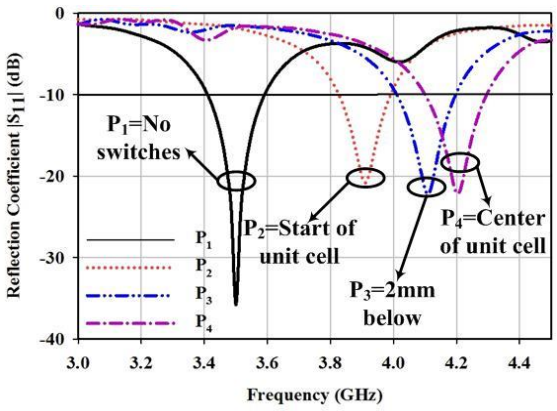

Fig. 5. Effect of location of switches at different positions.

V. RESULTS AND DISCUSSION

In this section different simulated and measured results of the proposed design are discussed in detail. These results include simulated results before and after miniaturization. It also includes simulated and measured values of the reflection coefficients of the prototype before and after frequency re-configurability. Simulated and measured radiation pattern is also explained in detail. Similarly simulated and measured efficiency and gain for both the configurations have also been presented in detail.

In Fig. 6 it is seen that an un-miniaturized DR resonates at 3.5GHz with a wider bandwidth. When its size is directly reduced without using AMC unit cells the resonance frequency shifts to higher range and it resonates at 4.8GHz because size of the DR has an inverse relationship with the resonance frequency. Figure 6 also shows that addition of AMC unit cells shifts back the resonance frequency and resonate the design at 3.5GHz. AMC unit cells are independent resonant structures which resonate at a specific resonance frequency. When AMC surface is coupled with the DR they support each other but the bandwidth is slightly reduced because net bandwidth is the combined effect of both the structures. AMC surface has slightly narrow bandwidth response (because of metallic nature) and DR has a wider bandwidth response after combining them with each other, the net result is slight reduction in the bandwidth.

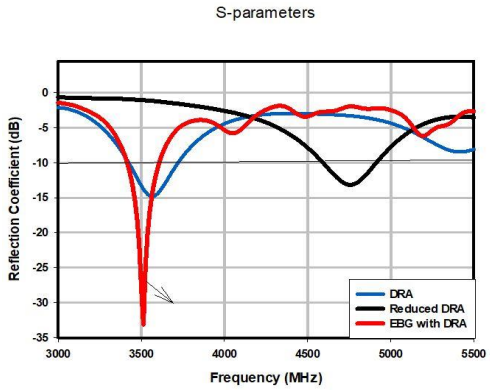

Fig. 6. Reflection coefficient of DRA before and after miniaturization.

The application of the AMC surface greatly reduced the DR size. The next step was to reconfigure the frequency by using the same AMC surface. Using the effect of changing equivalent capacitance after adding small micro-strip patches helped to reconfigure the frequency to WBAN wireless application. Switches in the form of small micro-strip patches are introduced in between the AMC unit cells which shifts the frequency to high range. Figure 7 shows that absence of the small micro-strip patches (switches) which represents OFF state resonates the design at 3.5GHz. The simulated and measured values are in close agreement. The simulated bandwidth is 200MHz and measured bandwidth is 180MHz. There is minor shift in the resonance frequency and also a reduction in the bandwidth. The shift in the resonance and reduction of the bandwidth is because of the fabrication inaccuracies. Provision of fine fabrication can overcome this problem.

Figure 8 shows the reconfigured prototype frequency when all switches are ON. When switches are positioned at the mid of the AMC unit cells, frequency is reconfigured to 4.2GHz for WBAN application. Simulated bandwidth is 200MHz and measured bandwidth is 230MHz. Simulated and measured resonance values are close enough with a slight difference in the bandwidth because of intolerances due to fabrication. A good and more accurate fabrication can overcome this problem.

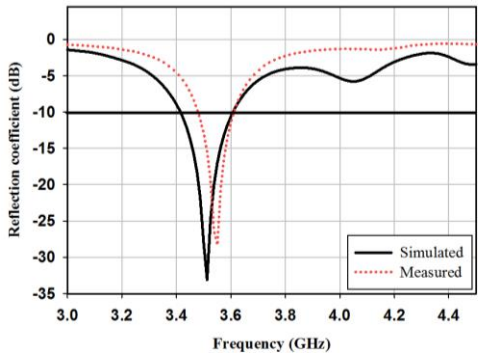

Fig. 7. Simulated and measured reflection coefficient in OFF state.

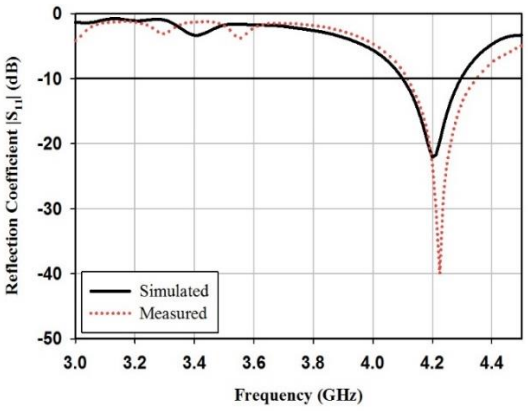

Fig. 8. Simulated and measured reflection coefficient in ON state.

Table 2: Comparison of the current work with already published work

No.	Antenna Type	DR Volume	Re-configurability	Design Complexity	Gain	Efficiencies	% Bandwidth
1	Compact RDRA [10]	0.12λ×0.17λ×0.5 λ	Reconfigurable	Simple	5.8dBi	N/A	8%, 16% and 65%
2	Compact RDRA [12]	0.13λ×0.41 λ×0.06 λ	reconfigurable	Simple	N/A	N/A	85% and 14%
3	RDRA with tunnel [11]	0.13λ×0.13 λ×0.27 λ	reconfigurable	Complex	5.0dBi	N/A	60% and 50%
This work	RDRA	0.12λ×0.12λ×0.058 λ	Reconfigurable	Very simple	6.87dBi	88%	14.2%, 16%

Table 3: Performance analysis of the overall design

Switching State	Simulated Bandwidth	Measured Bandwidth	Simulated Efficiencies	Measured Efficiencies	Simulated Gain	Measured Gain
OFF	3.4-3.6 GHz	3.45-3.6 GHz	87%	85%	6.8dBi	6.7dBi
ON	4.1-4.3 GHz	4.13-4.37 GHz	76%	74%	6dBi	5.8dBi

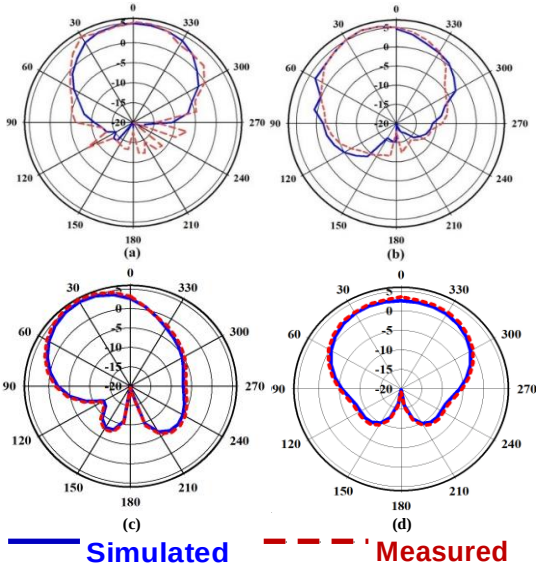

Fig. 9. (a) and (b) show the Simulated and measured E-field and H-field in OFF state, respectively. Similarly, (c) and (d) show simulated and measured E-field and H-field when switches are in ON state, respectively.

Figure 9 shows the simulated and measured radiation pattern for both the switching configurations. The far field radiation pattern is presented in the form of the E-field and H-field. Figures 9 (a) and (b) show the radiation patterns of the design when all switches are in OFF state. From Fig. 9, it is quite clear that radiation pattern for both the E-field and H-field is stable and mainly broad side and focused towards 0°. The value of peak gain is 6.87dBi. Moreover, simulated and measured parameters are in close agreement. A minor deviation is due to the lack of accuracies in the prototype fabrication.

Similarly, Figs. 9 (c) and (d) show the radiation pattern when switches are in ON state. The radiation pattern at 4.2GHz is stable, focused towards 0° and is broadside. The simulated and measured values of the radiation pattern are in close matching which shows that measured values follows strictly the simulated values that define the stability of the design. Thus at both the resonance frequencies the simulated and measured radiation pattern is stable with the good values of gain. This also clarify that switching only changes the frequency of the prototype while the radiation pattern is still stable at the same position.

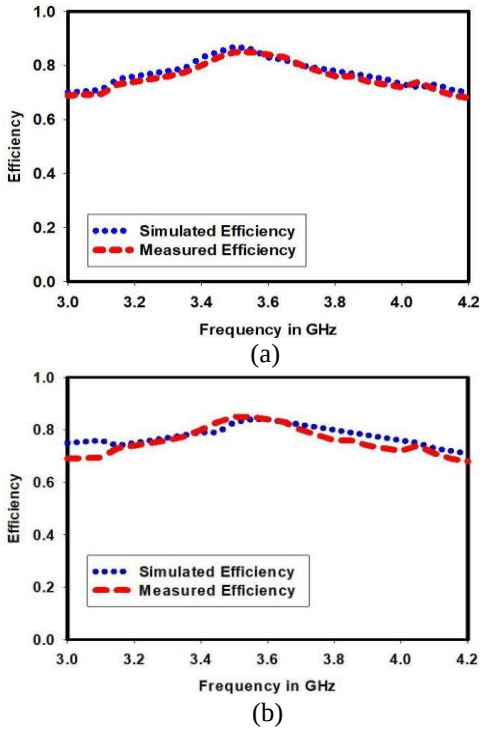

Fig. 10. Efficiencies of the design: (a) when switches are in OFF position, and (b) when switches are in ON position.

In Fig. 10 detailed analysis of the efficiencies for both the arrangements has been presented. In the OFF switching configuration, the simulated efficiency of the design is 87% while measured values of the efficiency is close to the simulated value which is 85%. Similarly in ON switching configuration the efficiency of the design at 4.2GHz is 76% while measured values of the efficiency at the same frequency is 74%. Thus, the simulated and measured values are in close agreement.

Figure 11 shows the simulated and measured values of the gain for both the configurations. For configuration I, the simulated value of the gain is 6.8dBi and measured value is also in very close matching except with a minor deviation at 3.5GHz and 4.2GHz. Similarly, after re-configurability, the simulated value has maintained its value at 6dBi but measured value is slightly less than the simulated one i-e 5.8dBi, however this slight deviation in both the cases is acceptable.

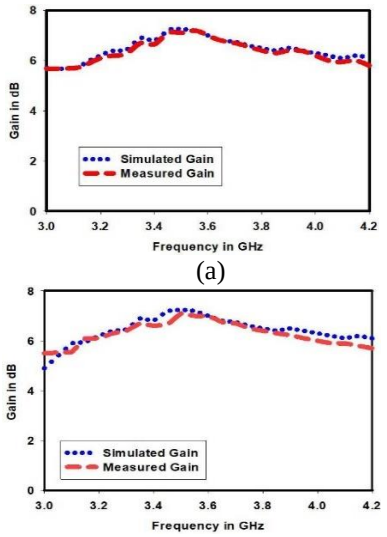

Fig. 11. (a) Gain of the design when switches are in OFF position, and (b) when switches are in ON position.

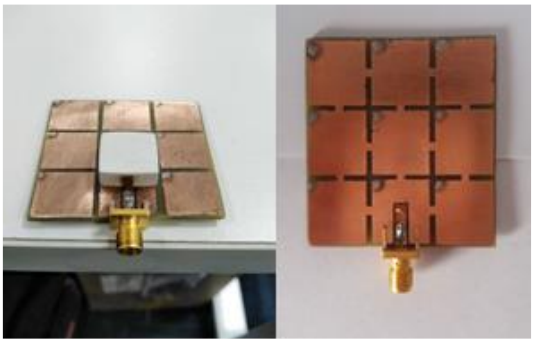

Fig. 12. (a) Represents miniaturized Prototype, and (b) shows the AMC surface with ideal switches.

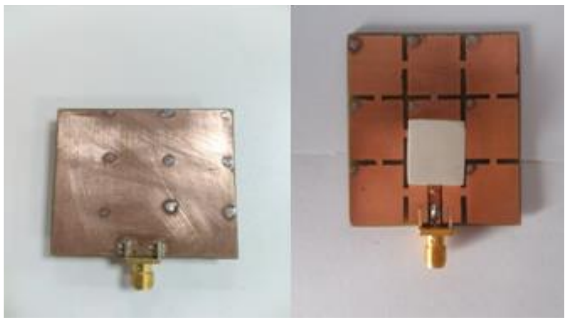

Fig. 13. (a) Rear View of the Prototype, and (b) miniaturized prototype with ideal switches.

In Table 2, a comparison of different published work with the proposed work has been presented. The work in [10] comprises of rectangular DR with relatively smaller volume and simple design. The value of gain is good with two switching operations to achieve three resonance frequencies. The design reported in [12] also represents a compact reconfigurable design with two resonance frequencies. The third design as reported in [11] for re-configurability has relatively large volume with a low value of gain. There are two resonance frequencies for two switching configuration. In comparison to the afore-mentioned examples, our design has the minimum volume with a very good value of peak gain by simply using AMC surface while simultaneously providing re-configurability. Using the same AMC surface, two switching operations are performed, which in return, generate two resonance frequencies with much better impedance width.

Table 3 shows the performance analysis of the prototype. When all switches are OFF the prototype has a good simulated and measured value for 5G applications. Thus, the design operates at 3.5GHz and 4.2GHz with the help of ideal switches (micro-strip slabs) placed between the two unit cells. In OFF state at low frequency, the value of gain and efficiencies are relatively higher. Similarly in ON state, due to metallic nature of the AMC surface the value of the efficiencies and gain has slightly reduced but still they are good enough to establishment the communication between uplink and down link. The design is fabricated for measuring the simulated results. Figure 12 and Fig. 13 give complete detail of the fabricated design.

VI. CONCLUSION

We presented a novel miniaturized frequency reconfigurable DRA design. In the proposed design, we achieved miniaturization with the help of AMC surface containing nine AMC unit cells. Using the ideal switches between the same AMC surface, the design is reconfigured to another wireless application. For both the switching configuration, the design has a stable radiation

pattern with good value of the realized gain. Also for both the operating frequencies, the prototype has good values of efficiencies as observed through the measurements reported. Thus the proposed design is good enough for real time mentioned applications.

REFERENCES

[1] M. S. Alam, N. Misran, B. Yatib, and M. T. Islam, "Development of electromagnetic band gap structures in the perspective of microstrip antenna design," *Int. J. Antenna Propag*., p. 22, 2013.

[2] Y. M. Pan, P. F. Hu, X. Y. Zhang, and S. Y. Zheng, "A lowprofile high-gain and wideband filtering antenna with metasurface*," IEEE Trans. Antennas Propag*., vol. 64, no. 5, pp. 2010-2016, May 2016.

[3] Z. N. Chen, "Bandwidth enhancement of a single-feed circularly polarized antenna using a meta-surface," *IEEE Antennas Propag. Mag*., vol. 50, no. 2, pp. 39-46, Apr. 2016.

[4] H. Gromath and R. Otin, "Specific absorption rate computations with a nodal-based finite element formulation," *Prog. Electromagn. Res*., vol. 128, pp. 399-418, 2012.

[5] F. Costa, A. Monorichio, S. Talaricos, and F. M. Valeri, "An active highimpedance surface for low-profile tunable and steerable antennas," *IEEE Antenna Wirel. Propag. Lett*., vol. 676-680, p. 7, 2008.

[6] R. Dewan, M. K. A. Rahim, I. M. Hamid, M. R. Hamid, H. A. Majid, and M. E. Jalil, "Multiband frequency-reconfigurable antenna using meta-material structure of electromagnetic band gap," *Appl. Phys. A*, vol. 16, p. 123, 2016.

[7] J. Dong, S. Wang, and G. Hu, "Design of reconfigurable ultrawide band antenna with switchable single/dual/triple band notch functions," *Applied Computational Electromagnetics Society Journal*, vol. 34, no. 1, Jan. 2019.

[8] N. A. Al-Shalaby and S. M. Gaber, "Design of dielectric resonator band stop/band pass filters," *Applied Computational Electromagnetics Society Journal*, vol. 34, no. 8, Aug. 2019.

[9] T. Apperley and M. Okoniewski, "An air-gap-based frequency switching method for the dielectric resonator antenna," *IEEE Antennas Wireless Propag. Lett*., vol. 13, pp. 455-458, 2014.

[10] S. Danesh, M. K. A. Rahim, M. Hamidi, M. R. Hamid, and J. Majid, "Frequency reconfigurable rectangular dielectric resonator antenna," *IEEE Antennas Wireless Propag. Lett*., vol. 12, pp. 1331-1334, 2013.

[11] S. Dhar, K. Patra, R. Ghatak, B. Gupta, and D. R. Poddar, "Reconfigurable dielectric resonator antenna with multiple polarisation states," *Antennas Propag*., vol. 12, no. 6, pp. 895-902, 2018.

[12] B.-J. Liu, J.-H. Qiu, S.-C. Lan, and G.-Q. Li, "A wideband-to-narrowband rectangular dielectric resonator antenna integrated with tunable bandpass filter," *IEEE Access*, vol. 7, 2019.

[13] S. Danesh, S. K. A. Rahim, and M. Khalily, "A wideband trapezoidal dielectric resonator antenna with circular polarization," *Progress in Electro-magnetics Research L*, vol. 34, pp. 91-100, 2012.

Shahid Khan was born in Landikotal, Pakistan in 1986. He received the B.S. degree in Communication Engineering from the University of Engineering and Technology Peshawar Pakistan and M.S. degree in Satellite Navigation and Related Applications from Politecnico de Torino Italy in 2011. Currently he is doing his Ph.D. from University de Lorraine France. He is working on the Development of Reconfigurable Dielectric Resonator antenna for different wireless applications. Before joining University de Lorraine he worked as a Lecturer in Comsats University Abbottabad from 2012 to 2017.

Hazrat Ali received his B.Sc. and M.Sc. degrees in Electrical Engineering in 2009 and 2012 respectively. He did his Ph.D. in 2015 from University of Science and Technology Beijing, China. He is currently Assistant Professor at Department of Electrical and Computer Engineering, COMSATS University Islamabad, Abbottabad Campus. At CUI, he is the member of the signal processing and machine learning research group. He is also the Course Head for Digital Signal Processing course. His research interests lie in unsupervised learning, generative and discriminative approaches, and speech and medical image processing. He is Associate Editor at IEEE and served as Reviewer at IEEE Access, IEEE Transactions on Neural Networks and Learning Systems, IEEE Transactions on Emerging Topics in Computational Intelligence.

Syed Usman Ali Shah did his bachelor in Telecommunication and Networks from Hazara University Pakistan. He did his Masters from Comsats University Islamabad, Abbotabad Campus in 2017. His has worked on a number of project including microstrip patch antennas, dielectric resonator antennas, reconfigurable antennas.

Haider Ali was born in 1984. He completed his B.S. degree in Telecom Engineering from NUCES, Pakistan, in 2007. He received his Doctorate and a M.S. degree in Electronics Engineering from Politecnico Di Torino, Italy, in 2010, and completed his Ph.D. in Electronics & Communication Engineering from there in 2014. He is currently working as Assistant Professor at the Department of Electrical Engineering, and Technology, University of Technology, Nowshera, Pakistan. His research interests include data acquisition systems, renewable energy materials, power electronics systems, design and development of antenna, radio frequency (RF) front end and telecommunication subsystem for small satellites.

Tanougast Camel was born on May 10, 1972 in Thionville – France. He did his Ph.D. degree from Laboratory LIEN - Univ. Henri Poincaré Nancy 1 in 2011. His Ph.D. thesis topic was "Methodology for Temporal Partitioning for System on Chip Implementation based Run Time Reconfigurable Technology". Currently he is Head of the ASEC Team (smart embedded and sensor systems). He is also serving as a Full Professor in Institute of Higher Learning in Electronics and Automation, University of Lorraine, France. His research interests are Self-organised system based run time reconfigurable technology, Custom Computing and Embedded Systems for Image/Video and Signal applications using FPGAs, Secure Communications and radio communication, reconfigurable embedded and RF systems for different wireless applications. He has authored and co-authored more than 100 articles and conference papers.

Retrodirective Transceiver Utilizing Phased Array and Direction Finder

Mohammed Aseeri, Waleed Alomar, Hamad Alotaibi, and Abdulrahman Aljurbua

National Center for Telecommunications and Defense System Technologies (TDST)
King Abdulaziz City of Science and Technology (KACST), P.O. Box 6086 Riyadh 11442, Saudi Arabia
Center of Excellence for Microwave Sensor Technology (CMST), University of Michigan, Ann Arbor, USA
masseri@kacst.edu.sa

Abstract ─ Retrodirectivity have several important applications in communication and in wireless power transfer. In this paper, frequency sensitive retrodirective transceiver is proposed. It receives a signal and infers its direction from its frequency spectrum, then it can transmit a new signal back to the same or other direction at the designer wish. To determine the direction of the coming signal, a 0.85-1.15GHz frequency scanning phased array antenna is used so that the received signal would have a distorted spectrum with the maximum amplitude frequency component linked to the direction of the signal. Based on the frequency scanning, the retrodirectivity system can be used for wireless power transfer or for reactive jamming. Special circuit is designed to receive the signal with strongest power and to isolate the frequency component with maximum amplitude. Phase-locked loop (PLL) circuit is used to link such frequency to specific phase shift that is introduced to the transmitter array antenna to send a new signal to the same direction of the received signal. ADS simulation is performed to demonstrate the performance of each block.

Index Terms─ Frequency component isolation circuit, frequency scanning antenna array, retrodirective antenna.

I. INTRODUCTION

The Retrodirectivity refers to the process of retransmitting a signal to the same direction it arrived from without knowing its direction in advance [1]. It has many advantages like reducing the interference with other signals in addition to reducing power demand since the transmission will be in single direction. The two most common methods used to implement retrodirectivity are Van Atta array and phase conjugate methods.

Van Atta array method [2] works by interconnecting receivers and transmitters in a way that makes the last receiving element in phase with the first transmitting element. Doing this ensures the signal will be transmitted back to the same destination it came from. Several variations have been done to improve the performance of the array but they share the same principle [3-4]. Phase conjugate method [1] operates by introducing a phase shift at each receiving element which makes them out of phase with the transmitting elements, hence, transmitting the signal in the same direction of reception. There are multiple variations on the method as well, they use the same principle with different methods to introduce the phase shift [5-7].

The main shortcoming of both methods, however, is that they retransmit the signal with the same frequency it arrives with making them inflexible towards changing the content and the nature of the signal to be retransmitted. Frequency scanning phase array is an antenna whose radiation pattern changes with frequency. Recently, there have been multiple publications that uses this concept for different applications [8-10].

In this work, a new method for retrodirectivity that utilizes frequency scanning is proposed. The method separates the receiving and transmitting units which give the transmitter the freedom to send any signal back to same direction or for that matter to any other direction. Frequency scanning receiver receives specific frequency optimally from specific direction making the optimally received frequency a signature that tells about the direction of the signal. The system have flexibility to be designed according to any specific bandwidth and that based on the operation principle required. So, in the transceiver circuit can be used to transmit any signal to a specific direction that is not known by the transmitter. For example, the circuit can be used for jamming a signal at unknown direction or it can be used to transmit a wireless power to a device at unknown direction [11].

II. TRANSCEIVER COMPONENTS

A. Receiving antenna array

In this work, a four element serially fed phased array antenna have been used as in (Fig. 1). It consists of four receivers connected serially by transmission lines.

At a fixed distance and azimuthal angle, the radiation pattern formula for such antenna is given by [12]:

$$S(\theta) = S_e(\theta) \left| \sum_{n=1}^{N} a_n \, e^{j\psi_n} \, e^{j\,(n-1)\,k\,d\cos(\theta)} \right|^2, \quad (1)$$

where,

Submitted On: April 13, 2020
Accepted On: May 29, 2020
https://doi.org/10.47037/2020.ACES.J.350914

$S_e(\theta)$: Radiation pattern for single element.
a_n: Amplitude of the received signal at n[th] element.
ψ_n: Phase of n[th] element due to transmission line delay.
k: Wave number ($\frac{2\pi}{\lambda}$).
d: The interelement spacing.
θ: The angle from which the signal is received.
N: Number of antennas.
If the transmission lines are designed to have integer multiples of 2π (zero) phase shift at the center frequency (i.e., 1 GHz), ψ_n will relate to frequency as follows:

$$\psi_n = 2\pi\, n\, m\, \frac{\lambda_0}{\lambda}, \tag{2}$$

where λ_0 is the wavelength at center frequency (1GHz), λ is the wavelength at the frequency under consideration and n is introduced because there are n transmission lines connecting n[th] antenna to the port. m is an integer above 1 for the designer choice to control the phase change sensitivity when frequency changes. Moreover, if the interelement spacing is chosen to be half wavelength at center frequency, its multiplication with wave number will be:

$$\boldsymbol{k\, d} = \frac{2\pi}{\lambda} * \frac{\lambda_0}{2} = \frac{\lambda_0}{\lambda}\, \pi. \tag{3}$$

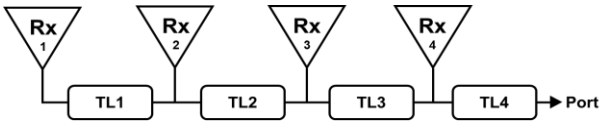

Fig. 1. Serially fed array antenna along with the transmission lines.

With the previous relations, (1) can be written as:

$$S(N,\lambda,m,\theta) = S_e(\theta)\left|e^{-j\frac{\lambda_0}{\lambda}\pi\cos(\theta)}\right|^2 \times \left|\sum_{n=1}^{N} a_n\, e^{j\,2\pi\, n\, m\frac{\lambda_0}{\lambda}}\; e^{j\, n\, \frac{\lambda_0}{\lambda}\pi\cos(\theta)}\right|^2. \tag{4}$$

In this design we assumed using an omnidirectional antenna. However, any antenna who has a half power beam width more than the scanning range of the antenna can be used. If omnidirectional individual antennas (i.e., having a radiation pattern independent of θ) are chosen, $S_e(\theta)$term can be ignored because only the normalized pattern is of concern. The same is true for any magnitude of phase term (i.e., $|e^{-jx}|$) which leads to:

$$S(\gamma) = \left|\sum_{n=1}^{N} a_n\, e^{jn\gamma}\right|^2, \tag{5}$$

where,

$$\gamma = \pi\, \frac{\lambda_0}{\lambda}\, (2m + cos\,\theta) = \pi\, \frac{f}{f_0}\, (2m + cos\,\theta). \tag{6}$$

Since the signal is received from a far distance, all a_ns are the same and equal unity. Having this in mind, (5) becomes a well-known sum that can be simplified to [12]:

$$S(\gamma) = \frac{\sin\left(\frac{N\gamma}{2}\right)^2}{\sin\left(\frac{\gamma}{2}\right)^2}. \tag{7}$$

Using (6) to substitute for γ, the closed-form formula for radiation pattern becomes:

$$S(N,f,m,\theta) = \frac{\sin\left(\frac{N}{2}(\pi\frac{f}{f_0}(2m+\cos\theta))\right)^2}{\sin\left(\frac{1}{2}(\pi\frac{f}{f_0}(2m+\cos\theta))\right)^2}. \tag{8}$$

Using MATLAB, the relation in (8) versus θ is plotted at different frequencies (Fig. 2).

As can be seen from the radiation pattern, each frequency has a 'preferable' direction at which it is optimally received. Therefore, if a signal that has uniform frequency spectrum within 0.85-1.15 GHz is sent, the frequency spectrum of the signal after it is received will be distorted. Depending on the direction of the signal, some frequencies will be received better than others. Figure 3 shows the frequency spectrum of a uniform signal after reception from different angles. The plot is generated from (8) after fixing N to 4 and m to 2.

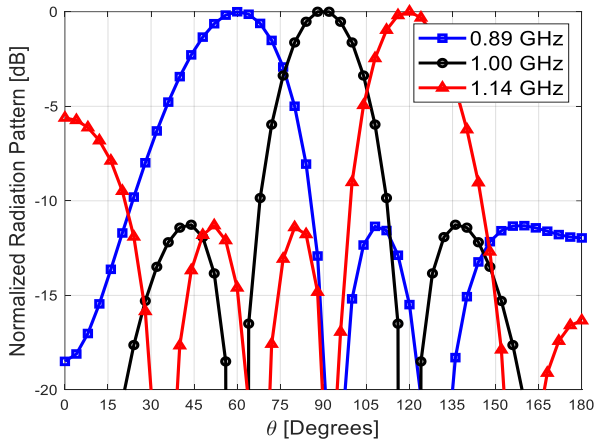

Fig. 2. Normalized pattern Vs θ at different frequencies (N=4, m=2).

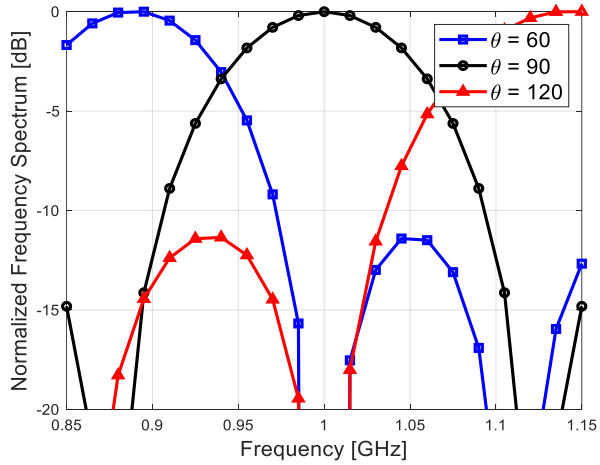

Fig. 3. Frequency spectrum of a uniform signal after reception.

B. Frequency component isolation circuit

The goal of this circuit is to take the signal with distorted spectrum and isolate the frequency component that has the maximum amplitude so that the signal direction is determined. Towards that end the circuit performs four operations which are down conversion, frequency sampling, filtering and comparison.

Down conversion is done to simplify the electronics needed to perform the other operations. After that comes the frequency sampling operation which is essential to make the filters - in the later stage - able to extract single frequency components from continuous spectrum. Mathematically, the signal out of the mixer will be:

$$m(t) = m_{Received}(t) * \cos(2\pi f_c\, t). \quad (9)$$

If the signal $m(t)$ is repeated and delayed by constant T_0:

$$g(t) = \sum_{n=-\infty}^{+\infty} m(t - nT_0). \quad (10)$$

Its Fourier transform will be the following [13]:

$$G(2\pi f) = \sum_{n=-\infty}^{+\infty} \frac{2\pi}{T_0} M\left(n\frac{2\pi}{T_0}\right) \delta(2\pi f - n\frac{2\pi}{T_0}). \quad (11)$$

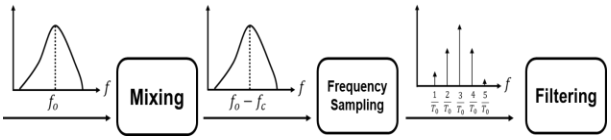

Fig. 4. Block diagram illustration of mixing and sampling.

Where the capital letters refer to the Fourier transform of the respected functions and $\delta(*)$ is the Dirac delta function. As can be seen, the transform is a set of samples in frequency domain and their separation can be controlled by adjusting T_0. Therefore, a basic delay loop can be used to repeat the signal in time domain which corresponds to sampling in frequency domain. Figure 4 illustrates the mixing and sampling operations in block diagram. It should be noted that the closer the samples to each other, the more accurate the direction estimation is at the expanse of high requirements for filters to isolate the very closely sampled frequency components. After sampling in frequency, filtering and comparison are required in order to determine the frequency sample with highest amplitude. This is especially important for the later stage in which Phased-locked-loop (PLL) is used to convert the frequency into a DC voltage to be used in transmitter's phase shifters. PLL cannot lock on signals with multiple frequency components, hence the need to eliminate all components but the one with highest amplitude. If the scene is divided into N (even) directions (angles), N bandpass filters are required for filtering so that the frequency component corresponding to each direction get isolated in order to be compared to the rest.

In comparison operation, the output of each filter branches out into two branches where one branch gets rectified and the other branch is connected to a voltage-controlled (VC) switch. The rectified signals get compared by a comparator and the output of the comparator is connected to the VC switches so that only the component with higher amplitude passes. The comparison operation is done in multiple stages with each stage reducing half of the components, the last stage results in a single surviving component that indicates the direction of the received signal. Figure 5 shows block diagram illustration of the filtering and comparison.

The last part of the circuit is a PLL that converts the surviving frequency component to a DC voltage (at the input of the VCO inside the PLL) that is used by the phase shifters in the transmitting antenna array.

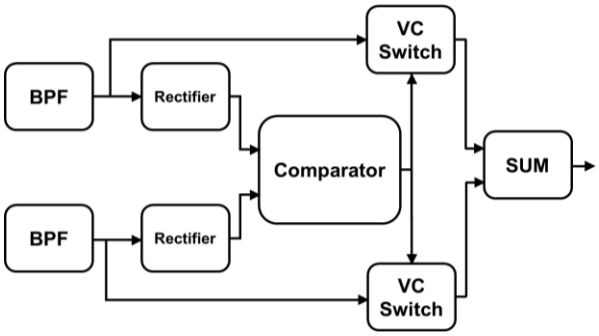

Fig. 5. Filtering and comparison part for two frequency components.

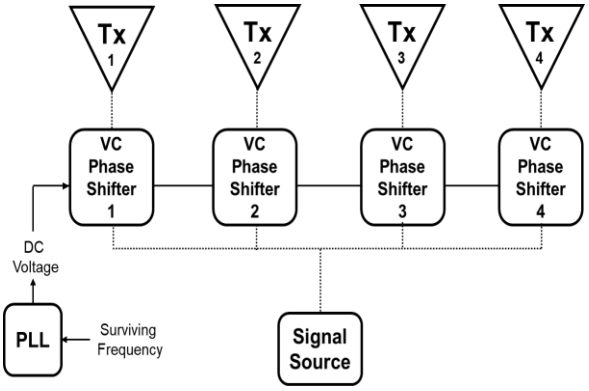

Fig. 6. Transmitting antenna array.

C. Transmitting antenna array

The array consists of four elements connected in parallel with each element preceded by VC phase shifter as in Fig. 6. The phase shifters are designed to give the following phase:

$$\psi_{Tx(n)} = 2\pi\, n\, r\, DC\_Voltage, \quad (12)$$

where n is the antenna's number and r is a design parameter. r is chosen in such a way that (12) equals negative of (2) which leads to transmission in the same direction of reception, it also can be chosen to make the antenna radiates in opposite direction or any direction in

between at the designer wish. Furthermore, it should be noted the transmitted signal source is independent of the received signal adding more freedom to the transceiver compared to other retrodirectivity methods.

III. SIMULATION RESULTS AND DISCUSSION

A. Receiving antenna array results

To verify the mathematical analysis that led to (8), Harmonic Balance (HB) simulation in ADS software was used. Utilizing Principle of Reciprocity, the receiving antenna was modelled as transmitting antenna. The network has 5 terminals, one is the feeding port and the other four represent antennas and they are serially connected by microstrip transmission lines each of electrical length 4π - corresponding to m=2 in (2). The spatial delay ($e^{jnkd\cos(\theta)}$) was modelled by ideal transmission line. Figure 7 shows the ADC circuit used in the simulation. A non-ideal transmission line is used to connect the antenna elements. These line are TL1, TL2, TL3, and TL4. There is a very good agreement between the results obtained by ADS simulation and the theoretical relation derived above which confirms the validity of the derivation. The results in Figs. 8 and 9 are from ADS based on a non-ideal transmission line to include the effect of the dispersion and the group delay.

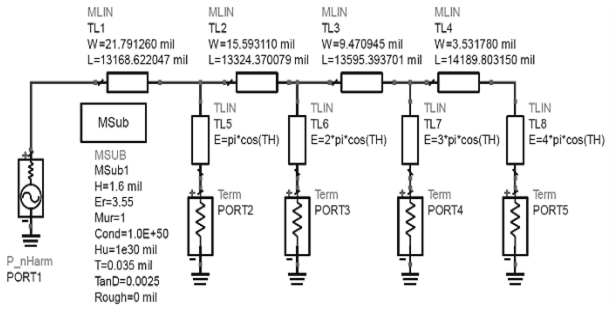

Fig. 7. ADS circuit for receiver.

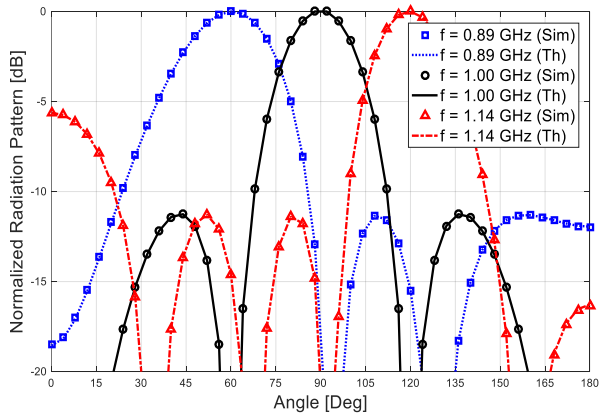

Fig. 8. Simulation results at different frequencies.

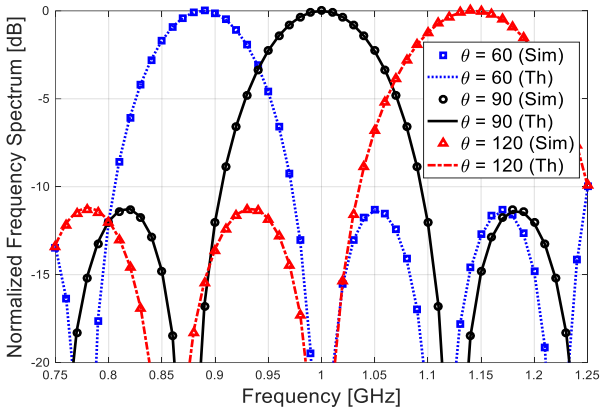

Fig. 9. Reception frequency spectrum at different angles.

B. Frequency component isolation circuit results

To demonstrate the circuit performance, a signal peaked at 0.89 GHz like the one in (Fig. 9) is inputted to the circuit. Figure 10 and Fig. 11 show the ADS circuit used for mixing and sampling and the simulation results respectively. The scan range is directly proportional to the bandwidth and the beam width of the antenna. This circuit can work at scan angle 18^0o or 0^0.

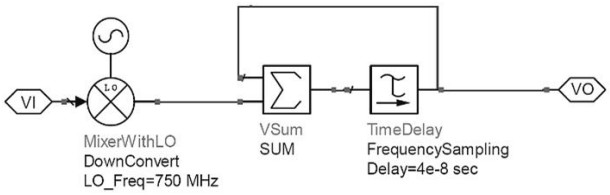

Fig. 10. ADS circuit for mixing and frequency sampling.

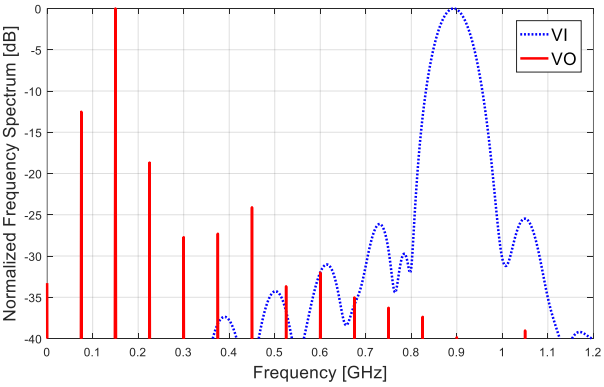

Fig. 11. ADS simulation results for mixing and frequency sampling.

After the down conversion and sampling comes filtering and comparison. For simplicity, the simulation is done for two frequency components only (i.e., 75 and 150 MHz) but the same block can be used again and again to filter all components and isolate the one with

highest amplitude. The ADS circuit used to build the block is shown in (Fig. 12) and the HB simulation results are shown in (Fig. 13). All other components were suppressed except the one with highest amplitude.

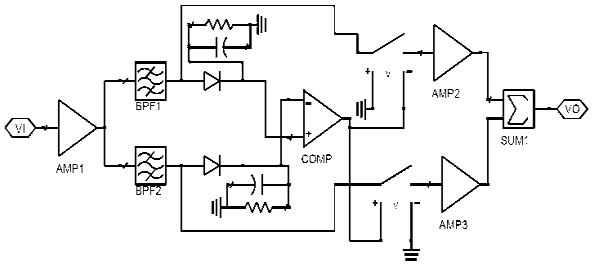

Fig. 12. ADS circuit for filtering and comparison block for two frequency components.

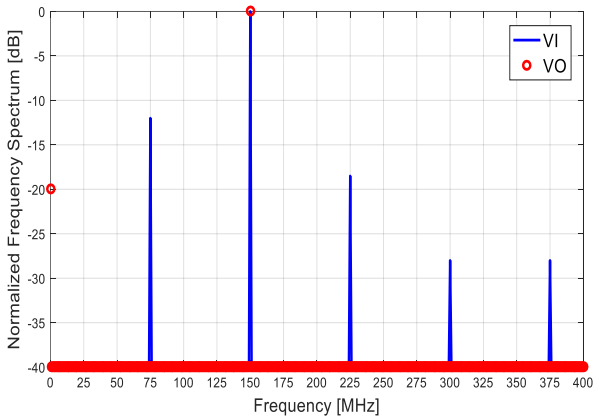

Fig. 13. ADS simulation results for filtering and comparison block.

Having the harmonic with highest amplitude isolated from the rest, it needs to be converted to a frequency proportional DC voltage. This is done by taking the input signal of VCO in PLL circuit. Figure 14 and (Fig. 15) show the PLL circuit in ADS and the PLL characteristics (i.e., DC vs frequency) respectively.

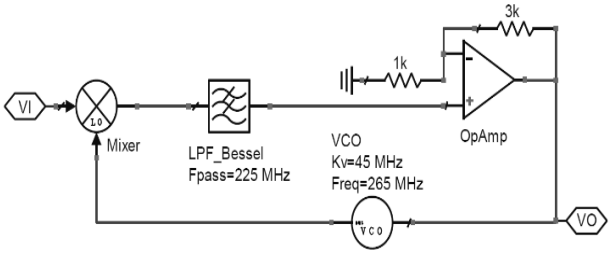

Fig. 14. ADS circuit PLL.

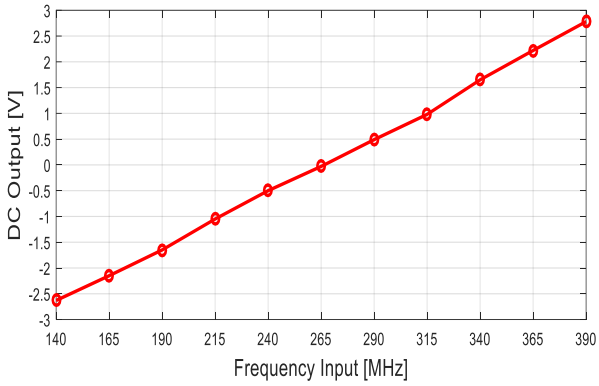

Fig. 15. PLL characteristics.

C. Transmitting antenna array results

The DC voltage is feed to set of DC varactor-based reflection phase shifters [14] that have phase characteristics (phase vs DC) similar to transmission lines characteristics (phase vs frequency) with the DC linked to frequency by PLL curve in (Fig. 15). Figure 16 shows the ADS circuit for phase shifter while (Fig. 17) shows its characteristics.

Based on the characteristics, connecting two phase shifters in series is equivalent to one transmission line phase shift in (2). Therefore, for the first antenna we need two phase shifters and the second we need four and so on. Having the phase shifters designed and tuned, the transmitter circuit is constructed in ADS as in (Fig. 18) it should be noted that the source at the port is independent of the received signal.

Using such circuit, HB simulation was performed at 1GHz (the transmitted signal frequency). The resulting transmission radiation pattern as compared to the reception radiation pattern is shown in (Fig. 19).

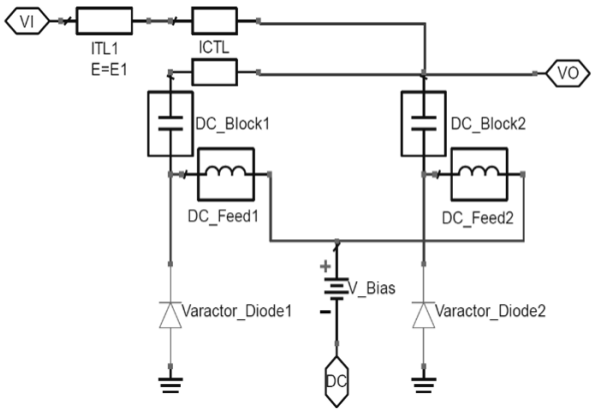

Fig. 16. ADS circuit for one phase shifter. V_Bias and E1 (electrical length) are used to control the characteristics of the phase shift.

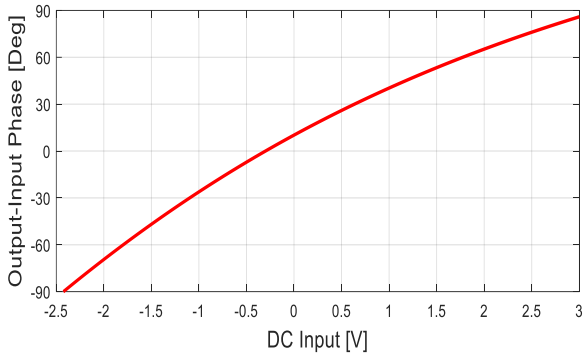

Fig. 17. Characteristics of two phase shifters connected in series.

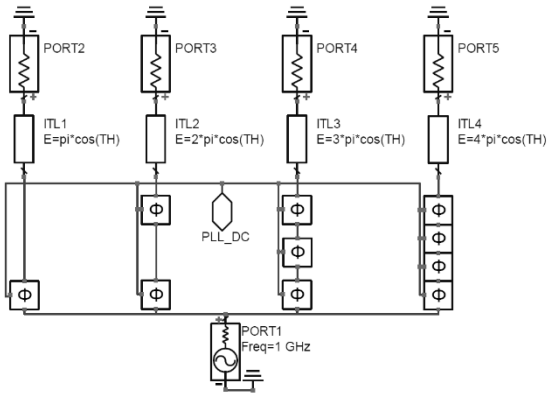

Fig. 18. ADS circuit for transmitter.

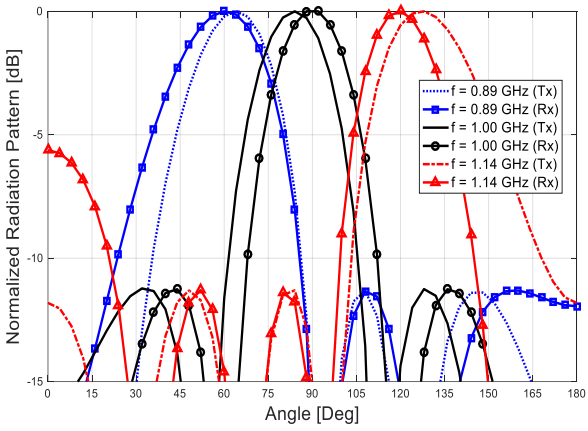

Fig. 19. Transmission (not marked) and reception (marked) radiation patterns for different directions (frequencies) of the received signal.

VI. CONCLUSION

In this paper, a new method for retrodirectivity that utilizes frequency scanning phase array antenna was presented. In detail conceptual explanation for each part of the transceiver was provided. The method was verified using ADS simulation for each part of the transceiver. The system have the ability to transmit the signal to any location other than the direction of arrival and to transmit a signal has different waveforms than the received one and have flexibility to be designed according to any specific bandwidth and that based on the operation principle required.

Future work can be made more comprehensive by using two antennas for reception, one omnidirectional antenna and one frequency scanning antenna. Dividing the two received signals from these antennas will produce a reception frequency spectrum as if the transmitted signal was uniform in frequency. This will make the system work irrespective of frequency spectrum uniformity of the received signal.

ACKNOWLEDGMENT

This work was funded by King Abdulaziz City of Science and Technology (KACST). The authors therefore, acknowledge with thanks KACST technical and financial support.

REFERENCES

[1] L. Chen, Y. C. Guo, X. W. Shi, and T. L. Zhang, "Overview on the phase conjugation techniques of the retrodirective array," *Int. J. Antennas Propag.*, vol. 2010, 2010.

[2] E. Sharp and M. Diab, "Van Atta reflector array," *IRE Trans. Antennas Propag.*, vol. 8, no. 4, pp. 436-438, 1960.

[3] S.-J. Chung and K. Chang, "A retrodirective microstrip antenna array," *IEEE Trans. Antennas Propag.*, vol. 46, no. 12, pp. 1802-1809, 1998.

[4] K. S. B. Yau, "Development of a passive retro-directive Van Atta array reflector at X-band," *2013 Int. Conf. Radar - Beyond Orthodox. New Paradig. Radar, RADAR*, pp. 398-402, 2013.

[5] S. C. Yen and T. H. Chu, "A retro-directive antenna array with phase conjugation circuit using sub-harmonically injection-locked self-oscillating mixers," *IEEE Trans. Antennas Propag.*, vol. 52, no. 1, pp. 154-164, 2004.

[6] C. Wu and Y. Guan, "The design of phase conjugation mixer in retro-directive antenna array," *2014 Int. Conf. Comput. Intell. Commun. Networks*, pp. 112-115, 2014.

[7] P. D. H. Re, S. K. Podilchak, S. Rotenberg, G. Goussetis, and J. Lee, "Retrodirective antenna array for circularly polarized wireless power transmission," *2017 11th Eur. Conf. Antennas Propag.*, pp. 891-895, 2017.

[8] S. Nusenu, "Development of frequency modulated array antennas for millimeter-wave communications," *Wiley Hindawi, Wireless Communications*

and Mobile Computing, 2019.

[9] M. Kim, T. Gu, and H. G. Ryu, "Design and Mobile Tracking Performance of a Retro-Directive Array (RDA) Antenna System," *Lecture Notes of the Institute for Computer Sciences, Social Informatics and Telecommunications Engineering*, vol. 306, Springer, Cham, 2019.

[10] M. Alibakhshikenari, B. S. Virdee, A. Andújar, J. Anguera, and E. Limiti, "Frequency beam steering antenna for millimeter wave checkpoint scanners," pp. 1238-1240, 2017.

[11] M. Ettorre, W. A. Alomar, and A. Grbic, "Radiative wireless power transfer system using wideband, wideangle slot arrays," *IEEE Transactions on Antennas and Propagation*, vol. 65, 2017.

[12] F. T. Ulaby, *Fundamentals of Applied Electromagnetics*, Media, To Robbins, 2004.

[13] C. L. Phillips, J. M. Parr, and E. A. Riskin, *Signals, Systems and Transforms*, Fourth. Pearson, pp. 231-236, 2008.

[14] Microwaves101, "Varactor Phase Shifters." [Online]. Available: https://www.microwaves101.com/encyclopedias/varactor-phase-shifters [Accessed: 07-May-2019].

Mohammed Aseeri is currently an Associate Professor at King Abdulaziz City for Science and Technology (KACST), National Centre for Telecommunications and Defense Systems Technologies (TDST) and Co-PI at Center of Excellence for Microwave Sensor Technology (CMST) in a joint project between KACST and University of Michigan (UoM) at USA. His Ph.D. in Electronics from the University of Kent, Canterbury, England. He has participated as a Researcher at the Australian National University (ANU in Australia.

Waleed Alomar received the B.Sc. degree in Electrical Engineering with First Honors from King Saud University, Riyadh, SA, in 2005. He received his master degree in Electrical Engineering, his master degree in Applied Economic and his Ph.D. in Electrical Engineering from University of Michigan, US. He is working as Director and Assistant Prof. for the Center of Microwave Sensor Technology at KACST, Saudi Arabia.

Hamad Alotaibi received the B.Sc. degree in Electrical Engineering with First Honors from King Fahd University of Petroleum and Minerals, Dhahran, Saudi Arabia, in 2017. Since January 2018, he has been working as a Researcher for the Center of Microwave Sensor Technology at King Abdulaziz City for Science and Technology, Riyadh, Saudi Arabia.

Abdulrahman Aljurbua received the B.Sc. degree in Electrical Engineering with First Honors from King Fahd University of Petroleum and Minerals, Dhahran, Saudi Arabia, in 2017. Since August 2017, he has been working as a Researcher for the Center of Microwave Sensor Technology at KACST, Saudi Arabia.

Near-field BER and EVM Measurement at 5.8 GHz in Mode-stirred Metal Enclosure

Mir Lodro, Chris Smart, Gabriele Gradoni, Ana Vukovic Dave Thomas, and Steve Greedy

George Green Institute for Electromagnetics Research-GGIEMR
University of Nottingham, University Park, NG72RD, United Kingdom
mir.lodro@nottingham.ac.uk

Abstract – This work presents over-the-air (OTA) performance, near-field bit-error-ratio (BER), and error vector magnitude (EVM) measurement using software-defined radio (SDR) in the mode-stirred metal enclosure at 5.8 GHz. The metal enclosure is stirred at 5.8 GHz using metallic paddle rotating with uniform speed. Paddle rotation creates a uniform electromagnetic field in the metal enclosure. The electromagnetic field environment in the metal enclosure can be controlled by loading the cavity with absorbing material. Field absorption can be different depending on the amount of absorbing material and location of the absorbers in the metal enclosure. It is shown that signal attenuation increases as we increase the number of absorbers. BER and EVM are measured in this environment and the performance of SDR based digital receiver is analyzed in this environment at RF frequency of 5.8 GHz.

Index Terms – BER, EVM, Metal Enclosure, OTA Measurements, Reverberation Chamber, SDR, USRP B210.

I. INTRODUCTION

The metal enclosure is a perfectly reflecting environment and when stirred with mode-stirrer it acts as a small reverberation chamber (RC). This environment exhibits a rich isotropic multipath fading environment. It's suitable for testing for wireless communication systems. Reverberation chambers of various sizes have been traditionally used for electromagnetic compatibility and electromagnetic interference analysis, however, it has also been used for the testing of wireless communication system [1]. One or two mode-stirrers have been used to create multipath fading. With adequate stirring and the number of absorbers multipath fading can be controlled inside the chamber [2]. Reverberation chambers are also used for testing of antennas for determining the total radiation efficiency [3], radiated power [4], antenna efficiency [3, 5], backscattering measurement [6], diversity gain [7] and total isotropic sensitivity measurement [8]. BER measurements are performed in the reverberation chamber in [1]. Different techniques to create a specific multipath fading environment are present in the literature. SDR based measurements and SDR based testing of antennas are presented in [9] and [10, 11] respectively. RC has been used to test more sophisticated communication systems for throughput measurements [12]. We tested QPSK receiver in an anechoic chamber with USRP X310 and measured BER and OTA performance under different noise levels [13, 14]. This article is divided into five sections. After the introduction in Section I, Section II highlights the importance of near-field measurements, Section III explains transmitter and receiver baseband models. Section IV details the near-field measurement setup in the mode-stirred cavity. Section V shows measurement results. Section VI presents the conclusion and future aspect of this work.

II. NEAR-FIELD MEASUREMENTS

Near-field measurements are becoming popular as the generated traffic volume and the demand for high data rate transmission has grown manifolds. This has led to the quest for the design, development, and integration of high data rate short-range wireless communication in the near-field. The potential applications are in 5G/6G dense connectivity [15–17], server racks and wireless chip-to-chip communication or board-to-board communication [18]. The existing form of near-field communication takes place using inductive and capacitive coupling for contactless payment and short-distance smart readers for low-rate applications. However, it's not a feasible solution for applications that are area-constraint and require high transmission rates such as wireless inter-core communication and wireless chip-to-chip communication [19]. RF communica-

Submitted On: April 10, 2020
Accepted On: May 26, 2020

https://doi.org/10.47037/2020.ACES.J.350915

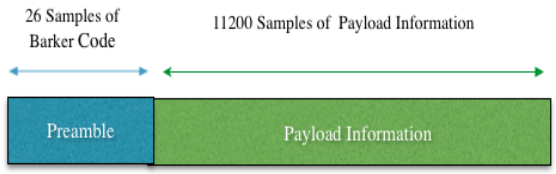

Fig. 1. Frame format of QPSK receiver.

tion using monopoles or printed patch antennas is required. Radiation boundary around antennas is classified in three regions as reactive near-field, radiative near-field, and far-field [20]. These fields are proportional to antenna dimension D and the operating wavelength of λ. Hence the reactive near-field:

$$Near - field = 0.62\sqrt{\frac{D^3}{\lambda}}. \quad (1)$$

For antenna dimension, $D = 8cm$, the near-field boundary in our case starts at $6cm$. However, the distance d between transmit and receive monopoles is around $5cm$ which is below the near-field boundary of $6cm$.

III. TRANSMITTER AND RECEIVER BASEBAND MODEL

A. Transmitter baseband model

QPSK transmitter consists of bits generation, QPSK modulation, and root raised cosine transmitter filter. Bits generation block generates frames of sample size 11226×1. Each frame consists on payload and preamble as shown in Fig. 1. The payload is useful data which is 100 'Hello World' messages. The payload is scrambled to create an equal number of ones and zeros. Scrambling is helpful for timing recovery at the receiver. The preamble is created by using a 13-bit Barker code, and it is oversampled by a factor of two. Barker code exhibits excellent correlation properties, hence it's suitable for frame detection. Scrambled bits produced by bits generation block are QPSK modulated. The modulated symbols are upsampled by raised cosine transmit filter with pulse shaping factor of 0.35. Raised cosine transmit filter produces samples at the rate of 400 kbps. These samples are transferred to B210 USRP from host PC over USB3.0 cable and after RF upconversion, signals are transmitted over the air.

B. Receiver baseband model

The receiver design is more challenging than the transmitter since multipath fading introduces signal attenuation, phase-shift, and delay in the transmitted signal. The received signal is not only affected by fading in the channel but other hardware imperfections at the transmitter and receiver including power amplifier non-linearity and filtering-imperfections. This signifies the complexity of wireless communication receiver design. Hence, the QPSK receiver consists of automatic gain control (AGC) which stabilizes weak signal amplitude as it's important for optimum loop design for carrier symbol synchronization. AGC stabilizes the input signal to a constant level for subsequent stages in the QPSK receiver. Raised cosine receive filter performs matched filtering with the pulse-shaping factor of 0.35. Synchronization is vital for the optimal performance of the wireless receiver. Frequency and timing synchronization can be performed by using external 10 MHz reference (REF) and 1 pulse-per-second (PPS) timing signal from Octoclock-G or it can be performed using digital receiver blocks in the baseband model at host PC. We used digital synchronization stages to compensate for any frequency and timing offset. Hence, the QPSK receiver employs different synchronization stages such as coarse frequency compensation, symbol synchronization, carrier synchronization, and frame synchronization followed by the data decoding stage. Synchronization techniques for digital receiver design are discussed in [21–24].

1. *Coarse Frequency Compensation*: This stage of the digital receiver produces a rough estimate of frequency offset. This works on averaging of the output of the correlation-based algorithm. There is still a residual frequency offset present. The performance and accuracy of this stage are affected by the maximum frequency offset. Following coarse frequency compensation timing recovery and fine frequency compensation is performed.

2. *Symbol Synchronization*: Symbol synchronization performs timing recovery based on Gardner's time-invariant algorithm. Timing recovery is achieved using PLL which is defined by normalized loop bandwidth, damping factor, and detector gain. Critically damped PLL locks quickly to correct symbol timing and hence introduces little *timing jitter*.

3. *Fine Carrier Synchronization*: This stage compensates the residual frequency offset present in the signal that was not compensated by the coarse frequency compensation stage. This stage uses PLL which tracks the residual frequency offset and phase offset in the signal. The damping factor and normalized loop bandwidth are tunable. PLL is critically damped so that it quickly locks to the intended phase while introducing little 'phase noise'.

4. *Frame Detection and Frame Synchronization*: Frame boundary detection is performed by a 13-bit Barker code that was used as preamble in the transmitted frames. Frame detection and frame alignment are done using the Barker code autocorrelation peak. The threshold designed for peak detection is critical for this block.

5. *Data Decoding*: Here phase ambiguity resolution, QPSK demodulation and payload retrieval is preformed. Phase ambiguity subsystem rotates the received signal by estimated phase offset and correct data is demodulated. Payload information is descrambled and decoding bits are converted to 'Hello World' characters visualized on diagnostic visualizer.

IV. MEASUREMENT SETUP

We have used a brass metal enclosure with dimensions of $h \times \ell \times w$ of $45\,cm \times 37\,cm \times 55\,cm$. The brass metal enclosure has a mode-stirrer whose rotation is controlled using a battery-operated motor. The metal cavity is a perfectly reflecting environment and when excited at 5.8 GHz it produces rich isotropic multipath (RIMP) fading environment. The sole purpose is to create a multipath fading environment. The Tx and Rx monopoles are in line-of-sight of each other. QPSK modulated signals are transmitted using USRP B210 which is connected to host PC over a USB cable. For parameters under consideration, there were some instances of underflow and overflow during the measurements and execution of the baseband model. USRP B210 is a low-cost RF solution for testing of wireless communication systems algorithms and RF measurements. USRPB210 is based on analog Devices AD9361 RFIC. It can operate in full-duplex 2x2 multiple-input multiple-out (MIMO) up to 56 MHz single-channel bandwidth. Figure 2 shows a measurement setup where two Tx and Rx monopoles are installed in near-field facing down in the cavity when the lid of the metal cavity is closed. The measurement setup shows mode-stirrer inside the brass cavity which stirs the electromagnetic field.

V. MEASUREMENT RESULTS

In this section, we show different measurement results recorded during the operation of the baseband model. The first component of the baseband receiver model is AGC which stabilizes the received signal and it's controlled using PLL. Figure 3 shows input to AGC and the stabilized signal with PLL step size. It's shown that PLL locks quickly when step size is increased from 0.001 to 0.01. Additionally, there could be a frequency offset present between transmitter and receiver. In Fig. 4 top plot shows frequency offset and the bottom plot shows mean frequency offset estimated at the receiver. This frequency offset can be compensated separately using separate baseband Tx and Rx models and subsequently removed at the receiver. Subsequent stages of the receiver include symbol timing error. Figure 5 shows timing error at the receiver. It can be seen that the timing errors are dominant at the start of the receiver. There are no timing errors after the SDR system has stabilized. Similarly Fig. 6 shows timing error recovery which struggles when there is low Tx gain.

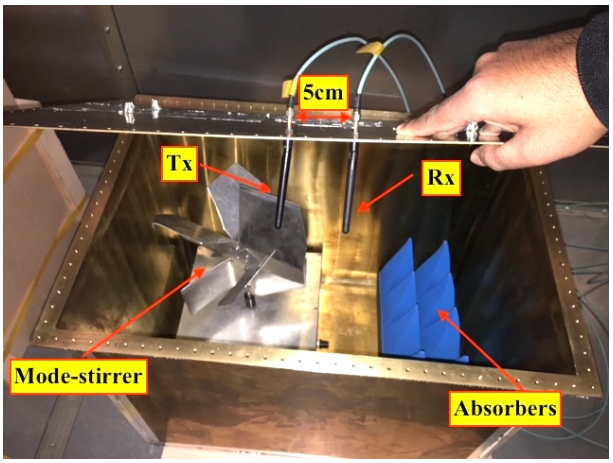

Fig. 2. SDR based near-field EVM and BER measurement setup in metal enclosure.

Table 1: System design parameters

Parameter	**Values**
Frequency	$5.8GHz$
Tx/Rx Antenna	Monopoles
Symbol Time	$5\mu s$
Sample Rate	$400KHz$
Payload Length	11200
Header Length	26
Message Bits	11200
Frame Time	$0.0281s$
Filter Order	10
Roll-off	0.35
USRP Frame Length	11226
USRP Interpolation Factor	50

Figure 7 shows detection metric for each received frame. This frame detection metric used to correctly decode the received frame if the metric exceeds a designed threshold. Figure 8 shows autocorrelation of full-frame which has a peak at 26th sample in the received frames which signifies the availability of Barker code based header of length 26.

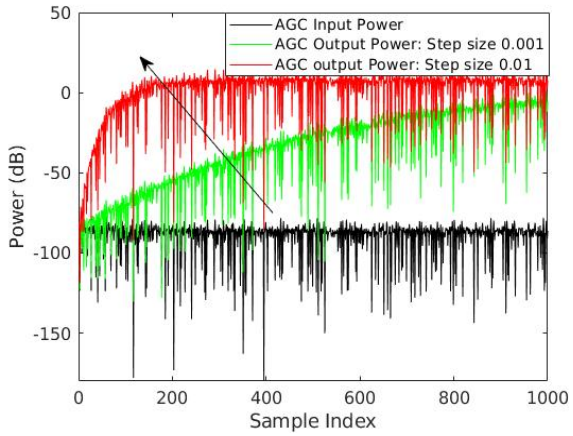

Fig. 3. Input and output of AGC with step size of 0.01 and 0.001 respectively.

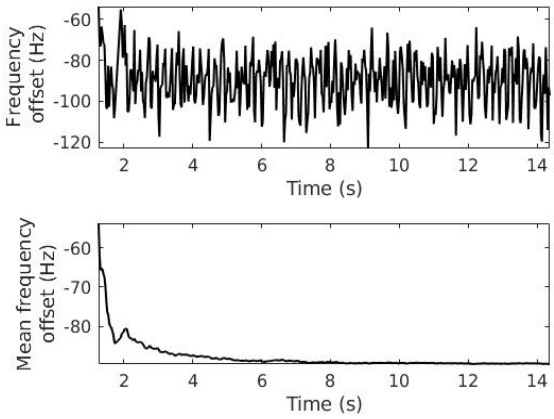

Fig. 4. Frequency offset and mean frequency offset estimation in (Hz).

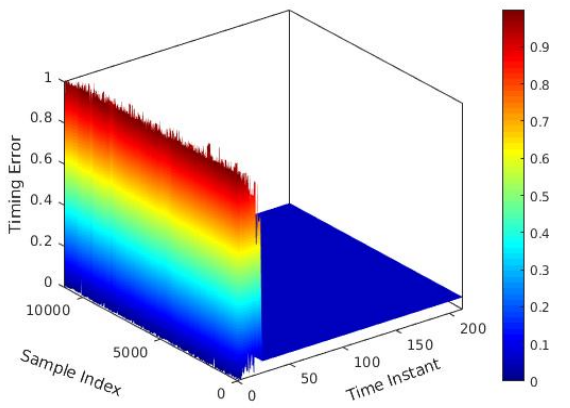

Fig. 5. Symbol timing error.

Figure 9 shows the diagram for the measurement of phase angle for phase ambiguity resolution. The output of the phase offset estimator subsystem that's used to correct phase ambiguity resolution of

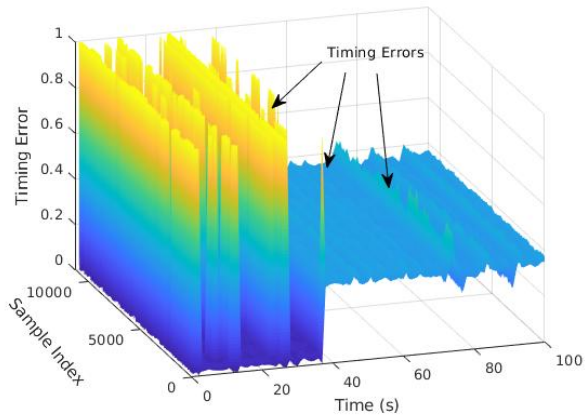

Fig. 6. Timing errors in the near-field at 5.8 GHz when Tx gain was 54 dB.

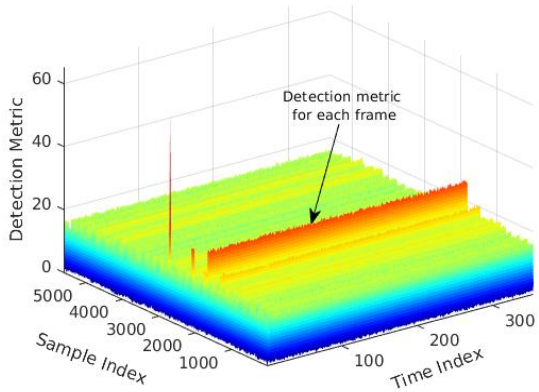

Fig. 7. Detection metric for each received frame.

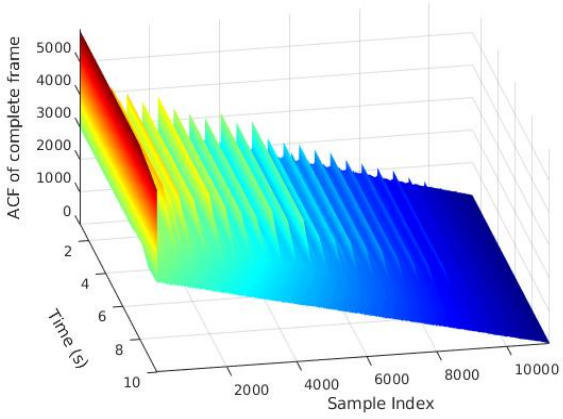

Fig. 8. Autocorrelation of full frame.

the QPSK system for data decoding is shown in Fig. 10.

Additionally, there were timing errors at low transmit gains and the QPSK constellation diagram converted into a blob of noise from ideal constella-

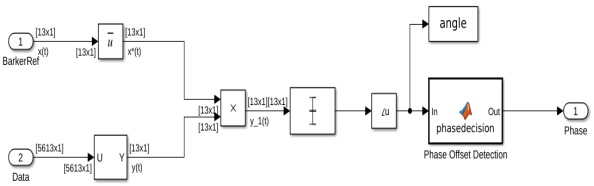

Fig. 9. Phase angle estimate block diagram.

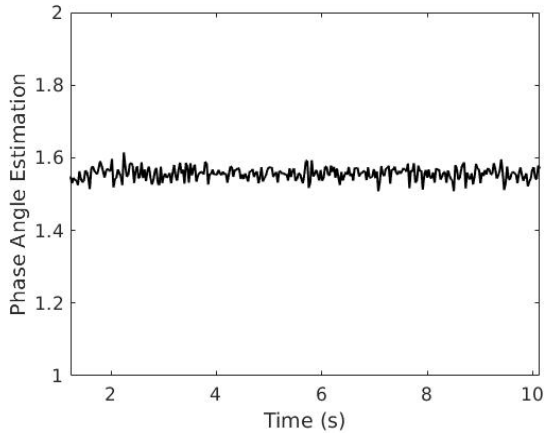

Fig. 10. Phase angle estimate for phase ambiguity resolution.

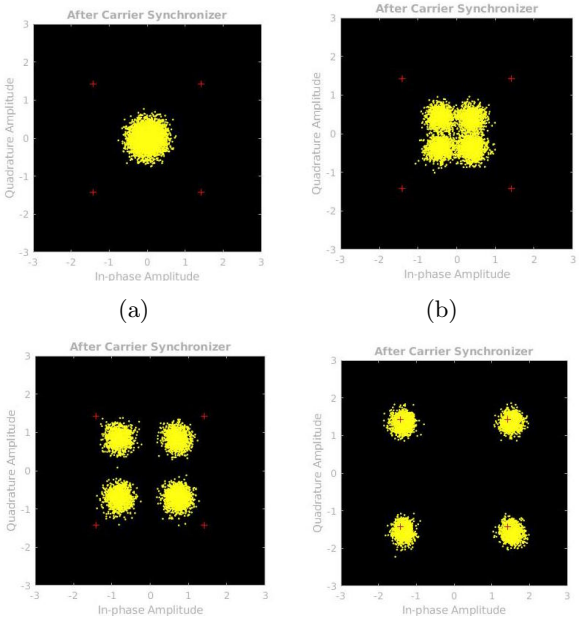

Fig. 11. QPSK constellation diagram at low Tx gains.

tion points and re-emerged smoothly to attain lock at ideal constellation diagram as shown in Fig. 11. The smashing and re-emergence of constellation diagram was continuously observed. This was consistent with the timing errors as shown in Fig. 5.

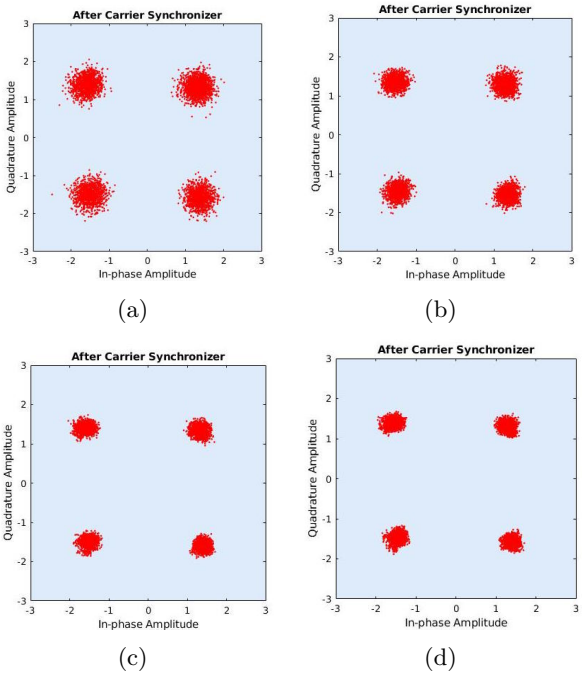

Fig. 12. QPSK constellation diagram after carrier synchronization: (a) Tx Gain=30 dB, EVM=16%, (b) Tx Gain=35 dB, EVM=12%, (c) Tx Gain=40 dB, EVM=11%, and (d) Tx Gain=45 dB, EVM=10%.

Figure 13 shows cross-correlation of 500 received packets with Barker code. A peak is observed at every 26th sample in the packet which is header length corresponds to 13-bit Barker code oversampled by a factor of 2.

A. EVM measurements

It's Euclidean distance between ideal constellation point and the received constellation points in IQ plane. Figure 12 shows a constellation diagram and corresponding measured EVM when the Tx gain was varied from 30 dB to 45 dB with a step size of 5 dB. With an increase in Tx gain hence an increase in SNR, the received QPSK samples get concentrated around ideal QPSK symbols. Such an increase in SNR also results in a decrease in EVM magnitude. It can be seen from Fig. 12 that EVM has decreased from 16% to 10%. Further increase in EVM is not observed in the current receiver structure because of the increased noise floor no matter how large we increase the gain. This behavior was observed in the far-field in large reverberation chamber under different fading conditions and indoor laboratory environments as well. Figure 14 shows instantaneous EVM in percent of QPSK at five runs. The EVM remains constant at around 11% EVM.

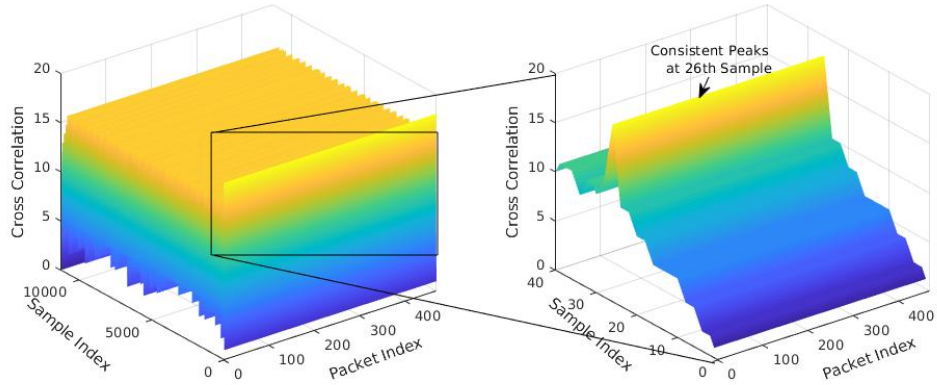

Fig. 13. Cross correlation of full frame and Barker code.

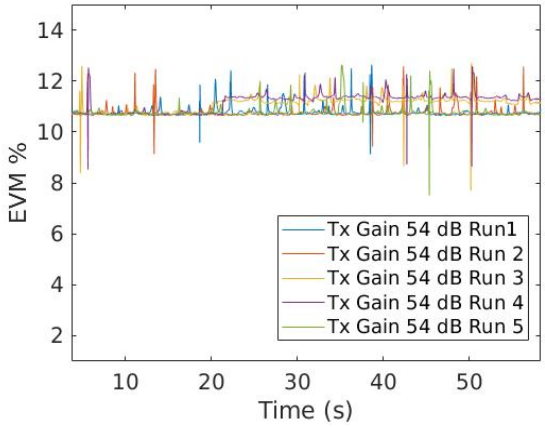

Fig. 14. EVM in the near-field at five runs when Tx gain is set to 54 dB.

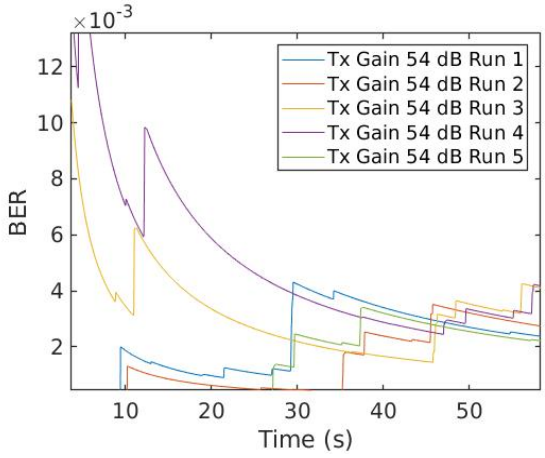

Fig. 15. BER measurements.

B. BER measurements

BER is one of the key performance indicators of digital communication systems, where the transmitted bits are compared with the received bits. If a large number of bits are erroneously received then the system has high BER, however, this is compensated by different receiver design stages as mentioned in previous sections. BER measurement is shown in Fig. 15. It can be seen that the BER at instants is very small and then there are transitions in BER curves. BER decreases at every run and it suddenly increases and then decreases. This is consistent with underflow and overflow in the system model. Underflow and overflow is an important issue for sensitive BER measurements using SDR. There could be other potential reasons to mention the degradation of BER. Shielding ineffectiveness of RF daughter boards in SDRs. The BER measurements are affected when the measurements are performed when Tx and Rx are located on the same RF cards. Variation in BER pattern can also be attributed to near-field effect or failure and instant recovery of one of the stages of the digital receiver including PLL based loops in carrier phase synchronization and timing recovery.

VI. CONCLUSION AND FUTURE WORK

In this work, we have shown the OTA performance of the digital receiver in near-field in a mode-stirred metal enclosure. The performance of different stages of the digital receiver is checked in the mode-stirred metal cavity. We measured AGC performance, frequency offset, timing error, and frame detection metrics of the digital receiver in the near-field. We observed that degradation factors of complete wireless communication system key performance indicators (KPIs) can be attributed to proper PLL design in the AGC, timing recovery, Tx/Rx gains, frame detection metrics. We performed BER measurement in the metal enclosure and enlisted possible BER degradation factors and

suggested ways to overcome BER degradation factors. The future aspect of this study is to optimize BER and EVM measurements using meta-surface based Large Intelligent Surface (LIS) structures.

REFERENCES

[1] E. Genender, C. L. Holloway, K. A. Remley, J. M. Ladbury, G. Koepke, and H. Garbe, "Simulating the multipath channel with a reverberation chamber: Application to bit error rate measurements," *IEEE Transactions on Electromagnetic Compatibility*, vol. 52, no. 4, pp. 766–777, 2010.

[2] E. Genender, C. Holloway, K. Remley, J. Ladbury, G. Koepke, and H. Garbe, "Use of reverberation chamber to simulate the power delay profile of a wireless environment," in *2008 International Symposium on Electromagnetic Compatibility-EMC Europe*, pp. 1–6, IEEE, 2008.

[3] C. L. Holloway, H. A. Shah, R. J. Pirkl, W. F. Young, D. A. Hill, and J. Ladbury, "Reverberation chamber techniques for determining the radiation and total efficiency of antennas," *IEEE Transactions on Antennas and Propagation*, vol. 60, no. 4, pp. 1758–1770, 2012.

[4] G. Koepke and J. Ladbury, "Radiated power measurements in reverberation chambers," in *56th ARFTG Conference Digest*, vol. 38, pp. 1–7, IEEE, 2000.

[5] H. G. Krauthäuser and M. Herbrig, "Yet another antenna efficiency measurement method in reverberation chambers," in *2010 IEEE International Symposium on Electromagnetic Compatibility*, pp. 536–540, IEEE, 2010.

[6] A. Sorrentino, G. Ferrara, M. Migliaccio, and S. Cappa, "Measurements of backscattering from a dihedral corner in a reverberating chamber," *Newsletter-Applied Computational Electromanetic Society*, vol. 33, pp. 91–94, 2018.

[7] K. Rosengren and P.-S. Kildal, "Radiation efficiency, correlation, diversity gain and capacity of a six-monopole antenna array for a MIMO system: Theory, simulation and measurement in reverberation chamber," *IEE Proceedings-Microwaves, Antennas and Propagation*, vol. 152, no. 1, pp. 7–16, 2005.

[8] C. Orlenius, P.-S. Kildal, and G. Poilasne, "Measurements of total isotropic sensitivity and average fading sensitivity of CDMA phones in reverberation chamber," in *2005 IEEE Antennas and Propagation Society International Symposium*, vol. 1, pp. 409–412, IEEE, 2005.

[9] A. Hussain, B. P. Einarsson, and P.-S. Kildal, "Mimo ota testing of communication system using sdrs in reverberation chamber [measurements corner]," *IEEE Antennas and Propagation Magazine*, vol. 57, no. 2, pp. 44–53, 2015.

[10] A. Hussain, A. A. Glazunov, B. . Einarsson, and P.-S. Kildal, "Antenna measurements in reverberation chamber using USRP," *IEEE Transactions on Antennas and Propagation*, vol. 64, no. 3, pp. 1152–1157, 2016.

[11] P. Nayeri and R. L. Haupt, "A testbed for adaptive beamforming with software defined radio arrays," in *2016 IEEE/ACES International Conference on Wireless Information Technology and Systems (ICWITS) and Applied Computational Electromagnetics (ACES)*, pp. 1–2, IEEE, 2016.

[12] N. Olano, C. Orlenius, K. Ishimiya, and Z. Ying, "WLAN MIMO throughput test in reverberation chamber," in *2008 IEEE Antennas and Propagation Society International Symposium*, pp. 1–4, IEEE, 2008.

[13] M. Lodro, C. Smartt, I. Maricar, A. Vukovic, D. Thomas, and S. Greedy, "BER measurement and OTA performance of QPSK receiver in an anechoic chamber," 2018.

[14] M. Lodro, "BER measurements and RF performance of digital wireless communication systems using USRP X310," *Measurements*, p. 1/40, 2018.

[15] A. Costanzo and D. Masotti, "Energizing 5G: Near-and far-field wireless energy and data trantransfer as an enabling technology for the 5G IoT," *IEEE Microwave Magazine*, vol. 18, no. 3, pp. 125–136, 2017.

[16] Z. Zhang, Y. Xiao, Z. Ma, M. Xiao, Z. Ding, X. Lei, G. K. Karagiannidis, and P. Fan, "6G wireless networks: Vision, requirements, architecture, and key technologies," *IEEE Vehicular Technology Magazine*, vol. 14, no. 3, pp. 28–41, 2019.

[17] W. Saad, M. Bennis, and M. Chen, "A vision of 6G wireless systems: Applications, trends, technologies, and open research problems," *IEEE Network*, 2019.

[18] J. Karedal, A. P. Singh, F. Tufvesson, and A. F. Molisch, "Characterization of a computer board-to-board ultra-wideband channel," *IEEE Communications Letters*, vol. 11, no. 6, pp. 468–470, 2007.

[19] H. Yordanov and P. Russer, "Wireless inter-chip and intra-chip communication," in *2009 European Microwave Conference (EuMC)*, pp. 145–148, IEEE, 2009.

[20] C. A. Balanis, *Antenna Theory: Analysis and Design*, John Wiley & Sons, 2016.

[21] U. Mengali, *Synchronization Techniques for Digital Receivers*, Springer Science & Business Media, 2013.

[22] R. W. Stewart, K. W. Barlee, D. S. Atkinson, and L. H. Crockett, *Software Defined Radio Using MATLAB & Simulink and the RTL-SDR*, Strathclyde Academic Media, 2015.

[23] M. Rice, *Digital communications: A Discrete-time Approach*, Pearson Education India, 2009.

[24] H. Meyr, M. Moeneclaey, and S. A. Fechtel, *Digital Communication Receivers: Synchronization, Channel Estimation, and Signal Processing*, Wiley Online Library, 1998.

Mir Lodro is a Ph.D. student at George Green Institute for Electromagnetics Research-GGIEMR, University of Nottingham, UK. He has received a Master of Research-MRes in Electrical and Electronic Engineering from the same university in 2015. His areas of research interests are SDR based prototype development for channel measurements and modeling, wireless digital receiver design, reverberation chamber based measurements, channel modeling for short-range wireless communication such as wireless chip-to-chip communication, MIMO measurements, Large Intelligent Surface (LIS), 5G/6G wireless communication.

Chris Smart has received his MEng. and Ph.D. degrees in Electrical and Electronic Engineering from the University of Nottingham in 1991 ans 1995 respectively. Following two years working as a Research Assistant at the University of Nottingham, he joined BAE SYSTEMS where he worked on 2D and 3D full field time domain techniques for electromagnetic field simulation for aerospace applications. In 2007 he re-joined the George Green Institute for Electromagnetics Research at the University of Nottingham as a Research Fellow where his research interests include the development and application of computational electromagnetics methods and the development techniques for time domain measurement of electromagnetic field including near-field methods, with applications to EMC and EMI studies.

Gabriele Gradoni received the Ph.D. degree in electromagnetics from the Università Politecnica Delle Marche, Ancona, Italy, in 2010. In 2008, he was a Visiting Researcher with the Time, Quantum Electromagnetics Team, National Physical Laboratory, Teddington, U.K. From 2010 to 2013, he was a Research Associate with the Institute for Research in Electronics and Applied Physics,University of Maryland, College Park, MD, USA.From 2013 to 2016, he was a Research Fellow with the School of Mathematical Sciences, University of Nottingham, U.K. Since 2016, he has been an Associate Professor of mathematics and electrical engineering with the University of Nottingham. His research activity is in probabilistic and asymptotics methods for propagation in complex wave systems, wave chaos, and MIMO wireless systems. He is a member of the American Physical Society and the Italian Electromagnetics Society. He was a recipient of the URSI Commission B Young Scientist Award in 2010 and 2016, and the Gaetano Latmiral Prize in 2015. Since 2014, he has been the URSI Commission E Early Career Representative.

Ana Vukovic was born in Nis, Serbia, in 1968. She received the Diploma of Engineering degree in electronics and telecommunications from the University of Nis, Nis, Yugoslavia, in 1992 and the Ph.D. degree from the University of Nottingham, UK in 2000. From 1992 to 2001, she was a Research Associate with the University of Nottingham. In 2001, she joined the School of Electrical and Electronic Engineering, University of Nottingham, as a Lecturer. Her research interests are electromagnetics with a particular emphasis on applications in optoelectronics, microwaves and EMC.

Dave Thomas is a Professor of Electromagnetics Apllications and Director of The George Green Institute for Electromagnetics Research, The University of Nottingham, UK. His research interests are in electromagnetics compatibility, electromagnetics simulation, power system transients and power system protection. He is member of CIGRE and convenor for Joint Working Group C4.31 "EMC between communication circuits and power systems", Chair of COST Action IC 1407 "Advanced Characterisation and Classification of Radiated Emissions in Densely Integrated Techniques (AcCREDIT)" and member of the EMC Europe International Steering Committee.

Steve Greedy was born in Cardiff, UK. He received the MEng. and Ph.D. degrees in 1998 and 2002 from the University of Nottingham. He is an Associate Professor within George Green Institute for Electromagnetics Research. His interests are in the area of experimental and computational electromagnetics with a focus on techniques used in the study of electromagnetics compatibility and signal integrity, specifically mechanisms that impact performance of wired and wireless communication systems.

A Method Using Magnetic Eddy Current Testing for Distinguishing ID and OD Defects of Pipelines under Saturation Magnetization

Yue Long [1], Songling Huang [1*], Yang Zheng [2], Shen Wang [1], and Wei Zhao [1]

[1] State Key Laboratory of Power Systems, Dept. of Electrical Engineering
Tsinghua University, Beijing, China
long-y17@mails.tsinghua.edu.cn, huangsling@mail.tsinghua.edu.cn, wangshen@mail.tsinghua.edu.cn, zhaowei@tsinghua.edu.cn

[2] Key Laboratory of Nondestructive Testing and Evaluation of AQSIQ
China Special Equipment Inspection and Research Institute, Beijing, China
zhengyangchina@126.com

Abstract ─ Distinguishing the inside (ID) and outside (OD) defect is an essential problem for the oil and gas pipeline nondestructive testing in engineering. The most widely used solution is to combine a magnetic flux leakage (MFL) section and a second section. For the strong magnetic field environment of the MFL, the second section and the MFL section are usually located at different mechanical positions, which leads to an increase in the length of the pipeline inspection gauge (PIG) and a decrease in the reliability. In this paper, a new impedance measurement method and the concept of the defect impedance angle are proposed to distinguish the ID and OD defects of pipelines under saturation magnetization, which based on the magnetic eddy current testing (MECT). The proposed ID & OD detection method can work with the MFL in the same mechanical position. Meanwhile, the proposed method also has the advantage that the discrimination criteria of the ID and OD defect keeps consistent with the classic eddy current testing (ECT). Furthermore, the robustness and sensitivity of the proposed method are discussed and verified by physical experiments.

Index Terms ─ Impedance measurement, inside and outside defects, magnetic eddy current testing, the defect impedance angle.

I. INTRODUCTION

The pipeline has been widely used in oil and gas transmission projects [1-3]. At present, the total length of oil and gas pipelines has been far more than 10^5 km in China [2,3]. The operating environment of pipelines is relatively harsh, and it is corroded by mud or seawater for a long time, which causes corrosion, and gradually forms defects under the pressure of the transported medium [4,5]. To prevent the occurrence of oil and gas leakage accidents, the pipeline inspection gauge (PIG) is developed for automated non-destructive testing (NDT) of oil and gas pipelines.

The shapes and actual structures of defects for oil and gas pipelines are complex and diverse. There are defects on the inside (ID) or outside (OD) of the pipeline wall [5-8, 10]. In different applications, the impact on the service life of the pipeline, caused by ID or OD defects, is not the same. For marine pipelines, the major cause of the pipeline accident is the ID defect, while for onshore pipelines, OD defects are the main factors threatening the safety of pipelines [7]. In addition, this distinction is essential for pipeline operators to take preventive measures inside or outside the pipeline [8]. Furthermore, it has reference value for pipeline repair work. Therefore, distinguishing the ID and OD defects of the pipeline is essential and meaningful.

For oil and gas pipelines, there are common NDT methods, such as ultrasonic testing (UT) [9], electromagnetic acoustic transducer (EMAT) [10], infrared thermography (IRT) [11], magnetic flux leakage (MFL) [12], eddy current testing (ECT) [5], etc. However, UT requires the couplant, and the inspection speed of UT and EMAT may be lower than the speed of pipeline oil and gas. IRT is more suitable for working outside the pipeline. Therefore, their applications are limited in the actual inspection project. And MFL detection has become the most widely used technology in the field of PIG due to its clear principle, low cost, simple structure and high reliability [13]. However, MFL detection is disabled to distinguish the ID and OD defects [14]. At present, the solution for the pipeline estimation typically uses a '1+1' plus-scheme, in which the MFL detection is selected as the primary unit, mainly responsible for detecting and quantifying the defects. Meanwhile, a second section is set up separately, together with the results of the MFL to distinguish the ID and OD defects. There are usually three options for the

Submitted On: October 24, 2019
Accepted On: July 5, 2020
https://doi.org/10.47037/2020.ACES.J.350916

secondary unit: ECT detection, weak magnetic flux leakage (WMFL) detection, and permanent magnetic field perturbation (PMP) detection.

MFL combined with ECT detection is the most classic method. When the coil passes the defects on the pipeline, the eddy current will be distorted, which can be used to detect defects. Because of the skin effect, it is ID defects that can be detected only by ECT [5]. If the MFL detects a defect while the ECT does not, the defect is an OD defect. Therefore, the MFL and ECT detection results can be added to determine whether it is an ID or OD defect. For example, ROSEN [7] and BARC [8] separated the MFL detection section and the shallow internal corrosion detection section, which is based on ECT. Korea Gas Corporation [15], Hagen Schempf [16] and Albert Teitsma [17] all proposed a comprehensive pipeline inspection robot, in which the detection system consists of the completely independent modules in spatial position: MFL and remote field eddy current testing (RFECT), and other modules.

MFL combined with PMP detection is the most widely used method. PMP detection is that a permanent magnet is surrounded by concentric coils for picking up magnetic field disturbance signals due to defects. The PMP theory and the PMP sensor framework for NDT were first proposed by Yanhua Sun [18]. In 2011, Sun pointed out that the identification of ID and OD defects can be achieved by PMP detection, with the addition of MFL detection [19]. By comparing with MFL detection and ECT detection, Shiwei Liu further elaborated the principle and application of PMP detection [20].

WMFL detection has been developed as one possible method for studying pipeline defects located either ID or OD the structures. Ma Yilai has found that the leakage magnetic field strength of the OD defect in WMFL is much smaller than in MFL. It is possible to distinguish ID and OD defects by combining MFL and WMFL [14]. B. Liu points out that the axial signal of WMFL detection can be used to identify the ID defect [21]. There are many ways to implement the weak magnetic field: some are in the adjacent area outside the closed magnetic circuit composed of NS poles [14], and some directly use the residual magnetism [22].

However, the above three methods have obvious shortcomings. Their principle is to make the ID defects to be detected and OD defects to be not. So, the methods must be added to the MFL detection; otherwise, the OD defects may be missed. Worse, ECT, PMP, and WMFL detection must work under unsaturation magnetization environment, because the saturation magnetization environment of MFL detection will destroy the skin effect of ECT detection and the special magnetic field environment of PMP or WMFL detection. So, the MFL section and other additional detection section are required to be in different mechanical positions. Separating the MFL section from the other detection section will significantly increase the length and costs of the detection system. More seriously, it will reduce its reliability and passing-pipe ability of PIG. How to solve the problem of distinguishing ID and OD defects under saturation magnetization is of great significance.

This paper will propose a detection method based on magnetic eddy current testing (MECT), which can work with MFL in the same mechanical position. That is to say, the proposed MECT method is capable of distinguishing between ID and OD defects in a saturated magnetization environment. It will achieve the fusion of the defect shape detection unit (MFL) and the defect position (ID or OD) detection unit, rather than two units separated by mechanical position. The structure of this paper is shown as following. Firstly, a composite electromagnetic field model is built to analyze the tiny difference between ID and OD defects on the condition of saturation magnetization. Then, one algorithm of impedance measurement based on DFT is proposed. Under the saturation magnetization, the simulation verification and experimental verification of the ID and OD defect distinguishing models are carried out. Based on the experimental results, combined with the characteristics of the ID and OD defects under saturation magnetization, the effectively distinguishing method is discussed.

II. METHODS

A. The composite electromagnetic field model

Since the axes of the coil and the pipe are orthogonal, the two-dimensional (2D) model in the cylindrical coordinate system cannot describe the distribution of the magnetic field in the vicinity of the defect well, so a three-dimensional (3D) model needs to be constructed.

Governing equations

In the conductor region, the oil and gas pipeline is made of ferromagnetic material, and its magnetic permeability μ satisfies the BH curve. In the vicinity of the defects, the different magnetic field strength makes μ not completely uniform. Simultaneously, it is assumed that the conductivity σ does not change substantially with time or space. Therefore, under saturation magnetization, the eddy current governing equation based on the A-V formulations is as follows:

$$\begin{cases} \nabla\times\left(\nabla\times\left(\dfrac{\boldsymbol{A}}{\mu}\right)\right)+\sigma\left(\nabla\dfrac{\partial V}{\partial t}+\dfrac{\partial \boldsymbol{A}}{\partial t}-\boldsymbol{v}\times\nabla\times\boldsymbol{A}\right)=0, \\ \nabla\cdot\sigma\left(\nabla\dfrac{\partial V}{\partial t}+\dfrac{\partial \boldsymbol{A}}{\partial t}-\boldsymbol{v}\times\nabla\times\boldsymbol{A}\right)=0. \end{cases} \tag{1}$$

In the air region, the conductivity σ can be regarded as 0, and the magnetic permeability μ is a constant. The eddy current equation is:

$$\nabla\times\frac{1}{\mu}\nabla\times\boldsymbol{A}=0\,. \tag{2}$$

In addition, the gauge condition of $\boldsymbol{A}$, $\nabla \cdot \boldsymbol{A} = 0$ must be considered. Where V is the time integral electric scalar potential, $\boldsymbol{A}$ is the magnetic vector potential, $\boldsymbol{J}$ is the current density, $\boldsymbol{H}$ is the magnetic field formed by the current in the specimen, $\boldsymbol{B}$ is the magnetic flux density, and $\boldsymbol{v}$ is the speed of PIG.

b. Simulation model

A 3D model is implemented using finite element software-ANSYS Maxwell, which includes PIG and the pipeline with OD or ID defects and shown in Fig. 1 (a). 2D sections of the model are shown as Figs. 1 (b),(c). The integrated probe of PIG includes the coils array for MECT detection and a Hall sensor for MFL detection. The lift-off distance of MFL and MECT is 6.5 mm from the pipe surface, and the diameter and thickness of the pipe are 223 mm and 10 mm. Defects are all cylindrical, 10 mm in diameter and 4 mm in depth. The outer diameter of the coil is 8mm, the height is 4mm, and the number of turns is 300. The pipeline has been saturated magnetized by permanent magnets with the remanence of 1.39 T, and the iron yoke is utilized to constrain magnetic lines between permanent magnets.

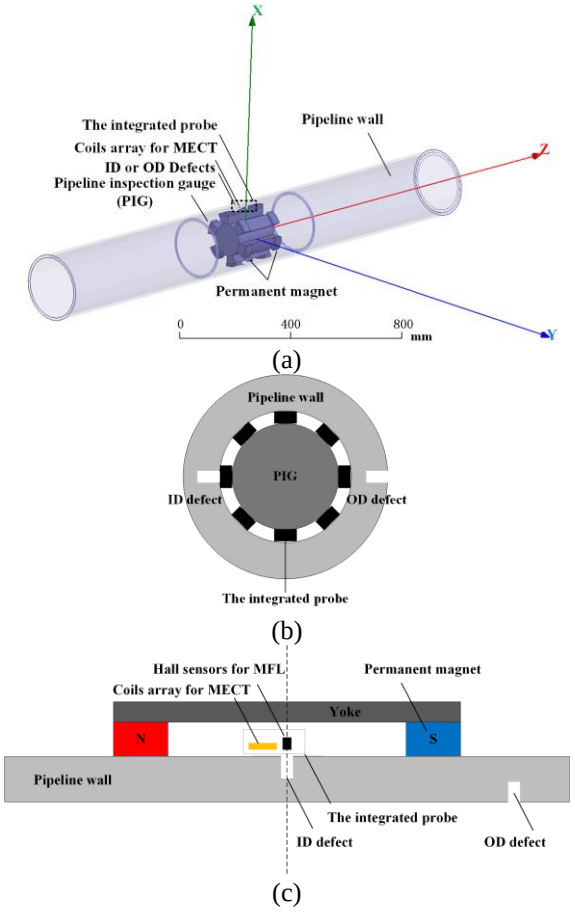

Fig. 1. The finite element model of the composite electromagnetic field model: (a) 3D model, (b) the cross-sectional view, and (c) the cutaway view.

Due to the superposition of the static magnetic field, eddy current field and motion field, a transient magnetic solver has been chosen. The excitation of coils is provided by a dual-arm differential bridge circuit, which at the same time acts as the input of phase sensitive detectors (PSD). The circuit simulation is implemented using Maxwell Circuit Editor. Essentially, it is co-simulation that combines the circuit and electromagnetic field. Furthermore, Dirichlet boundary conditions are applied to the external air model taking into account the characteristics of the composite electromagnetic field.

After inputting the field information, the initial meshing setting is required. To resolve the contradiction between the large volume of the pipe and the small volume of the defect, different grid sizes are selected in different regions. To better simulate the skin effect, the ferromagnetic material has been layered. The last thing to set is the limit of solution error and the number of iterations. In the selection of the model boundary and the initial grid, it is necessary to ensure the setting saturation, that is, when the model boundary is further extended or the initial grid is further subdivided, the result of the solution fluctuates only within an acceptable range.

B. The implementation of impedance measurement

In classical ECT under the condition of unsaturated magnetization, PSD [23-25] and complex impedance analysis [26-29] are the most useful methods to extract valid signal. PSD mainly consists of two parts: the multiplier and the low pass filter, as shown in Fig. 2. Analog multiplier can't satisfy excellent linearity and can't do a good four-quadrant operation. So, this paper has developed the digital PSD by DFT, which is easy to execute on an embedded system.

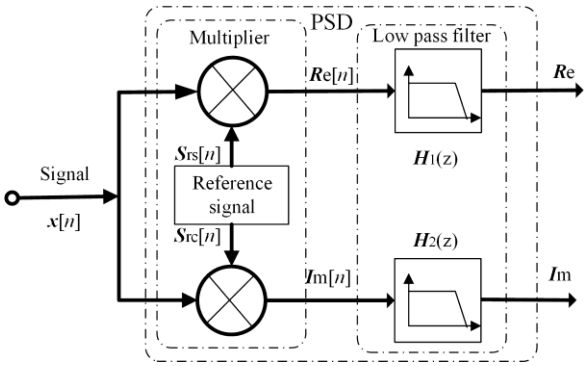

Fig. 2. A classical digital orthogonal PSD.

In a digital PSD, the signal input $x[n]$ can be sampled by ADC and assumed to the equation (3):

$$x[n] = A_0 \sin\left(\frac{2\pi n}{N} + \varphi_0\right), \tag{3}$$

where A_0, φ_0 is the amplitude and phase of the signal. N is the number of samples per cycle, related to frequency

f_0 and sample rate. n is the index of the sequence.

In the field of digital signal processing, the discrete Fourier transform (DFT) is as below:

$$X(k)=\frac{1}{M}\sum_{n=0}^{MN-1}x(n)W_N^{nk},\ W_N=\exp\left(-\mathrm{j}\frac{2\pi}{N}\right), \quad (4)$$

where N is the number of samples per period. M is the number of the period.

Taking k = 1, the conversion between complex exponents and sine and cosine can be obtained:

$$W_N^{\ nk}=\exp\left(-\mathrm{j}\frac{2\pi}{N}nk\right)\Big|_{k=1}=\cos(2\pi\frac{n}{N})+\mathrm{j}\sin(2\pi\frac{n}{N}), \quad (5)$$

where sine and cosine functions are orthogonal, and served as the reference inputs for the orthogonal PSD as the equation (6):

$$S_{\mathrm{rs}}[n]=\sin\left(\frac{2\pi n}{N}\right),\ S_{\mathrm{rc}}[n]=\cos\left(\frac{2\pi n}{N}\right). \quad (6)$$

To simplify the system and increase the speed of calculation, the reference signal $S_{\mathrm{rc}}(n)$ and $S_{\mathrm{rs}}(n)$ are discrete trigonometric function sequence with zero phase and fixed frequency that can be pre-stored in the microprocessor.

Therefore, $x(n)W_N^{nk}$ in equation (3) means that the reference signals $S_{\mathrm{rc}}(n)$ and $S_{\mathrm{rs}}(n)$ are multiplied by input signal $x(n)$. So, $x(n)W_N^{nk}$ can be equivalent to the multiplier shown in Fig. 2. The real and imaginary parts of the output are as follows:

$$R_{\mathrm{e}}(n)=\frac{A_0}{2}\left[\cos(\varphi_0)-\cos\left(\frac{4\pi n}{N}+\varphi_0\right)\right], \quad (7)$$

$$I_{\mathrm{m}}(n)=\frac{A_0}{2}\left[\sin(\varphi_0)+\sin\left(\frac{4\pi n}{N}+\varphi_0\right)\right]. \quad (8)$$

In addition, summation and averaging in equation (3) can be equivalent to the mean filter, which corresponds to the low-pass filter shown in Fig. 2. The filtered real and imaginary parts of the impedance can be obtained:

$$\begin{cases} R_{\mathrm{e}}=\mathrm{R_e}\left(X(1)\right)\approx\frac{A_0}{2}\cos(\varphi_0), \\ I_{\mathrm{m}}=\mathrm{I_m}\left(X(1)\right)\approx\frac{A_0}{2}\sin(\varphi_0). \end{cases} \quad (9)$$

The noise reduction ratio (*NRR*) for Mean filter is noticeable:

$$NRR=\frac{1}{MN}. \quad (10)$$

As a result, the digital orthogonal PSD has been designed by DFT. In the microprocessor carried by the PIG, the real-time calculation of the impedance can be realized by calculating the first-order DFT.

III. SIMULATION AND EXPERIMENTS

A. Simulation results

The results of the simulation are shown as Fig. 3, the coils have a certain magnetic concentration capability under the strong magnetic background. When the coils are directly below the non-defective pipeline wall, the magnetic fields induced by the two coils are identical. When the coils are located directly below the ID defect, the magnetic field induced by the coil aligned with the defect is greater than the other one, and the imbalance of the magnetic field induced by the two coils appears. When coils are directly below the OD defect, both coils have the relatively large induced magnetic field, and the induced magnetic field near the defect is also larger, but the imbalance is not as obvious as the situation of the ID defects. The imbalance of the induced magnetic field will cause the imbalance impedance of the two coils, which can be processed and amplified by the differential bridge circuit and PSD.

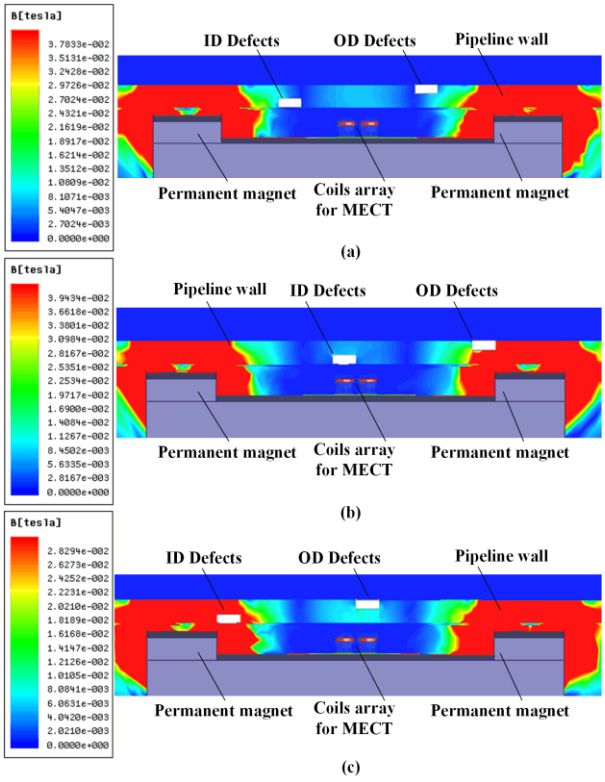

Fig. 3. A 3D finite element model of the composite electromagnetic field model: (a) coils under the pipe wall without defects; (b) coils under the ID defect; (c) coils under the OD defect.

B. The MECT system in physical experiments

The thickness of the pipe wall is 9.80 mm, while the outer diameter is 219 mm. And the size of the defects on specimen are described as Table 1 and Fig. 4 (a).

Table 1: The size of the defects on specimen

The Defects	Diameter	Depth
ID defect	8.22 mm	4.61 mm
OD defect	9.34 mm	4.50 mm

Consistent with the simulation model, the pipeline has been saturated magnetized by permanent magnets with the remanence of 1.39 T. A yoke made of magnetically permeable material is used to constrain the formation of a magnetic circuit to reduce leakage of the air magnetic field. The MFL module and MECT module are integrated together by IC design, as shown in Fig. 4 (b). The excitation of the coil and the pickup of the signal are achieved by a differential bridge circuit on the IC. The algorithm of impedance measurement based on DFT has been implemented by a digital signal proposing (DSP) on board. And the output data are stored in memory via a high speed serial bus.

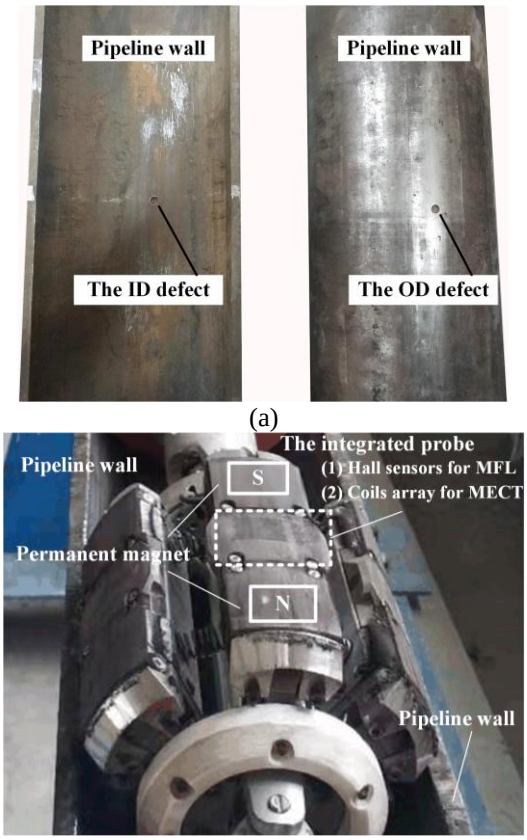

Fig. 4. (a) The semicircular pipeline specimen with an ID defect (left) or OD defect (right); (b) the MECT system.

C. The output of the differential bridge circuit

The output of a differential bridge circuit, the same as the differential input of PSD is shown as Fig. 5. When coils scan through the ID defect, the envelope of the differential signal frequency-modulated by the excitation signal exhibits the characteristics of a double wave crest and a three wave trough, while the wave crest and the wave trough are not prominent when coils scan through the OD defect. For OD and ID defects, both amplitude and phase have changed, and the degree of change is different. However, the amplitudes of the signals of OD and ID defects are similar. Worse, the magnitudes of the effective signal and noise are comparable. And it can be seen from Fig. 5 that the signal-to-noise ratio of a single variable, amplitude or phase, is not large enough to meet industrial applications. Therefore, the subsequent PSD is required to give the result with the combination between the amplitude and phase.

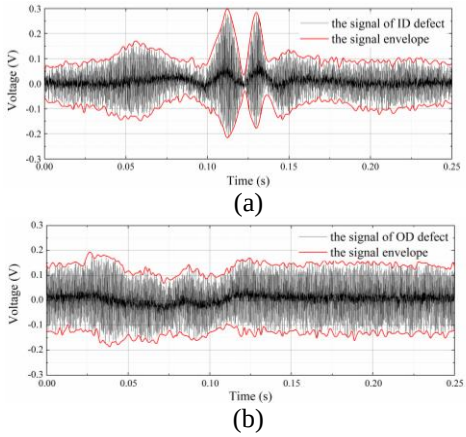

Fig. 5. The output of the differential bridge circuit: (a) when the coils sweep through ID defect; (b) when the coils sweep through OD defect.

D. The measurement result of PSD based on DFT

The driving frequency of the excitation signal is 62.5 kHz, while the sampling rate of the ADC chip is 2 MHz. The number of samples per DFT is 1024. The number of samples per cycle is 32. Each calculation takes 32 cycles.

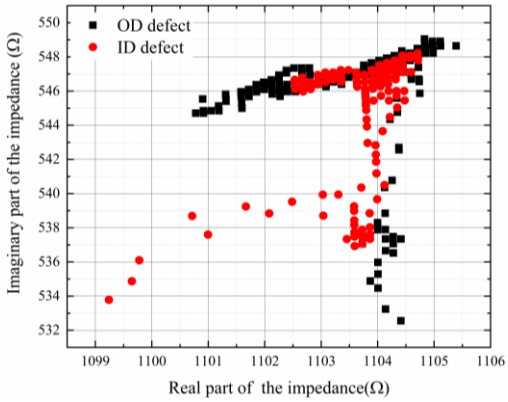

Fig. 6. The complex impedance plane of MECT detection (the pipe wall is under saturation magnetization).

When it is under the condition of saturation magnetization, the impedance feature of typical ID and OD defects is shown in Fig. 6 (a). It can be found that it is ‘T’ shape, not the shape of “8” character in classical

ECT. It can also be found that there are subtle differences included in the general similarity, in local impedance patterns of the ID and OD. When the coil passes ID defects, the main change of the impedance is the decrease of the imaginary part, which is the inductance component. But for OD defects, the resistance decreases drastically, while inductance decreases.

IV. RESULTS AND DISCUSSION

A. The computational domain

To synchronize the variables, such as the maximum, minimum, average of the impedance and so on, a computational domain is defined and can speed up calculations drastically. The computational domain is a certain amount of points near the lowest local inductance. The number of data points that can fully describe the characteristics of the complex impedance plane and maximize the calculation speed is optimal. This paper uses the closed curve of 'T'-type impedance plane as the basis for judging the optimal number of data points in the computational domain.

B. The algorithm based on the defect index for distinguishing the ID and OD defects

In Fig. 6 (a), it can be found that when the coil passes through the ID or OD defects, the inductance will decrease to a similar extent. Therefore, (I_{max} - I_{min}) can be used as a reference value. Meanwhile, (R_{Imin} - R_{ave}) is used to characterize the variation of the resistance of the coil as it passes through the defect. And the defect index is defined in the abbreviated conference version of this paper [30]. Which can use the local data to characterize the graphical features of different defects and analyze the position of defects, whether in the ID or OD:

$$\zeta_O = \frac{R_{I_{min}} - R_{ave}}{I_{max} - I_{min}}, \tag{11}$$

where I_{max} and I_{min} represent the maximum and minimum values of the imaginary part in the computational domain. R_{Imin} represents the real part value corresponding to I_{min}, while R_{ave} represents the real part of the analysis data in the computational domain.

According to the conference version of this paper, the ratio of the defect index of ID and OD is about ten times, which means that the defect index has a strong anti-interference for resolving the defect location.

C. The algorithm based on the defect impedance angle for distinguishing the ID and OD defects

This paper further considers that the ID defect impedance plane is '*T*'-type of italic while the OD is 'T'-type of the normal one. Furthermore, the angle between a horizontal and vertical cross of 'T' or '*T*' is defined as the defect impedance angle (DIA).

The horizontal cross of 'T'-type impedance plane is used as a reference value, which is more statistically significant than (I_{max}-I_{min}). The vertical cross of 'T'-type impedance plane can be characterized by the relationship between the impedance point (R_{Imin}, I_{min}) and the points of the intersection of the horizontal cross and the vertical cross. The point (R_{Imin}, I_{min}) contains information such as the depth and position of the defect, and will not change as the computational domain changes.

For the ID defect in the experiment, the specific algorithm is implemented as follows. First of all, the point (R_{Imin}, I_{min}) is found and equal to (1099.241, 533.787), and the two points of the intersection of the horizontal cross and the vertical cross are (1104.182, 546.688) and (1104.320, 546.690).

Secondly, the reference line can be described by linear regression in the horizontal cross of 'T'-type impedance plane. Using (x, y) to represent the value of the defect impedance plane, the equation of the reference line can be assumed as follows:

$$h_\theta(x) = \theta_0 + \theta_1 x. \tag{12}$$

A cost function $J(\theta_0, \theta_1)$ is set, and θ_0 and θ_1 can be obtained by finding the minimum value of cost function:

$$\underset{\theta_0,\theta_1}{\text{minimize}}\, J(\theta_0,\theta_1) = \frac{1}{2N}\sum_{i=1}^{N}\left(h_\theta(x^{(i)}) - y^{(i)}\right)^2, \tag{13}$$

where N means the number of impedance points on the horizontal cross of 'T'-type impedance plane.

Therefore, the reference line of ID defect is obtained as follow:

$$h(x) = 0.581x - 94.663. \tag{14}$$

Thirdly, combining the point (R_{Imin}, I_{min}) and the two points of the intersection of the horizontal cross and the vertical cross, the line characterizing the defect features can be obtained:

$$g(x) = 2.575x - 2297.1. \tag{15}$$

Lastly, the angle between the reference line and the defect feature line is set to DIA. This angle characterizes the "phase" information of the defect feature. DIA of the ID defect is 38.605°. The reference line, defect feature line and DIA of the ID defect are shown as Fig. 7 (a).

Through the above method, the characteristic value of the OD defect in the experiment can also be calculated. The reference line and the defect feature line of OD defect are shown as Expression (16) and Expression (17), respectively:

$$h(x) = 0.786x - 320.37, \tag{16}$$

$$g(x) = 84.7x - 93011. \tag{17}$$

Therefore, the DIA of the OD defects is 51.149°. The reference line, defect feature line and DIA of the OD defect are shown as Fig. 7 (b).

It can be seen from Fig. 7 that the DIAs of the ID and OD defects are obvious different. The DIA of the ID defect is less than 40°, while the OD defect one is greater than 40°. This result is consistent with the ASME standard for classical ECT. In ASME standard, for thin-walled non-ferromagnetic metal materials, the phase of the ID

defect is specified to 0-40 degrees and the OD one to 40-160 degrees [31]. Therefore, the ID and OD defects of the pipelines under saturation magnetization can be quickly distinguished. The advantage that the discrimination criteria of the ID and OD defect keeps consistent with the classic ECT will bring a lot of benefits, such as subsequent data processing methods for MECT can be compatible with the classic ECT method.

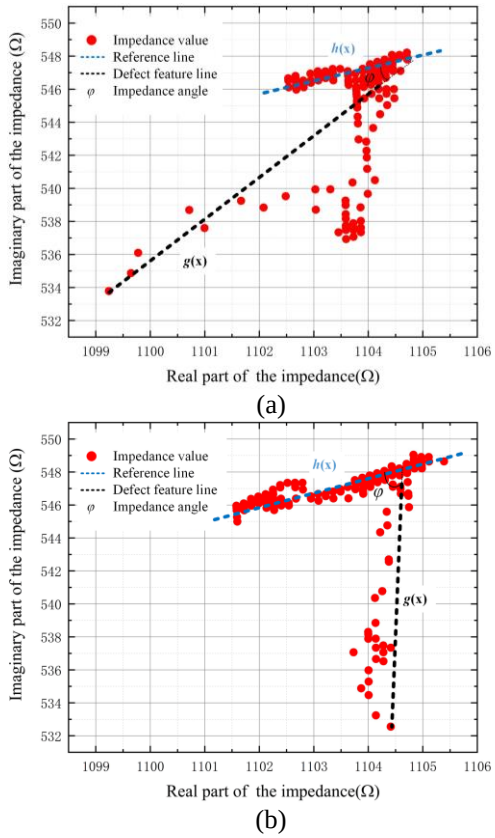

Fig. 7. The reference line, the defect feature line and the DIA: (a) ID defect and (b) OD defect.

D. The robustness of the algorithm based on the defect impedance angle

Compared with the defect index method, this method also has the advantage of being almost unaffected by the size of the computational domain. This method uses statistical methods to obtain the impedance characteristics so that the stability of the results is more robust than the independent method of the defect index method. This conclusion can be demonstrated in Table 2.

Table 2: The defect impedance angle under different computational domains

The Impedance Angle	M = 200	M = 300
ID defect	38.605°	38.545°
OD defect	51.149°	48.229°

M means the number of impedance points in the entire computational domain. Even if the size of the computational domain changes, the DIA remains essentially unchanged. The DIAs of ID defect are always less than 40 degrees, and the OD ones are greater than 40 degrees.

E. The comparison with MFL & ECT combination method

The ID & OD defects have been distinguished successfully by MECT detection. To compare with MECT, the MFL plus ECT detection [7,8] has been conducted on the pipeline specimen in Fig. 4 (a), and the experimental results of the ECT are shown in Fig. 8. It is the standard shape of "8" character as that in classical ECT, which is far different from that in MECT detection.

As shown in Fig. 8, the phase shift method is used to extract the valid signal in ECT. The detection signal is rotated in the complex impedance plane until the noise or OD defect signal coincides with the horizontal axis, so the ID defect signal is automatically separated from the horizontal axis, and it can be detected by determining whether the vertical axis component in the complex impedance plane reaches the threshold. Combined with separate MFL results, ECT can distinguish ID & OD defects. But when the pipe wall is under saturation magnetization, "T" shape in the complex impedance plane cannot be rotated coincide with the x-axis and eliminating the vertical component. Therefore, it is not possible to distinguish ID & OD defects by the amplitude of the Y-axis component. Therefore, ECT section is required to be in a different mechanical position with MFL section, which may significantly increase the costs and reduce the reliability. And MECT overcomes these shortcomings in principle.

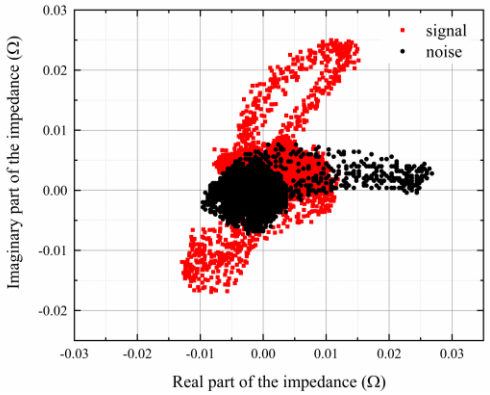

Fig. 8. The complex impedance plane of ECT detection (the specimen is under non-magnetized conditions).

In addition, due to the high permeability of ferromagnetic materials, ECT's ability to inspect pipelines is limited. The skin depth of ECT is as follow:

$$\delta = \frac{1}{\sqrt{f\pi\mu\sigma}}, \quad (18)$$

where σ and μ are the conductivity and permeability of the pipeline, f is the frequency of the excitation current in ECT. The excitation frequency f is generally 1-100 kHz, so the skin depth δ on the ferromagnetic pipeline is generally about 1 mm [28,29,32], which is much smaller than the thickness of the oil and gas pipeline wall. When the pipe wall is under saturation magnetization, the permeability μ reduces several-hundred times, and the skin depth δ will increase ten times in MECT, which covers the range of pipe thickness.

F. The sensitivity of MECT detection

Since the excitation circuit and dual-arm differential bridge circuit of MECT are analog circuits, and followed by PSD with extremely high signal-to-noise ratio, the sensitivity is mainly determined by the accuracy of the ADC and the circuit threshold of the PSD circuit.

For NDT of pipelines, the sensitivity of the inspection system is usually evaluated by the percentage of the defect depth in the thickness of the pipeline wall. To describe the sensitivity, the paper sets two extreme experiments. The paper selects a relatively shallow ID defect to test whether MECT is not sensitive enough to identify the defect and produce a missed judgment. At the same time, the paper also selected a relatively deep OD defect to test whether MECT would misjudge it as an ID defect. The geometric parameters of these two defects are shown in Table 3. And the thickness of the pipe wall D is 8 mm. The depth of ID defects is the minimum depth that needs to be detected in routine engineering inspection. The depth of the OD defect has exceeded half the thickness of the pipe wall, which is a fatal threat to the safe transmission of oil and gas, and it is very easy to be mistakenly identified as an ID defect.

The calculated impedance angle is also shown in Table 3, and it can be found that even in the low signal-to-noise ratio case (shallow ID defect or deep OD defect), MECT can still distinguish between ID and OD defects.

Table 3: The size of the defects on specimen

Defects	Diameter	Depth	Impedance Angle
ID	11.67 mm	0.135 D	30.417°
OD	8.10 mm	0.718 D	69.162°

V. CONCLUSION

Based on the problem that under the saturation magnetized condition, the MFL detection and classical ECT detection and so on cannot distinguish the ID and OD defects. This paper firstly builds a composite electromagnetic field model to analyze the infinitesimal difference between ID and OD defects on the condition of saturation magnetization by the MECT method. The implementation of impedance measurement based on DFT has been proposed to achieve MECT detection. ANSYS simulation model verified the tiny difference between ID and OD defects. The physical experiment obtained the time domain waveform and impedance plane of the coil impedance. It has been found that the impedance plane of MECT under saturation magnetization showed a 'T' shape instead of the '8' shape of the ECT under unsaturation magnetization. Furthermore, the definition and calculation method of the DIA of MECT under saturation magnetization are proposed, and the conclusion that is consistent with ECT is obtained: an ID defect with an impedance angle less than 40 degrees and an OD defect with an impedance angle greater than 40 degrees.

The experiment proves that the method has stronger robustness because it uses the statistical characteristics of the defect impedance, which has a promising significance of engineering application. The MECT method based on impedance angle has high sensitivity and can still distinguish between ID and OD defects very well in the low signal-to-noise ratio case.

Combining MECT with MFL detection, the location (in the ID or OD) and the type of defect can both be solved, which provides a comprehensive solution for the pipeline estimation. MECT can work with the MFL in the same position, which will reduce the mechanical length of the PIG and improve reliability.

ACKNOWLEDGMENT

This research was supported by the National Natural Science Foundation of China (NSFC) (No. 51677093) and the National Key Scientific Instrument Development Projects (No. 2013YQ140505).

REFERENCES

[1] J. Feng, F. Li, S. Lu, J. Liu, and D. Ma, "Injurious or non-injurious defect identification from MFL images in pipeline inspection using convolutional neural network," *IEEE Transactions on Instrumentation and Measurement*, pp. 1-10, 2017.

[2] X. Chen, Z. Wu, W. Chen, R. Kang, X. He, and Y. Miao, "Selection of key indicators for reputation loss in oil and gas pipeline failure event," *Engineering Failure Analysis*, vol. 99, pp. 69-84, 2019.

[3] J. Zhou, J. Peng, G. Liang, and T. Deng, "Layout optimization of tree-tree gas pipeline network," *Journal of Petroleum Science and Engineering*, vol. 173, pp. 666-680, 2019.

[4] A. Cosham, P. Hopkins, and K. A. Macdonald, "Best practice for the assessment of defects in pipelines–Corrosion," *Engineering Failure Analysis*, vol. 14, no. 7, pp. 1245-1265, 2007.

[5] J. Yin, M. Lu, and D. Pineda, "Full-signature real-time corrosion detection of underground casing pipes," *IEEE Transactions on Instrumentation and*

Measurement, vol. 49, pp. 120-128, 2000.

[6] R. Palanisamy and W. Lord, "Prediction of eddy current probe signal trajectories," *IEEE Transactions on Magnetics*, vol. 16, no. 5, pp. 1083-1085, 1980.

[7] T. Beuker and B. Brown, "Monitoring of top of line corrosion with eddy current technology combined with magnetic flux leakage method," *Corrosion 2010 NACE International*, 2010.

[8] D. Mukherjee, S. G. Manral, S. Chand, S. Dhage, S. Bahuguna, S. Saha, S. K. Lahiri, S. Mukhopadhyay, and A. Kumar, "Development of secondary sensor system based on eddy current technology for in-line inspection tool," *Barc Newsletter*, 2013.

[9] W. T. Peter and X. Wang, "Characterization of pipeline defect in guided-waves based inspection through matching pursuit with the optimized dictionary," *NDT & E International*, vol. 54, pp. 171-182, 2013.

[10] Z. Wang, S. Huang, Q. Wang, S. Wang, and W. Zhao, "Time of flight extraction of dispersive Lamb wave by ridge analysis," *In 2018 International Applied Computational Electromagnetics Society Symposium-China (ACES), IEEE*, pp. 1-2, 2018.

[11] S. Bagavathiappan, B. B. Lahiri, T. Saravanan, J. Philip, and T. Jayakumar, "Infrared thermography for condition monitoring - A review," *Infrared Physics & Technology*, vol. 60, no. 60, pp. 35-55, 2013.

[12] J. Chen, "3-D defect profile reconstruction from magnetic flux leakage signals in pipeline inspection using a hybrid inversion method," *Applied Computational Electromagnetics Society Journal*, vol. 32, no. 3, pp. 268-274, 2017.

[13] Y. Shi, C. Zhang, R. Li, M. Cai, and G. Jia, "Theory and application of magnetic flux leakage pipeline detection," *Sensors*, vol. 15, pp. 31036-31055, 2015.

[14] M. Yilai and L. Li, "Research on internal and external defect identification of drill pipe based on weak magnetic inspection," *Insight: Non-Destructive Testing & Condition Monitoring*, vol. 56, no. 1, pp. 31-34, 2014.

[15] D.-K. Kim, H.-R. Yoo, S.-H. Cho, S.-J. Koo, D.-K. Kim, J.-S. Yoo, and Y.-W. Rho, "Inspection of unpiggable natural gas pipelines using in-pipe robot," *International Conference on Advanced Engineering Theory and Applications*, pp. 364-373, 2016.

[16] H. Schempf, E. Mutschler, A. Gavaert, G. Skoptsov, and W. Crowley, "Visual and nondestructive evaluation inspection of live gas mains using the Explorer™ family of pipe robots," *Journal of Field Robotics*, vol. 27, no. 3, pp. 217-249, 2010.

[17] A. Teitsma, "Remote field eddy current inspection of unpiggable pipelines," *Office of Scientific & Technical Information Technical Reports*, 2004.

[18] Y. Sun, Y. Kang, and C. Qiu, "A permanent magnetic perturbation testing sensor," *Sensors & Actuators A: Physical*, vol. 155, no. 2, pp. 226-232, 2009.

[19] Y. Sun, Y. Kang, and C. Qiu, "A new NDT method based on permanent magnetic field perturbation," *NDT & E International*, vol. 44, no. 1, pp. 1-7, 2011.

[20] S. Liu, Y. Sun, M. Gu, C. Liu, L. He, and Y. Kang, "Review and analysis of three representative electromagnetic NDT methods," *Insight*, vol. 59, no. 4, pp. 175-183, 2017.

[21] B. Liu, Y. Cao, H. Zhang, Y. R. Lin, W. R. Sun, and B. Xu, "Weak magnetic flux leakage: A possible method for studying pipeline defects located either inside or outside the structures," *NDT & E International*, vol. 74, pp. 81-86, 2015.

[22] V. Babbar and L. Clapham, "Residual magnetic flux leakage: a possible tool for studying pipeline defects," *Journal of Nondestructive Evaluation*, vol. 22, no. 4, pp. 117-125, 2003.

[23] X. Ren and S. Liu, "Experimental study of phase sensitive detection technique in ECT system," *In 2014 International Conference on Machine Learning and Cybernetics, IEEE*, vol. 1, pp. 121-125, 2014.

[24] D. L. Birx and S. J. Pipenberg, "A complex mapping network for phase sensitive classification," *IEEE Transactions on Neural Networks*, vol. 4, no. 1, pp. 127-135, 1993.

[25] L. S. Obrutsky, V. S. Cecco, S. P. Sullivan, and D. Humphrey, "Transmit receive eddy current probes for circumferential cracks in heat exchanger tubes," *Materials Evaluation*, vol. 54, no. 1, pp. 93-98, 1996.

[26] F. Lingvall and T. Stepinski, "Automatic detecting and classifying defects during eddy current inspection of riveted lap-joints," *NDT & E International*, vol. 33, no. 1, pp. 47-55, 2000.

[27] J. M. Prince and B. P. Hildebrand, "Low-frequency electromagnetic (eddy-current) holography for imaging in conductors," *Applied Optics*, vol. 32, no. 26, pp. 4960-4971, 1993.

[28] B. Helifa, M. Féliachi, I. K. Lefkaier, B. Fouad, A. Zaoui, and N. Lagraa, "Characterization of surface cracks using eddy current NDT simulation by 3D-FEM and inversion by neural network," *In Workshop Problem*, vol. 15, pp. 10, 2016.

[29] H. A. Sabbagh, R. K. Murphy, E. H. Sabbagh, J. Aldrin, J. Knopp, and M. Blodgett, "Computational electromagnetics and model-based inversion: A modern paradigm for eddy-current nondestructive evaluation," *Applied Computational Electromag-*

netics Society Journal, vol. 24, no. 6, pp. 533-540, 2009.

[30] Y. Long, S. Huang, J. Yu, W. Zhao, and S. Wang, "A method of distinguishing the ID and OD defect of the pipe under saturation magnetization," *2018 International Applied Computational Electromagnetics Society Symposium - China (ACES)*, pp. 1-2, 2018.

[31] D. H. Hur, M. S. Choi, H.-S. Shim, D. H. Lee, and O. Yoo, "Influence of signal-to-noise ratio on eddy current signals of cracks in steam generator tubes," *Nuclear Engineering and Technology*, vol. 46, no. 6, pp. 883-888, 2014.

[32] G. Rubinacci, A. Tamburrino, and S. Ventre, "Eddy current imaging of surface breaking defects by using monotonicity based methods," *Applied Computational Electromagnetics Society Journal*, vol. 23, no. 1, pp. 46-52, 2008.

Yue Long received the B.S. degree from School of Automation Science and Electrical Engineering, Beihang University, Beijing, China, in 2017. He is currently pursuing a Ph.D. degree within the Department of Electrical Engineering, Tsinghua University. His major research interests include electromagnetic measurement and nondestructive evaluation.

Songling Huang received the bachelor's degree in Automatic Control Engineering from Southeast University, Nanjing, China, in 1991, and the Ph.D. degree in Nuclear Application Technology from Tsinghua University, Beijing, China, in 2001.

He is currently a Professor within the Department of Electrical Engineering, Tsinghua University. His research interests include nondestructive evaluation and instrument techniques.

Yang Zheng received his B.Sc. degree in Mechanical Engineering and Automation from BeiHang University in 2007 and Ph.D. degree in Mechanical Engineering from Beijing University of Technology in 2012.

Now He works as a Research Fellow in China Special Equipment Inspection and Research Institute. He works on the non-destructive testing and evaluation techniques, mainly including inspection methods study, instruments development and standards development. His current research interests include electromagnetic acoustic transducers and material magnetic testing methods.

Shen Wang received the bachelor's and Ph.D. degrees in Electrical Engineering from Tsinghua University, Beijing, China, in 2002 and 2008, respectively.

He is currently an Associate Professor within the Department of Electrical Engineering, Tsinghua University. His research interests include nondestructive testing and evaluation, and virtual instrumentation.

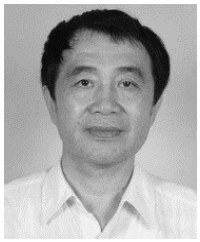

Wei Zhao received the bachelor's degree in Electrical Engineering from Tsinghua University, Beijing, China, in 1982, and the Ph.D. degree from the Moscow Power Engineering Institute Technical University, Moscow, Russia, in 1991.

He is currently a Professor within the Department of Electrical Engineering, Tsinghua University. His research interests include modern electromagnetic measurement and instrument techniques.

An Analytical Model of a New T-cored Coil Used for Eddy Current Nondestructive Evaluation

Siquan Zhang

Department of Electrical and Automation
Shanghai Maritime University, Shanghai, 201306, China
sqzhang@shmtu.edu.cn

Abstract ─ A model of an axisymmetric probe with a new T-core coil that can be used in eddy current testing is developed. The truncated region eigenfunction expansion (TREE) method is used to analyze the coil impedance problem of the T-core coil located above a multi-layer conductive material. First, the magnetic vector potential expressions of each region are formulated, then the coefficients of the magnetic vector potential are derived by using the boundary conditions, finally, the closed form expression of the coil impedance is obtained. The normalized impedance changes of the T-core coil caused by the presence or absence of the multi-layer conductor are calculated using Mathematica. The presented T-core coil is compared with I-core coil and air-core coil. The effects of the T-core parameter a_2, relative permeability μ_f and the thickness of the top section on the change in the coil impedance are discussed respectively. The analytical calculation results are compared with the results of finite element method, and the two agree very well, which verifies the correctness of the proposed T-core coil model.

Index Terms ─ Analytical model, coil impedance, eddy current testing, non-destructive evaluation, T-core coil, truncated region eigenfunction expansion.

I. INTRODUCTION

In eddy current testing (ECT), probes with ferrite cores of different shapes have been widely used to locate cracks, corrosion and other defects in multilayer conductive structures. Compared with the air-core coils, the ferrite-core coils have many advantages, such as concentrating magnetic flux, reducing magnetic flux loss and shielding external interference. Therefore, in eddy current detection, the ferrite-core coil probe can obtain a larger impedance change signal, so the defects in the conductor are easier to find and evaluate. I-core coils have already been investigated, and they can obtain better results than air-core coil in ECT [1-5]. Here we propose a new cored-coil as shown in Fig. 1, which is very similar to the I-core coil, here we call it T-core coil. The T-core coil can be obtained easily by adding a flat cylindrical core above the I-core, but the T-core has a better flux concentration effect than the I-core. On the other hand, if coils of the same size are used, the size of the T-core probe can be smaller than the C-core probe [6] and the E-core probe [7, 8]. No discussion related to T-core probes has been found in the literature, so it is necessary to investigate its application potential in ECT.

The problem of a T-core probe located above a layered half-space of conducting material is solved using the method of truncation region eigenfunction expansion (TREE) [9-11]. Azimuthal component of magnetic vector potential A_φ is expressed in the form of a series of orthogonal appropriate eigenfunctions involving discrete eigenvalues. Applying the Dirichlet boundary condition in the truncation surface is equivalent to a vanishing normal component of magnetic field. By truncating the solution domain, the solution can be expressed as a series form rather than as an integral. The most important advantage of the method is that by a careful selection of the discrete eigenvalues and the corresponding eigenfunctions, the field continuity can be satisfied at these different boundaries and interfaces simultaneously. And the numerical implementation is more efficient and the error control is easier. Firstly, a filamentary coil [12] was used in the analysis, then the expressions that describe the magnetic vector potentials of each region were derived. The closed form expression for the impedance of the T-core coil above the multi-layer conductor was obtained. The analytical calculation results obtained by the TREE method were compared with the finite element method (FEM) [13,14], which showed a very good agreement.

II. SOLUTION

The problem to be analyzed first is shown in Fig. 2. A filamentary coil excited by a harmonic current $Ie^{j\omega t}$ is wound around a T-core with relative magnetic permeability μ_f . The probe is located above a two-layer conducting half space with conductivity σ_6 and σ_7. The plane z = 0 coincides with the bottom of the core.

Submitted On: October 28, 2019
Accepted On: July 5, 2020

https://doi.org/10.47037/2020.ACES.J.350917

According to the problem geometry, seven regions are formed. Using the Bessel functions J_n and Y_n, discrete eigenvalues were computed.

The eigenvalues q_i for regions 1, 5, 6, and 7 of Fig. 2 are the positive real roots of the equation:

$$J_1(q_i b) = 0\,, \tag{1}$$

where $J_1(x)$ is the Bessel function of the first kind. Because regions 2, 3, 4 comprise two sub-regions, the magnetic core and the air, so according to their radial dependences, the expressions of the magnetic vector potential for these two sub-regions can be analyzed as below.

For region 2:

$$A_{1core} = A_E J_1(m_i r), \quad 0 \le r \le a_2, \tag{2}$$

$$A_{1air} = A_E B_{1F} J_1(m_i r) + A_E C_{1F} Y_1(m_i r), \quad a_2 \le r \le b, \tag{3}$$

where m_i are the corresponding discrete eigenvalues.

Equations can be obtained from the continuity of B_r and H_z on the interface $r = a_2$, which yield the following expressions for B_{1F} and C_{1F}:

$$B_{1F} = \frac{\pi m_i a_2}{2}[J_1(m_i a_2)Y_0(m_i a_2) - \frac{J_0(m_i a_2)Y_1(m_i a_2)}{\mu_f}], \tag{4}$$

$$C_{1F} = \frac{\pi m_i a_2}{2} J_1(m_i a_2)J_0(m_i a_2)(\frac{1}{\mu_f} - 1)\,. \tag{5}$$

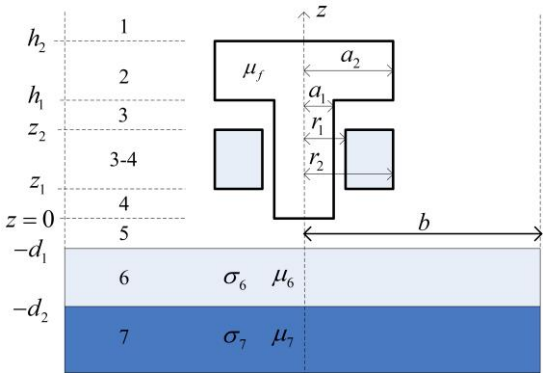

Fig. 1. Rectangular cross section T-core coil located above a layered conductive half-space.

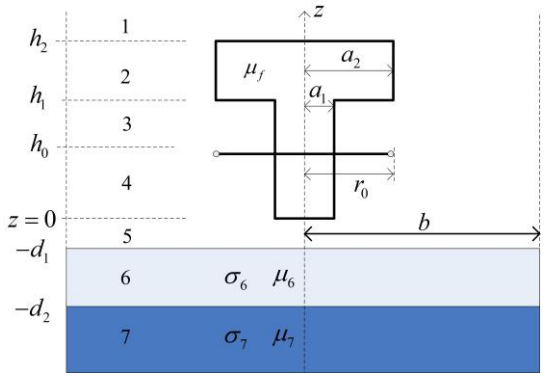

Fig. 2. Filamentary T-core coil located above a layered conductive half-space.

Since at the truncation boundary $r = b$, $A_\varphi(b, z) = 0$ must be satisfied, the following equation is obtained:

$$L_1(m_i b) = 0\,, \tag{6}$$

where

$$L_1(m_i r) = B_{1F} J_1(m_i r) + C_{1F} Y_1(m_i r)\,. \tag{7}$$

The eigenvalues m_i are the positive real roots of (6).

Using the same method to region 3 and 4 in Fig. 2, since the boundary condition must also be met, the following equation is formed:

$$R_1(p_i b) = 0\,, \tag{8}$$

where

$$R_1(p_i r) = B_{2F} J_1(p_i r) + C_{2F} Y_1(p_i r)\,, \tag{9}$$

$$B_{2F} = \frac{\pi p_i a_1}{2}[J_1(p_i a_1)Y_0(p_i a_1) - \frac{J_0(p_i a_1)Y_1(p_i a_1)}{\mu_f}], \tag{10}$$

$$C_{2F} = \frac{\pi p_i a_1}{2} J_1(p_i a_1)J_0(p_i a_1)(\frac{1}{\mu_f} - 1)\,. \tag{11}$$

The eigenvalues p_i are the real positive roots of (8).

The magnetic vector potential of each region was written as follows using matrix notation:

$$A_1(r, z) = J_1(\mathbf{q}^{\mathbf{T}} r)\mathbf{q}^{-1} e^{-\mathbf{q}z}\mathbf{C}_1, \tag{12}$$

$$A_2(r, z) = \begin{matrix} J_1(\mathbf{m}^{\mathbf{T}} r) \\ L_1(\mathbf{m}^{\mathbf{T}} r) \end{matrix} \mathbf{m}^{-1}(e^{-\mathbf{m}z}\mathbf{C}_2 - e^{\mathbf{m}z}\mathbf{B}_2) \quad \begin{matrix} 0 \le r \le a_2 \\ a_2 \le r \le b \end{matrix}, \tag{13}$$

$$A_3(r, z) = \begin{matrix} J_1(\mathbf{p}^{\mathbf{T}} r) \\ R_1(\mathbf{p}^{\mathbf{T}} r) \end{matrix} \mathbf{p}^{-1}(e^{-\mathbf{p}z}\mathbf{C}_3 - e^{\mathbf{p}z}\mathbf{B}_3) \quad \begin{matrix} 0 \le r \le a_1 \\ a_1 \le r \le b \end{matrix}, \tag{14}$$

$$A_4(r, z) = \begin{matrix} J_1(\mathbf{p}^{\mathbf{T}} r) \\ R_1(\mathbf{p}^{\mathbf{T}} r) \end{matrix} \mathbf{p}^{-1}(e^{-\mathbf{p}z}\mathbf{C}_4 - e^{\mathbf{p}z}\mathbf{B}_4) \quad \begin{matrix} 0 \le r \le a_1 \\ a_1 \le r \le b \end{matrix}, \tag{15}$$

$$A_5(r, z) = J_1(\mathbf{q}^{\mathbf{T}} r)\mathbf{q}^{-1}(e^{-\mathbf{q}z}\mathbf{C}_5 - e^{\mathbf{q}z}\mathbf{B}_5)\,, \tag{16}$$

$$A_6(r, z) = J_1(\mathbf{q}^{\mathbf{T}} r)\mathbf{u}^{-1}(e^{-\mathbf{u}z}\mathbf{C}_6 - e^{\mathbf{u}z}\mathbf{B}_6)\,, \tag{17}$$

$$A_7(r, z) = -J_1(\mathbf{q}^{\mathbf{T}} r)\mathbf{v}^{-1} e^{\mathbf{v}z}\mathbf{B}_7, \tag{18}$$

where

$$\mathbf{u} = \sqrt{\mathbf{q}^2 + j\omega\mu_6\mu_0\sigma_6}\,, \tag{19}$$

$$\mathbf{v} = \sqrt{\mathbf{q}^2 + j\omega\mu_7\mu_0\sigma_7}\,, \tag{20}$$

where J_i and Y_i are Bessel functions of i order. $J_1(\mathbf{q}^{\mathbf{T}} r)$, $J_1(\mathbf{m}^{\mathbf{T}} r)$, $L_1(\mathbf{m}^{\mathbf{T}} r)$, $R_1(\mathbf{p}^{\mathbf{T}} r)$ and $J_1(\mathbf{p}^{\mathbf{T}} r)$ are line vectors, $\mathbf{q}^{-1}, \mathbf{m}^{-1}, \mathbf{p}^{-1}, \mathbf{u}^{-1}, \mathbf{v}^{-1}$ and exponentials $e^{\pm\mathbf{q}z}$, $e^{\pm\mathbf{m}z}, e^{\pm\mathbf{p}z}, e^{\pm\mathbf{u}z}, e^{\mathbf{v}z}$ are diagonal matrices. $\mathbf{C}_i$ and $\mathbf{B}_i$ are column vectors of unknown coefficients.

Applying the interface conditions (continuity of B_z and H_r) between the seven regions of Fig. 2, the equations for calculation of the unknown vector coefficients can be obtained.

For the coil of rectangular cross-section shown in Fig. 1, the coil has width r_2-r_1, height z_2-z_1 and N wire turns, the magnetic vector potential A_φ in the various regions can be calculated using superposition in an integration form:

$$A(r,z)=\int_{r_1}^{r_2}\int_{z_1}^{z_2}A(r,z,r_0,z_0)dr_0dz_0\,. \tag{21}$$

Once the magnetic vector potentials of the regions 3, 4 and 3-4 in Fig. 2 are determined, the impedance of the coil in Fig. 1 can be calculated by integrating $rA_{3\text{-}4}$ over the cross section of the coil:

$$Z=\frac{j2\pi\omega i_0}{I^2}\int_{r_1}^{r_2}\int_{z_1}^{z_2}rA_{3-4}(r,z)drdz, \tag{22}$$

where

$$i_0=\frac{NI}{(r_2-r_1)(z_2-z_1)}. \tag{23}$$

The final expression of a T-core coil impedance can be obtained:

$$\begin{aligned}Z=&\frac{j\omega\mu\pi N^2}{(r_2-r_1)^2(z_2-z_1)^2}\chi(\mathbf{p}r_1,\mathbf{p}r_2)\mathbf{p}^{-4}\\&[2(z_2-z_1)\mathbf{p}+e^{\mathbf{p}(z_1-z_2)}-e^{\mathbf{p}(z_2-z_1)}\\&+\mathbf{W}_1\mathbf{W}_2^{-1}\mathbf{W}_3]\mathbf{p}^{-3}\mathbf{D}^{-1}\chi(\mathbf{p}r_1,\mathbf{p}r_2),\end{aligned} \tag{24}$$

where

$$\chi(x_1,x_2)=\int_{x_1}^{x_2}xR_1(x)dx\,, \tag{25}$$

$$\mathbf{W}_1=(e^{-\mathbf{p}z_1}-e^{-\mathbf{p}z_2})\mathbf{C}_{47}-(e^{\mathbf{p}z_2}-e^{\mathbf{p}z_1})\mathbf{B}_{47}\,, \tag{26}$$

$$\begin{aligned}\mathbf{W}_2=&(\lambda_1\mathbf{F}^{-1}\mathbf{G}+\lambda_2\mathbf{F}^{-1}\mathbf{G}^*)e^{-\mathbf{p}h_1}\mathbf{C}_{47}\\&-(\lambda_1\mathbf{F}^{-1}\mathbf{G}-\lambda_2\mathbf{F}^{-1}\mathbf{G}^*)e^{\mathbf{p}h_1}\mathbf{B}_{47},\end{aligned} \tag{27}$$

$$\begin{aligned}\mathbf{W}_3=&(\lambda_1\mathbf{F}^{-1}\mathbf{G}-\lambda_2\mathbf{F}^{-1}\mathbf{G}^*)(e^{\mathbf{p}(h_1-z_1)}-e^{\mathbf{p}(h_1-z_2)})\\&-(\lambda_1\mathbf{F}^{-1}\mathbf{G}+\lambda_2\mathbf{F}^{-1}\mathbf{G}^*)(e^{\mathbf{p}(z_2-h_1)}-e^{\mathbf{p}(z_1-h_1)}),\end{aligned} \tag{28}$$

$$\begin{matrix}\lambda_1\\ \lambda_2\end{matrix}=(\mathbf{T}-\mathbf{U})e^{\mathbf{m}(h_1-h_2)}\pm(\mathbf{T}+\mathbf{U})e^{\mathbf{m}(h_2-h_1)}\,, \tag{29}$$

$$\begin{matrix}\mathbf{B}_{47}\\ \mathbf{C}_{47}\end{matrix}=\frac{1}{2}(\mathbf{N}^{*-1}\mp\mathbf{H}^{-1})\mathbf{E}\mathbf{C}_{57}+\frac{1}{2}(\mathbf{N}^{*-1}\pm\mathbf{H}^{-1})\mathbf{E}\mathbf{B}_{57}\,, \tag{30}$$

$$\begin{aligned}\begin{matrix}\mathbf{B}_{57}\\ \mathbf{C}_{57}\end{matrix}=&\frac{1}{2}e^{\pm\mathbf{q}d_1}(\mu_6^{-1}\mp\mathbf{q}\mathbf{u}^{-1})e^{\mathbf{u}d_1}\mathbf{C}_{67}\\&+\frac{1}{2}e^{\pm\mathbf{q}d_1}(\mu_6^{-1}\pm\mathbf{q}\mathbf{u}^{-1})e^{-\mathbf{u}d_1}\mathbf{B}_{67},\end{aligned} \tag{31}$$

$$\begin{matrix}\mathbf{B}_{67}\\ \mathbf{C}_{67}\end{matrix}=\frac{1}{2}e^{\pm\mathbf{u}d_2}(\frac{\mu_6}{\mu_7}\pm\mathbf{u}\mathbf{v}^{-1})e^{-\mathbf{v}d_2}\,, \tag{32}$$

and

$$\mathbf{B}_{n7}=\frac{\mathbf{B}_n}{\mathbf{B}_7}\,, \tag{33}$$

$$\mathbf{C}_{n7}=\frac{\mathbf{C}_n}{\mathbf{B}_7}\,, \tag{34}$$

where **T**, **U**, **G**, **G***, **H** and **N*** are full matrices; **E**, **F**, and **D** are diagonal matrices, and they are defined as in [3], [4] and [6].

III. RESULTS AND DISCUSSIONS

The parameters in Table 1 were used in calculating the impedance of the T-core coil shown in Fig. 1. The proposed T-core coil is a new type of ECT probe, the parameters shown in Table 1 are set according to the parameters of the air-core coil and I-core coil in the references. The calculation was implemented in Mathematica using (24). In the calculations, the solution domain was truncated according to the parameter b = 60 mm, and the number of summation terms N_s = 60. The analytical calculation results were compared with the results of the finite element method. The Maxwell package was used, the meshes of triangles were 10866 and they can be refined using manual method.

In order to determine the discrete eigenvalues m_i and p_i, the FindRoot[] function was applied. The integral (25) was calculated using the expansion of the Struve and Bessel functions [2,10,15] by the aid of the BesselJ[], BesselY[] and StruveH[]. The matrices **D**, **F**, **H**, and **N*** were inverted using function Inverse[].

First, the impedances of the probes located above the layered conductor were calculated as $Z = R + jX$, then the conductor is removed ($\sigma_6 = \sigma_7 = 0$), the impedances of the probes were calculated as $Z_0 = R_0 + jX_0$. The changes in resistance and reactance were calculated as $\Delta R = R - R_0$ and $\Delta X = X - X_0$ respectively.

In order to verify the effectiveness of the proposed T-core coil in eddy current testing, the impedance changes of the I-core coil and the air-core coil were also calculated. In Fig. 1 and Fig. 2, when $a_2 = a_1$, the T-core becomes the I-core, so the I-core has the same inner core radius a_1, the same height h_2 and the same relative permeability μ_f = 500 with the T-core. If μ_f = 1, the ferrite-core coil becomes an air-core coil.

Table 1: Coil, core and conductor parameters used in calculation

Inner core radius	a_1	2 mm
Outer core radius	a_2	6 mm
Inner core height	h_1	6 mm
Outer core height	h_2	8 mm
Relative permeability	μ_f	500
Inner coil radius	r_1	2.2 mm
Outer coil radius	r_2	6 mm
Offset	z_1	0 mm
Parameter	z_2	5 mm
Number of turns	N	600
Liftoff	d_1	1 mm
Parameter	d_2	3 mm
Relative permeability	μ_6, μ_7	1
Conductivity	σ_6, σ_7	10 MS/m
Radius of the domain	b	60 mm

The calculations were performed for 31 different frequencies ranging from 100 Hz to 100 kHz. Figure 3 and Fig. 4 show the changes in resistance and reactance normalized in relation to reactance X_0 obtained from the analytical calculation and FEM for an air-core coil, an I-core coil and a T-core coil. As can be seen from the

figures, the calculated results of the TREE method agree with the FEM results very well. At the same excitation frequency, whether it is resistance or reactance, the impedance changes of the T-core coil are the largest among the three coils.

The inductances L_0 of the air-core coil, the I-core coil and the T-core coil are calculated as 1.769 mH, 4.219 mH, and 6.098 mH respectively. At the same excitation frequency, the T-core coil is more sensitive than the I-core coil and the air-core coil.

Figure 5 shows an impedance plane diagram for the frequency f varying from 100 Hz to 100 kHz. The calculation results of TREE method and FEM method can be matched accurately.

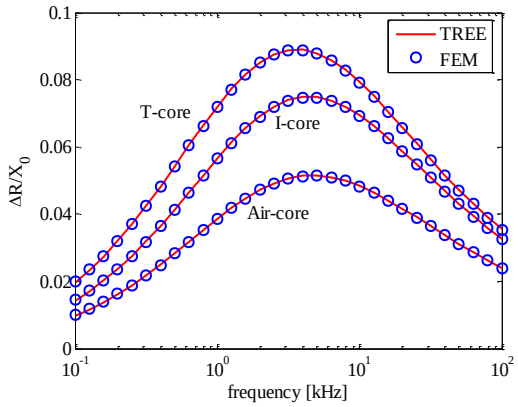

Fig. 3. Real part of the normalized impedance change as a function of frequency for an air-core coil (μ_f = 1), an I-core coil and a T-core coil (μ_f = 500).

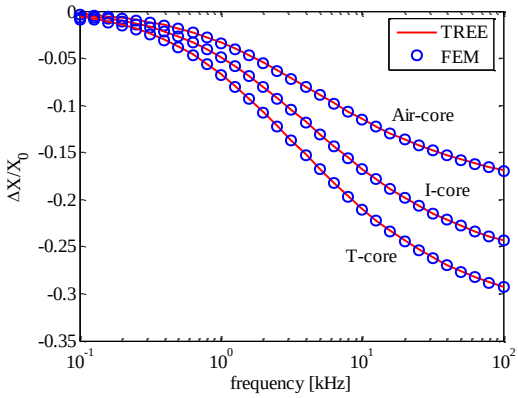

Fig. 4. Imaginary part of the normalized impedance change as a function of frequency for an air-core coil (μ_f = 1), an I-core coil and a T-core coil (μ_f = 500).

Table 2 shows the real parts of impedance change in a T-core coil obtained using FEM and TREE methods for several frequencies. The parameters used in the TREE method and the FEM method are the same as Table 1. In all cases, the relative errors between analytical results and FEM results are less than 0.5%, which shows they agree very well. If the truncated radius and the number of summation terms of the TREE method are increased, the accuracy of the calculation can also be improved. It took about 2 seconds to complete an impedance calculation using TREE method, which is less than the 4 seconds taken by the FEM on a computer with 3.70 GHz Pentium processor and 16 GB RAM. In the case of a large number of impedance calculations, the TREE method will show more advantage in computation speed than FEM.

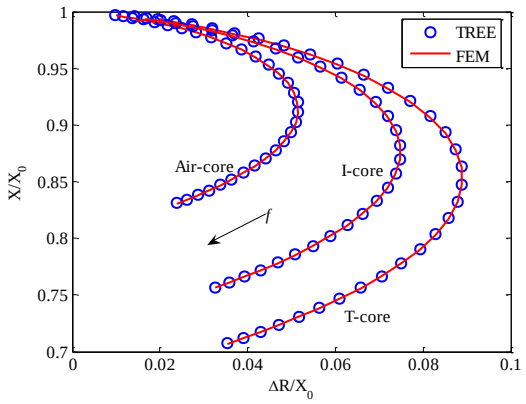

Fig. 5. Impedance plane diagram for an air-core coil (μ_f = 1), an I-core coil and a T-core coil (μ_f = 500) (frequency varying from 100 Hz to 100 kHz).

Table 2: Real part of impedance changes of a T-core coil obtained using FEM and TREE methods

f (kHz)	FEM (Ω)	TREE (Ω)	Error (%)
0.5	1.04256	1.0378	-0.45
1	2.7598	2.7478	-0.43
5	16.8613	16.8048	-0.33
10	30.3275	30.2416	-0.28
100	135.5627	135.2262	-0.25

Figure 6 and Fig. 7 show the relationship between the impedance change in the T-core coil and the length of a_2. The change in the impedance of the T-core coil increases as the length of a_2 increases. When a_2 is approximately 4.4 mm, the T-core coil shows the maximum sensitivity, and then as a_2 increases, the sensitivity decreases gradually.

The influence of the relative permeability μ_f of the T-core on the change in coil resistance is shown in Fig. 8, where f = 4 kHz and a_2 = 6 mm. When the relative permeability μ_f of the T-core is less than 1000, the ΔR value increases significantly with the increase of μ_f, when the relative permeability μ_f of the T-core is greater than 1000, the ΔR value increases slowly with the increase of relative permeability.

The relationship between the thicknesses of the top

section of the T-core and the change in coil resistance is shown in Fig. 9, where $f = 4$ kHz, $a_2 = 6$ mm and $\mu_f = 500$. Although the ΔR will increase as the thickness of the top section of T-core increases, the size of the probe will increase accordingly. Therefore, a more appropriate choice is to make the thickness of the top section of the T-core consistent with the size of the other parts of the core.

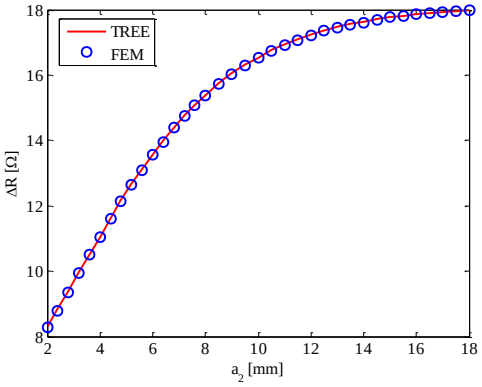

Fig. 6. Real part of the impedance change as a function of a_2 for a T-core coil ($\mu_f = 500$).

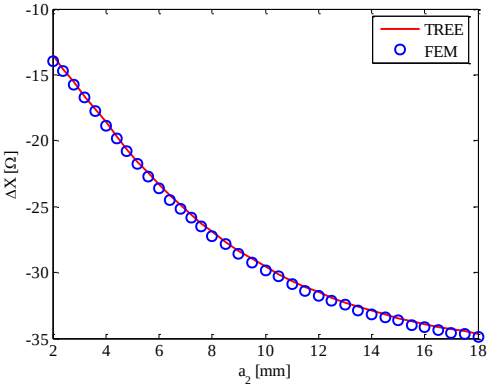

Fig. 7. Imaginary part of the impedance change as a function of a_2 for a T-core coil ($\mu_f = 500$).

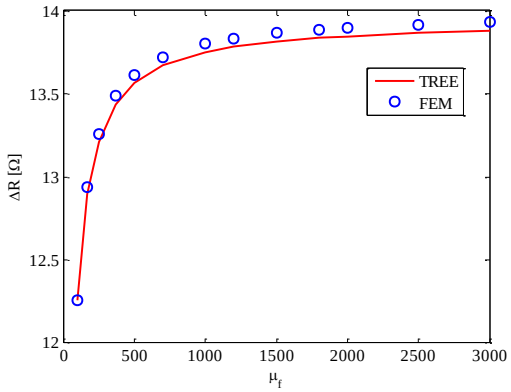

Fig. 8. Real part of the impedance change as a function of μ_f for a T-core coil.

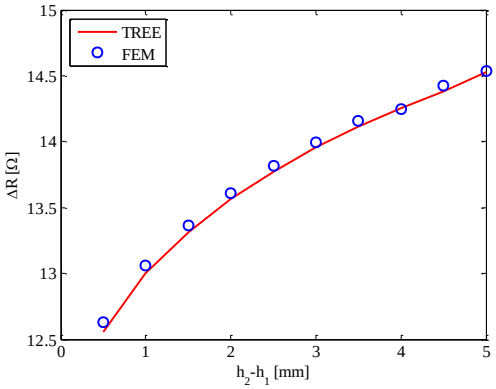

Fig. 9. Real part of the impedance change as a function of h_2-h_1 for a T-core coil.

IV. CONCLUSION

This paper presents an analytical model of a T-core coil placed over a multi-layer conductor. The final expression of the coil impedance obtained by the TREE method is in a closed form and can be fast implemented in softwares such as Mathematica or Matlab. The analytical model is verified by the finite element method. Compared with the I-core coil with the same inner core radius, the same height and the same relative permeability, the proposed T-core coil has higher magnetic flux concentration and shielding effect. The T-core can be used in the same probe together with the I-core to achieve better test results. The analytical T-core probe model can be used in computer simulation, or it can be directly applied in the detection of defects in multi-layer conductors. The solution also can be extended to more complex conductive structures with defects.

REFERENCES

[1] T. P. Theodoulidis, "Model of ferrite-cored probes for eddy current nondestructive evaluation," *J. Appl. Phys.*, vol. 93, no. 5, pp. 3071-3078, 2003.

[2] Y. Lu, J. R. Bowler, and T. P. Theodoulidis, "An analytical model of a ferrite-cored inductor used as an eddy current probe," *J. Appl. Phys.*, vol. 111, no. 10, pp. 103907-10, 2012.

[3] G. Tytko and L. Dziczkowski, "I-cored coil probe located above a conductive plate with a surface hole," *Measurement Science Review*, vol. 18, no. 1, pp. 7-12, 2018.

[4] G. Tytko and L. Dziczkowski, "An analytical model of an I-cored coil located above a conductive material with a hole," *The European Physical Journal Applied Physics.*, vol. 82, no. 21001, pp.1-7, 2018.

[5] Y. Li, Y. Wang, Z. Liu, I. M. Z. Abidin and Z. Chen, "Characteristics regarding lift-off intersection of pulse-modulation eddy current signals for evaluation of hidden thickness loss in cladded

conductors," *Sensors.*, vol. 19, no. 4102, pp. 1-14, 2019.

[6] H. Bayani, T. Theodoulidis, and I. Sasada, *Application of Eigenfunction Expansions to Eddy Current NDE: A Model of Cup-Cored Probes.* London, U.K.: IOP Press, pp. 57-64, 2007.

[7] F. Sakkaki and H. Bayani, "Solution to the problem of E-cored coil above a layered half-space using the method of truncated region eigenfunction expansion," *Journal of Applied Physics*, vol. 111, no. 7, pp. 2829-64, 2012.

[8] G. Tytko and L. Dziczkowski, "Calculation of the impedance of an E-cored coil placed above a conductive material with a surface hole," *Measurement Science Review*, vol. 19, no. 2, pp. 43-47, 2019.

[9] T. P. Theodoulidis and J. R. Bowler, "The truncated region eigenfunction expansion method for the solution of boundary value problems in eddy current non-destructive evaluation," *Rev. Progr. Quant. Non-Destruct. Eval.*, vol. 24A, pp. 403-408, 2004.

[10] T. P. Theodoulidis and E. E. Kriezis, *Eddy Current Canonical Problems (With Applications to Non-destructive Evaluation)*. Tech Sci. Press, Duluth, Georgia, pp. 106-121, 2006.

[11] F. Jiang and S. Liu, "Calculation and analysis of an analytical model for magnetic field monitoring based on TREE in eddy current testing," *Applied Computational Electromagnetics Society Journal*, vol. 33, no. 12, pp. 1489-1497, 2018.

[12] G. Tytko and L. Dziczkowski, "Fast calculation of the filamentary coil impedance using the truncated region eigenfunction expansion method," *Applied Computational Electromagnetics Society Journal*, vol. 33, no. 12, pp. 1461-1466, 2018.

[13] H. Zaidi, L. Santandrea, G. Krebs, Y. Le Bihan, and E. Demaldent, "FEM technique for modeling eddy-current testing of ferromagnetic media with small skin depth," *IEEE Trans. Magn.*, vol. 50, no. 2, pp. 129-132, 2014.

[14] B. Helifa, M. Féliachi, I. K. Lefkaier, B. Fouad, A. Zaoui, and N. Lagraa, "Characterization of surface cracks using eddy current NDT simulation by 3D-FEM and inversion by neural network," *Applied Computational Electromagnetics Society Journal*, vol. 31, no. 2, pp. 187-194, 2016.

[15] I. S. Gradshtein and I. M. Ryzhik, *Tables of Integrals, Series, and Products*. New York, Academic Press, 1980.

Siquan Zhang received the Ph.D. degree in Material Processing Engineering from the South China University of Technology, Guangzhou, China. His current research interests include eddy current testing, analytical model in non-destructive testing.